CORE-SHELL HETEROSTRUCTURED NANOWIRES ON FOREIGN SUBSTRATES

CORE-SHELL HETEROSTRUCTURED NANOWIRES ON FOREIGN SUBSTRATES FOR USE IN OPTO-ELECTRONIC APPLICATIONS

By

PARSIAN KATAL MOHSENI, B.Eng.

A Thesis
Submitted to the School of Graduate Studies
in Partial Fulfilment of the Requirements
for the Degree
Doctor of Philosophy

McMaster University

DOCTOR OF PHILOSOPHY (2011) McMaster University

(Engineering Physics) Hamilton, Ontario

TITLE: Core-Shell Heterostructured Nanowires on Foreign Substrates for use in Opto-Electronic Applications

AUTHOR: Parsian Katal Mohseni, B.Eng.
(McMaster University)

SUPERVISOR: Dr. Ray R. LaPierre

NUMBER OF PAGES: xxvii, 269

Abstract

The Au nanoparticle-assisted growth of coaxially heterostructured III-V compound semiconductor nanowires (NWs) on foreign substrates, through gas-source molecular beam epitaxy, was explored. The structural properties of GaP/GaAsP NW systems were characterized through extensive electron microscopy-based techniques, leading to several key findings. A core-multishell NW architecture was defined, based upon the combination of seed-mediated axial growth and sidewall diffusion-mediated radial growth regimes. The formation of undesirable stacking faults, characterized as zincblende insertions within an otherwise wurtzite crystal, was effectively eliminated through the control of seed supersaturation. Thus, a novel method for the elimination of stacking faults and achievement of phase-purity in NW heterostructures was realized. The non-uniformity of group V adatom incorporation within NW segments composed of ternary III-V compounds was also investigated. The effects of preferential P-incorporation and passivating GaP shell layers on the optical properties of GaAsP core segments were determined through spectroscopic characterization techniques.

Furthermore, the growth of GaAs NWs on several foreign substrates, including single crystalline Si substrates, stainless steel foils, glass substrates with polycrystalline Si buffer layers, carbon-nanotube (CNT) composite films, and highly-ordered pyrolytic graphite (HOPG), was explored. Growth on HOPG was shown to proceed according to a Ga-assisted mechanism, for which a qualitative growth model was proposed. Au-nanoparticle mediated growth was achieved on all other surfaces. The CNT composite films were selected as the most suitable substrate for the fabrication of NW-based opto-electronic devices. Flexible photovoltaic cells were fabricated using this nano-hybrid material, demonstrating a conversion efficiency of 0.32% under mechanical flexure up to a bend radius of 12.5 mm. The GaAs NWs were confirmed to be the active light-harvesting medium, while the CNT films served as flexible substrates and back-side electrodes. This work is presented as a novel route towards the realization of low-cost, flexible NW-based opto-electronic device applications.

Acknowledgments

I would like to express my gratitude, first and foremost, to my thesis supervisor, Dr. Ray LaPierre. I was recently reminded of our first conversation concerning nanowires, roughly two years prior to the start of my graduate studies. There was a remarkable sense of excitement and wonder in that conversation; a sense that has been a part of every discussion we have shared on the topic since then. His commitment, guidance, patience, and encouragement will always be appreciated. I thank him for giving me the freedom to explore uncharted waters and I thank him for twisting my arm when it was needed.

I am also grateful to the members of my supervisory committee, Dr. Alex Adronov, Dr. Adrian Kitai, and Dr. John Preston, for imparting constructive feedback and providing valued insight.

If not for the efforts of Dr. Brad Robinson, this work would simply have not been possible. I am indebted to him, not only for MBE growths and the stimulating discussions we shared on the same topic, but also for offering his refreshing perspective on everything from geo-politics to poetry! In the same light, I would also like to thank Dr. Shahram Ghanad-Tavakoli for MBE growths and for providing much valued research advice.

The staff and research associates of the CEDT deserve tremendous recognition. I am particularly grateful to Doris Stevanovic and Dr. Zhilin Peng for being so meticulous and patient during our clean-room training sessions, for opening my eyes to unforeseen processing obstacles, and for always being willing to help. Thanks to Dr. Doug Bruce and Graham Pearson for further training and support. Additionally, I would like to express my appreciation for everyone at the CCEM, including Dr. Steve Koprich, Chris Butcher, Andy Duft, Fred Pearson, Julia Huang, Dr. Nadi Braidy, Dr. Christian Maunders, and Dr. Carmen Andrei, for providing continued advice and assistance.

I sincerely value the collaborations which I have had the opportunity and privilege to be part of during my graduate studies. I am truly grateful to Dr. Alex Adronov and Dr. Gregor Lawson for their partnership. Our strengths were complementary and I am grateful to have worked with them. I am greatly indebted to Dr. Yuri Pusep. I thank him for challenging me and for motivating me. Moreover, I would like to thank him for his hospitality and generosity during my stay at São Carlos. I also would like to thank Dr. Ariano De Giovanni Rodrigues, not only for sharing his expertise on the topic of Raman scattering, but also for an unforgettable tour of Rio! Thanks to Dr. David Comedi and Dr. Jonathan Baugh for our enlightening discussions. Furthermore, I would like to extend my gratitude to Dr. Gregor Weihs, Dr. Christophe Couteau, and Harishankar Jayakumar for their co-operation in optical characterization experiments.

I would like to thank my friends and fellow 'LaPierre Research Group' members, both past and present, including Martin, Hanna, Subir, Chris, David, Mike, Nuzhat, Ahmed, Nooshin, Jonathan, and Andrew. I am privileged to have shared this wonderful experience with each and every one of them, and have enjoyed the classes, conferences, lunches, experiments, discussions, and get-togethers more because they were present.

On a personal note, I would like to express my appreciation to my closest friends, Babak, Nima, Sina, Lori, Rachel, Adam, Albert, Khaled, Isaac, Leah, and Erin for the laughs and tears we have shared over the past few years. In particular, I extend my heartfelt gratitude to (soon-to-be Dr.) Babak Behnam Azad. Thanks for keeping me sane, brother!

I would like to thank my family. To my parents, thank you for believing in me; thank you for sacrificing so that I could have; thank you for teaching me the value of hard work; and thank you for instilling within me a sense of curiosity. To my brother and sister, thank you for supporting and inspiring me. It comforts me to know that I can rely on you for anything. To my favourite Hamiltonian cousin, thanks for putting up with me during comps season! It has been amazing getting to know you once again, after so many years apart.

I would like to gratefully acknowledge the financial support of the Department of Engineering Physics, the Ontario Graduate Scholarships, the Ontario Centres of Excellence, and the Canadian Institute for Photonic Innovations.

Dedicated with loving gratitude to my parents, Behjat & Masoud Katal Mohseni.

To become who we are – human beings who are new, unique; who give themselves laws; who create themselves! To that end we must become the best students and discoverers of everything lawful and necessary in the world: we must become physicists in order become creators in this sense. So, long live physics! And even more so, that which compels us to turn to physics – our honesty!

– F. W. Nietzsche –

Table of Contents

Chapter 4 GaAs Nanowires on Foreign Substrates 133

List of Figures

List of Tables

List of Acronyms

μ-PL	Micro-Photoluminescence
AES	Auger Electron Spectroscopy
ATEM	Analytical Transmission Electron Microscopy
BSE	Backscattered Electron
CCD	Charge-Coupled Device
CL	Cathodoluminescence
CMOS	Complementary Metal-Oxide-Semiconductor
CNT	Carbon-Nanotube
CVD	Chemical Vapour Deposition
DI	Deionized
EBIC	Electron-Beam Induced Current
EDXS	Energy Dispersive X-ray Spectrometry
EELS	Electron Energy-Loss Spectroscopy
EL	Electroluminescence
ES-MBE	Elemental-Source Molecular Beam Epitaxy
FFT	Fast Fourier Transform
FIB	Focussed Ion Beam
FWHL	Full-Width at Half-Length
FWHM	Full-Width at Half-Maximum
GS-MBE	Gas-Source Molecular Beam Epitaxy
HAADF	High-Angle Annular Dark-Field
HF	Hydrofluoric Acid
HOPG	Highly-Ordered Pyrolytic Graphite
HR-TEM	High-Resolution Transmission Electron Microscopy
ITO	Indium-Tin-Oxide
LbL	Layer-by-Layer
LED	Light-Emitting-Diode
LMIS	Liquid Metal Ion Source
LO	Longitudinal Optical
MOVPE	Metal Organic Vapour Phase Epitaxy
M-PL	Magneto-Photoluminescence
MQW	Multiple Quantum-Well
NP	Nanoparticle
NW	Nanowire
P3HT	Poly(3-Hexylthiophene)
PE	Primary Electron
PE-CVD	Plasma-Enhanced Chemical Vapour Deposition
PEI	Poly(Ethylene Imine)
PET	Polyethylene Terephthalate

PL	Photoluminescence
PV	Photovoltaic
RHEED	Reflection High-Energy Electron Diffraction
RIE	Reactive Ion Etching
RS	Raman Scattering
RTA	Rapid Thermal Annealing
SAD	Selected Area Diffraction
SE	Secondary Electron
SEM	Scanning Electron Microscopy
SI	Secondary Ion
SIM	Supply Interruption Method
SL	Superlattice
STEM	Scanning Transmission Electron Microscopy
STM	Scanning Tunnelling Microscopy
SWNT	Single-Walled Nanotube
TEM	Transmission Electron Microscopy
TMI	Trimethylindium
TO	Transverse Optical
UHR-TEM	Ultra High-Resolution Transmission Electron Microscopy
UHV	Ultra-High Vacuum
UV	Ultraviolet
VLS	Vapour-Liquid-Solid
Wz	Wurtzite
Zb	Zincblende

Chapter 1

Background and Motivations

The study of semiconductor nanowires is one of a multifaceted nature, relying, at its core, upon a foundation of solid-state physics. The controlled growth of such high aspect ratio, single crystalline structures is rooted in the seminal work of Wagner and Ellis, first presented in the 1960's, and is understood, to this day, based on their model of the vapour-liquid-solid (VLS) mechanism for the bottom-up assembly of adatoms, leading to the anisotropic formation of crystals [1]. Since then, the nanowire field has developed into one of the most active research areas in nanoscience and nanotechnology [2]. The high degree of interest in the field is due, in one respect, to the wealth of information these pseudo one-dimensional structures provide for the realm of crystal growth. In another respect, semiconductor nanowires present a medium through which the landscape of the semiconductor devices industry can be appreciably reshaped and advanced, through novel device architectures and improved performance capabilities.

This chapter is intended to serve as a source of relevant background information, providing for the reader the requisite introductory concepts related to the growth of nanowires (NWs) and the scope of their integration within opto-electronic devices. Starting with Section 1.1, a brief overview of several notable

NW-based opto-electronic devices published in recent literature is presented. Our focus is shifted, in Section 1.2, towards specific motivations for the employment of coaxially heterostructured NWs in photovoltaic applications. In Section 1.3, we explore the VLS mechanism as related to the growth of NWs composed of III-V semiconductor compounds. This discussion is extended to the assembly of both axial and coaxial NW heterostructures. Finally, the chapter is brought to a close by defining the scope and framework of the Thesis, in Section 1.4, alongside the contributions made to the field in the course of its culmination.

1.1 – Nanowire-Based Optoelectronics

Throughout the course of the past decade, a multitude of novel nanowire-based opto-electronic devices have been demonstrated as the result of extensive academia- and industry-driven research. The surge of widespread interest in the field can be principally attributed to several key advantages offered by nanowires, in contrast to conventional thin-film-based devices. These advantages will be outlined in the following discussion, in relation to specific archetypical opto-electronic applications.

First, nanowires allow for an unprecedented variety of material combinations, as compared to planar crystal growth. In the case of thin film deposition, lattice-matching between the substrate and epilayer is an essential constraint. When one material is deposited upon a dissimilar substrate of sufficiently disparate lattice constant, strain is consequently induced at the hetero-interface leading to the formation of dislocations beyond a critical epilayer thickness [3]. In contrast, growth of lattice mismatched material systems can be accommodated by nanowires, as their lateral surfaces effectively permit the relaxation of the induced elastic strain [4]. In fact, on account of a nanowire's large surface area to volume ratio and small contact area with the substrate, strain relaxation can occur within several atomic layers from the interface [5].

One particular avenue of exploration exploiting the notion of otherwise incompatible material combinations, through NW growth, is the monolithic integration of III-V semiconductor compounds with silicon-based platforms. Although, silicon is the material of choice and reigns supreme as the dominant backbone of the microelectronics industry [6], its use in large scale and economically competitive light-emitting applications remains, to date, unfulfilled [7]. Integration of optically active compounds, such as GaAs, with Si would cohesively bridge the gap between the photonics and electronics realms, on a united platform, and forward the progression of optical computing technologies. Several research groups have successfully achieved photoluminescence (PL) from III-V compound semiconductor NWs grown on Si substrates [8-12]. However, the more difficult task of inducing optical emission through electrical excitation from similar material systems has only been, as yet, presented twice. Svensson et al. have demonstrated electroluminescence (EL) from single core-shell GaAs-InGaP NWs on Si substrates with GaP buffer/nucleation layers [13], while Tomioka et al. have employed core-multishell GaAs/AlGaAs NW ensembles on Si substrates in the fabrication of their light-emitting diodes (LEDs) [14].

In addition to their incorporation within LEDs, III-V NWs have also been integrated within other key opto-electronic devices as the active medium, including bio-sensors [15, 16], photodetectors [17-20], lasers [21,22], and single photon sources [23, 24]. The motivation for the use of NWs in such systems is rooted in the several basic advantages they offer. First, NWs offer routes towards continual miniaturization of devices, allowing for the adaptation of compound semiconductor technologies to, and compatibility with, trends directed towards ever decreasing scales in the microelectronics realm [25]. This miniaturization also inherently benefits the electro-optics realm, for example, through the production of NW-based display systems with lower power consumption and improved spatial resolution [2].

The unprecedented dimensional and morphological control over a device structure, offered through the growth of NWs, is another of their key benefits. Having a large ratio of surface to bulk states in an NW is advantageous for sensing applications [15]. Furthermore, being able to form heterojuntions in both axial and radial architectures using NWs allows for control over dimensional properties leading to novel devices which exploit unique quantum confinement effects [26, 27]. Of notable importance is the potential to use NWs for so called 'nanotree' or branched-NW structures. Such architectures have been demonstrated using various III-V material systems [28-30], and are particularly remarkable with respect to photovoltaic applications (discussed in the following section), where enhanced absorption and large p-n interfacial areas are required. Controlled growth of NW heterostructures also expands the possibilities for novel display applications wherein multiple or tuneable emission can be achieved [31-33].

As mentioned previously, the substrates on which NWs can be grown are not simply limited to the material from which the NWs themselves are composed. The relaxation of this constraint, as compared to standard planar deposition techniques, allows for the assembly of NW structures on so called 'foreign substrates'. Here, the term *foreign* implies that the substrate and over-laying atomic layers can be disparate with respect to their chemical composition, lattice constant, thermal coefficient of expansion, and crystal structure. With no need for precise registration of atomic columns in adjacent layers, several advantages can be exploited. Particularly, in the case of III-V semiconductor compound growth, this translates to substantial cost reductions as expensive float-zone fabricated substrates can be avoided without compromising the epilayer crystal quality. Furthermore, growth of optically efficient materials can be achieved on non-rigid platforms allowing for added device functionality in the form of mechanical flexibility. This very concept was first demonstrated by Nadarajah et al. in the form of ZnO NW-based LEDs grown on transparent and flexible polyethylene terephthalate (PET) foils with indium-tin-oxide (ITO) buffer layers [34].

Finally, we turn our attention to the advantages offered by bottom-up growth processes associated with NW assembly, as compared to top-down fabrication schemes. In this respect, patterned VLS-type NW growth, achieved through electron beam lithography or nano-imprint lithography for the positioning of metal seed particles, presents a means for the fabrication of large-area devices with individual component dimensions below the diffraction limit; a condition that could otherwise not be realized through standard photolithographic processing methods. Large area patterning of NW building blocks has proven to be a suitable technique for the fabrication of novel photonic crystal structures, allowing for unique light guidance and optical pulse trapping applications [35, 36]. Additionally, patterned NW arrays have been demonstrated as effective media for the guidance of neuronal network growth [37] and site-specific differentiation of embryonic stem cells [38]. Bottom-up NW growth schemes have also been utilized in the fabrication of complex three-dimensional architectures for multifunctional electronics applications [39]. The departure from top-down fabrication methods motivates a progressive path towards a new generation of devices that need not be bound to the spatial resolution limits of photolithography or the wet-processing techniques associated with etchants and photoresistive chemicals. However, it should be noted that, ultimately, a paradigm shift from top-down to bottom-up processing methods relies not only upon improved fabrication practices but also on economic incentives [40].

In this section, little has been said with regards to the incorporation of NWs within solar cell applications. As this particular topic is the primary device focus of this Thesis, the following section will be dedicated entirely to the motivations behind the implementation, and scope of the research in the field, of NW-based photovoltaics.

1.2 – Nanowire-Based Photovoltaics

Over the past 3 years, NW-based photovoltaic applications have acquired a surge of interest. The relevance of these pseudo-one-dimensional structures to the field and motivations behind their pursuit stems chiefly from five distinct advantages which they provide. Two of these characteristics have been defined in the previous section; namely, the added functionality associated with growth of high quality crystals on foreign substrates and the inherent economical incentives associated with lower material consumption. Otherwise, three advantages offered by NW incorporation exist that are particular to photovoltaic energy harvesting applications.

Firstly, with NW structures, by tuning growth parameters it is possible to control the dopant modulation in radial geometries. As an example, an n-type core can be encapsulated by an intrinsic shell which can, in turn, be enveloped by an external p-type shell. The active interface, described as a p-i-n motif in this example, thus, extends along the longitudinal axis of the NW. This allows for the decoupling of photon absorption and carrier transport/collection into orthogonal directions [41]. In this geometry, shell thicknesses can be tuned to the diffusion lengths of the photo-generated carriers [42]. A short collection length means that bulk recombination of electrons and holes can be substantially reduced, promoting more efficient carrier collection [43].

Next, it should be noted that a collective group of NWs, either patterned as an array or randomly situated with respect to one another in an ensemble, provide superior light absorption characteristics compared to an equivalent volume of the same material in bulk form [44]. The considerable inhibition of reflectance losses has been attributed to improved index matching of the NW medium to air [45] and to the strong multiple scattering of light leading to improved light trapping [46]. The suppression of diffuse optical reflectance can be optimized through control of the diameter, pattern periodicity, pitch, packing fraction, and index of refraction of the NWs [44, 46]. Thus, the use of NW ensembles can circumvent one of the critical limitations of standard planar solar cells by minimizing surface reflectance [43].

Finally, NWs are inherently suited for next-generation solar cell designs that could not otherwise be realized by their planar geometry counterparts. One example of such a design is the multiple quantum-well (MQW) solar cell. As carrier density enhancement occurs in the plane of quantum wells due to confinement effects, MQW designs are anticipated to provide improvements in conversion efficiencies [45]. While MQW schemes have been shown to enhance short-circuit currents under solar illumination, an associated decline in open-circuit voltage also results, in part due to the recombination of carriers in defect sites along the device structure caused by strain relaxation [47]. As previously mentioned, in NW systems, strain is relaxed along the sidewalls and, therefore, not associated with the formation of dislocation defects. For this reason, a NW-based MQW solar cell would alleviate the compromise between short-circuit current and open-circuit voltage, thereby providing improved conversion efficiency [45].

Various NW-based photovoltaic prototypes have been demonstrated to date. For the sake of a more concise discussion, we shall limit our review to solar cells having incorporated NWs, grown in accordance to the VLS mechanism, as the active light-harvesting medium. Within this scope, group IV semiconductors have been more widely investigated than compound III-V materials. This is primarily due to the ease of market integration (CMOS compatibility) and the associated cost advantages offered by Si. However, because of its nearly ideal room temperature bandgap, with respect to single p-n junction configuration solar cells [48], GaAs has also been investigated as a pertinent photovoltaic material.

Single silicon-based NW solar cells with axial junction configurations have been demonstrated with conversion efficiencies as high as 0.46 % by the Atwater Group [49] and 0.5 % by Lieber and colleagues [43]. In contrast, the implementation of a coaxial junction geometry in single Si NW was shown to lead to an enhanced efficiency of 3.4 % [50]. Ensemble Si NW solar cells have been fabricated on multicrystalline Si on glass substrates [51] and on flexible metal foil sheets [52], both designs having rendered a maximum conversion efficiency of 0.1 %. A similar solar cell design employing ensemble-contacted Si NWs with core-shell architectures on single-crystalline Si (100) substrates demonstrated 1.0 %

conversion efficiency, and were shown to be improved to 1.8 % efficiency with passivation of the NW sidewall surfaces [53].

Gallium arsenide NW-based photovoltaics have also been demonstrated in recent years with various designs and configurations. A device based on a collection of core-shell p-n junction GaAs NWs grown on GaAs (111)B substrates was fabricated by Czaban and coworkers with an optimal efficiency of 0.83 % [54]. A similar design using n-doped GaAs NWs encapsulated in a poly(3-hexylthiophene) (P3HT) polymer matrix was shown to improve the overall efficiency to 1.04 % [55]. Another ensemble design, wherein p-type GaAs NWs were grown on an n-type GaAs (111)B substrate, was optimized to render a conversion efficiency of 1.65 % [56]. In comparison, a single coaxial p-i-n structured NW has been shown to allow for efficiencies as high as 4.5 % [57].

As evident by the comparison of the peak efficiencies of the solar cells reviewed in this section, the performance of a device is largely dependent upon the structural design of the NWs employed therein. In the following section, the VLS mechanism for bottom-up assembly of NWs and the main growth parameters responsible for control over their morphology will be considered.

1.3 – The Vapour-Liquid-Solid Mechanism for Heterostructured Nanowire Growth

The assembly of one-dimensional nanostructures can be realized through various methods. The different techniques share a unifying attribute in that they permit an enhancement of the crystal formation rate along one particular axis (or its suppression along the other axes), thereby promoting anisotropic growth and the layer-by-layer assembly of a one-dimensional structure. In the most general sense, nanowire growth techniques can be categorized into two classes; namely, template-directed and free-standing growth techniques [58]. Template-directed methods rely on spatial confinement of the growing crystal by physically impeding growth along all but one axis. Thus, a predefined structure is formed, limited to the resolution scales of the impeding template and bound to its confines. Examples of such processes include planar deposition within aligned thin-film crack structures [59], pore-filling [60], and v-growth template growth [61]. In contrast, free-standing NWs are not spatially restricted by physical confinement. The formation of these nanostructures typically relies upon dissimilar growth or etch rates along different crystallographic directions. Example of this fabrication method include self-assembly through aqueous electroless etching [62,63], mask-mediated selective-area growth [64], and particle-assisted NW growth [65]. The four growth techniques discussed thus far are pictorially represented in Figure 1.1.

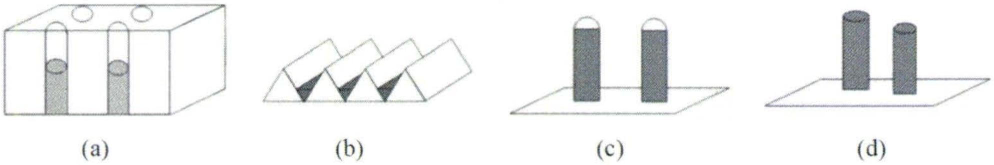

Figure 1.1 – Representation of typical one-dimensional nanostructure assembly techniques. (a) Template-assisted pore-filling method (b) V-groove template method (c) Particle-assisted growth method (d) Particle-free self-assembly method. Adapted from [58].

Based on the direct relation to the focus of this Thesis, the following discussion on NW growth will primarily deal with the particle-assisted assembly method of free-standing NWs. This approach, most commonly realized through the VLS growth mechanism, is of particular significance as it allows for the fabrication of a remarkable variety of material systems and is unrestricted to size limitations imposed by the spatial resolution of lithographic processes.

1.3.1 – Historical Basis of the Vapour-Liquid-Solid Mechanism

The conception of the VLS mechanism is attributed to Wagner and Ellis, and stems from investigation into impurity-catalyzed growth of Si crystals, at the Bell Telephone Laboratories in the early sixties [1]. Their experiments focussed on the hydrogen reduction of $SiCl_4$ on Si {111} substrates with Au droplets placed on their surfaces, at elevated temperatures. The result was the growth of micron-scale Si whiskers, aligned parallel to the substrate normal, with characteristic hemispherical Au tips, whose lateral extent matched the diameter of the whiskers, themselves. It was concluded that, at the growth temperature, an Au-Si alloy droplet had formed which acted as either a preferential sink for the incident vapour-phase Si atoms, or as a *"catalyst for the chemical process involved"* in the dissociation of inbound precursor molecules. The droplet alloy was said to *"ride"* atop the crystal as it continued to form. In their seminal paper, Wagner and Ellis outlined the three main characteristics of these microstructures: (1) the Si crystal, grown with a whisker morphology, necessarily required an impurity (namely, the Au seed) for its formation; (2) a small droplet, characterized as an Au-Si alloy, was present atop the fully assembled crystal upon the termination of growth; (3) the Si whiskers contained no screw dislocations. The latter trait was of added significance as anisotropic growth of conical or pyramidal crystals (similarly, extended in one axis, as in the case of micro-whiskers) were previously known to have stemmed from the presence of screw dislocations [66]. Thus, the VLS mechanism, a process wherein a liquid-phase impurity-based alloy acts as the preferential decomposition site for vapour-phase precursors leading to the formation of a localized, solid-phase seeded crystal, was introduced.

The next major contribution toward an understanding of the VLS process is credited to Givargizov, based on his considerations of the growth kinetics and growth rate dependences of free-standing Si columns with diameters ranging from hundreds of nanometres to several microns [67]. In this publication, the four main progressive stages of VLS growth were first delineated: (1) the vapour-phase mass-transport of precursor species; (2) the dissociation of precursors at the vapour-liquid interface and the subsequent incorporation of adatoms within the liquid seed; (3) diffusion of the growth material in the liquid droplets; and (4) supersaturation of the alloy, leading to solid-phase precipitation of growth material at the liquid-solid interface and continual incorporation within the underlying crystal lattice. It was argued that the fourth stage was chiefly responsible for the determination of growth rate. The growth rate of the nano- and micro-wires was also related to their diameter and growth conditions, such as temperature and molar concentration of precursors. Furthermore, Givargizov asserted that a minimum critical diameter exists, below which NW growth would not prevail. This was attributed to the Gibbs-Thomson effect and rationalized by the following argument: since the vapour pressure of reactants entering a liquid particle is inversely proportional to the radius of the particle, then it follows that when the size of the alloyed seed is reduced, the solubility of the growth material increases. Thus, at a critical seed diameter, the equilibrium solubility of Si atoms in the Au droplet increases such that the requisite supersaturation condition is not satisfied. The other notable conclusions of this work are that the assembly of a monolayer can proceed from a polycentric nucleation mechanism and that the Au-based droplet should be characterized as a physical catalyst, as opposed to a chemical catalyst.

The earliest demonstration of particle-assisted growth of free-standing nanometre-scale III-V compound semiconductor crystals, via the VLS mechanism, was by the Hiruma Group at the Hitachi Central Research Laboratory in the early 1990's [68, 69]. They had first published on the formation of ultra-fine InAs

NWs on GaAs (111)B substrates, within windows of photolithographically patterned SiO_2 masks [68]. In this work, the driving force instigating crystal formation was not clarified. However, it was later discovered that during the etching process employed in the formation of their SiO_2 masks, sub-monolayer quantities of Au were unintentionally deposited as impurities on the sample surface [69]. During sample heating, the impurity atoms had clustered to form Au nanoparticles, allowing for the subsequent formation of InAs NWs, when trimethylindium (TMI) and AsH_3 precursors were supplied in a metal organic vapour phase epitaxy (MOVPE) system. Though accidental in its nature, the experiment led to several key conclusions: (1) III-V compound semiconductor-based NWs can be grown according to the VLS mechanism; (2) In this system, the liquid droplet is an alloy composed primarily of Au and the group III element; (3) Lower annealing temperatures, established prior to the onset of growth, favour the incomplete formation of liquid droplets; (4) Higher annealing temperatures, instead, force the coalescence of Au particles and lead to the growth of NWs with larger diameters. As empirically observed by the Hitachi researchers, metal particle formation is a nontrivial affair and of critical influence on NW morphology. Various methods exist for the preparation of seed droplets on growth surfaces, which can be extended to accommodate a variety of material combinations.

1.3.2 – Formation of Metallic Seed Droplets

The approaches to decorating semiconductor substrate surfaces with metal particles for the growth of NWs can be classified in two categories: randomly distributed particle preparation and position controlled particle arrangement. Both have their own inherent practical advantages and the implementation of either technique is ultimately application dependent. The preparation of randomly distributed metallic nanoparticles is less process-intensive and the fewer fabrication steps are associated with significant cost benefits. The drawbacks, however, include morphological inconsistencies amongst the NWs rendered and their inhomogeneous placements relative to one another. The main methods practiced in this approach are colloidal nanoparticle deposition through drop-casting, spray/spin-coating on a substrate [70-72], covalent self-assembly of colloidal nanoparticles or chemical functionalization of surfaces with nanoparticles [73-76], and nanoparticle formation through thermal dissociation of thin films [77-79].

In contrast, position controlled particle arrangement leads to patterned nanowires with identical morphologies aligned in site-specific, arrayed formations. Yet, this approach is associated with higher fabrication costs, more processing steps, lower throughput, and higher risk of surface contamination [65]. In this class, the examples of nanoparticle decoration methods include electron-beam lithography [35, 80], porous-alumina masked Au deposition [81-83] , nanoimprint lithography [36, 84], and block-copolymer assisted nanolithography [85, 86].

Based on the advantages listed above, all metal seed particles prepared for the purposes of this Thesis project were done so through dissociation of a thin film, drop-casting of colloidal particles, or chemical functionalization, dependent upon the substrate processing limitations and the desired application.

1.3.3 – The Vapour-Liquid-Solid Growth Mechanism

1.3.3.1 – Qualitative Description

For the sake of a concise qualitative description of the VLS mechanism, our discussion will be limited to Au-assisted growth of III-V compound semiconductor NWs via gas-source molecular beam epitaxy (GS-MBE). Although, it has been demonstrated that III-V NWs can be grown using a variety of metallic seeds [87-89], the use of Au droplets is by far the most prevalent practice. This stems from the combined beneficial properties of gold, including its chemical inertness to oxygen, thermal stability, and ability to form low-temperature alloys in liquid phase with a variety of growth material [90].

Figure 1.2 schematically represents the main steps involved in the basic VLS model. Initially, a thin Au film, with thickness on the order of 10 Å, is deposited upon the substrate of choice (Figure 1.2 (a)). Upon annealing, the film dissociates into a randomly distributed collection of Au nanoparticles with varying sizes (Figure 1.2 (b)). The uniformity in the size distribution is dependent upon the initial thickness of the film, such that thicker films favour the formation

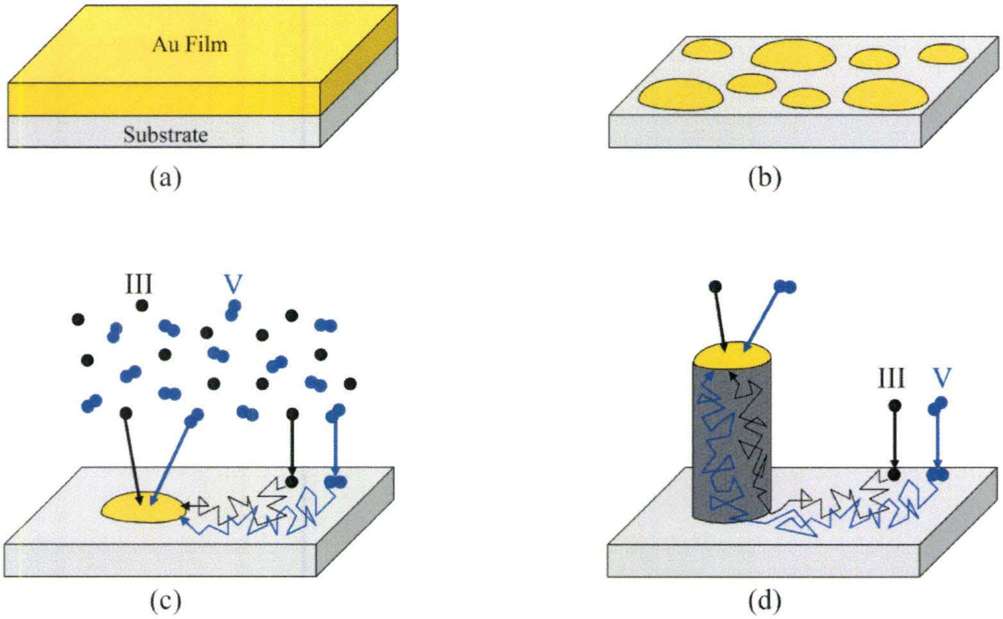

Figure 1.2 – Representation of the vapour-liquid-solid growth process. (a) Deposition of Au film on substrate surface. (b) Thermal dissociation of film and formation of liquid Au nanoparticles. (c) Introduction of vapour-phase growth species and alloying with Au. (d) Supersaturation of the alloy, nucleation, and NW growth.

of particles with greater diameter variances. In a GS-MBE system, wherein group III adatoms are supplied as monomers, while group V species are supplied as dimers, the group sequence is initiated by the introduction of the growth material in an ultra-high vacuum environment. At the growth temperature, the growth species (mainly, group III [90]) form a liquid-phase alloy with the Au droplet, due to arrival through either direct impingement or after diffusion on the substrate (Figure 1.2 (c)). Once the concentration of growth material within the droplet increases to a critical value, a supersaturation condition is achieved. At this point, solid-phase nucleation occurs at the interface formed by the liquid alloy and the underlying substrate. A persistent in-flux of vapour-phase adatoms ensures a steady-state regime, whereby continual nucleation is maintained under the seed, such that the seed is lifted further from the substrate with the formation of each atomic layer of the crystal (Figure 1.2 (d)). Thus, a one-dimensional crystal is formed (namely, the NW), spatially limited by the extent of the Au droplet.

The positions and relative densities of NWs are dictated by those of the Au droplets which, in turn, are functions of the pre-growth annealing parameters. Nanowire diameters (in a purely axial growth regime) are also limited to the diameters of the hemispherical nanoparticles. The cessation of growth is marked by the termination of the group III flux and, so, NW lengths are determined by the duration of growth. The assembly of constituent atomic planes in a NW crystal preferentially occurs along the <111> direction of the cubic lattice [91, 92]. This arises from the fact that the greatest areal density of bonds is associated with the <111> direction, while the corresponding {111} atomic planes have been shown to possess a minimum surface free energy [93]. As such, the growth direction of NWs can be tuned by the appropriate choice in surface orientation of the substrates employed; NWs will tend to grow orthogonal to substrate surfaces with <111> normals, at 35.3° relative to substrate surfaces with (100) orientations, etc..

The role of the liquid seed in the VLS process is as an atomic sink. In this sense, the seed activates an enhanced growth rate at the interface it shares with the underlying substrate, as compared to surfaces containing no alloyed droplets. The enhanced growth rate is attributed to: (1) A higher reaction rate of growth species with seed surfaces than with substrate surfaces and, (2) adatom diffusion fluxes, directed from the substrate and NW sidewalls towards the seed [94]. A non-equilibrium steady-state regime is induced as a result of an enduring in-flux of adatoms. Thus, a chemical potential difference is created, between the liquid-phase and solid-phase which forces crystal nucleation as a means of re-establishing equilibrium. The thermodynamic driving force for NW growth is, therefore, supersaturation of the alloyed solution and can be expressed as [94]:

$$\Phi = exp(\Delta\mu_{LW}/kT) - 1 \tag{1.1}$$

where, $\Delta\mu_{LW} = (\mu_L - \mu_W)$ is the difference in chemical potential between liquid seed, μ_L, and the underlying NW, μ_W, k is the Boltzmann constant, and T is the growth temperature. On this basis, it is realized that the growth species are subjected to two phase-transformations, first from vapour to liquid and, second, from liquid to solid; Hence, the appropriately termed VLS mechanism.

Until now, we have only considered growth of axial NWs, while the practical significance of coaxial structures had previously been emphasized. The fabrication of core-shell structures through MBE relies on radial growth and is partially attributed to particle-free or vapour-solid growth. The qualitative rationalization of radial growth is as follows: As a NW grows according to the VLS mechanism, adatoms reach the alloyed nanoparticle at the tip through direct impingement or surface diffusion. As adatoms migrate to the site of an existing NW, they may diffuse along the sidewalls. So long as the NW height is sufficiently low, the diffusive adatoms will migrate and reach the tip with near-

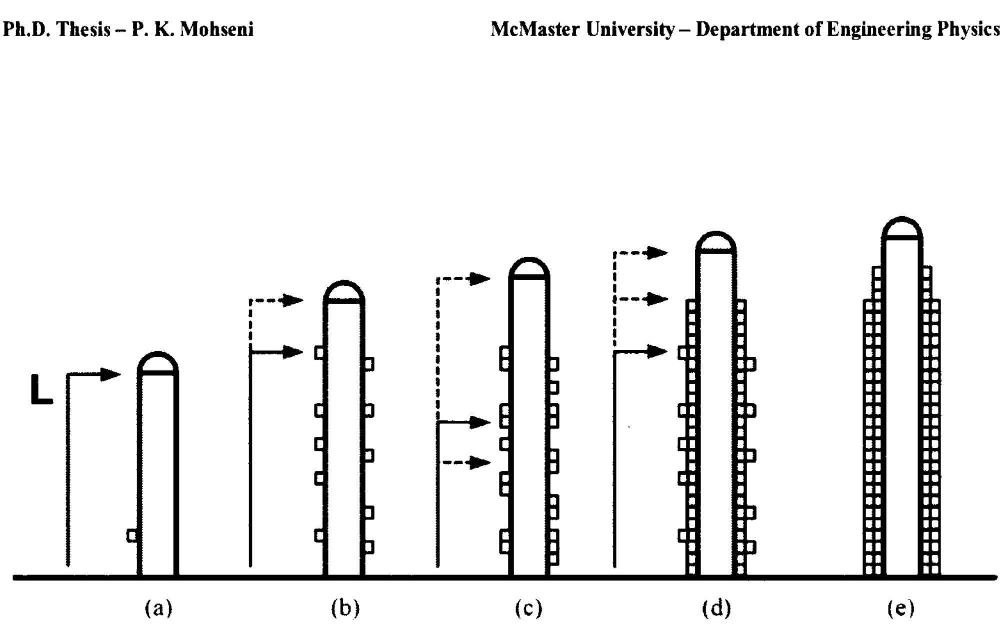

Figure 1.3 – Evolution of nanowire growth with tapered morphology. (a) Adatom diffusion lengths exceed NW length, L. Adatoms reach seed with near-unity probability. (b) NW length exceeds adatom diffusion lengths. Sidewall nucleation occurs. (c) Layer-by-layer growth mode ensues in tandem with VLS-type axial growth. (d) Completion of monolayer of radial growth followed by the re-initiation of sidewall nucleation. NW diameter becomes greater than nanoparticle diameter. (e) Transition towards step-flow growth mode. Preferential incorporation at step-edges leads to tapered NW morphology. Adapted from [95].

unity probability (neglecting desorption effects). However, once the NW length exceeds the diffusion length of the adatoms, island nucleation will commence upon the sidewalls. In other words, sidewall nucleation occurs once the migrating adatoms "exhaust" their diffusion lengths *en route* towards the Au seed [95]. Subsequently, a layer-by-layer growth regime ensues, allowing the completion of a monolayer on the sidewalls while the seed-mediated axial growth simultaneously persists. This process is successively renewed upon the formation of a sidewall monolayer, such that the growth occurs in the radial direction and the NW diameter exceeds that of the nanoparticle at its tip. Upon significant radial growth, a transition occurs whereby step-flow growth proceeds due to preferential assembly of adatoms at step edges. The evolution of particle-free layer-by-layer and subsequent step-flow growth on the sidewalls results in the growth of a NW with a tapered tip [95]. Through suitable control of the growth parameters and timely exchanges of growth species fluxes, heterostructured NWs can be fabricated with core-shell morphologies, such that material compositions are modulated axially and radially. This will be further elaborated in section 1.3.3.3.

1.3.3.2 – Material Conservation Model for Growth

Building upon the qualitative framework, described in the previous section, more quantitative understandings of the VLS mechanism have been presented in various publications, based upon the kinetics and thermodynamics of the growth process [77, 96-99]. In this section, however, we review a material-conservation model for the growth of III-V core-shell NWs by GS-MBE [100], as this model more precisely accounts for the growths relevant to the current work. This model defines the time-evolution of growth in two distinct processes: first, a purely axial growth mode (regime A) followed by a tandem, axial and radial growth mode (regime B).

In regime A, group III adatoms are considered to impinge upon the Au seed, NW sidewalls, and substrate surface with a flux J [atoms/nm^2/s] or, otherwise stated, at a nominal planar growth rate of V [nm/s]. The flux source is oriented at an angle α to the substrate normal and the NW formed has a collection area of $(R_0 + r_0)$, where R_0 is the fixed radius of the NW. As depicted in Figure

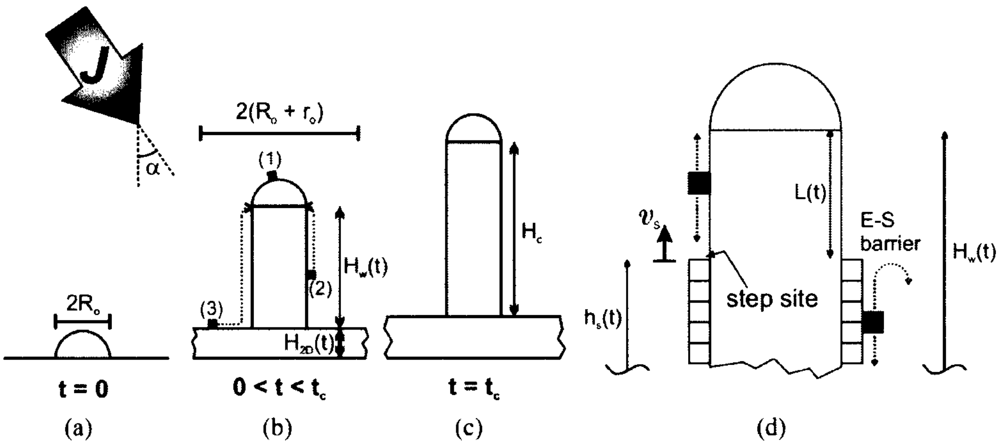

Figure 1.4 – Illustrative guide to material conservation model parameters. (a) Au droplet prior growth. (b) NW grown prior to reaching critical height. Adatoms at stages (1) to (3) represent impingement upon the Au seed, NW sidewalls, and substrate, respectively. (c) NW grown to critical height at time, t_c. (d) Representation of NW tip and illustration of parameters used to model regime B growth. Adapted from [100].

1.4 (a), the height of the NW, $H_w(t)$, is measured from the surface of the simultaneously deposited planar film, with thickness $H_{2D}(t)$, to the base of the Au droplet at the NW tip. At a finite time after growth initiation, t_c, the NW reaches a critical height, H_c. Thus, the volumetric rate of change of the NW is defined by:

$$\frac{d(Vol)}{dt} = \pi R_0^2 \left\{ \frac{d[H_w(t) + H_{2D}(t)]}{dt} \right\} \tag{1.2}$$

As shown in Figure 1.4 (b), the incoming group III adatoms can reach the seed from three contributing pathways: (1) direct impingement upon the Au droplet, (2) impingement upon the sidewalls and subsequent diffusion to the seed, and (3) arrival at the seed after impingement upon the substrate followed by diffusion. Each of these sources contributes to the total volumetric rate of change. The change in volume as a result of the first source of adatoms can be expressed as:

$$\frac{d(Vol)_1}{dt} = \chi_A\, \pi R_0^2 \left(\frac{J}{\rho}\right) \cos\alpha = \chi_A\, \pi R_0^2 V \cos\alpha \tag{1.3}$$

where χ_A represents the fraction of impinging adatoms that have absorbed upon the Au nanoparticle and ρ represents the group III atomic density. Next, upon appropriate geometrical consideration, it can be resolved that the volumetric rate of change attributed to the second source of growth material can be designated by:

$$\frac{d(Vol)_2}{dt} = 2\xi_A V R_0 H_w(t) \sin\alpha \tag{1.4}$$

where ξ_A denotes the fraction of particles that have been incorporated into the NW upon adsorption on the sidewall followed by diffusion to the tip. Finally, the contribution of the third source to the total rate of volume change is formulated as:

$$\frac{d(Vol)_3}{dt} = \varphi_A \pi V[(R_0 + r_0)^2 - R_0^2] \cos\alpha \tag{1.5}$$

where φ_A represents the fraction of adatoms having contributed to the NW structure after adsorption within a distance, r_0, from the NW base and subsequent migration towards the Au seed.

Summing the three contributions and substituting their totality into equation (1.2) leads to a differential equation, which upon imposition of the boundary conditions, has a solution of the form:

$$H_w(t) = \frac{\pi R_0}{2\xi_A \sin\alpha}\left\{\left[\frac{\varphi_A[(R_0 + r_0)^2 - R_0^2]}{R_0^2} + \chi_A\right]\cos\alpha - \eta\right\}\left[\exp\left(\frac{2\xi_A \mathrm{V}\sin\alpha}{\pi R_0}\right) - 1\right] \tag{1.6}$$

Here, the authors of ref. [100] have accounted for the role of the planar deposition as a fraction of the nominal growth rate, such that $dH_{2D}(t)/dt = \eta V$.

After a finite growth period, $t > t_c$, all further growth will occur in accordance to a regime B process. Thus, once the NW height reaches H_c, the contribution from diffusive adatoms having adsorbed on to the substrate will be modified as they will have "exhausted" their diffusion lengths prior to arrival at the Au seed. In this regime, adatoms impinging upon the NW sidewalls along a length, $L(t)$, near the tip, depicted in Figure 1.4 (d), will either incorporate into the axial growth after reaching the seed or add to the height of the sidewall step edges through step-flow incorporation. In this model, the axial growth rate of the step-edge is referred to as the step-velocity, v_s, and is comparable to the axial growth rate of the NW. Furthermore, adatoms diffusing towards the NW tip on previously existing sidewall layers, formed by step-flow growth, are assumed to be reflected on account of an Ehrlich-Schwoebel (E-S) barrier [101, 102].

The purely axial component of growth in regime B can only be attributed to those adatoms impinging directly on the seed or those impinging on the sidewalls along $L(t)$. Here, the fractional adatom contributions of each source have to be reconsidered as χ_B, ξ_B, and φ_B. Particularly, the later parameter in regime B will only account for the fraction of particles which incorporate radially. Considering these modifications and a suitable adjustment in boundary conditions, the authors reach the following expression for the time-evolution of NW height in regime B:

$$H_w(t) = (H_c - v_s t_c - \kappa)\left\{\exp\left[\frac{2\xi_B V sin\ \alpha}{\pi R_0}(t - t_c)\right]\right\} + v_s t + \kappa \qquad (1.7)$$

where κ is defined as:

$$\kappa = \frac{\pi R_0}{2\xi_B sin\ \alpha}\left[v_s\left(\frac{1}{V} - \frac{2\xi_B t_c sin\ \alpha}{\pi R_0}\right) - \chi_B \cos\alpha + \frac{2\xi_B h_{si} sin\ \alpha}{\pi R_0} + \eta\right]$$

The parameter h_{si} represents the height of the initial monolayer shell that formed immediately following $t = t_c$. Figure 1.5 (a) plots NW height as a function of time in regime B. Here, it can be seen that for various adatom incorporation fractions and initial step heights, the axial growth rate is abruptly reduced after the critical height is reached. This is attributed to the reduced collection of growth species by the Au seed due to adatom diffusion limitations at times beyond t_c.

With respect to the radial growth component in regime B, it is assumed in the mass conservation model that a cylindrical shell is formed with an inner radius equivalent to that of the Au seed, R_0, and an outer radius of R(t), with a height of $h_s(t) = v_s(t - t_c) + h_{si}$. Neglecting the effects of adatom desorption prior to incorporation, the contributions to the rate of change of the shell volume from direct impingement on the sidewalls and collection from the substrate can be represented as $[2R(t)h_s(t)Vsin(\alpha)]$ and $\{\varphi_B \pi V[(R(t) + r_0)^2 - R(t)]cos(\alpha)\}$, respectively. Thus, the radial growth rate component in regime B is represented as:

$$\frac{dR(t)}{dt} + \frac{v_s[R^2(t) - R_0^2] - \varphi_B V r_0^2 \cos\alpha}{2R(t)[v_s(t - t_c) + h_{si}]}$$

$$= V\left\{\frac{\sin\alpha}{\pi} + \frac{\varphi_B r_0 \cos\alpha}{[v_s(t - t_c) + h_{si}]}\right\} \qquad (1.8)$$

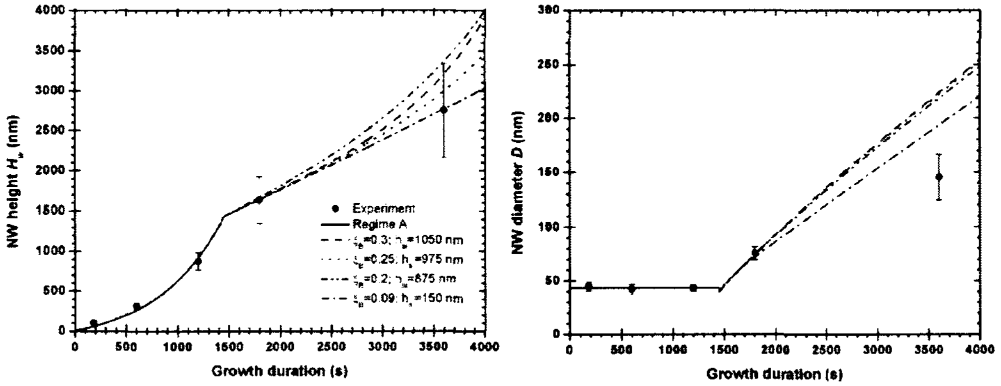

(a) (b)

Figure 1.5 – Time-evolution of (a) NW height and (b) NW diameter. Adatom incorporation fractions are varied from 0.09 to 0.3, while initial steps heights are varied between 150 nm and 1050 nm, according to the material conservation model. Full-circular points on both plots represent the corresponding experimental data obtained from GaAs NW growths. Adapted from [100].

Figure 1.5 (b) shows NW diameter evolutions as a function of time in the regime B growth mode, based on the solution to equation (1.8). It can be seen that a constant diameter exists earlier in the growth, corresponding to a pure axial growth regime prior to t_C. As the growth evolution progresses, the NW diameter will increase due to sidewall nucleation and step-flow growth mode. The circular points on the plots represent the experimental data acquired from sample sets of GaAs NWs grown by Au-assisted GS-MBE. The deviation of the data from the theoretical curves has been primarily attributed to competition for diffusive adatoms from neighbouring NWs and local shadowing effects associated with high density NW growth [100]. In the following section, the current model for VLS-based growth of core-shell structures will be used as a platform for a discussion on NW morphology control, realized through the tuning of growth parameters.

1.3.3.3 – Dependences of Morphology Upon Growth Parameters

The resultant morphology of a III-V semiconductor NW depends predominantly upon four controllable parameters. These parameters are the size of the metal seed employed, the growth temperature, the ratio of the group V growth species flux to that of the group III species, and the growth rate. Although each parameter places a particular influence, which can be experimentally evaluated, it is the sum of the contributions that leads to the final NW morphology.

The size of a metallic nanoparticle accommodating growth is chiefly responsible for the growth rate of a NW and, therefore, ultimately determines its morphology for a fixed growth period. The pioneering work of Givargizov and Chernov on this relationship led to the conclusion that one-dimensional structures grown from larger seed particles grow at a faster rate in comparison to those grown from smaller particles [67, 103]. Here, the square root of the axial growth rate was linearly related to the inverse of the particle's diameter. The relationship was justified by the Gibbs-Thomson effect, whereby an increased vapour pressure leads to an increase in solubility of the growth species in seed particles with smaller diameters. Thus, a critical seed diameter was defined, below which no crystal growth could transpire.

Contrary to the Givargizov-Chernov model, when supersaturation of the liquid seed is considered as the driving force for crystal growth and the surface-diffusion of vapour phase adatoms arriving at the seed is accounted for, the relationship between growth rate and diameter is strongly modified. In this scope, it has been demonstrated through several theoretical models and empirically verified [77, 79, 96, 97, 104] that the axial growth rate decreases with increasing particle diameter. More specifically, it has been argued in the relevant literature published throughout the past decade that the diffusion-mediated axial growth rate is proportional to either $1/R$ or $1/R^2$, where R is the radius of the metal seed particle [94]. Thus, thinner wires grow longer than thicker ones during the same growth period. Furthermore, Johansson et al. contend that for NWs grown with seeds in the diameter range of 20 nm to 100 nm, through MOVPE and MBE, under high supersaturation levels, the Gibbs-Thomson effect can be effectively neglected [96]. Indeed, the NWs of interest, grown for the purposes of this Thesis project, are in this class.

The effect of growth temperature on NW morphology can be influential in two respects. Prior to growth, before significant alloying of the growth species and Au seed is permitted, the effect of an increase in temperature is the enhancement of Au particle coalescence through surface migration [105]. The enhanced agglomeration of neighbouring seeds produces NWs with larger effective diameters, which, based on the above discussion on diffusion-mediated NW growth, results in a suppression of growth rate. Secondly, once the growth sequence is initiated, the growth temperature dictates the degree of adatom diffusion and desorption. As temperature is increased, adatoms will reach the Au seeds with higher probabilities on account of enhanced surface diffusion. However, beyond a certain critical temperature, growth will be limited by the desorption of growth species. Thus, a material dependent temperature window exists, wherein a critical growth temperature represents the ideal trade-off between enhanced diffusion of adatoms and their desorption from the substrate or NW [72, 99, 106-108].

The role of flux ratio of group V to group III species is unique to MBE- and MOVPE-based NW growth processes. In MBE, an increase in V/III flux ratio will have three main effects on the NW morphology [108]: (1) Inhibition of group III adatom diffusion, leading to the promotion of sidewall nucleation; (2) Compensation of group V adatom desorption effects at higher temperatures, forcing an enhancement of the axial growth rate; (3) Suppression of excess group III concentrations in the liquid alloy, allowing for the incorporation of fewer stacking faults. The first and second effect will be further discussed in Chapter 2, while the third effect will be explored in depth in Chapter 3. On the other hand, during MOVPE growth of NWs, an increase in V/III flux ratio at a fixed growth temperature results in the enhancement of surface growth at the expense of the NW growth rate [72]. The reduction in axial growth has been attributed to more efficient pyrolysis of group III precursors under higher input V/III fluxes [72].

Finally, we consider the effect of growth rate (equivalent to the deposition rate of planar films), or group III impingement rate, upon NW morphologies. At a reduced growth rate, the Au particles experience a prolonged incubation period, prior to the initial island nucleation. A prolonged incubation phase leads to an enhancement of particle coalescence and, therefore, a reduction in NW density and axial growth rate. The reduction in axial growth rate is, in turn, associated with an increase in the probability for diffusive adatoms to reach the Au seed. Thus, at lower growth rates, radial growth is suppressed. Furthermore, at higher group III impingement rates, the mean free path of group III adatoms prior to collisions is reduced, leading to a reduction in their diffusion lengths. As previously stated, reduced adatom diffusion promotes sidewall nucleation and radial growth. Thus, at higher group III impingement rates, NWs will adopt a tapered or "pencil-shaped" morphology, as demonstrated in the case of GaAs NWs grown via Au-assisted MBE [108].

1.3.4 – Perspectives on the Phase of the Alloyed Seed

Although great strides have been made in the development of a consistent and unified model for metal-particle assisted growth of group III-V NWs, a significant subject of controversy persists to this day. In this section, we review opposing perspectives on the phase of the alloyed seed employed in NW growth.

The phase of the seed has been called into question since 2001, when Kamins et al. [109] demonstrated the growth of Ti-assisted Si NWs, at growth temperatures far below the minimum eutectic point of Ti and Si alloys. The authors attributed the growth process to solid phase diffusion of Si through, or around, the $TiSi_2$ alloy at the NW tips. The growth of Au-assisted III-V NWs, by a similar vapour-solid-solid (VSS) mechanism, at growth temperatures where the corresponding Au-group III seeds are expected to be in the solid phase, was first reported by Persson et al. [110]. Nanowires composed of InAs [111], InP [112], GaAs [113], and AlAs [114] have been demonstrated via MOVPE growth, within temperature ranges lower than the minimum eutectic point of the associated alloys. Although it is well known that eutectic point depression arises in nanometre-scale metal-semiconductor alloyed particles [115], this phenomenon plays an insignificant role for particles with diameters greater than 20 nm [58]. Thus, in the case of the examples noted above, where seed particle diameters are on the order of several tens of nanometres, the VSS model could be justified.

In contrast, it has been argued that Au-assisted growth of III-V NWs via MBE occurs only when Au-based alloys are in liquid phase. Experimental verification of this claim comes about through *in-situ* reflection high-energy electron diffraction (RHEED) experiments wherein diffraction spots associated with solid-phase seed particles were only observed at temperatures below the minimum limit of the growth temperature window for InAs [99] and GaAs [106] NWs. Additionally, Harmand et al. showed, through electron diffraction experiments, that the observed Ga concentrations detected in Au seeds (under different growth termination conditions) can only be associated with Au-Ga alloys in liquid-phase at the growth temperature of their GaAs NWs [78].

1.3.5 – Definition of Stacking Faults

The traditional definition of the term "stacking fault" refers to the modification of the periodic stacking sequence of atomic planes in a crystalline structure, in the form of an additional or absent crystal plane. In the field of nanowire research, however, the same term is often more ambiguously used [91]. Both mirror-plane formations and inclusion of 4H polytype arrangements in otherwise zincblende structures are often referred to as stacking faults [91, 92, 94]. In the case of mirror-plane formation, the standard ...ABCABC... zincblende sequence (where each letter denotes one of three possible positions that each III-V atomic layer can occupy) is disrupted such that an ...ABC$\underline{A}$CBA... configuration arises and zincblende formation persists before and after the mirror-plane, $\underline{A}$. In contrast, 4H polytype formations consist of an ...ABAC... arrangement.

In the present work, the term stacking fault refers to the disruption of an otherwise wurtzite (...ABAB...) arrangement of crystal planes by zincblende inclusions [108]. This definition is maintained throughout the thesis, and is exemplified by the stacking arrangement of atomic layers shown in Figure 3.6.

1.4 – Approach and Thesis Framework

The ultimate purpose of the project presented here was the demonstration of a novel class of opto-electronic devices, employing core-shell NWs as their active element, grown on foreign substrates. For this endeavour to come to fruition, several key components were required. First, the possibility of heteroepitaxial growth of core-shell NWs on foreign single-crystalline substrates was needed. This process involved thorough structural and optical analysis of several NW architectures. The understanding gained from the growth and analysis of complex coaxial NW geometries allowed for the extension of this work to the growth of core-shell homostructures upon more functional substrates, lacking long range crystalline order, which were previously unexplored by the international NW research community. After a suitable material combination was reached, the focus then shifted towards device fabrication and optimization. The research process undertaken culminated in the demonstration of a novel NW-based, nano-hybrid material for flexible photovoltaic applications.

The experimental procedures used in the various stages of this work are individually reviewed in Chapter 2. Here, we begin with a discussion on the theoretical foundations, and experimental relevance to NW growth, of the GS-MBE deposition system. We then shift focus towards the characterization methods employed in our investigations. In particular, various electron microscopy methods and optical characterization processes are considered.

In Chapter 3, we present an extensive analysis of GaAsP/GaP coaxial NW heterostructures grown on Si (111) substrates. This chapter deals with the structural analysis of core-multishell and superlattice systems. Particular attention is given to the nature of stacking faults formed in these structures and a unique method is presented for their termination. Based on control over supersaturation levels, it is shown that phase purity can be achieved over extended NW lengths. This work led to two publications in the Institute of Physics journal, Nanotechnology [116, 117]. In this chapter, the influence of NW geometry on their optical properties is also explored. Here, the role of surface passivation and size effects on the confinement of carriers is discussed. This study, published in the Journal of Applied Physics [118], demonstrated that preferential incorporation of growth species can lead to the formation of compositionally disparate segments within ternary semiconductor NWs.

The growth of coaxial p-n junction GaAs NWs on various surfaces is explored in Chapter 4. The main substrates of interest explored included single crystalline Si (100) and (111) surfaces, stainless steel foils, polycrystalline Si films on glass substrates, carbon-nanotube (CNT) composite films, and highly-order pyrolytic graphite (HOPG) substrates. Through analysis of growth on HOPG surfaces it was discovered that a unique Au-free growth mechanism persists under particular growth conditions, for which a qualitative model is presented. It is concluded in the chapter that CNT composite films are the most suitable substrate of choice for further device fabrication. The structural, optical, and electrical properties of the hybrid GaAs NW-CNT mesh structures are explored and presented as previously published in Nano Letters [119].

The basis of the experimental findings presented in Chapter 4, on the growth and characterization of GaAs NWs on CNT sheets, is extended to opto-electronic device applications in Chapter 5. Here, this hybrid nano-material is employed in the fabrication of flexible solar cells. Device testing, performance, and optimization are presented. The studies presented in Chapter 5 have been recently accepted for publication in the IEEE Journal of Selected Topics in Quantum Electronics [120].

Chapter 2

Experimental Techniques Related to Growth, Structural Analysis, and Optical Characterization

The experimental procedures employed in the research presented within this Thesis are individually explored in this chapter. The methods of interest include crystal growth via GS-MBE, various electron microscopy based approaches for the characterization of sample structure and chemistry, and spectroscopic techniques for optical characterization. In an effort to provide the reader with a concise, yet comprehensive, perspective of the relevant techniques, each method of analysis will be discussed in terms of its generic applications, as traditionally associated with experiments involving planar bulk samples. Modifications of conventional experimental practices required for the analysis of nanowire (NW) samples will be presented where necessary.

2.1 – Gas-Source Molecular Beam Epitaxy

Molecular beam epitaxy is a method for the growth of single crystalline films through atomic deposition. Etymologically, the term epitaxy is derived from its Greek roots, insofar as the prefix, *epi*, implies the condition of existing upon or over, while the term, *taxis*, describes arrangement or co-ordination. In the literal sense, therefore, epitaxy means to "arrange upon". However, in common practice, as applied in technical jargon, the term refers to the growth process of a solid film on a crystalline substrate, wherein the atomic arrangement of the film, or epilayer, is an extension of the crystalline order of the substrate [121].

The foundation for MBE growth of III-V compound semiconductors was first revealed by Günther when he demonstrated the vacuum deposition of stoichiometric GaAs films through a three-temperature method, in 1958 [122, 123]. Building upon this platform some ten years later, Bell Telephone Laboratories researchers, Arthur and Cho, introduced systematic modifications which effectively established the modern MBE technique for crystal growth [124,125]. These modifications included the incorporation of cryopanels for impurity reduction, use of solid source effusion cells for the introduction of growth materials, and the implementation of reflection high energy electron diffraction (RHEED) for *in situ* crystal structure characterization.

As in other physical vapour deposition techniques, the formation of crystalline layers in MBE relies on the condensation of growth species from a supersaturated vapour upon a substrate whose temperature is maintained substantially below that of the source [126]. The formation of the film is dependent primarily upon the sticking coefficient of the growth materials and the difference between the source impingement flux and its re-evaporation flux from the substrate. The continual maintenance of stoichiometric growth of III-V compounds through MBE arises from the unique adsorption and desorption kinetics of group V species on group III-terminated surfaces. In the particular case of GaAs films, it is well known that As species (supplied either as dimer or tetramer compounds) exhibit high surface residency lifetimes only on Ga-terminated GaAs surfaces. Otherwise stated, the sticking coefficient of group V species depends upon the presence of group III species. Thus, the dissociative chemisorption of As compounds and incorporation of As atoms within a stoichiometric GaAs film relies on the consumption of surface-bonded Ga atoms, which can only be ensured if an excess of group V to group III flux exists [121, 126].

A schematic representation of the GS-MBE system used for all NW growths discussed in the ensuing chapters is shown in Figure 2.1. This system, built by SVT Associates, relies on the effusion of solid elemental group III sources supplied from a heated Knudsen cell, and hydride (AsH_3, PH_3, etc.) gas sources in tandem with thermally decomposing gas crackers for the supply of the

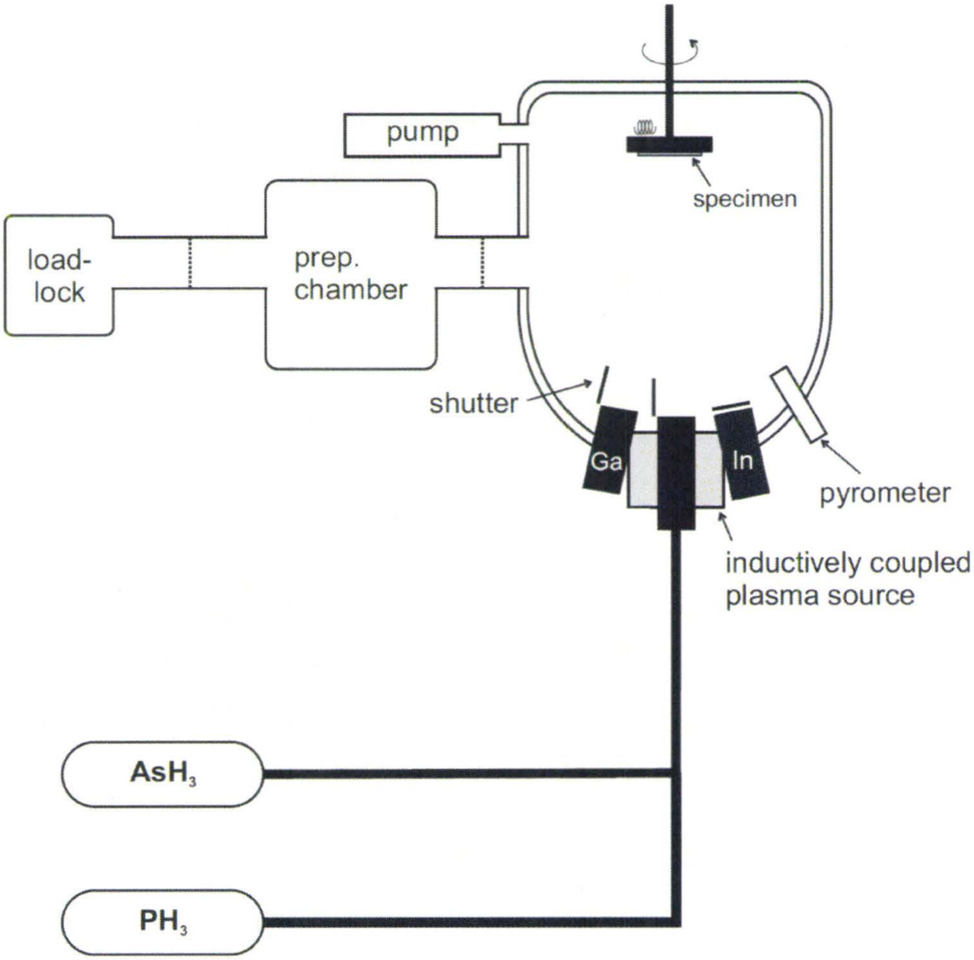

Figure 2.1 – Pictorial representation of the GS-MBE system at McMaster University, housed at the Tandem Accelerator Building. All NW growths performed for the purposes of the current work were realized by said system. Adapted from [127].

group V species. The former species are delivered as monomers, while the latter are predominantly supplied as dimers (As_2, P_2, etc.). All sources are directed toward a single substrate, in an inverted position, at an approximate angle of 35° with respect to the substrate normal. Turbo-molecular pumping is applied to the growth chamber for the maintenance of ultra-high vacuum (UHV) conditions, with base pressures ranging between 10^{-10} to 10^{-9} Torr. The vacuum sustained inside the reactor guarantees the arrival of adatoms, from the source to the substrate, with trajectories unperturbed by collisions with residual gasses, impurity atoms, or other effused adatoms. Thus, adatoms are transported by means of a true "molecular beam", wherein their mean free path exceeds the source-to-substrate distance. Shutters are located in front of the sources and mechanically operated so as to permit or block the flow of the effused species. Through this approach, heterostructures with atomically abrupt interfaces can be grown by appropriate source switching and quick shutter control. Growth temperatures are established through resistive heating of the substrate mount. An infrared pyrometer and a thermocouple placed at the front side of the substrate holder were used independently for temperature monitoring.

Crystal growth through MBE provides several advantages over MOVPE processes. First, MBE allows for lower temperature depositions without compromise of crystal quality. Second, control over monolayer deposition is possible as no turbulent gas flow exists to promote boundary layer challenges [3]. Third, the vacuum environment of MBE allows for *in situ* diagnostic methods such as RHEED [128] and mass spectroscopy [129]. Fourth, contrary to MOVPE methods, the use of toxic and pyrophoric metal-organic species is avoided in MBE practices [121].

The need for the use of group V hydride sources in GS-MBE, versus solid sources in elemental-source (ES)-MBE, is mainly based on the difficulties associated with depositing As- and P-based compounds in the latter approach. The difficulties stem from the large exponential increase in vapour pressure of these elements with increasing temperature. This makes control over As and P fluxes a complicated task. Also, large effusion cells are needed to cope with high vapour pressures, which create temperature control problems due to the low thermal conductivity of the materials from which they are comprised. In particular, ES-MBE schemes that employ red phosphorus as a material source are confronted with additional complications associated with the source's various allotropic forms. The P allotropes each have distinct vapour pressures, creating further beam flux control challenges. Finally, effusion sources used for the generation of P fluxes almost entirely produce P_4 molecules. These tetramers not only have a significantly lower accommodation coefficient in comparison to dimers, but also can lead to a build up of white phosphorus in the reaction chamber, which is prone to spontaneous ignition in oxygen rich environments [2].

For the purposes of the current study, several pre-growth sample preparation processes were employed, based on the particular substrate and growth processes. These methods will be individually discussed with respect to the distinct research purpose in the respective sections. All samples were loaded via a load-lock chamber and transferred to a preparation chamber for a degassing procedure (the specifics of which will be discussed, in turn, within each chapter) followed by a final transfer to the main reaction chamber. The samples rested on pre-fabricated molybdenum sample holders and secured in location with tantalum shims. The substrates resting on the holder stage were rotated during growth, at approximately 15 RPM, so as to limit the shadowing of peripheral substrate regions by the holder, and for improved deposition uniformity. All growths were conducted on 2-inch wafers or smaller cleaved/diced substrates indium-mounted to 2-inch wafers. In particular cases, where indium-mounting was an ineffective approach, substrates of choice were cleaved to approximately 5 mm by 10 mm rectangles and supported on a pre-fabricated molybdenum holder with six openings of the corresponding dimensions. In the growth chamber, once the growth temperature had been reached, the samples were subjected to an inductively-coupled H_2 plasma procedure for the desorption of native oxide layers and simultaneous formation of nanoparticles from previously deposited Au thin-film. This procedure occurred under a group V overpressure, ensuring that the decomposition of group V species at elevated temperatures would be prevented.

Growths were initiated by opening of the desired group III effusion cell. Depending on the NW structure, dopant modulation was performed by shuttering the effusion cells of Te, Be, or Si sources. Growth interruptions during heterostructure growths (described in full in Chapter 3) were performed by closing the shutter of the group III source, and subsequently re-opened after a designated period. All growths were terminated by closing the shutter of the group III effusion cell, while the sample cooled down at a rate of roughly 200 °C per hour, under a group V overpressure (exceptions are noted in Chapter 4). The group V fluxes were also terminated once the growth temperature registered less than 350 °C. After growths, the samples were removed from the MBE system and handled in ambient for characterization preparation procedures or device fabrication (unless otherwise stated, in the case of particular investigations).

2.2 – Fundamentals of Electron Microscopy Based Techniques

The direct imaging of nanoscopic structures is a task that requires microscopy techniques capable of achieving spatial resolutions beyond those permitted by optical means. Based on the classical Rayleigh criterion description [130], the smallest resolvable separation, or the resolution limit of an optical microscope, $(\Delta l)_{min}$, is approximated by:

$$(\Delta l)_{min} = \frac{0.61\lambda}{n \sin \beta} \tag{2.1}$$

where n is the viewing medium index of refraction, β is the semi-collection angle of the lens, and λ is the wavelength of the light employed. By this reasoning, the resolution limit of a typical light microscope is approximately half the wavelength of the light employed, or on the order of hundreds of nanometres in the case of visible light [131]. Thus, the need arises for the use of highly accelerated electrons with associated wavelengths tuneable to several orders of magnitude lower than that which can be achieved optically.

The "material-wave" hypothesis of electrons was set forth by de Broglie in 1925 and confirmed through the electron diffraction experiments of Thompson and Reid and Davisson and Germer in the following two years. This foundation was built upon by Knoll and Ruska, as early as 1931, in the fabrication of a rudimentary-form electron microscope [132]. The basic foundation established by de Broglie defines the associated wavelength of an electron as:

$$\lambda = \frac{h}{p} = \frac{h}{mv} \tag{2.2}$$

Here, h is the Planck constant and p describes the electron momentum, classified by the product of its velocity, v, and mass, m. The latter property can be further described by taking relativistic effects into account, such that:

$$m = \frac{m_0}{\sqrt{1 - \left(\frac{v^2}{c^2}\right)}} \tag{2.3}$$

where m_0 represents the electron rest mass and c is the speed of light. Considering the relativistic kinetic energy of an electron as, $E_k = (mc^2 - m_0c^2)$, such that $E_k = qV$, where q is the fundamental electron charge and V is the potential difference providing electron acceleration, one can express the electron wavelength as a function of the accelerating voltage by [133]:

$$\lambda = \frac{h}{\sqrt{2m_0qV\left(1 + \frac{qV}{2m_0c^2}\right)}} \tag{2.4}$$

The relativistic component, represented by the term in the brackets of the denominator, is of significance for the accurate calculations of electron wavelengths when potentials in excess of approximately 10^5 V are used. Thus, in the case of all transmission electron microscopy (TEM) and high voltage scanning electron microscopy (SEM), the relativistic approximation should be taken into account [133]. In the case of an electron being accelerated through a TEM column by a potential of 200 kV, its associated wavelength is calculated as approximately 2.5 pm.

Once an electron is first generated by an electron gun through either thermionic, Schottky, or field emission, it is subsequently accelerated by an anode cylinder. Its trajectory is then perturbed by a series of axially-symmetric magnetic lenses which provide focussing, magnification, and control over the maximum angle of the electron path relative to the optic axis. Although the true wavelength of the electrons can be on the order of pico-metres, aberrations suffered by the magnetic lenses employed results in an image resolution on the order of angstroms, in the case of contemporary TEM systems. Next, electrons are focussed onto the sample where they undergo a series of elastic and inelastic scattering events with the atomic constituents of the specimen, within a potential dependent interaction volume, thereby generating a variety of signals, as shown in Figure 2.2. The generated signals are electronic or photonic in nature, depending on the particular interaction of the primary electrons with the specimen, and translate characteristic information about the specimen structure and chemistry. The particular signals of interest and their detection schemes will be discussed in relation to the relevant microscopy techniques in the following sections.

2.2.1 – Scanning Electron Microscopy

The scanning electron micrographs presented in the current work were all obtained using a JEOL JSM-7000 F SEM, with the exception of those shown in Figures 2.4, 4.9, and 5.1, which were achieved with the use of a Zeiss SMT NVision40 SII CrossBeam system. Both systems are equipped with Schottky

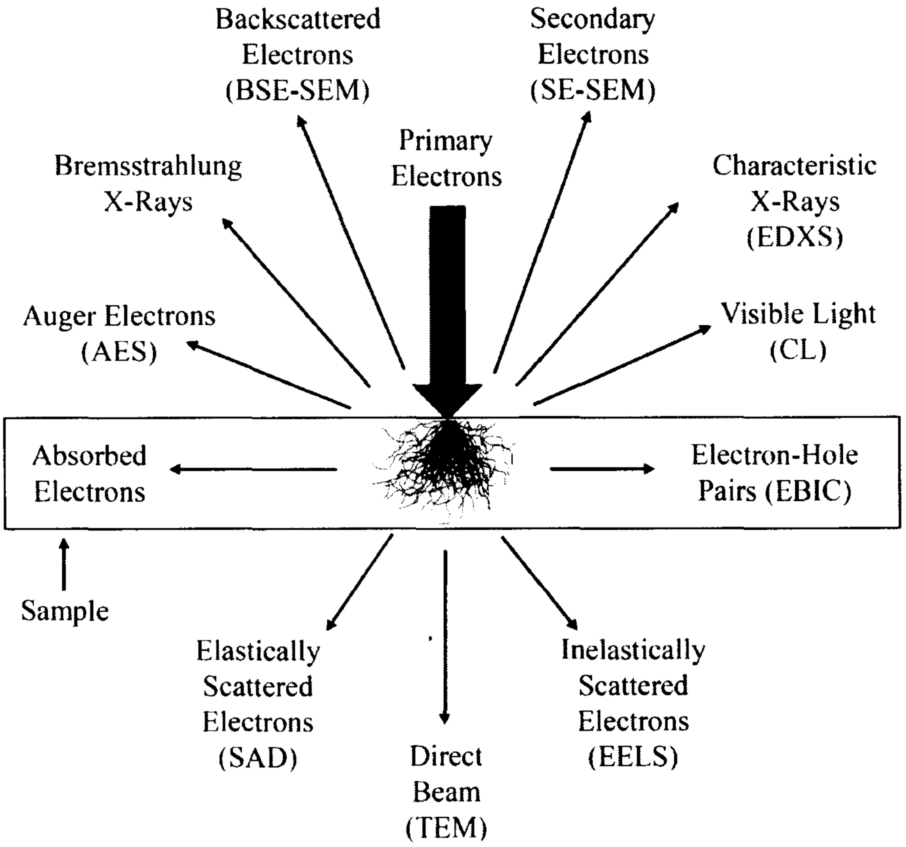

Figure 2.2 – Representation of signals generated upon interaction of a primary electron (PE) beam with a sample in typical electron microscopy experiments. The characterization method associated with each signal is denoted in parentheses, including Auger electron spectroscopy (AES), backscattered electron (BSE)-SEM, secondary electron (SE)-SEM, energy dispersive X-ray spectrometry (EDXS), cathodoluminescence (CL), electron-beam induced current (EBIC), electron energy-loss spectroscopy (EELS), TEM, and selected area diffraction (SAD). Below the sample surface, the interaction volume is depicted as comprised of individual primary electron trajectories. Adapted from [131].

type field-emission gun filaments for the generation of primary electron fluxes [134, 135]. The primary electron (PE) beam, or electron probe, is scanned, using deflection coils, across the sample surface in the x and y directions. The electron probe diameter, in the systems listed above, is expected to be on the order of 1 nm, enabling a corresponding resolution limit [136]. Through the raster scanning process, an external computer system associates a specific incident electron probe address (x, y) with the detected intensity of the corresponding signal generated from the sample. The signals are generated within a volume, limited by the penetration depth of PEs within the sample, wherein electron-specimen interactions transpire. The detected signals are each emitted from particular ranges within the interaction volume, as specified in Figure 2.3. For the purposes of the current study, the generated SEM signals of interest are those based upon the emission of secondary electrons (SEs) and backscattered electrons (BSEs).

Secondary electrons are generated when primary electrons eject loosely bound conduction electrons from the specimen, through inelastic scattering events. These are low energy electrons, on the order of several tens of electron-volts, which have low mean-free paths, such that they can only "escape" from the sample surface if they are generated at shallow depths. Typically, SEs are characterized as having an escape depth of roughly 10 nm. As such, this signal is predominantly responsible for translating topographic information about the specimen [133]. In the case of NW research, secondary electron mode imaging renders information about NW density, morphology, orientation, length and

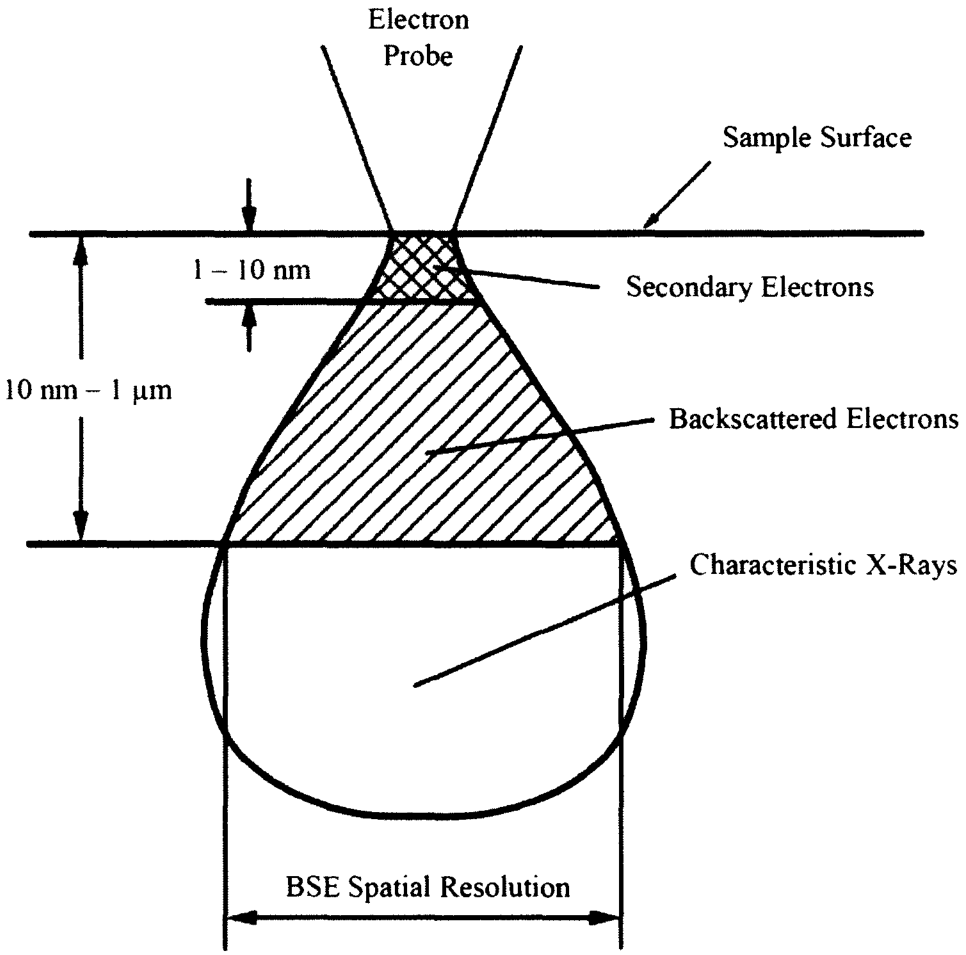

Figure 2.3 – Interaction volume of primary electrons with specimen atoms below the sample surface. Relative regions from which secondary electrons, backscattered electrons, and characteristic X-rays can escape, under typical SEM imaging conditions, is shown. Adapted from [137].

diameter. The ratio of the number of SEs escaping the sample surface per incident PE is referred to as the secondary electron yield. The SE yield depends upon the accelerating voltage of the PE beam and the relative angle of the samples with respect to the electron probe, as well as specimen composition and doping. As incident electron energies increase, their penetration depth increases such that SEs are only generated at greater depths and cannot effectively be liberated from the specimen surface. In contrast, irradiation of non-normal surfaces results in greater SE yield [136]. The detection of SEs, with respect to the SEM systems utilized in the current work, is achieved by Everhart-Thornley detectors (tandem scintillator and photomultiplier-tube arrangement), biased for preferential SE detection.

Backscattered electrons, on the other hand, arise when incident PEs undergo elastic (Rutherford-type) scattering events within the Coulombic field of the sample's atomic nuclei. When such a collision transpires, the incident electrons can be scattered at angles greater than 90° (hence, backscattered), and become ejected from the sample surface. The BSEs typically have energies within 0.2 % of the PE energy [133] and, therefore, have much greater corresponding mean-free path lengths, relative to SEs. Thus, a BSE signal can be both generated and liberated from greater depths within the sample. The backscattered coefficient is defined as the fraction of PEs that escape the sample surface as BSE's, and is highly dependent upon the atomic density of the specimen. As a result, BSE signals exhibit strong atomic number- or Z-contrast and translate information about the variations in sample chemistry. Typically, the higher the Z-number of the sample's constituents in a given region, the higher the resultant intensity contrast in the corresponding BSE mode SEM image of that region [133]. In the particular case of an Au-assisted GaAs NW, the tip will appear as a region of bright contrast, in comparison to the lower-Z GaAs structure, in a BSE image. In the previously listed SEM systems, the BSEs are detected using solid-state Robinson-type detectors. However, negatively biased Everhart-Thornley detectors could also be used to preferentially detect BSEs [136].

Tuning of SEM working conditions is an essential task for the limitation of artefact formation, avoidance of sample charge accumulation, and the acquisition of images that are accurate representations of the true sample. The main parameters that influence image formation, other than the sample material itself, include accelerating voltage, working distance, aperture size, and probe current [138]. At high accelerating voltages, the interaction volume increases, thereby reducing resolution. In this manner, smaller features, such as the lateral extent of a NW, can become transparent to the electron beam [133]. In the case of single NW imaging, cross-sectional imaging, and high-magnification planar imaging, lower accelerating voltages, ranging between 1.5 to 3 kV, were employed. However, a trade-off exists, as higher energy spreads associated with low-voltage electron probes result in the increase of chromatic aberrations. Working distance is defined as the distance between the centre of the objective lens system and the sample plane [138]. Increasing this parameter results in the reduction of the convergence angle between the PE beam and the optic axis, which, in turn, brings about a greater depth of focus. However, greater working distances are also associated with weaker lenses and, therefore, greater lens aberrations. It was experimentally determined that an appropriate compromise was reached at a working distance ranging between 4 to 6 mm; the SEM images presented in this Thesis were obtained within this range. Aperture diameters can also be controlled as an imaging parameter. The use of smaller diameter apertures ensures the reduction of chromatic and spherical aberrations. Although, diameter reduction can also increase the degree of PE diffraction from the aperture, the latter effect is less influential than the former aberrations suffered. In the current work, all images were obtained through a 50 μm and a 7.5 μm aperture, with respect to the JEOL and Zeiss SMT systems, respectively. Finally, the probe current is dependent upon the source brightness and largely influences the final probe diameter and, therefore, spherical aberrations [138]. For single NW or general high magnification imaging (magnification in excess of 100 000X) low emission current imaging was employed for resolution enhancement. It should be noted that, here, the intended definition of magnification is the ratio of the length of a feature in an image to the length of the corresponding sample feature, scanned by the PE probe [133].

Finally, the basic sample preparation processes utilized in SEM experiments is considered. For planar and tilted view SEM imaging, as-grown NW samples were adhered to Al-based SEM mounting stubs with either carbon-tape or liquid silver-based adhesives. In the case of undoped sample imaging, where carbon tape was the adhesive medium of choice, the sample substrate and Al stub were contacted using silver paste, so as to provide for a conductive pathway and limit sample charging [136]. For cross-sectional SEM imaging, samples were secured inside pre-fabricated grooves formed in the Al stubs, using Ag-paste. Thus, illumination by the PE beam occurred in the direction perpendicular to the NW growth axis, thereby reducing foreshortening effects [138].

2.2.2 – Focussed Ion Beam Techniques

The use of a focussed ion beam (FIB) system enables not only the imaging of nano-scale structures, but also site-specific material deposition and sputtering of material from samples, in predefined configurations through ion milling. The Zeiss SMT NVision40 SII CrossBeam system, which was used in particular SEM experiments, was also employed as the sole FIB system for all the related research presented here. This system is equipped with an ion beam column oriented at 54.5° with respect to the vertical electron beam column, in a dual-beam configuration. Gallium ions (Ga^+) are produced through field ionization of liquid-phase gallium wetted to a tungsten needle, at the tip of a liquid metal ion source (LMIS) [139]. Gallium is used as the material of choice for the production of high energy ions on account of its low melting temperature, volatility, and vapour pressure [140]. Furthermore, Ga^+ ions have sufficient mass for the effective milling of heavy elements [140] while their emission in the form of a focussed probe exhibits high angular intensity with small energy spreads [139]. The LMIS of the aforementioned Zeiss system is capable of generating a Ga^+ probe diameter of 4 nm [135]. Although a focussed ion beam system can be utilized for imaging, through the detection of ejected SEs and secondary ions (SIs), and for the neutralization of accumulated charges in tandem-SEM imaging experiments, its primary use in the current work was for milling in cross-sectional sample analysis and for sputtering and deposition processes during TEM sample preparation.

Sputtering of material from the sample surface is the result of inelastic collisions and energy transfer from high energy ions and the atomic or molecular constituents of the specimen. The removal of material occurs within a "collision cascade" region, wherein sample atoms have received energies in excess of their surface binding energy from incident ions [141]. Control over the raster scanning of the FIB enables site-specific milling. The sputtering yield, defined as the number of ejected particles per incident ion, is proportional to the accelerating voltage of the ion beam and the angle of incidence. It should be noted, particularly in the case of trench formation with depths greater than 1 μm, that re-deposition of sputtered material can transpire on surfaces formed within the milling site. This results in the degradation of the aspect-ratio of the generated trenches, roughening of their sidewalls, and the formation of characteristic V-shaped milled features. Re-deposition can be counter-acted by the reduction of beam current, modification of probe incidence angle, and local introduction of reactive gaseous species, such as Cl_2, I_2, or XeF_2 [139]. Through controlled milling and tandem-SEM imaging, site-specific and elastic strain-free tomography of sample features can be achieved with a dual-beam system.

The use of a FIB system also provides the capability of site-specific lamellae preparation for TEM analysis. In the current research, this extends to the ability to remove and investigate a particular NW of interest, from the as-grown sample. For this procedure, *in situ* FIB-induced deposition is required. To date, nearly a dozen materials have been reported to have been deposited via FIB, including Al, W, Au, Pt, Cu, Ta, Fe, Pd, SiO_2, and C [140]. In this scheme, a nozzle is inserted near the sample surface inside the FIB chamber, through which precursor gas species are introduced. As the precursors flood the sample surface at controllable incident fluxes, the Ga^+ ion beam is raster scanned across the surface area on which the desired deposition is intended. Thus, the incident ion flux allows for the localized dissociation of precursor gasses and subsequent material deposition. The remnant gaseous species of the decomposed precursors are then purged from the main chamber. In the current work, Pt and C layers were deposited through the decomposition of (methylcyclopentadienyl) trimethyl platinum and naphthalene precursors, respectively [139, 140].

In Figure 2.4, the various stages of thin-foil TEM sample preparation via FIB are shown. In this process, once the particular NWs of interest have been located (Figure 2.4(a)), carbon deposition is initiated over a rectangular area encompassing the NWs and their immediate vicinity (Figure 2.4(b)). Next, two trenches are ion-milled, adjacent to the longitudinal sides of the deposited carbon

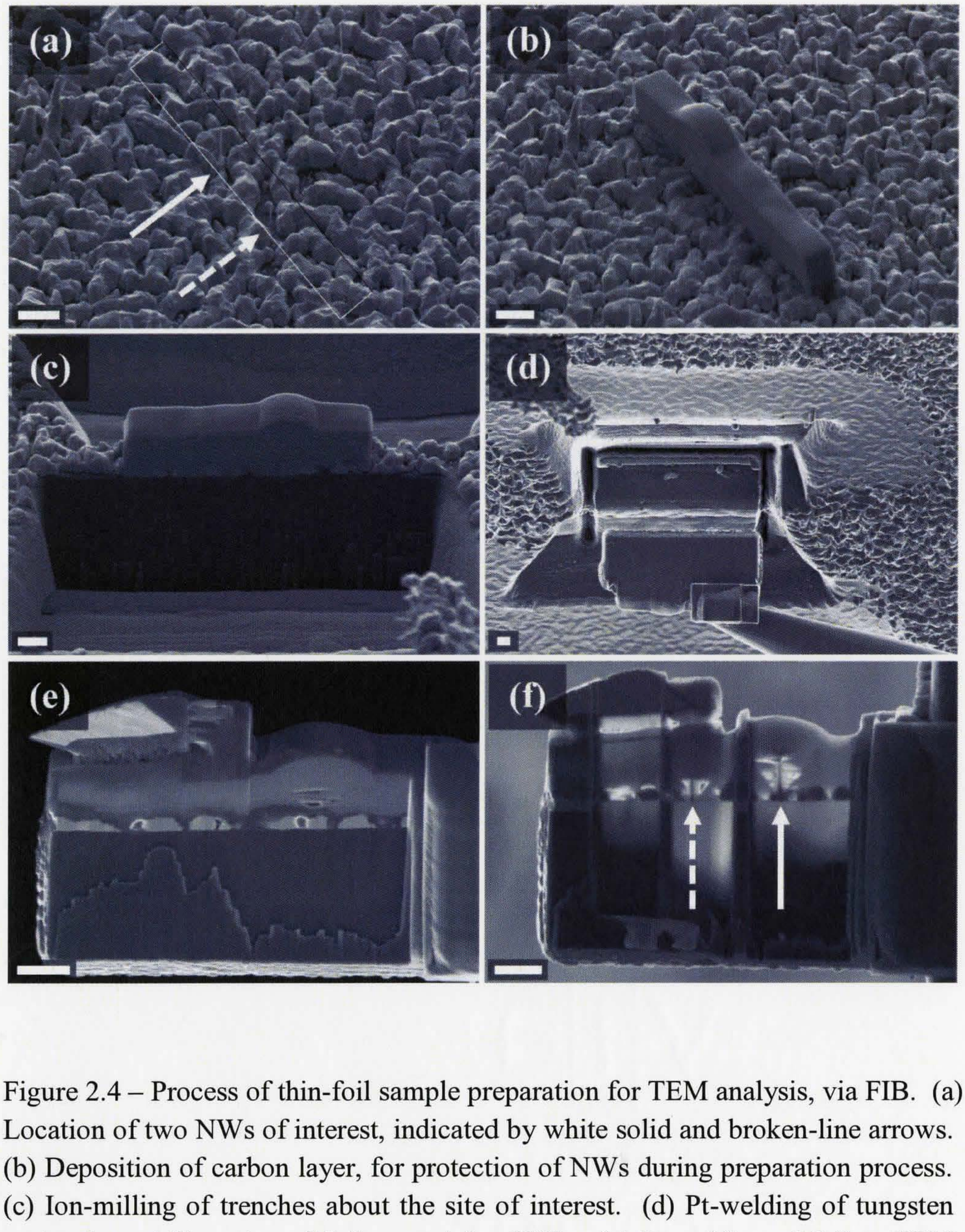

Figure 2.4 – Process of thin-foil sample preparation for TEM analysis, via FIB. (a) Location of two NWs of interest, indicated by white solid and broken-line arrows. (b) Deposition of carbon layer, for protection of NWs during preparation process. (c) Ion-milling of trenches about the site of interest. (d) Pt-welding of tungsten probe tip and liberation of foil, containing NWs. (e) Pt-welding of foil to TEM grid and removal of probe finger (f) Thinning of lamella, using fine probe current ion-beam. Here, the thin foil is electron-transparent at typical accelerating voltages employed in TEM. The location of the two original NWs of interest are once again designated by white solid and broken-line arrows, respectively All scale bars represent a 2μm length.

layer (Figure 2.4(c)). A micro-manipulator controlled tungsten tip is Pt-welded to the top of the C-deposited region between the two trenches, and a series of three ion beam line-scans allow for the liberation of a foil, containing the NW of interest (Figure 2.4(d)). The foil is then Pt-welded to a designated copper-based TEM sample holder, and a single FIB line-scan separates the tungsten probe finger (Figure 2.4(e)). Next, a series of fine probe-current milling sequences are used to thin both sides of the lamella, allowing for electron beam transparency in a TEM system (Figure 2.4(f)). Thus, particular NWs of interest can be removed from as-grown samples and studied using analytical TEM techniques.

2.2.3 – Transmission Electron Microscopy

Transmission electron microscopy relies on the scattering interactions of high energy electrons (> 100 keV) with the constituents of a sufficiently thin (< 250 nm) specimen. In this approach, a stationary electron probe is incident on the sample, in contrast to the raster scanning approach employed in SEM characterization. The high energies possessed by the impinging electrons, coupled with the minimal thickness of the specimen being probed, permit the penetration depth of the PEs to exceed the thickness of the sample. As such, the primary electrons are transmitted through the sample, with detected intensity contrasts representative of the internal structural make-up of the specimen. In conventional TEM experiments, two main contrast formation mechanisms are exploited; namely, mass-thickness contrast and diffraction contrast [131].

Intensity variations in a rendered TEM image can be related to the atomic mass and/or thickness of a particular region within the sample of interest. This mechanism provides qualitative information depending on the degree of PE absorption within the sample and the scattering angle of the transmitted electrons relative to the optical axis. Thicker segments within a particular sample region will inherently absorb more electrons (lower relative penetration depths), while regions containing high-Z elements cause the incident electrons to elastically scatter at higher angles away from the optical axis and impinge upon the limiting objective lens aperture at the back focal plane. In both scenarios, said electrons fail to be detected and the resultant TEM image consists of corresponding domains of dark contrast. This approach is referred to as bright-field imaging, wherein only the through- or direct-beam electrons are collected, while those that have been diffracted or scattered at larger angles are blocked by an aperture. This particular approach, applied to NW imaging, permits the precise determination of morphology and the delineation of regions of dissimilar elemental composition (for example, differentiation between Au tip and NW body).

In the analysis of crystalline samples containing grains of disparate atomic plane orientations, regions of phase non-uniformity, or structural defects, diffraction contrast is exhibited by the associated TEM image. As electrons become diffracted from the atomic planes, their trajectories can become altered such that the objective aperture prevents their collection. Thus, the crystalline domains with orientations satisfying the Bragg condition [142], will appear as regions of dark contrast, while regions which fail to diffract the incident electrons will appear brighter, in the corresponding image. Similarly, defects in a sample of single-phase crystallinity can diffract the primary beam and appear in an image as a dark region. This method can allow for the appearance of stacking faults in NW specimen, as will be further demonstrated in Chapter 3. It should be noted that proper NW orientation is of vital importance, in this approach, as stacking faults may fail to appear in NWs not aligned along the <-2 1 1 0> zone axis [108, 143]. Conversely, in dark-field imaging, the position of the objective aperture can be adjusted such that only a particular diffracted beam is collected. In this manner, specific grain orientations within a polycrystalline sample can be discerned in the resultant image as regions of bright contrast.

In addition to the two contrast mechanisms described above, in high-resolution transmission electron microscopy (HR-TEM) systems, phase contrast can also be employed. Here, a large objective aperture is chosen such that the diffracted beams and through beam can simultaneously be collected. The interference of multiple beams of different amplitude and phase results in the collection of a Fourier sum of signals, leading to a highly detailed image. Through this approach, lattice resolved images of atomic columns can be achieved [131, 136, 142].

Sample preparation, for all TEM experiments, was achieved through three main methods. Throughout this work, NWs of interest were sufficiently thin to allow for electron beam transparency at the requisite operating voltages, meaning that sample thinning was not necessary. Instead, for the analysis of single NW specimens, TEM sample preparation involved submerging a cleaved portion of the as-grown sample in a small volume (2 mL) of solvent, for removal of NWs from the substrate through an ultra-sonication procedure. The density of the NWs in the solution was controlled by optimizing the sonication period (10 – 120 s), as-grown sample area (25 – 100 mm^2), and the choice of solvent utilized (deionized water, methanol, acetone). Suspended NWs in solution were dispersed, from drops of 2 μL volume, to standard TEM carbon holey copper grids. Upon evaporation of the solvent, in ambient, the NWs of interest resided on the surface of the carbon sheaths for subsequent TEM analysis. In cases when the growth interface, formed between the NWs and substrate, was the subject of investigation, or when as-grown NW densities were too low to render adequate samples through a sonication procedure, then cross-sectional lamellae were produced. This was achieved either through the FIB-based techniques described in the previous section or through conventional rafting, thinning, and ion milling processes employed for the preparation of thin-film TEM samples [131, 136].

For conventional TEM experiments, a Philips CM12 TEM system was utilized, operating at an acceleration voltage of 120 kV. This system was primarily used for morphology and heterostructure analysis, investigations into stacking-fault formations, and for the accurate determination of NW diameters. For HR-TEM and analytical TEM experiments, including EDXS and SAD pattern acquisition (discussed in the following segments), a JEOL JEM 2010F system was employed, operated at 200 kV. All lattice-resolved images presented in the current work were obtained with this system, with the exception of those presented in Section 3.2. These images were generated using an FEI Titan 80-300 HB ultra high resolution transmission electron microscope (UHR-TEM), operated at 300 kV. All three systems are equipped with field emission electron sources and charge-coupled device (CCD) cameras for image acquisition.

2.2.4 – Scanning Transmission Electron Microscopy

In addition to single point or convergent beam imaging methods, the JEOL JEM 2010F microscope is equipped with scan coils allowing for the raster scanning of the fine electron probe. This allows for detection of transmitted or diffracted electrons, who's point of origin can be distinguished with respect to the scanning address of the incident beam, much as in the aforementioned case of SEM imaging. In the current work, two main characterization advantages offered by this scanning transmission electron microscopy (STEM) approach were exploited.

First, STEM characterization allowed for site-specific EDXS analysis of NW samples with resolutions on the order of 10 nm [136]. This was particularly beneficial in the heterostructured NW analysis, allowing for the differentiation of distinct radial layers. By taking point source measurements, line-scans, and planar maps of specific NW regions of interest, morphological and compositional information could be obtained. These will be further discussed in the following section.

The second characterization advantage is related to the high-angle annular dark-field (HAADF) detector employed in STEM imaging. The HAADF detector in the JEOL system is a ring-shaped Robinson detector, placed below the sample plane in the microscope column. Its large central opening allows the direct-beam electrons transmitted from the sample to be detected further down the column by the bright-field detectors. However, transmitted electrons directed at higher angles relative to the optical axis, resulting from high-angle scattering events within the sample, are collected by the annular detector. Thus, HAADF is less sensitive to Bragg scattering, thereby translating less information regarding crystal structure. The angular range of collected signals is determined by the inner and outer radii of the detector, and by choosing a large inner radius, the collection of electrons scattered to large angles is ensured. As the probability of elastic scattering at high angles is proportional to the square of the atomic number of the element from which scattering occurred [136], HAADF-STEM images demonstrate a high degree of Z-contrast. Thus, compositional variances within a single NW can be discerned, whereby regions of brighter contrast in the image are representative of higher-Z elemental make-up, in the corresponding sample region. As shown in Chapter 3, even stoichiometric non-homogeneities within a NW composed of the same ternary alloy can be distinguished in an HAADF image.

2.2.5 – Energy Dispersive X-Ray Spectrometry

As shown in Figure 2.2, inelastic scattering events between primary electrons and host atoms of a specimen in SEM and TEM experiments can result in the generation of Bremsstrahlung and characteristic X-rays. Bremsstrahlung or "breaking radiation" results from the deceleration of incident electrons in the intrinsic Coulomb field generated by the host nuclei and surrounding electrons. The deceleration is associated with an energy loss that is conserved by the emission of a photon. The Bremsstrahlung emission forms a continuous background spectrum in EDX spectra [138].

An inelastic collision between an incident electron and an inner-shell host electron can cause the ejection of the latter. For such a phenomenon to progress, the kinetic energy of the PE must exceed the critical binding energy of the inner-shell electron. This process results in the host atom being in an excited state, for a period on the order of 1 ps, after which the atom relaxes through the transition of an outer-shell electron to the inner-shell vacancy. The relaxation transition can result in two distinct energy compensating processes: (1) the emission of an Auger electron and (2) the emission of a characteristic X-ray. The energy of the emitted X-ray photon is therefore equal to the energy difference between the outer- and inner-shells of the host atom in which the relaxation process transpired. This energy difference is atomically characteristic and so the energy of the detected X-ray photons translates information regarding the presence of a particular element within the probed sample region [138].

The X-ray fluorescence yield, defined as the ratio of the number of photons generated to the number of inner-shell ionizations, increases with the Z-number of the corresponding sample element. The depth at which X-rays are generated is inversely proportional to the constituents' Z-number and density. It should be noted that since characteristic X-rays can escape from greater depths within the sample, in comparison to SE and BSE signals, the spatial resolution of an EDXS elemental map is lower than that of an SEM image. Characteristic X-ray photons are detected by liquid nitrogen cooled, Li-drifted p-i-n Si detectors operating in tandem with a pulse pile-up rejecter, mitigating the effects of simultaneously detected photons [136]. Furthermore, true features of X-ray spectra are vulnerable to distortions arising from the detection and pulse-processing procedures. These spectral variations include peak broadening, peak distortion, presence of escape peaks, sum peaks, internal fluorescence peaks, and absorption window edges [138].

As previously mentioned, EDXS analysis was employed in the current work in a variety of experiments. These include point analysis and elemental mapping for the compositional quantification of ternary alloys and determination of elemental group III concentrations within the Au-based alloyed seeds, line-scan analysis for the direct verification of heterostructure geometries, and full-spectra acquisitions for site-specific elemental detection. The atomic orbital transitions from which the detected X-rays originated (Kα, Kβ, Lα, etc.) will be presented throughout this Thesis, in relation to the corresponding EDXS experiment.

2.2.6 – Selected Area Electron Diffraction

When a crystalline specimen is illuminated by a large area incident electron beam, in TEM, sharp diffraction spots are generated in the back focal-plane of the objective lens. Diffraction occurs due to elastic scattering of the incident electrons from the atomic planes of the crystalline sample, which satisfy the Bragg relation [142]. By appropriate defocusing of the intermediate lens system, the generated diffraction pattern can be projected onto the image plane. A selected area diffraction (SAD) aperture is placed below the objective aperture, limiting the spatial extent of the specimen region from which diffracted electrons are collected [136]. Based on the particular experiment at hand, SAD diaphragms of varying diameters can be used, typically ranging between 1 to 100 μm [131].

Diffraction patterns reveal crystallographic information about the specimen, as each generated diffraction spot is the inverse-space representation of the set of real-space atomic planes present in the specimen. In SAD experiments involving single crystalline samples, the symmetry of a generated pattern, the relative spot separations, and the angles formed between spots, coupled with knowledge of the zone axis along which the sample is oriented, can be used to accurately index the resultant diffraction pattern. Thus information regarding the crystalline structure, phase-purity, growth direction, and plane separations of a given NW can be obtained through selected area diffraction investigations.

2.3 – Optical Characterization Techniques

This section explores the main optical characterization methods employed in the post-growth analysis of single NW and as-grown ensemble-NW specimens. Micro-photoluminescence (μ-PL) spectroscopy was utilized for the determination of temperature dependent bandgap energies of various NW material groups and for the qualitative evaluation of confinement effects in coaxial NWs of differing shell thicknesses. Low temperature magneto-photoluminescence (M-PL) spectroscopy was used for investigations on spatial confinement of carriers and surface passivation effects in core-shell heterostructured NWs. Also, Raman scattering spectroscopy was employed in the analysis of NW interface states and for the evaluation of ternary alloy compositions.

2.3.1 – Micro-Photoluminescence Spectroscopy

Photoluminescence (PL) spectroscopy is an attractive characterization technique as it allows for sensitive, non-contact, and non-destructive analysis, requiring simple, if any, sample preparation techniques. Furthermore, PL experiments are ideally suited for studies of thin epitaxial layers and low-dimensional systems as the penetration depth of the exciting beam is less than a micron, with lateral extent akin to the diffusion length of minority carriers [144]. The basis of PL concerns a non-equilibrium transition in which the absorption of optical energy induces the population of carriers in excited energy states whose spontaneous relaxation to the lowest available state is facilitated by a radiative energy conservation process, namely, the emission of a photon [145]. The characteristics of a spectrum produced by such radiative transitions are indicative of the properties of the material in which the process occurs. The position and profile of a PL spectrum determines not only the fundamental energy gap between the valence and conduction bands, but also the nature of intermediate dopant, impurity, or excitonic states as dependent upon parameters such as carrier concentration, temperature, alloy composition, heterojunction quality, and excitation intensity [146-148].

Gaining an understanding of the non-equilibrium recombination rate can be motivated by considering the simpler case of recombination under equilibrium conditions, as per the Roosbroeck-Shockley approach [149]. If we assume that the radiative recombination rate is equal to the optical generation rate of electron-hole pairs, then we can express the radiation emission rate as [150]:

$$R(\nu) = \int P(\nu)\rho(\nu)d\nu \tag{2.5}$$

where $P(\nu)$ and $\rho(\nu)$ represent, respectively, the probability of absorption per unit time and density of photons with frequency, ν. In turn, $P(\nu)$ can be expressed as:

$$P(\nu) = \frac{1}{\tau(\nu)} = \alpha(\nu)\left(\frac{c}{n}\right) \tag{2.6}$$

where $\tau(v)$ is the mean lifetime of a photon traveling in a medium with index of refraction, n, and c represents the speed of light in a vacuum. Moreover, the photon density is described by:

$$\rho(v) = \frac{8\pi v^2 n^3}{c^3} \frac{1}{\exp(hv/kT) - 1} dv \tag{2.7}$$

wherein, h, k, and T have the usual definitions.

In the case of highly pure crystals at low-temperatures, band-to-band and free exciton-mediated recombinations are the predominant radiative processes. However, when dopant concentrations in excess of 10^{15} cm^{-3} exist, then bound exciton-mediated recombination, donor-to-acceptor, band-to-donor, and band-to-acceptor transitions may also prevail. Generally, deep transitions (conduction band-to-acceptor, or donor-to-valence band) are more probable than their shallow (conduction band-to-donor or acceptor-to-valence band) counterparts; both processes, however, are less probable than conduction band-to-valence band transitions. Specifically, for GaAs, the electron lifetime in the conduction band has been calculated as 0.31 ns, compared to several nanoseconds for the lifetime of an electron in the donor band [150]. Thus, given sufficiently high dopant concentrations such that the conduction, valence, donor, and acceptor bands are all occupied, the radiative recombination associated with conduction-to-valence band transitions would be four times more probable in GaAs [150].

Nonradiative transitions also occur owing to recombinations through a continuum of states. A continuum can be thought of as a strong deformation of the band structure wherein multiple states exist within the fundamental energy gap.

Such a scenario arises in the case of dangling bonds at the surface of a material, where the lattice structure terminates. When carriers are within a diffusion length of the surface, they may recombine via the continuum, in a process void of photon emission. Metallic inclusions, localized defects, and strain effects can also produce a band perturbation sufficiently large to constitute a continuum. Thus, if photo-generated carriers have diffusion lengths that overlap with the effective radius of the inclusion, strain, or defect, then they may recombine in a nonradiative process through the traps of the intermediate continuum states [150].

The temperature at which a PL experiment is conducted will dramatically influence the resultant emission spectrum. Not only is the intrinsic carrier concentration increased with added thermal energy [151], but also the potential associated with an impurity level [150]. More generally, increased temperature influences the crystal structure of a material by increasing atomic oscillations relative to their equilibrium lattice positions. In semiconductors, the temperature dependent band gap energy, $E_G(T)$, is empirically defined according to the Varshni relation [152]:

$$E_G(T) = E_G(T = 0) - \frac{\alpha T^2}{T + \beta} \tag{2.8}$$

where α and β are adjustable, empirical parameters specific to each semiconductor material, and $E_G(T = 0)$ is the intrinsic band gap energy at 0 K.

Band tailing effects are more pronounced with increasing temperature and, as such, the PL emission peaks are shifted accordingly. Furthermore, increased thermal ionization reduces the effects of exciton-based transitions. Thus, spectral lines due to radiative excitonic effects are not well represented at higher temperatures. At higher temperatures, Auger effects are also increased as a result of greater carrier concentrations, while sharp spectral features are perturbed due to thermal broadening. Therefore, the most accurate PL spectra are obtained under cryogenic conditions, wherein thermally-activated non-radiative transitions are effectively quenched.

For PL experiments involving single NW specimens, presented in the current work, sample preparation was performed in a similar manner as in single NW TEM experiments. Ultrasonic NW removal in a 2 mL volume of solvent was performed for varying periods depending on the density of NWs on as-grown samples. Drops of 2 μL volume containing liberated NWs were then dispersed on SiO_2 capped Si (100) substrates, and the solvent was subsequently evaporated under ambient conditions. Thermal wet evaporation of an SiO_2 layer with approximate thickness of 350 nm ensured that substrate PL signal would not interfere with that of the probed NWs. Prior to PL investigations, the prepared samples were imaged in SEM such that the position, structure, and degree of isolation of single NWs could be determined. Both excitation and PL collection was achieved through an objective allowing for an excitation spot of roughly 2 μm diameter. Thus, a micro-photoluminescence (μ-PL) setup was achieved such that individually located NWs of known dimensions could be probed.

All μ-PL experiments discussed in this Thesis, were carried out in the Institute for Quantum Computing photonics laboratory at the University of

Waterloo. Experimental set-up and PL acquisition was performed by Dr. Christophe Couteau, under the supervision of Dr. Gregor Weihs. The setup involved placing the NW decorated substrates in a continuous flow helium cryostat, wherein the samples were cooled to a temperature of approximately 7 K. Excitation was provided using a laser, centered at 532 nm, at a power of 80 μW. The collected μ-PL signal was resolved by a liquid nitrogen-cooled Si CCD camera.

2.3.2 – Magneto-Photoluminescence Spectroscopy

In the presence of a strong applied magnetic field, the motion of free electrons within a semiconductor material becomes restricted to helical orbits, with cyclotron frequencies of $\omega_c = (|q|B/m_e)$, where q is the electron charge, B is the magnitude of the applied magnetic field, and m_e is the effective electron mass [153]. Quantization of electron orbitals results in the conversion of energy bands into a series of discrete energy levels, commonly referred to as Landau levels. The radius of the first orbital, corresponding to the lowest Landau level, is defined as the magnetic length and can be represented by:

$$L_B = \sqrt{\hbar/|q|B} \tag{2.9}$$

While the electron energies of motion in directions parallel to the orientation of the B-field remain unchanged, the energies in planes perpendicular to the applied field become quantized, according to:

$$E = \left(n + \tfrac{1}{2}\right)\hbar\omega_c + \frac{(\hbar k_z)^2}{2m_e} \qquad (2.10)$$

where, k_z represents the wave-vector in the z-direction of a Cartesian coordinate system (parallel to direction of the magnetic field) and n is the Landau quantum number of integer value [154].

Whereas a semiconductor material in a zero magnetic field exhibits a density of states, $g(E)$, proportional to $E^{1/2}$, the quantization effect imparted in a finite B-field modifies the density of states proportionality, such that a $E^{-1/2}$ dependence prevails, as depicted in Figure 2.5(a). Correspondingly, the otherwise spherical constant-energy surface or Fermi sphere is augmented in the presence of a sufficiently strong magnetic field, such that the permitted k-values reside on the surfaces of a set of concentric cylinders, oriented perpendicularly with respect to the field direction [153]. This has been pictorially represented in Figure 2.5(b). The radii of the concentric cylinders increase with the magnitude of the applied magnetic field.

For the detection of such quantum effects, the mean thermal energy of the system must be significantly less than the energy separation associated with the electrons in the Landau orbitals. The criteria, $kT << \hbar\omega_c$, requires that cryogenic conditions and high magnetic fields are provided.

The implication of magnetic quantization is that in magneto-photoluminescence (M-PL) experiments, wherein PL is obtained from samples placed under high applied fields, the collected spectrum will be blue-shifted with energies corresponding to the separation of the Landau levels. In the case of NW-

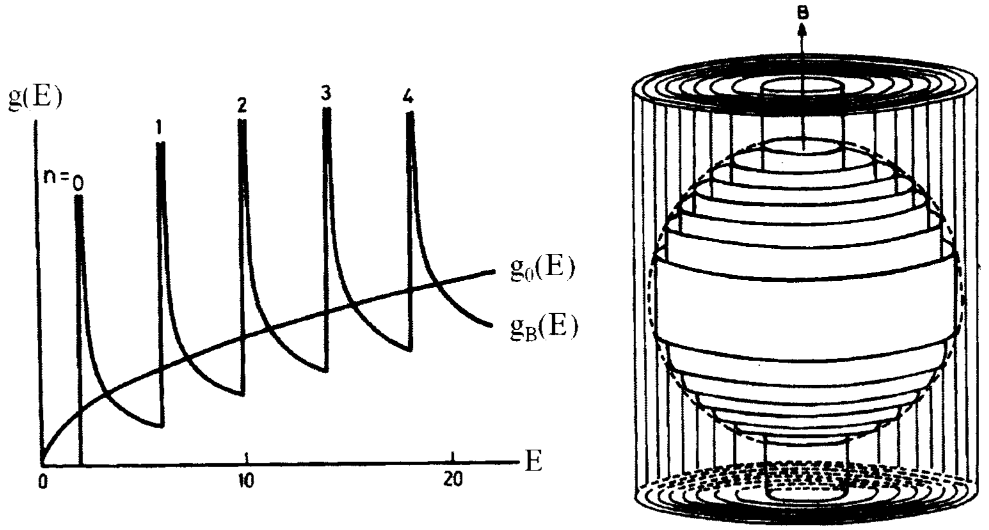

(a) (b)

Figure 2.5 – Energy level quantization in a magnetic field. (a) Comparison of density of states in a semiconductor sample under no applied magnetic field, $g_0(E)$, and a finite magnetic field, $g_B(E)$. (b) Representation of the Fermi sphere (dotted line) modified to concentric cylindrical constant energy surfaces (solid lines) in a magnetic field oriented parallel to the z-direction. Adapted from [153].

based experiments, so long as the NW diameter exceeds the magnetic length, then a corresponding blue-shift of the peak PL energy is expected. This means that by appropriate tuning of the magnetic length, the effective electronic diameter of the NW can be distinguished and confinement and surface-passivation effects can be investigated. These concepts will be further explored in Chapter 3.

Sample preparation for M-PL experiments presented in the current work involved mounting as-grown NW segments using a cryo-safe adhesive onto a Cu mount attached to a pull rod. The sample was subsequently inserted into a liquid helium bath in an Oxford Instruments optical cryostat fixed 1.6 K. An external superconducting magnet was employed for the induction of a field, ranging in

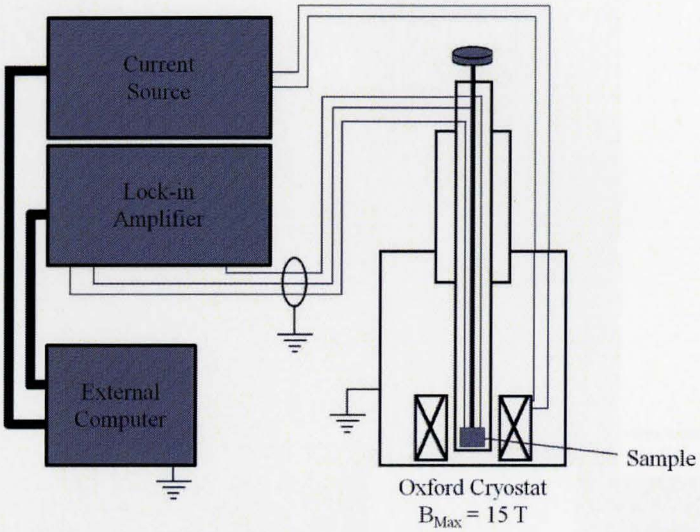

Figure 2.6 – Schematic representation of setup employed for M-PL experiments. The probed sample rests in the cryostat such that the applied magnetic field is oriented parallel to the NW growth axis.

magnitude between 0 and 15 T The experimental setup, allowing for the magnetic field to be oriented perpendicular to the substrate (parallel to the NW growth direction on (111) oriented surfaces), is shown in Figure 2.6. The M-PL measurements were carried out with an Ocean Optics, Inc. HR2000 high-resolution spectrometer and a 514.5 nm Ar^+ laser line was used for excitation.

2.3.3 – Raman Scattering Spectroscopy

Much like PL spectroscopy, Raman scattering (RS) spectroscopy is a non-contact and non-destructive optical characterization techniques, requiring simple sample preparation methods. In the current work, RS experiments were used to gain an understanding with regards to NW alloy composition, quality of heterointerfaces, and elastic strain. However, more general applications of RS techniques also involve the analysis of defects, implantation damage, band-offsets, carrier concentration and carrier mobility [151].

The inelastic interaction of an incident photon with optical phonon modes, associated with lattice vibrations of a crystalline sample, results in a scattering event yielding a photon with energy dissimilar to that of the incident photon. The energy difference is conserved in the generation or annihilation of an optical phonon, such that the energy conservations process can be defined as:

$$h\nu_s = h\nu_i \pm h\nu_p \tag{2.11}$$

where i, s, and p subscripts associated with frequency, ν, represent the incident photon, scattered photon, and phonon, respectively. The negative sign in Equation 2.11 is used to denote phonon emission in a Stokes-shifted scattering event, whereas the positive sign is used to represent phonon absorption in an anti-Stokes scattering event. The Stokes modes are typically collected in RS experiments, as the anti-Stokes scattering is exponentially less likely to occur [155].

During RS spectroscopy, the weakly scattered signal is collected, from which the Rayleigh scattered signal is filtered using a double monochromator. Based on the transverse optical (TO) and longitudinal optical (LO) phonon dispersion relations of the material group of interest, the scattered wavelengths are correlated to known values, translating compositional and strain-related information. In the case of ternary semiconductor alloys, such as $GaAs_{1-x}P_x$, GaAs-like and GaP-like TO and LO modes will be detected, the integral intensities, *I*, and relative frequencies, *v*, of which can be used to determine the stoichiometry of the alloy [156], according to:

$$v_{LO}^{GaP}(x) = 350.1 + 72.2x - 20.0x^2 \qquad (2.12)$$

$$v_{LO}^{GaAs}(x) = 291.1 - 25.5x \qquad (2.13)$$

$$x = \frac{I_{LO}^{GaP}}{I_{LO}^{GaP} + I_{LO}^{GaAs}} \qquad (2.14)$$

Furthermore, effects of tensile strain will manifest in an RS spectra in the form of a red-shifted signal peak, while an increased signal line-width can also arise as a result of inhomogeneous strain [151].

Sample preparation for RS investigations simply involved cleaving as-grown NW samples to sizes of approximately 50 mm^2 area and subsequent adhesion to Cu mount stages for cryo-vessel loading. All RS experiments presented in the current work were performed at the Universidade Federal de São Carlos, Brazil, by Dr. Ariano De Giovanni Rodrigues, under the supervision of Dr. José Galzerani. Scattering signals were collected, from samples maintained at approximately 10 K, through an Instruments S. A. T64000 triple grating spectrometer supplied with a liquid-nitrogen cooled CCD detector. Excitation was provided by an Ar$^+$ laser line centered at 514.5 nm.

Chapter 3

GaP/GaAsP Nanowires on Si Substrates

3.1 – Introduction

In this chapter, we explore the growth, structural characteristics, and optical properties of GaP/GaAsP coaxial nanowires (NWs) grown on Si (111) substrates. The monolithic integration of III-V compound semiconductor NWs with Si platforms represents a means of achieving high-quality growth of optically active, single crystalline structures on the preferred material of the microelectronics industry. Based on this motivation, several reports of such hybrid material combinations, grown via MOVPE and MBE, have been recently made with potential device applications such as optical interconnects, photovoltaic cells, light-emitting diodes (LEDs), and photodetectors [10, 11, 157-159].

Epitaxial core-multishell NW structures, as first demonstrated in the case of Si/Ge coaxial systems [160], allow for the stacking of differing material groups in the formation of radial heterostructures. In this geometry, a material of smaller bandgap energy can be encapsulated by two larger energy gap materials to provide quantum confinement of carriers in the central layer. This is particularly advantageous in LED applications as the carrier confinement allows for enhanced radiative recombination of electrons and holes [32]. For photovoltaics applications, the controlled fabrication of coaxial NW geometries translates into efficient collection of photo-generated carriers [54], a means for surface passivation [56], and the potential for the growth of tandem NW solar cells [41].

The growth of core-multishell GaP/GaAsP/GaP NWs is presented in Section 3.2. This work, reporting on the detailed structural characterization and compositional analysis of single NWs, has been previously published in Ref. [116]. The nature of stacking faults in such systems is examined through TEM analysis. In Section 3.3, previous studies of the 3-tiered GaP/GaAsP NWs are extended in an investigation focussed on the growth and characterization of 11-layered coaxial GaP/GaAsP superlattice heterostructured NWs. It is shown that the formation of stacking faults is dependent upon the supersaturation of growth species in the Au seed during growth, and a novel method for the alleviation of the lateral defects is demonstrated. This technique for growth of single phase NWs was reported in Ref. [117]. The chapter ends with Section 3.4, wherein preferential incorporation of adatoms in single NW layers composed of ternary alloys is discussed. Furthermore, the effect of surface passivation on the optical properties of GaP/GaAsP heterostructured NWs is presented, as previously published in Ref. [118].

3.2 – Core-Multishell Nanowire Growth and Structural Analysis

3.2.1 – Experimental Details

GaP/GaAsP/GaP segmented NWs were grown on Si (111) substrates. The Si (111) substrates were boron-doped at an approximate concentration of 10^{16} cm^{-3}. Prior to growth, the substrates were subjected to a 20 minute ultra-violet (UV) ozone treatment for growth of a sacrificial oxide layer and removal of surface-bonded hydrocarbons. The oxide layer was then etched for 30 seconds in a diluted 10:1 HF solution and rinsed in de-ionized water. The etched substrates were transferred in ambient air to an electron-beam evaporation system for the deposition of a 10 Å-thick film of Au, as determined by a quartz crystal thickness monitor. The Au-deposited samples were kept under high vacuum (10^{-8} Torr) in the electron-beam evaporation chamber until transported in ambient air to the growth chamber.

The growth was performed in a gas-source molecular beam epitaxy (GS-MBE) system, previously discussed in Section 2.1, wherein group III species (Ga) were supplied as monomers from a heated solid elemental effusion cell while the group V species were supplied as dimers (As_2 or P_2) from a hydride (AsH_3 or PH_3) gas cracker operating at a temperature of 950°C. Prior to the initiation of the growth, the Au-coated substrate was heated to a growth temperature of 510°C while being subjected to an inductively coupled hydrogen plasma treatment under a P_2 overpressure. This process allows for the formation of uniformly distributed Au-nanoparticles on the Si surface.

The growth was initiated by opening the shutter of the Ga effusion cell, whose temperature was preset to yield a nominal planar growth rate of 1 μm/h. The first GaP layer was nominally p-doped with Be to 10^{18} cm^{-3}, as determined by prior doping calibrations consisting of GaAs layers on (100) GaAs substrates. The GaP layer was grown for a duration of 20 minutes, at which point the Ga and Be shutters were closed for a growth interruption of 3 minutes. The subsequent layer was grown with an As/P flux ratio corresponding to a nominal composition of $GaAs_{0.6}P_{0.4}$, as determined from previous thin film calibrations on GaAs (100) substrates. The growth of this second layer was terminated after 10 minutes followed by a growth interruption of 3 minutes. The final layer, composed of GaP, was nominally n-doped with Si to 10^{18} cm^{-3}, as determined by prior doping calibrations (again consisting of GaAs layers on (100) GaAs substrates). Growth of the GaP layer was terminated after 10 minutes and the substrate cooled down from the growth temperature under a P_2 overpressure. Throughout the growth, the V/III flux ratio was maintained constant at 1.5.

After growth, the orientation, morphology and distribution of the as-grown NWs were studied using a JEOL JSM-7000 scanning electron microscope (SEM) in the secondary electron mode. NWs were suspended in a small volume of de-ionized water after a 1 minute sonication bath and applied to a carbon holey grid in preparation for transmission electron microscopy (TEM). Single NWs were subsequently investigated with a Philips CM12 TEM, a JEOL 2010F for high resolution transmission electron microscopy (HR-TEM) and analytical TEM (ATEM), and an FEI Titan 80-300 HB high resolution TEM. This latter instrument is equipped with a sextupole-based aberration corrector of the imaging lens system providing a resolution of 0.75Å (point resolution and information limit). After tuning the imaging lens system, residual spherical aberrations in the order of 1 μm were achieved. Composition analysis of the radial heterostructures was performed via energy dispersive X-ray spectroscopy (EDXS) in the JEOL 2010F using K_α X-ray transitions.

3.2.2 – Results and Discussion

First, the overall morphology of the NWs was examined by SEM. A cross-sectional SEM image of the NWs on the Si (111) substrate, shown in Figure 3.1, indicated that planar growth on the Si surface between the NWs (the regions not covered by Au) was limited to a thickness of roughly 120 nm. The wires were tapered with an average full-width at half maximum (FWHM) diameter of roughly 52 nm, and an average height of 5.1 μm as measured from the top surface of the two-dimensional film growth. The tapering is predominantly located near the tip of the NW with the remaining portion having a nearly uniform diameter. This tapered structure is attributed to a layer-by-layer growth mechanism on the NW sidewalls [95], as previously discussed in Section 1.3.3. The use of a 10 Å-thick Au film, as opposed to a 40 Å-thick film used in past growths performed

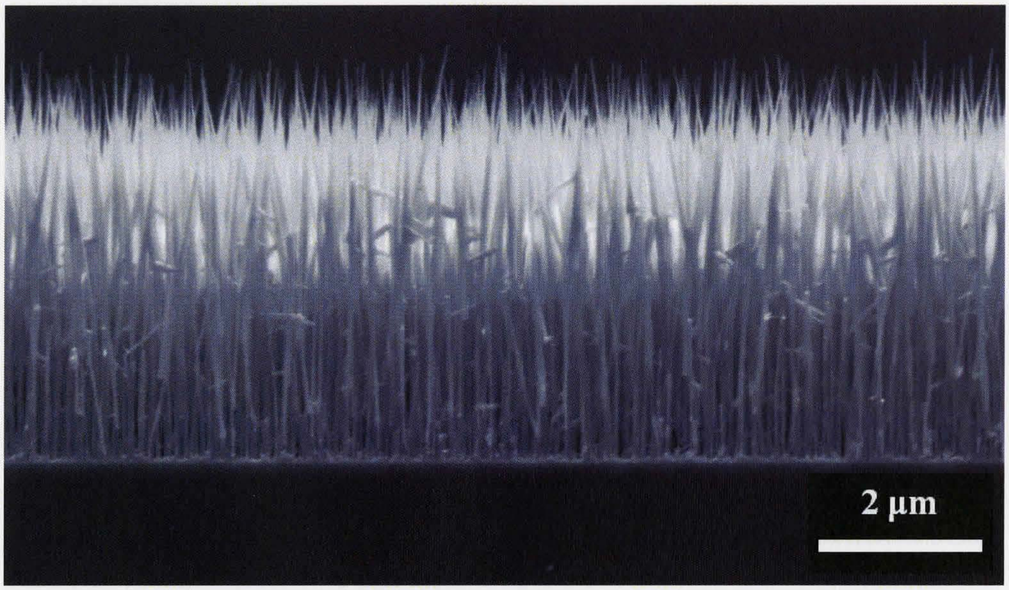

Figure 3 1 – Cross-sectional SEM image of as-grown GaP/GaAsP/GaP nanowires on Si (111). Planar deposition amongst the NW is visible on the substrate surface.

with the same MBE system [79], resulted in enhanced uniformity in seed size and distribution, leading to more densely packed NWs. The presence of Au nanoparticles at the NW tips, as indicated by EDXS, gave confirmation of the VLS growth mechanism.

Next, the composition of the NWs was examined using ATEM. A bright-field HR-TEM image and EDXS line-scans obtained from a single NW are shown in Figure 3.2. In Figure 3.2(a), results are shown for an EDXS line-scan along the axis of the NW (along the growth direction). In addition, a series of line-scans were performed across the diameter of the top, middle, and base segment of the NW, labelled 1, 2, and 3, respectively, in Figure 3.2(a). The corresponding EDXS results for the scans along lines 1, 2, and 3 are shown in Figures 3.2(b), (c), and (d), respectively The green, blue, and red lines correspond to EDXS counts of

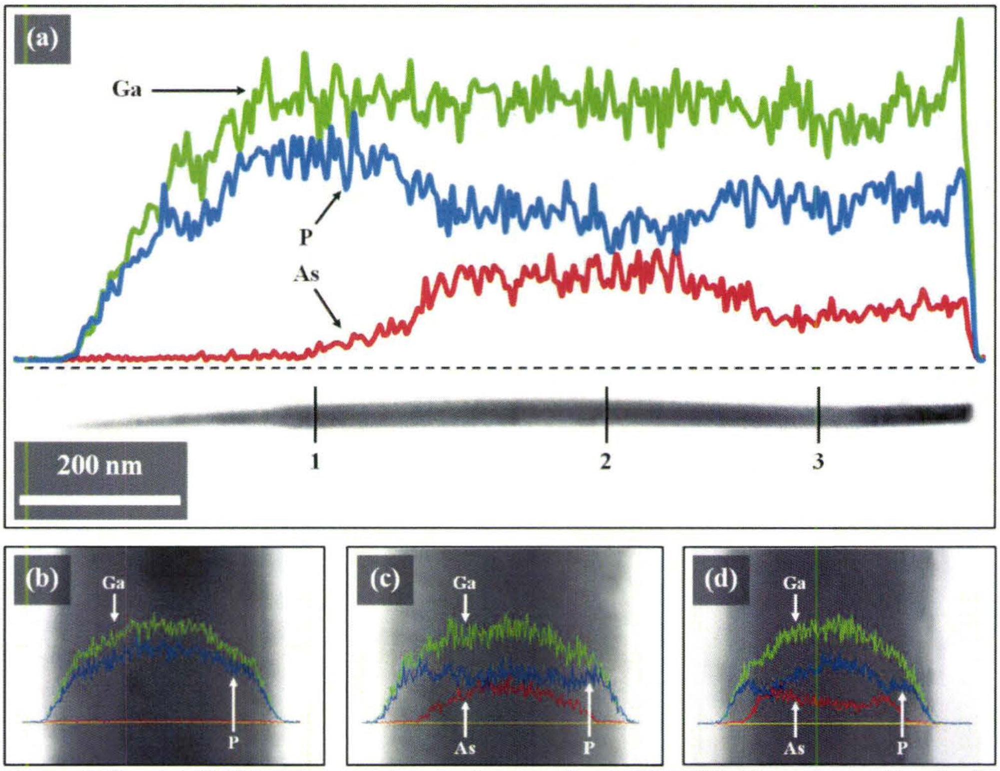

Figure 3.2 – (a) TEM image and superimposed axial EDXS line-scans of a single NW showing variations in Ga (green), P (blue), and As (red) compositions. The dotted line denotes the length of the line-scan across the center of the NW. (b) Radial EDXS scan corresponding to line 1 in (a) suggests an outer GaP shell at the NW tip. (c) Radial EDXS scan corresponding to line 2 in (a) shows the presence of a GaAsP layer in the center of the wire with a GaP shell. (d) Radial EDXS scan corresponding to line 3 in (a) indicates that a GaP core is encapsulated by a GaAsP shell, both of which are coated by a secondary shell of GaP.

elemental Ga, P, and As, respectively.

First, we focus on the tip of the NW. The Ga line-scan (green line) in Figure 3.2(a) indicates an approximately constant Ga content, as expected for both GaAsP and GaP segments, until the NW tip where the Ga signal decreases due to the NW tapering. A similar decrease is observed in the P signal (blue line) near the NW tip, while the As signal (red line) is negligible in this region, indicating that the tip of the NW is composed of GaP. The results of the EDXS scan along line 1, shown in Figure 3.2(b), confirm the GaP composition of the wire tip.

Next, we turn our attention to the middle segment of the NW. The line-scan along the NW axis in Figure 3.2(a) indicates the presence of both As and P near the middle segment. The results of the EDXS scan along line 2, shown in Figure 3.2(c), indicates that the As count (red line) is greatest in a core region, then vanishes in a sheath region of the NW. Accordingly, the P count (blue line) is greatest in the NW sheath and is somewhat lower in the core region. These results suggest that, in the middle segment of the NW, there exists a GaAsP core surrounded by a GaP shell.

Finally, we consider the base segment of the NW. The axial line-scan in Figure 3.2(a) indicates a P content which is somewhat greater compared to the middle segment, and lower compared to the NW tip. Correspondingly, the As content in the base is noticeably lower in relation to the middle segment and greater in relation to the NW tip. The results of the EDXS scan along line 3 of Figure 3.2(a), shown in Figure 3.2(d), indicate a negligible As content along the NW sheath, indicating an outer GaP shell as observed previously for the middle segment of the NW. Moving towards the NW core, the P signal (blue line) is observed to decrease, while the As signal increases, suggesting an inner sheath region of GaAsP, also similar to the earlier results for the NW middle segment. Finally, at the NW core, the P signal (blue line) is maximum, while the As signal (red line) decreases, suggesting a predominantly GaP core composition. Note that

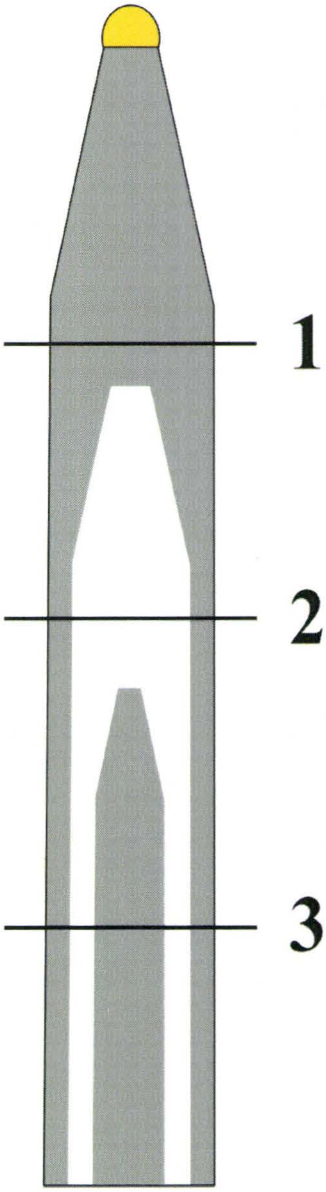

Figure 3.3 – Conceptual representation of the core-multishell NW structure. The shaded regions illustrate the GaP layers, while the white region is representative of the GaAsP layer. The hemispherical Au particle is evident at the top of the nanowire. The lines labelled 1, 2, and 3 are in positions equivalent to shown in Figure 3.2(a).

As is still detected in the core region at the base of the NW due to the presence of a GaAsP layer, encapsulating the GaP core.

Consideration of the above axial and radial EDXS line-scans lead us to conclude that the GaP-GaAsP-GaP segmented growth is best described by the core-multishell arrangement shown conceptually in Figure 3.3. The growth begins with a segment of GaP resulting in the core of the NW (inner shaded region). Axial VLS growth at the Au-wire interface and unseeded radial growth on the NW sidewalls results in a shell of GaAsP, represented by the white region of Figure 3.3. Finally, the growth of a terminating GaP segment produces the outer shell of GaP (outer shaded region). As a result, an EDXS scan across line 1 will measure the GaP outer sheath only as presented in Figure 3.2(b). An EDXS scan across line 2 will measure the GaP sheath at the NW edges, and a GaP sheath superimposed on the GaAsP core near the NW centre, as presented in Figure 3.2(c). Finally, an EDXS scan along line 3 will measure in projection through the thickness the GaP sheath near the NW edges, followed by the GaP/GaAsP/GaP three-layer structure closer to the NW centre, and finally the entire GaP/GaAsP/GaP/GaAsP/GaP five-layer stack along the NW centre.

EDXS point measurements were taken at the center of the GaAsP layer (middle segment) of several NW specimens, to determine the absolute composition within this region. Due to the inhomogeneous arrangement (core-shell structure) of As and P atoms along the radial direction of each NW, a cylindrical approximation method was used to determine the composition of the

GaAsP layer alone. In this method, the atomic concentration of phosphorus was measured in a region where the GaAsP core is encapsulated by the GaP shell. Using this information in conjunction with the thickness of the respective layers at the point of the measurement (as determined from the radial EDXS line-scans), a thickness weighted average value for the measured composition may be determined according to:

$$C_{cs}D = C_s(D-d) + C_c d \tag{3.1}$$

where C_s, C_c and C_{cs} are the phosphorus atomic concentration values as measured in the GaP shell (50% P), the GaAsP core, and the combined GaP/GaAsP/GaP region, respectively. D represents the total thickness of the NW at the point of measurement, and d is the diameter of the GaAsP layer alone at the point of measurement. A compositional variance was calculated to be in the range of $GaAs_{0.79}P_{0.21}$ to $GaAs_{0.72}P_{0.28}$ amongst the several NWs that were examined, with an error in absolute composition of roughly 5%. A range of group V atomic concentrations among different wires is anticipated due to the competition for growth material in the VLS regime where the metallic nanoparticles are of varying size and distribution.

Next, the crystal structure of the NWs was analyzed. A selected area diffraction (SAD) pattern was obtained in the JEOL 2010F system from the middle GaAsP segment of a NW. The resulting SAD pattern, shown in Figure 3.4, indicated a wurtzite crystal structure for the <2-1-10> zone axis and a NW growth direction along <0001>. Unlike the GaAsP region, inspection of the GaP

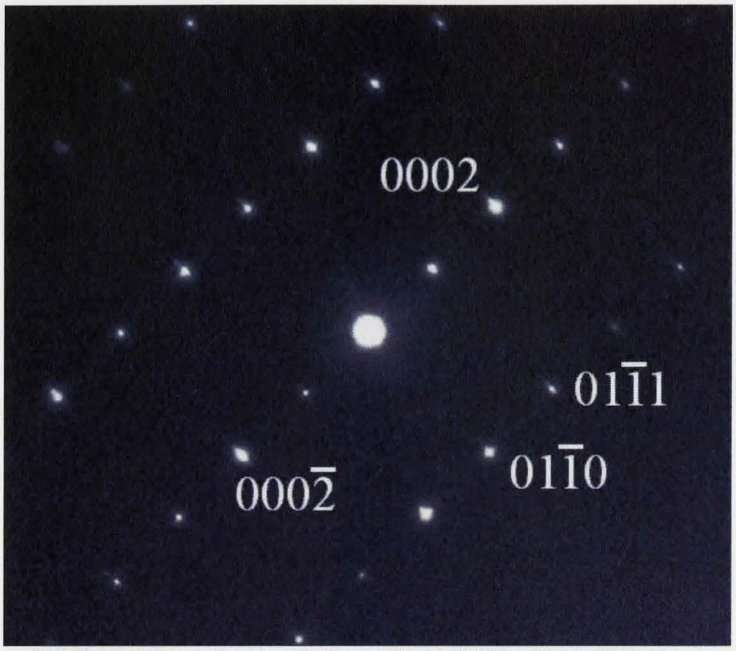

Figure 3.4 – SAD pattern obtained from the middle GaAsP segment of a core-multishell NW

regions near the tip and base of the NW, revealed the frequent incidence of stacking faults as demonstrated by the HR-TEM image in Figure 3.5 for the base region of a NW This image, and the corresponding SAD pattern, shown in the inset, revealed a wurtzite crystal structure interrupted periodically with stacking faults. This periodicity in the stacking faults is manifested as the streaking in the SAD pattern in the inset in Figure 3.5.

To further examine the nature of the stacking faults, the NWs were also examined with the improved resolution of the aberration corrected TEM, as shown in Figure 3.6, for the base region of a NW where three distinct atomic stacking sequences, labelled A, B, and C, are observed. Due to the suppression of the delocalization in the images related to aberration correction, it is possible to

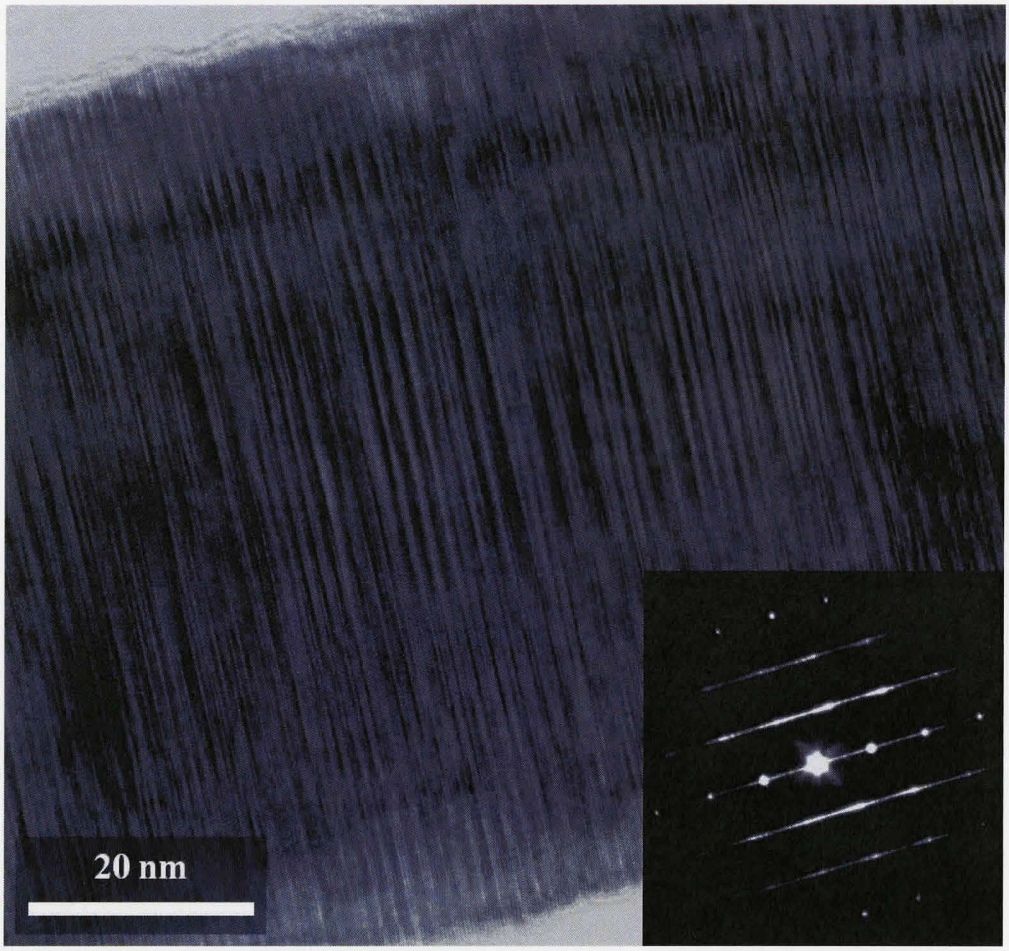

Figure 3.5 – HR-TEM image of a region near the NW base revealing the periodicity of stacking faults in the GaP layer The Au particle (not shown) is towards the top-right. The inset shows the corresponding SAD pattern.

directly visualize the interface between the nanowire and vacuum. The images demonstrate the clean surface and the arrangement of the atoms in the outer layers of the nanowire and related surface steps. Predominantly, an ABAB stacking sequence is present, indicative of the wurtzite structure. However, this structure is periodically interrupted by C atomic layers, indicated by an arrow in the inset of Figure 3.6, which is representative of a stacking fault consisting of a short

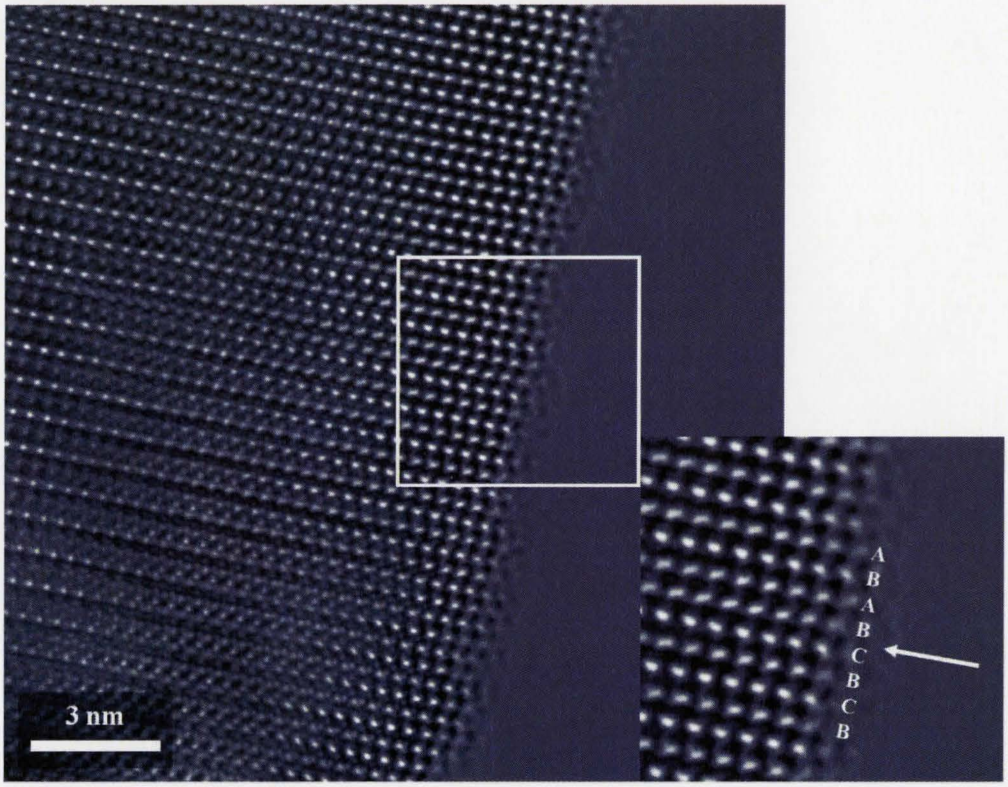

Figure 3.6 – Aberration-corrected HR-TEM image taken along a NW sidewall. The white rectangle represents the boundaries of the magnified image shown in the inset. The white arrow in the inset points towards a stacking fault corresponding to a change in atomic stacking sequence denoted by the letters A, B, and C. Au particle (not shown) is towards the top.

segment of zincblende structure [161-163]. Further from the surface of the NW, the thickness increases rapidly and the contrast in the image is not directly interpretable and the changes in stacking sequence are, as a consequence of this, less obvious.

The incidence of stacking faults varied significantly along the length of the NW as indicated by comparison of the SAD pattern in Figure 3.4 (defect-free GaAsP segment) with the inset of Figure 3.5 (base GaP region with stacking faults). To further illustrate this variation in frequency of stacking faults, we first examine the GaP-to-GaAsP transition close to the base of the NW. Figure 3.7(a) shows a high-angle annular dark-field (HAADF) image of a single NW acquired in the JEOL 2010F, while Figure 3.7(b) shows a bright-field image of the identical NW (the NW top is towards the left). The HAADF image is sensitive to compositional variation, revealing the GaP core region near the base of the NW (right side of Figure 3.7(a)), the GaAsP shell (middle segment of the NW), and the GaP outer shell (left side of Figure 3.7(a)). Elemental As, having higher atomic number than P, appears brighter in the HAADF image. The bright-field image in Figure 3.7(b), on the other hand, is sensitive to the NW structure revealing contrast due to the stacking faults (vertical lines intersecting the NWs). These results reveal that the stacking faults coincide with the GaP base segment of the NW, while the GaAsP middle segment is nearly free of defects.

Next, we examined the GaAsP-to-GaP transition close to the top of the NW. The HAADF and bright-field images shown in Figures 3.7(c) and (d),

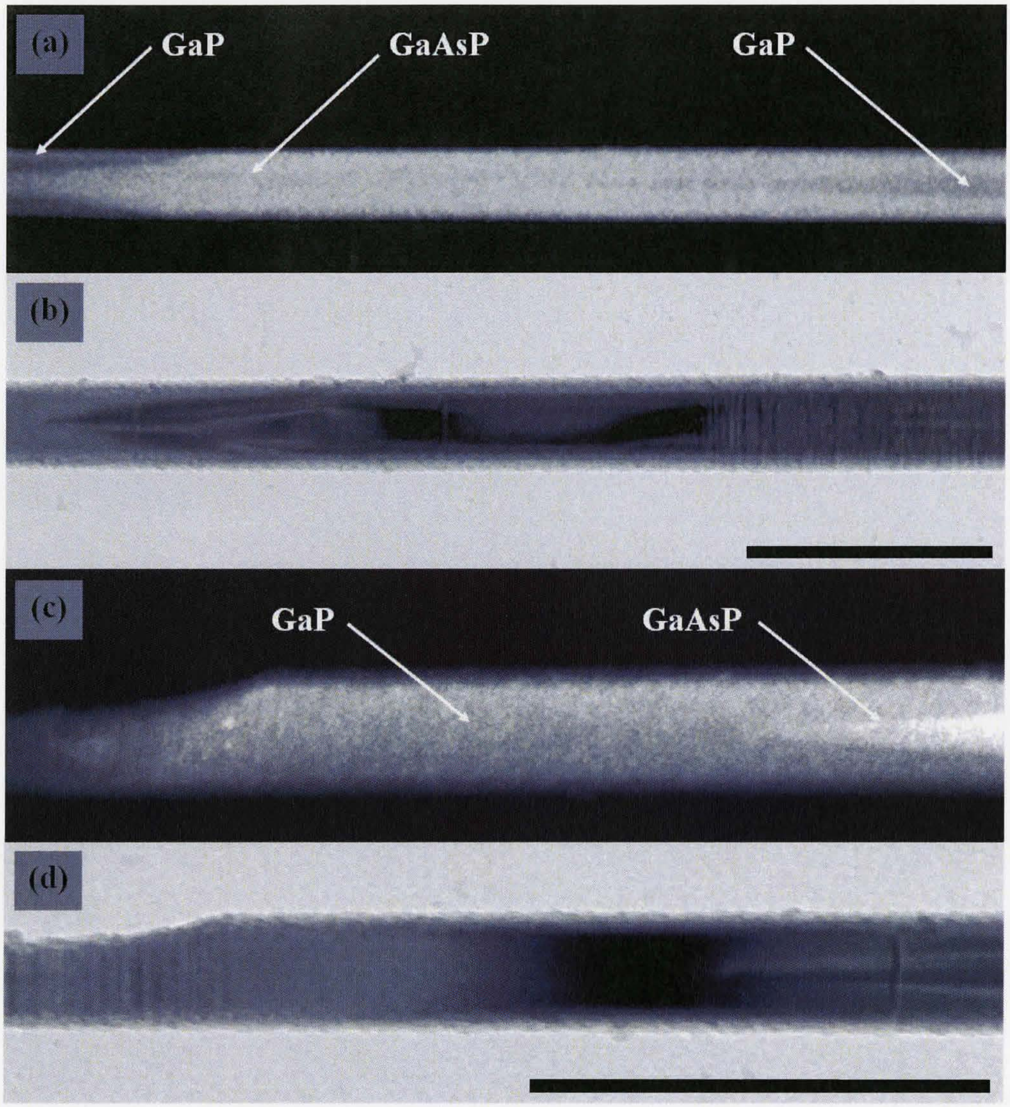

Figure 3 7 – (a) HAADF image of the center region of a NW The GaP layers (dark regions) are shown to encapsulate the GaAsP layer (bright region). (b) Corresponding bright-field TEM image of the wire shown in (a). The stacking faults evident at the wire base (right-hand side of image) are dramatically reduced with the onset of the GaAsP layer (c) HAADF image near the NW tip showing the termination of the GaAsP layer within the GaP shell. (d) Corresponding bright-field TEM image of the same NW segment as (c). A defect-free region exists (center of image) following the GaAsP/GaP interface. The stacking faults reappear (left-hand side of image) as the growth continues and persist until the Au tip. The NW top is towards the left in each image. Scale bars represent a length of 200 nm.

respectively, reveal a region of GaP that is devoid of stacking faults immediately following the termination of the GaAsP layer. The defects are observed to be reintroduced within the GaP segment after a length of over 200 nm and subsist up to the Au/GaP interface at the NW tip (not shown in Figure 3.7).

It had been previously reported, in the case of GaAsP/GaP heterostructured NWs, that stacking faults existed near the top of a long GaAsP segment, while GaP segments immediately following the GaAsP layer revealed very few stacking faults. This change in stacking fault density was reported to be a result of compositional dependence of the NW growth mechanisms [95]. However, the present study suggests that NWs are free of stacking faults for a certain growth period following a growth interruption associated with the material transitions. Similar results were also reported for the growth of InP NWs, where an initial wire height of about 300 nm was found free of stacking faults, above which the crystal structure becomes disrupted and the formation of stacking faults becomes frequent [164]. In the present study, it would appear that the segment of GaAsP is shorter than the critical height above which faults are introduced, meaning that the GaAsP remains defect-free. The regular periodicity of the faults in the defected regions of GaP suggests that their formation is rooted in a dependence upon a cyclical growth process. The growth interrupted interfaces appear to disrupt this cyclical process resulting in a defect-free region of the NW for a certain growth period. The observation of stacking faults in the base, where there is a layered core-multishell heterostructure, and also in the NW tip, where only a single GaP structure exists, leads to the conclusion that the presence of faults does not depend on strain effects induced at lattice-mismatched radial heterointerfaces. Instead, the formation of stacking faults in GaP/GaAsP NW systems is dependent upon the supersaturation of growth species in the Au-seed, as presented in the following section on superlattice heterostructured NWs.

3.3 – Superlattice Heterostructured Nanowire Growth and Structural Analysis

Although tremendous gains have been made towards achieving a more complete understanding of the underlying structural, electrical, and optical properties of semiconductor NWs, certain unresolved challenges remain and persistently inhibit their incorporation into mainstream device fabrication. The phase purity of NWs grown according to the vapour-liquid-solid (VLS) mechanism is one such concern. Typically, VLS growth results in the formation of NW structures with stacking faults, lamellar twins, or polytypic inclusions incorporated throughout the crystal [113, 165]. Both zincblende (Zb) and wurtzite (Wz) phases may occur in III-V semiconductor NWs as a consequence of the small difference in internal energy (<24 meV per octet pair) between the two structures [162, 166, 167]. In fact, it is a thoroughly reported observation that while certain III-V materials assume a cubic Zb structure in bulk, the preferential atomic stacking arrangement in NWs tends towards that of the hexagonal Wz arrangement [110, 116, 157]. In such systems, stacking faults, characterized as intermittent insertions of Zb in an otherwise Wz phase, can be observed.

As stacking faults adversely affect the fundamental material properties of NWs [168, 169], a pressing need exists for their elimination. Several successful methods for the elimination of stacking faults have been demonstrated including growth on (001) [168] or (111)A [170], as opposed to the usual (111)B, orientated substrates as well as post-growth epitaxial burying of NWs [171]. In Section 3.2 we demonstrated the growth of stacking fault-free segments within GaP/GaAsP core-multishell NWs. These segments, extending over 200 nm in length, were observed following the GaP-to-GaAsP and GaAsP-to-GaP interfaces. We now extend those previous studies by demonstrating the growth of stacking fault-free core-multishell superlattice (SL) heterostructured GaAsP/GaP NWs with a single Wz phase, achieved by a growth interruption technique.

3.3.1 – Experimental Details

Prior to each NW growth, a 10 Å Au film was deposited on Si (111) substrates via electron beam evaporation equipped with a quartz crystal thickness monitor. The samples were then transported in ambient air to a gas source molecular beam epitaxy system (GS-MBE). After an *in-situ* inductively coupled H_2 plasma treatment at 550 °C, the Au films disseminate into uniformly distributed nanoparticles on the substrate surface. NW growth was carried out in the GS-MBE system, wherein Group III monomers (Ga) were supplied from a solid elemental effusion cell and Group V dimers (As_2 and P_2) were supplied from a hydride gas cracker operating at 950 °C. The growth temperature, V/III flux ratio, and nominal 2-D growth rate were fixed at 510 °C, 1.5, and 1 μm/hr, respectively.

Five NW groups (groups A – E) were grown via GS-MBE. The NW groups are depicted pictorially in Figure 3.8 and summarized in Table 3.1, together with results discussed below. Group A NWs in Figure 3.8(a) consisted of a single GaP composition and were grown over a duration of 20 minutes. Group B NWs in Figure 3.8(b), also composed of GaP grown over a total period of 20 minutes, were periodically subjected to 10 growth interruptions. Specifically, after the first ten minutes of growth, a 3 minute interruption, wherein the shutters of the Group III effusion cells were closed while maintaining a Group V overpressure, was introduced followed by a 1 minute growth period. This process was repeated 10 times for a total growth period of 20 minutes. Group C NWs in Figure 3.8(c), as discussed in Section 3.2, were grown with a 3-tiered core-multishell structure. The initial layer, composed of GaP, was grown over a period of 20 minutes. This segment was coated with a GaAsP layer for a period of 10 minutes, followed by another GaP segment grown for 10 minutes. 3-minute growth interruptions were introduced prior to the onset of each new layer. Group D NWs in Figure 3.8(d) consisted of a GaP/GaAsP superlattice architecture, extending along the vertical and radial direction. The sample growth began with a GaP base, grown over a period of 10 minutes. After the initial GaP segment, 10 alternating layers of GaAsP and GaP were grown for 1-minute durations with 3-minute growth interruptions introduced between subsequent layers. Finally, group E NWs in Figure 3.8(e) were grown with identical structures to those in Group D but without the growth interruptions. For the sake of consistency, all GaAsP

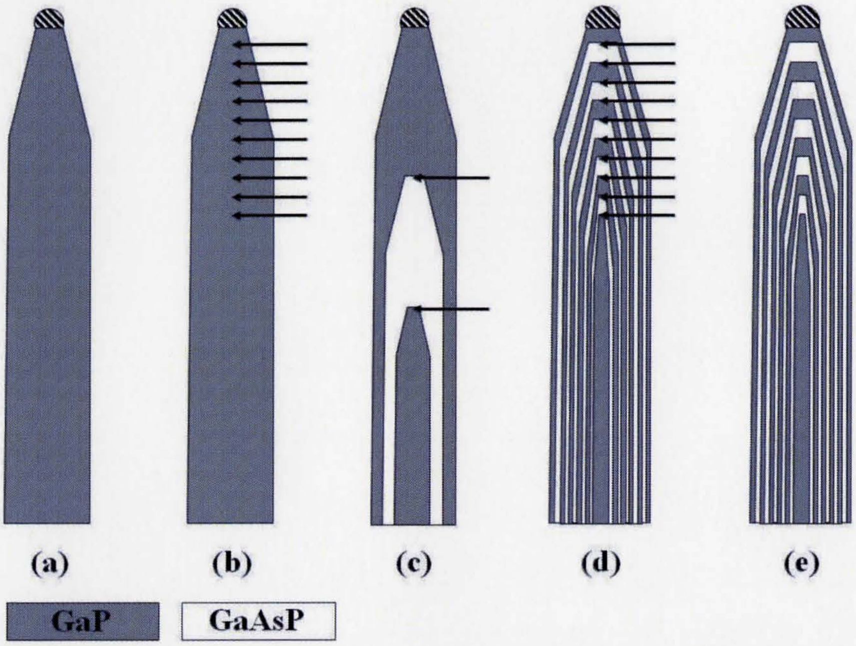

Figure 3.8 – Pictorial representation of NW groups A – E. Shaded and white regions represent GaP and GaAsP layers, respectively Arrows each depict the introduction of a 3 minute growth interruption. The diagonally striped regions represent the Au seeds at the NW tips. Nanowire segments are not drawn to scale.

Table 3 1 – Sample descriptions and results amongst NW groups A – E.

NW Group	**Sample Description**	**Duration of Growth Interruption (min)**	**Density of Stacking Faults[a] (nm^{-1})**
A	GaP (no growth interruptions)	0	0.70
B	GaP (10 growth interruptions)	3	0.40[b]
C	3-tiered GaP/GaAsP/GaP (2 growth interruptions)	3	0[b]
D	GaP/GaAsP superlattice (10 growth interruptions)	3	0[b]
E	GaP/GaAsP superlattice (no growth interruptions)	0	0.24

[a] Stacking fault densities were averaged over several NWs.

[b] Measured along NW segments grown immediately after a growth interruption.

layers were grown at an As/P flux ratio corresponding to a nominal composition of $GaAs_{0.6}P_{0.4}$, as determined from previous thin film calibrations on GaAs (100) substrates. All growths were terminated by closing the shutter of the Ga cell while allowing the sample to cool under a Group V overpressure.

After growth, the NWs were examined to distinguish the role of gas phase switching and growth interruptions in the formation of stacking faults. Cross-sectional analysis of as-grown NWs was conducted using a JEOL JSM-7000 scanning electron microscope (SEM) for direct comparison of NW lengths amongst different samples. The as-grown NWs were removed from the Si substrates by a 60 second ultra-sonication treatment, while suspended in a small volume of de-ionized water. The suspended NWs were dispersed upon holey carbon-coated copper grids for structural and compositional analysis using a Philips CM12 transmission electron microscope (TEM) and a JEOL 2010F high resolution transmission electron microscope (HR-TEM). High angle annular dark field (HAADF) imaging and energy dispersive x-ray spectroscopy (EDXS) was also employed in the latter instrument. For each NW group, similar results were consistently observed over a population of several dozen NWs.

3.3.2 – Results and Discussion

Dramatic differences in the formation of stacking faults were observed by TEM amongst the different NW groups. These results are summarized in Table 3.1. First, GaP NWs belonging to group A exhibited a large number of densely packed faults, on the order of 0.70 nm^{-1}, distributed regularly throughout their length, as shown in Figure 3.9(a). Stacking faults in group B NWs, however, where periodic growth interruptions were introduced, were sparser in comparison to those in group A, at a density of roughly 0.40 nm^{-1}, as shown in Figure 3.9(b). All values of stacking fault densities reported represent average values measured over several NWs from each sample. Hence, it would appear that growth interruptions in GaP reduced the density of stacking faults by almost a factor of two.

As previously discussed, group C NWs were grown with a three-tiered (GaP/GaAsP/GaP) core-multishell heterostructure, as illustrated in Figure 3.8(c). Comparison of Figures 3.7(a) and 3.7(b) reveals that the first segment (GaP core) exhibited many densely packed lateral Zb insertions. The introduction of the initial growth interruption at the GaP-to-GaAsP interface resulted in the growth of a region with no stacking fault formation. After a certain length, over 200 nm, stacking faults reformed within the GaAsP layer. A second growth interruption, introduced at the GaAsP-to-GaP interface (shown in Figures 3.7(c) and 3.7(d)), then resulted in the formation of a second region along which the reformed stacking fault sequence was once again quenched. This analysis confirms the coincidence of the stacking fault elimination with the point of compositional change. As in samples A and B, the gas phase switching appeared to play an important role in the stacking fault formation.

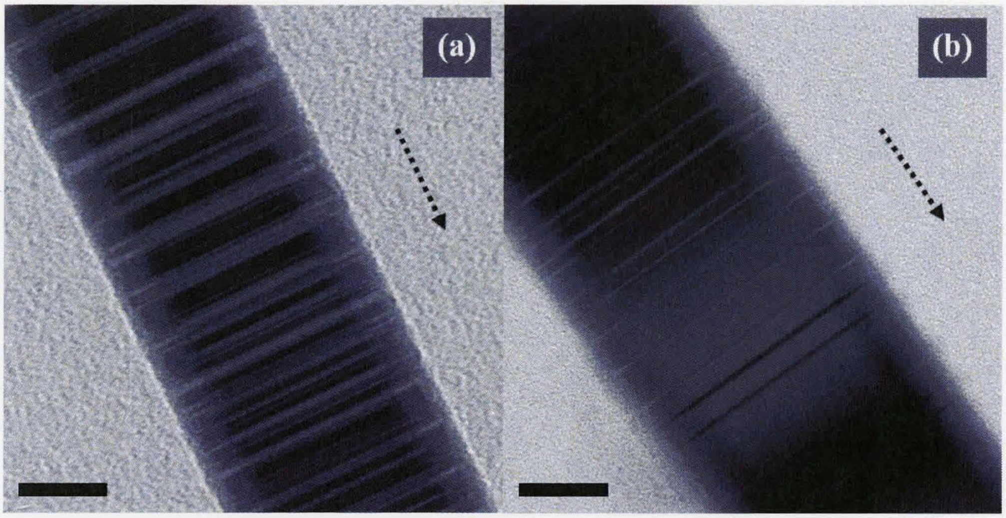

Figure 3.9 – TEM images of single (a) Group A NW and (b) Group B NW In the case of Group B NWs, repeated growth interruptions were introduced, leading to the formation of fewer stacking faults. Scale bars designate a 20 nm length. Broken line indicators point toward the NW tips.

To further examine the role of growth interruptions and material transitions on stacking faults, we turn our attention now to sample D, the superlattice sample with growth interruptions. Figure 3.10 shows a TEM image of a typical Group D NW Elemental counts of Ga (green), As (blue), P (red), and Au (yellow) as obtained through an EDXS line-scan are superimposed on the TEM image. An axial SL heterostructure can be discerned by considering the variation in counts of P and As. At the NW base (left), the significant excess of P, in comparison to As, is indicative of a predominantly GaP base region. Moving towards the NW tip (right), the As content is observed to increase to the point where As and P counts are comparable, signifying the onset of the initial GaAsP segment. Beyond this point, the As counts are seen to decline and rise repeatedly 9 times. Segments along the NW where both As and P counts are comparable

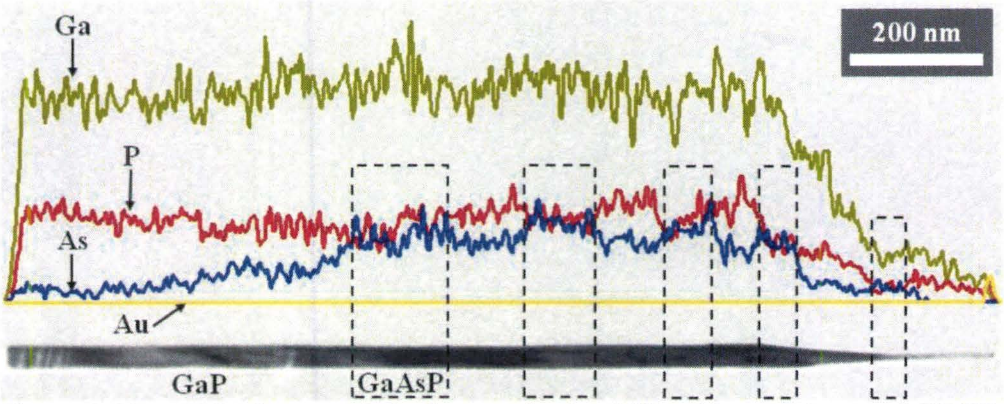

Figure 3.10 – TEM image of single superlattice NW with superimposed EDXS line-scans showing elemental counts of Ga (green), As (blue), P (red) and Au (yellow). 11 distinct segments are observed corresponding to the 11 layers within the superlattice. Segments wherein As and P counts overlap are indicative of the GaAsP layers outlined by dashed boxes, while P rich segments are characteristic of GaP layers.

correspond to GaAsP insertions (shown as boxed regions), while P rich segments are representative of GaP insertions. Correspondingly, ten alternating segments of GaAsP and GaP are observed, indicative of the ten-tiered SL heterostructure. Each successive GaAsP layer is observed to decrease in length from the bottom to the top of the NW. This phenomenon is more pronounced towards the NW tip and can likely be attributed to the decreasing growth rate of NWs due to diffusion-limited supply of adatoms from the base, with increasing NW length.

The tapered morphology of the NW in Figure 3.10 has previously been attributed to layer-by-layer growth based on nucleation of the diffusive adatoms on the NW sidewalls [95]. To confirm this, a HAADF image along the centre of a Group D NW is shown in Figure 3.11. Contrast variations are indicative of alternating shells of GaP (dark regions) and GaAsP (bright regions). It is evident

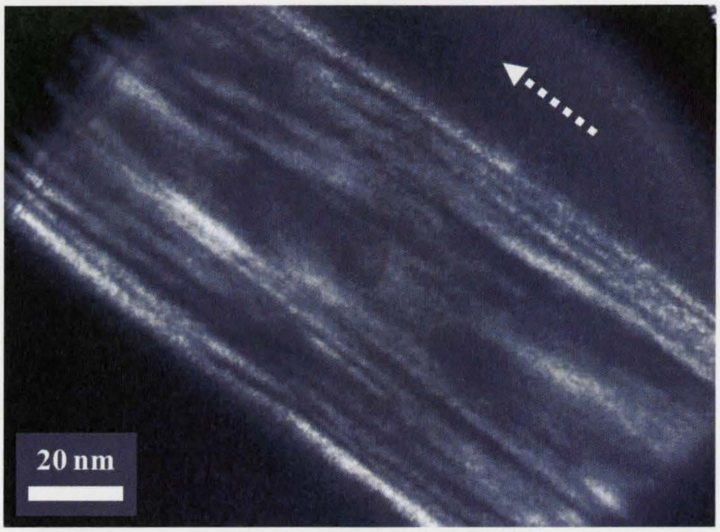

Figure 3 11 – Dark-field TEM image obtained from the central region of a group D superlattice NW Contrast variations across the NW width show the radially alternating layers of GaAsP (bright contrast) and GaP (dark contrast), confirming the core-multishell arrangement of the structure. The broken line indicator points toward the NW tip.

that sidewall deposition occurs concurrently with axial VLS growth causing a radially heterostructured architecture within the SL NWs. The thickness of each shell is measured up to 5 nm. Thus, the structure of the SL NWs can be accurately described as a GaP core with 10 alternating shells of GaAsP and GaP, as depicted in Figure 3.8(d).

TEM analysis, for example in Figure 3.12, indicated a large number of stacking faults in the group D NWs, with densities matching those of Group A, until roughly the longitudinal midpoint, where they were observed to terminate abruptly Beyond this point, the remainder of the NWs grew in a single Wz phase, with no lateral Zb insertions, as confirmed by selective area diffraction (SAD) analysis. The SAD pattern shown in Figure 3.12(b), corresponding to the

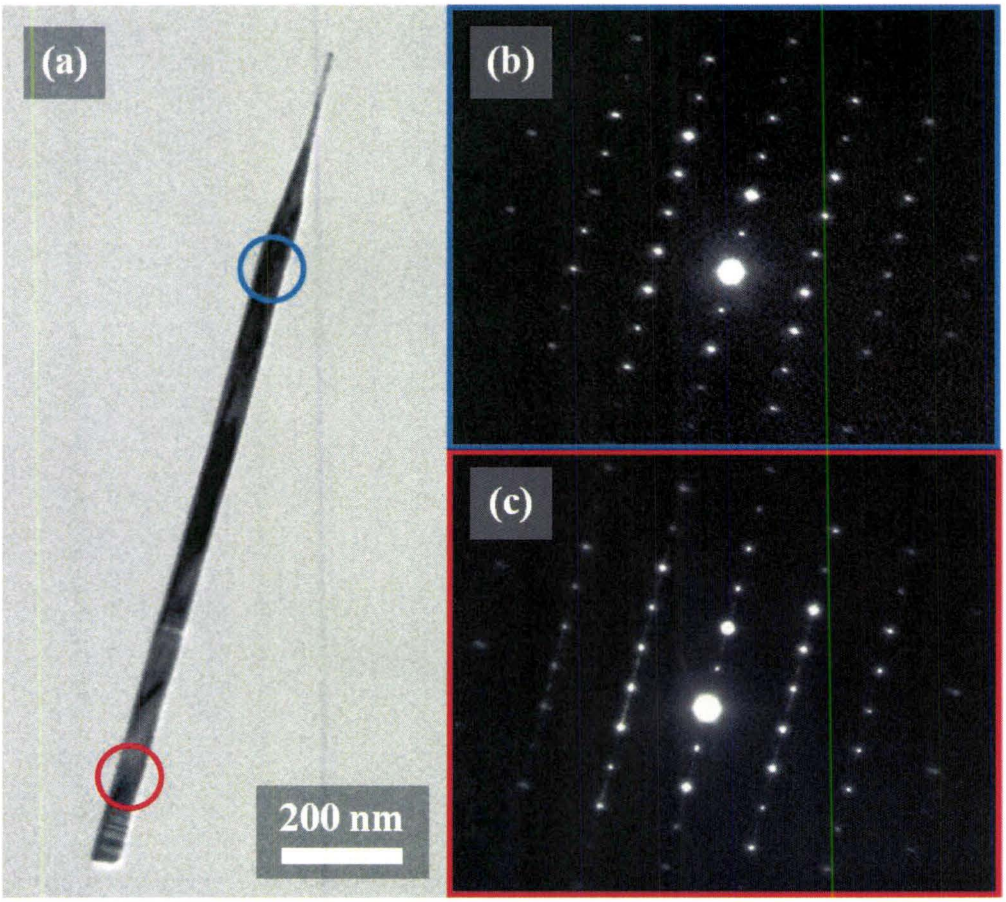

Figure 3.12 – (a) Single NW TEM image of a group D NW. (b) SAD pattern obtained from the NW tip region (upper blue circled region in (a)). (c) SAD pattern obtained from the NW base (lower red circled region in (a)).

circled region near the top of Figure 3.12(a), was obtained near the NW tip and is indicative of a single-phase Wz crystal oriented along the <-2 1 1 0> zone axis. NW segments with lengths up to 1.2 μm were formed free of stacking faults. In contrast, the SAD pattern shown in Figure 3.12(c), corresponding to the circled region near the bottom of Figure 3.12(a), was obtained from a region near the NW base, where numerous densely packed stacking faults were observed. Streaking in the [0001] direction in this instance was observed, indicative of the pseudo-periodic arrangement of stacking faults in this region.

Next, the material composition of the group D NWs at the stacking fault termination point was examined. In Figure 3.13, a TEM image near the stacking fault termination point is superimposed with EDXS line-scans showing elemental counts of Ga (green), As (blue), and P (red). Moving along the growth direction (from right to left), the stacking faults cease to appear past the centre of the image. Coincident with this region, the line-scan shows an increase in elemental counts of As and decrease in P, indicative of the initial GaAsP layer. Thus, the termination of stacking faults is coincident with the initial growth interruption and the material change from GaP to GaAsP.

The length of stacking fault-free segments in group D NWs was dependent upon the diameter of the Au seeds at the NW tips. To illustrate this point, Figure 3.14(a) and (b) show TEM images of two group D SL NWs with 14 nm and 9 nm Au diameters, respectively. The NW with the larger Au tip (a) exhibited an abrupt termination of stacking faults as described above, while the NW with the

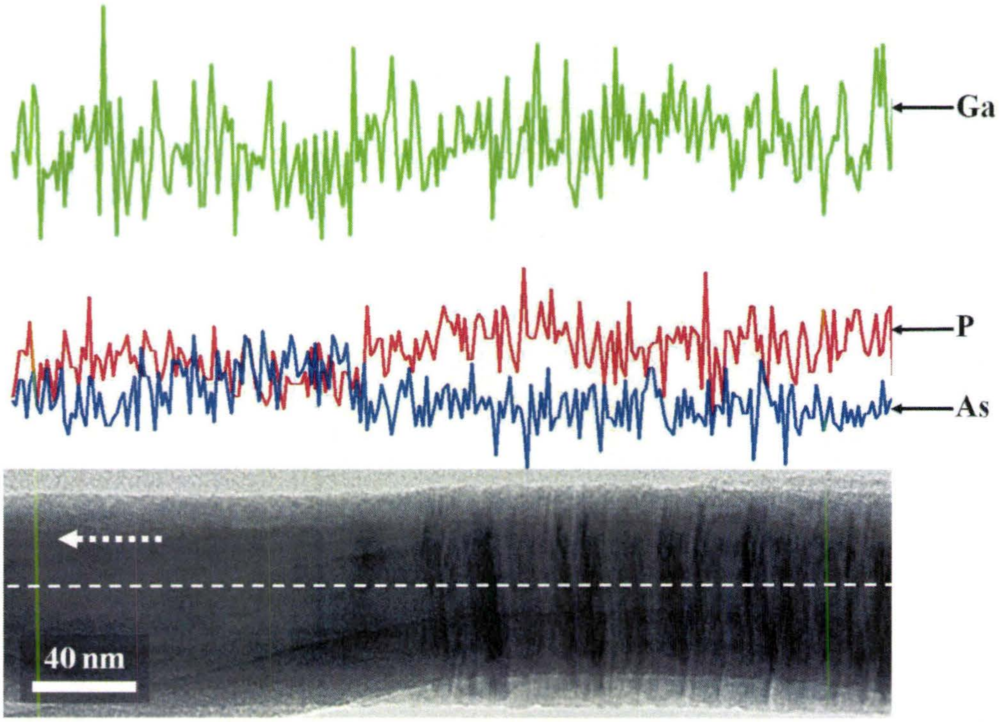

Figure 3.13 – TEM image and superimposed EDXS counts of Ga (green), As (blue), and P (red). The termination of stacking faults in the growth direction (right to left) coincides with a region where P counts decrease as As counts increase, showing that the lateral defects are eliminated with onset of the initial GaAsP layer. The broken line indicator points toward the NW tip.

smaller Au tip (b) consisted of several segments of fault-free growth, each followed by the reappearance of Zb insertions. This effect will be elaborated further in the discussion.

Finally, group E NWs (not shown), though identical in structure to group D NWs but without growth interruptions, exhibited stacking faults throughout their lengths at a density of roughly 0.25 nm^{-1}. Cross-sectional SEM analysis revealed a mere 2% difference in lengths between group D and E NWs. This leads to the argument that the introduction of growth interruptions in group D

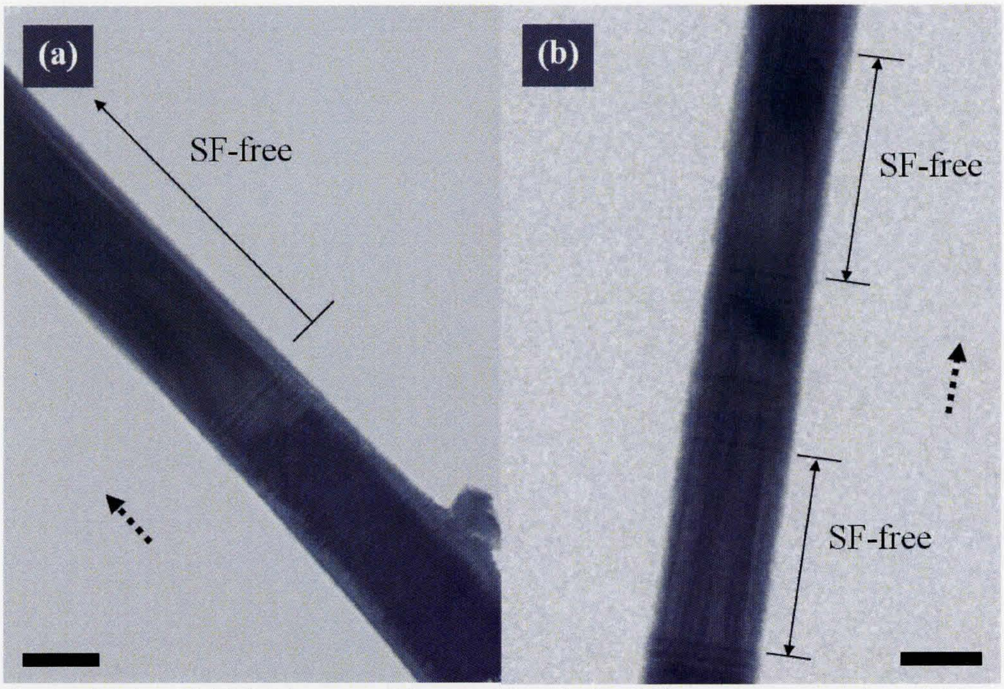

Figure 3 14 – (a) TEM image of the stacking fault (SF) termination point within a group D NW with Au diameter of 14 nm. Beyond this point, no further stacking faults were observed. (b) TEM image of initial stacking fault termination region within a group D NW with 9 nm Au diameter. The reappearance of stacking faults shows that the suppression of Zb insertions is dependent upon the Au seed diameter and, hence, the growth rate of the NW Scale bars designate a 50 nm length. The broken line indicators point toward the NW tips.

NWs places no substantial affect upon the NW growth rate.

Theoretical considerations on the matter of Zb/Wz polytypism in thin film semiconductors have been reported in view of the compositionally variable temperature dependence [172], the scaling of structural energy difference with effective orbital ionicity [173], and the critical fractional ionic characteristic [167] of a given material. However, the case of VLS grown NWs is further complicated by the dynamic nature of the metal-semiconductor alloy employed as a physical catalyst. Akiyama et al. [162] have shown that phase bistability in NWs relates to the ratio of the lateral facet area to the NW volume. This was shown to result in a critical diameter, dependent upon the ionicity of a material, with which both Wz and Zb layers can form. Dubrovskii et al. [98] also have shown that the formation of polytypic arrangements in semiconductor NWs occur as a result of a surface energy decrease on the faceted sidewalls, below a material dependent critical radius. Finally, Glas et al [174] previously suggested that 2-D nucleation occurs preferentially at the vapour-liquid-solid triple phase line where Zb forms when the supersaturation of Group III (and possibly Group V) adatoms is less than some critical value and conversely, that single phase Wz formation is favorable at high supersaturation. However, it has been shown that Wz with Zb insertions (stacking faults) occur in GaAs at high Ga or low As impingement rate, while single phase Wz occurs at low Ga or high As impingement rate [108]. The latter results suggest the existence of some critical Group III/V supersaturation below/above which a transition from polytypic growth to primarily Wz growth occurs.

In the present studies, growth interruptions were executed by shuttering the Ga source while maintaining the group V beam flux. During the growth interruption we expect the Ga to be purged from the Au particle by reaction with group V species, resulting in a low Ga supersaturation in the Au particle until growth is resumed. Compositional analysis of the Au particle, based on EDXS point measurements, revealed no significant Ga content within the seed, further substantiating the argument for the purging of Group III species during growth interruptions. Consistent with the results described above for GaAs growth, we speculate that once growth is resumed, a transient period occurs where the Group III supersaturation is below some critical concentration favouring fault-free Wz NW segments. As growth proceeds, increasing Ga supersaturation returns the nanowire to a polytypic Wz/Zb phase. With respect to homoepitaxially grown GaAs NWs, it has been reported that under conditions similar to the growth interruptions discussed here, where Group V pressures are maintained in the absence of Group III pressures, a "cooling neck" occurs leading to a characteristic narrow tip of dissimilar phase [108, 110]. Such an effect was not observed amongst any of the NWs investigated in the current study. The basis for the absence of a visible neck formation after growth interruptions in our heteroepitaxially grown GaAsP/GaP systems remains a topic of further examination.

The diameter dependence of stacking faults discussed with regards to Figure 3.14 can be attributed to the dependence of growth rate upon seed diameter. NW growth rates are inversely proportional to the diameters of the Au seeds at their tips [79, 175]. Thus, it is expected that in faster growing NWs with smaller particles, growth interruptions are not introduced at sufficiently high frequencies, thereby allowing for the reformation of stacking faults in each segment as steady-state concentrations are established in the Au particles. From these results, we conclude that if growth interruptions are repeatedly introduced between sufficiently short NW segments, then the reappearance of defects can be suppressed and phase purity can be sustained over the entire length of a NW.

3.4 – Influence of Compositional Variances and Passivating GaP Shell Layers on the Optical Properties of GaAsP Core Segments

Recent research efforts have led to the demonstration of a variety of novel opto-electronic device applications in which semiconducting nanowires (NWs) are used as the active medium [13-24]. Nonetheless, integration of NW-based applications within mainstream markets is hindered by some fundamental roadblocks, one of which involves a more complete understanding of the role of surface passivation in confinement effects [176].

In this section, we consider the structural and optical properties of GaP/GaAsP core-shell NWs grown according to the VLS mechanism. We show that radial and axial layers are distinctly self-arranged within a single segment of a ternary semiconductor NW, resulting in increased P incorporation near the centre of the NW. The effect of this compositional variance and the influence of a passivating GaP shell on the optically active GaAsP regions are investigated through Raman scattering (RS), photoluminescence (PL), and magneto-photoluminescence spectroscopy (M-PL).

3.4.1 – Experimental Details

NWs were grown on (111)-oriented n-type Si substrates. Pre-growth surface processing of the Si substrates was initiated with a 20 minute ultraviolet (UV) ozone treatment and subsequent wet-etching of the surface oxide in a 10:1 diluted buffered HF solution. Seeds for the NW growth were achieved by electron-beam evaporation of Au with thickness of 10 or 40 Å as measured by a quartz crystal monitor. All substrates were stored under high vacuum (10^{-8} Torr) to inhibit surface contamination until transfer to the growth chamber.

NW growth was performed in a gas-source molecular beam epitaxy (GS-MBE) system, where Group III monomers were supplied from a heated solid elemental effusion cell and Group V dimers from a hydride gas cracker operating at 950 °C. The P_2 flux was initiated at 350 °C as the substrate temperature was ramped from room temperature to the NW growth temperature. Upon stabilization at the growth temperature, the As_2 flux was initiated. At the substrate temperature of 520 °C, growth was initiated by opening the shutter of the Ga effusion cell, 60 s after the initiation of the As_2 flux.

Three NW samples of different sizes and structures were grown and investigated in the current study, henceforth referred to as samples A, B, and C. Details of the NW growth are provided in Table 3.2. Sample A NWs were grown using a 10 Å Au film and composed of a single segment of $GaAs_{1-x}P_x$, with an As/P flux ratio adjusted to yield a nominal composition of $x = 0.4$, based upon previous calibrations of thin films grown on GaAs (100) substrates. The growth duration of sample A NWs was 30 minutes. Sample B NWs were grown in an identical manner to that of sample A with the addition of a single, stoichiometric GaP segment, grown for a duration of 10 minutes, and serving as a passivation layer to the GaAsP core. Thus, the sample B NWs were grown to inherently contain GaAsP/GaP core-shell heterostructures. Sample C NWs were grown under identical conditions as sample A except a 40 Å Au film was employed in sample C rather than the 10 Å Au film used in sample A. All growths were conducted at a V/III flux ratio of 1.5. The group III effusion cell temperature was stabilized to yield a nominal planar growth rate of 1 $\mu m \cdot h^{-1}$. The growths were terminated by closing the shutter of the Ga effusion cell, and the sample was gradually cooled down from the growth temperature under a P_2 overpressure. Pictorial representation of the three NW samples based on our structural analysis is shown in Figure 3.15 as will be discussed further below.

Structural and compositional analysis of the NW samples was performed after growth. A JEOL JSM-7000 scanning electron microscope (SEM) was employed in the cross-sectional analysis of as-grown NW samples, particularly in the determination of average NW heights. Single NW specimens, ultrasonically removed in solution from the Si substrates and deposited upon holey carbon-coated copper grids, were examined with a Philips CM12 transmission electron microscope (TEM). In addition, compositional analysis was performed in various positions along the NW length by embedding NWs in an epoxy resin (vinyl cyclohexene dioxide) [177] cured at 70 °C, followed by the removal of lateral

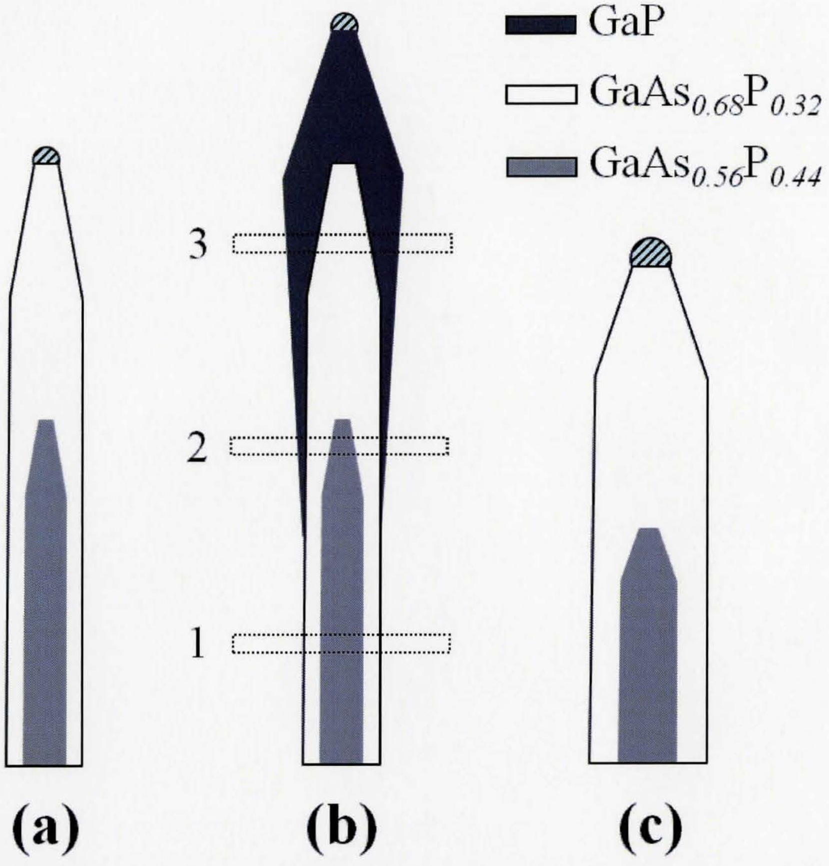

Figure 3 15 – Pictorial representation of sample A, B, and C NW structures. The NWs are not drawn to scale. White and light gray segments represent As-rich and P-rich GaAsP layers, respectively The dark gray segment of the sample B NW signifies the GaP layer Dotted boxes, labelled 1, 2, and 3, correspond to the regions of interest on the ultramicrotomed lamellae presented in Figures 3.18 and 3 19 The striped segments at the NW tips represent the Au seed nanoparticles.

Table 3.2 – Descriptions and dimensions of NW groups A – C.

NW Group	**Au Film Thickness (Å)**	**Growth Sequence**	**NW Height (μm)**	**NW FWHL Diameter (nm)**
A	10	30 min GaAsP	3.75	53
B	10	30 min GaAsP + 10 min GaP	5.50	96
C	40	30 min GaAsP	3.50	101

lamellae with average thicknesses of roughly 80-100 nm, using an ultramicrotomy procedure, at a slicing angle of approximately 5°. Lamellae were subsequently placed upon TEM grids and sputter coated with a thin film of carbon (roughly 5 nm) to further reduce superficial electron beam-induced damage. The lamellae were examined by high angle annular dark field (HAADF) characterization and energy dispersive X-ray spectrometry (EDXS) using a JEOL 2010F high-resolution transmission electron microscope (HR-TEM).

Raman scattering (RS), photoluminescence (PL) and magneto-photoluminescence (M-PL) were performed to study the lattice vibrations and electron excitations of samples A – C. The investigation of the lattice vibrations (phonons) by Raman scattering allowed a structural characterization of the NWs, while photoluminescence provided information about the electronic structure of the NWs. Raman scattering was collected from the surface of the samples at a temperature T = 10 K in the back-scattering configuration with an Instruments S.A. T64000 triple grating spectrometer supplied with a liquid nitrogen-cooled CCD detector. The PL measurements were carried out at T = 1.6 K with an Ocean Optics Inc. HR2000 high-resolution spectrometer in an Oxford Instruments optical cryostat with a superconducting magnet with magnetic field of 10 T oriented parallel to the nanowires. The 5145 Å line of an Ar^+ laser was used for excitation in RS and PL measurements.

3.4.2 – Results and Discussion

The average NW heights were determined in cross-sectional SEM images by measuring the distance between the planar surface and the top of the Au seeds at the NW tips. Representative cross-sectional SEM images of all NW samples are shown in Figure 3.16. The NW heights were measured to be approximately 3.75 μm, 5.5 μm, and 3.5 μm, for sample A, B, and C NWs, respectively. The SEM images revealed that the NWs were tapered near their tips, while also exhibiting reverse tapering near their bases, as shown in the inset of Figure 3.16(b) and depicted in Figure 3.15(b). Therefore, the diameters of NWs was quantified via their average full-width at half-length (FWHL) as measured in TEM from a population of 100 sonicated NWs per sample. The average FWHLs of the NWs were determined to be 53 ± 11 nm for sample A, 96 ± 9 nm for sample B, and 101 ± 20 nm for sample C NWs. Figure 3.17 shows a comparison of the normalized FWHL distributions for each NW sample, fit to a Gaussian distribution, wherein the above uncertainty values represent one standard deviation. The above results are summarized in Table 3.2.

The larger diameter of sample B compared to sample A NWs is attributed to the presence of the passivating GaP shell in sample B but not A. In contrast, the disparity between average FWHL values observed for sample A and sample C NWs is the consequence of the thicker Au film employed in the growth of sample C NWs. The thicker Au film results in larger Au nanoparticles upon annealing. The length of NWs is inversely proportional to the Au seed particle diameter due

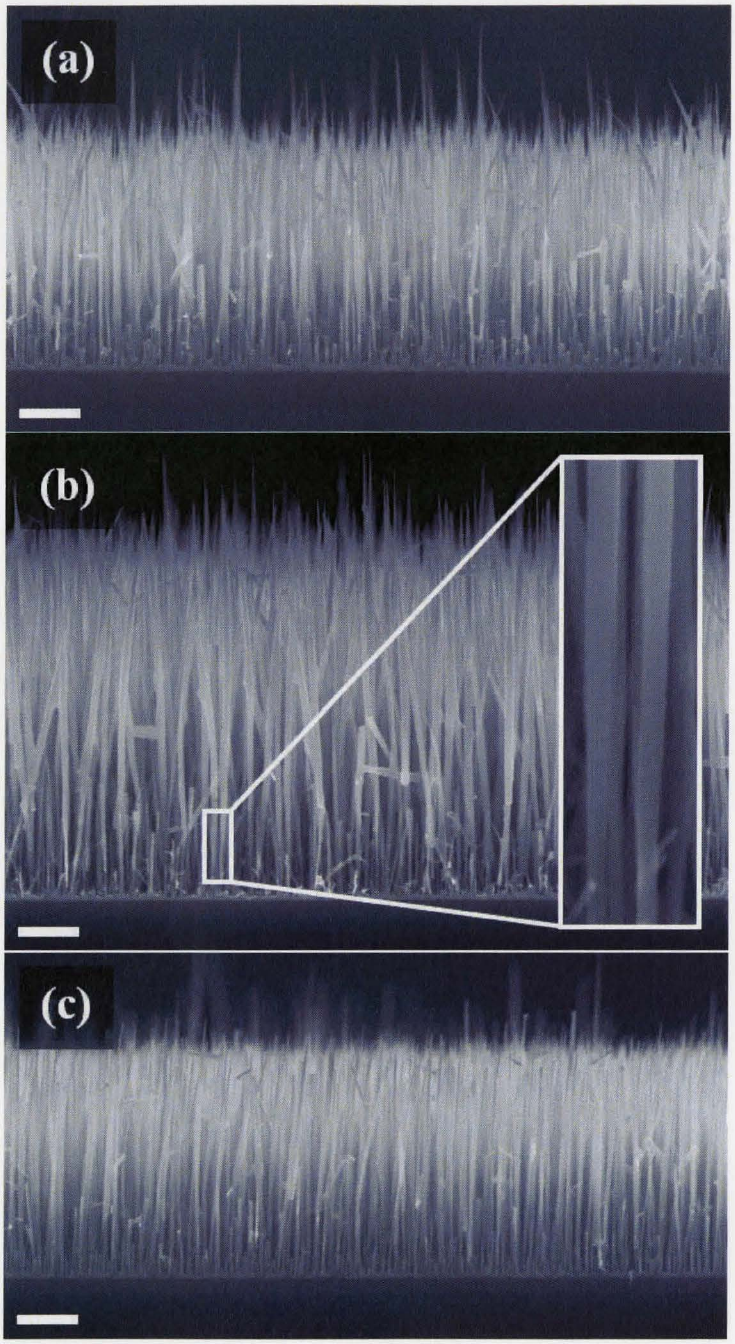

Figure 3.16 – Cross-sectional SEM images of as-grown NW samples A (a), B (b), and C (c). The highlighted region and inset in (b) further illustrates the reverse tapering phenomenon, due to shadowing effects. All scale bars represent a 1 μm length.

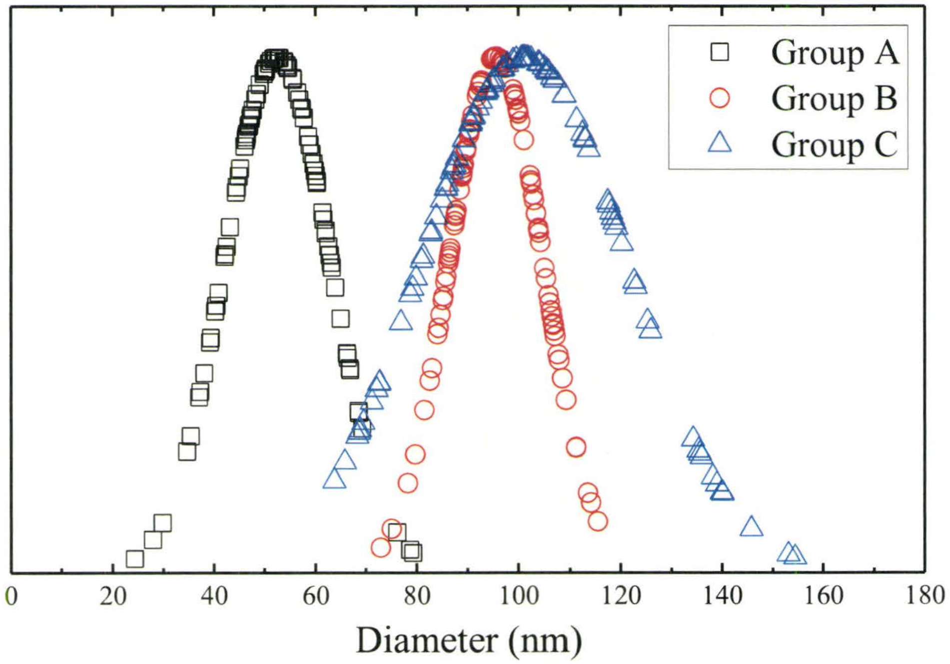

Figure 3.17 – FWHL NW diameters of samples A (black squares), B (red circles), and C (blue triangles), fit to a Gaussian distribution. The profiles represent sample sets of 100 single NWs.

to a simple material conservation principle [117, 175]. Larger Au nanoparticles therefore result in the growth of thicker, yet shorter, structures.

In Section 3.2, the P content in the ternary alloy segment of the core-multishell NWs, grown under identical conditions as the present study, was determined to be 33%, at most, along the longitudinal centre of the NW, based on a cylindrical approximation technique involving EDXS mapping and HAADF imaging of individual NWs. In the current study, a more accurate determination of the structure and composition of the NWs were achieved by examining lamellae cut from the sample B NWs. Sections removed from the NW bases, mid-section, and tips (represented in Figure 3.15 as boxes 1, 2, and 3, respectively) were probed in EDXS experiments to determine the elemental distributions across the NW diameter at various lengths along the NW. Figure 3.18 shows a HAADF image of a lamella removed from the base region of a sample B NW (box 1 in Figure 3.15) with superimposed EDXS linescans, indicative of the elemental concentrations of Ga (green), As (blue), and P (red). While the elemental counts of Ga are observed to be constant across the NW diameter, the As and P counts, in contrast, are noted to deviate from a homogenous profile within the centre. In the NW centre, the elemental concentration of As atoms declines, whereas the concentration of P atoms rises. Thus, a P-rich region is evident near the radial centre of the GaAsP NW. EDXS mapping in several NWs indicated a region with composition of $GaAs_{0.56}P_{0.44}$ near the NW centre (depicted as the grey region in Figure 3.15) with a surrounding composition of $GaAs_{0.68}P_{0.32}$ (depicted as the white region in Figure 3.15). The GaP passivating layer was notably absent from the base of the NWs which can be explained by shadowing effects (see also the inset of Fig. 3.16(b)). The GaP shell is initiated after the GaAsP segment is completed. At this point, the NWs have already reached a certain critical height where shadowing from neighboring NWs could limit the direct impingement near each NW base [79, 178]. As a result, the GaP shell is absent near the base of the NWs, as depicted in Figure 3.15.

Next, a cross-sectional segment removed from the central region of a sample B NW (box 2 in Figure 3.15) was examined, as shown in Figure 3.19. Here, EDXS measurements indicated a homogenous composition of $GaAs_{0.68}P_{0.32}$,

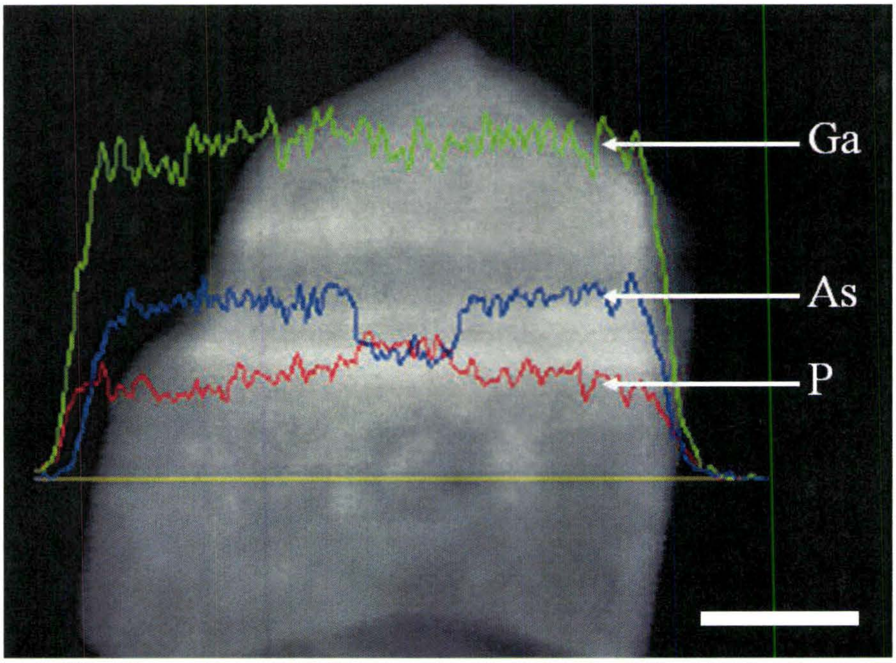

Figure 3.18 – HAADF image showing the cross-section of a single sample B NW near its base (corresponding to box 1 in Figure 3.15). EDXS linescans, representative of elemental Ga (green), As (blue), and P (red), are superimposed. The decrease in the As-profile and increase in P-profile observed near the centre corresponds to the region of dark contrast, and demonstrates the presence of a P-rich region near the NW centre. The scale bar represents a 20 nm length.

in close agreement with our previous cylindrical approximation method, discussed in Section 3.2. Although no notable variation in the As/P ratio could be spatially resolved by EDXS, a centrally localized region of dark contrast was resolved in the HAADF image, associated with the presence of a small P-enriched inner region within the GaAsP layer. Towards the circumference, the dramatic decrease in As counts and sharp increase in P counts is characteristic of the presence of the passivating GaP layer, which is also evident by the darker contrast along the NW circumference.

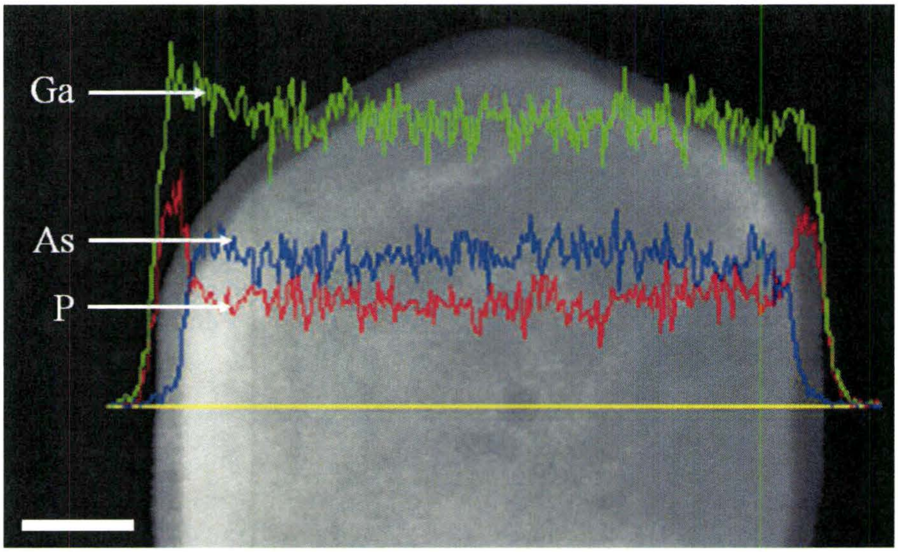

Figure 3.19 – Cross-sectional HAADF image and superimposed EDXS lines-cans showing elemental counts of Ga (green), As (blue), and P (red), obtained from the axial mid-section of a single sample B NW (corresponding to box 2 in Figure 3.15). A passivating GaP shell is seen as an outer disk of dark contrast. A central spot of dark contrast shows the location of a small P-rich region near the NW centre, which is unresolved by the EDXS line-scan. The scale bar represents a 20 nm length.

Similar EDXS scans obtained from the tips of sample B NWs (not shown) demonstrated a GaAsP core diameter reduction and an increase in the thickness of the GaP shell as depicted by box 3 in Figure 3.15. Previous investigations into the nature of MBE-grown core-multishell NW heterostructures, involving the same material samples, has led us to conclude that the aforementioned effect is a result of the tapered or 'pencil-shaped' morphology of NWs grown under similar conditions as depicted in Figure 3.15 [108, 116]. EDXS mapping indicated a homogeneous composition of $GaAs_{0.68}P_{0.32}$ in this tip region of the NW, identical to the composition of the NW mid-section and outer regions of the NW base.

Based on the above EDXS analysis, a P-enrichment occurs in the centre of the base region of the NWs with a composition of approximately $GaAs_{0.56}P_{0.44}$. A composition of $GaAs_{0.68}P_{0.32}$ was measured throughout other regions of the NW. Initially, the main contribution to NW growth is adatom impingement on the substrate surrounding each NW, followed by adatom diffusion to the Au particle resulting in axial NW growth or direct nucleation on the NW sidewalls resulting in radial growth. A thermodynamic model for the incorporation of group V species in InGaAsP films during GS-MBE growth [179] indicated the preferential incorporation of As compared to P, suggesting a longer diffusion length before incorporation of P_2 compared to As_2 on the substrate surface. Therefore, the species with longer diffusion length (P_2) would be expected to contribute more to axial growth of the NW that would lead to P-enrichment of the NW centre as we observed, as compared to the species with shorter diffusion length (As_2) that would contribute more to radial growth of the NW. When the NW becomes sufficiently long, the contribution to axial growth due to adatom diffusion from the substrate diminishes and the main contribution to NW growth then changes to direct impingement near the Au seed particle at the top of the NW. In this case, differences in As_2 and P_2 diffusion on the NW sidewalls and the Au seed particle may become less significant, which limits the P-enrichment near the base of the NWs.

Raman spectra of samples A – C are shown in Figure 3.20. The GaAs-like and GaP-like transverse optical (TO) and longitudinal optical (LO) phonons were

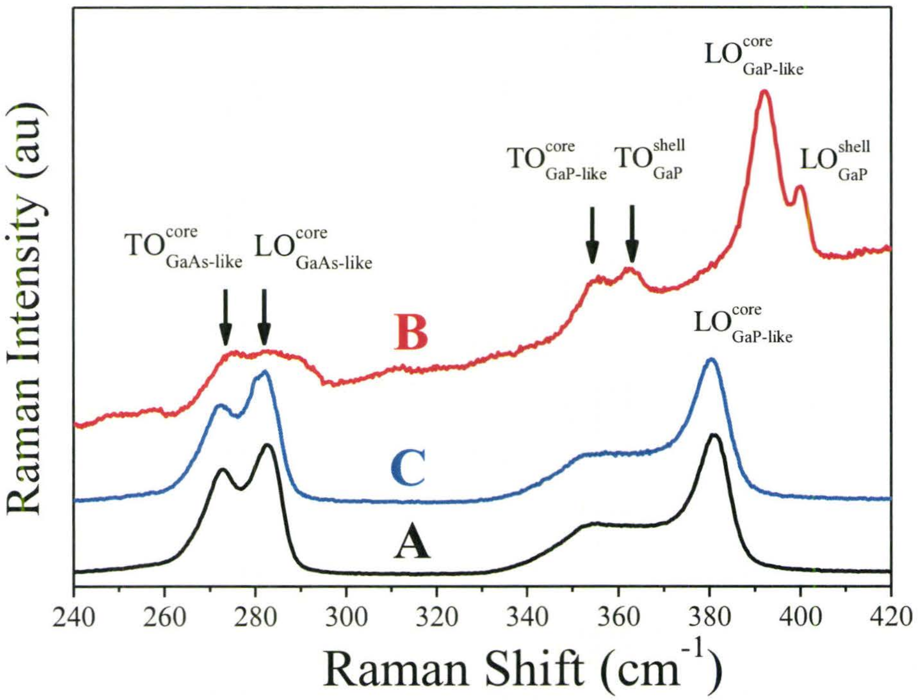

Figure 3.20 – Raman scattering spectra obtained from as-grown NW samples A (black), B (red), and C (blue) measured at 10 K. The spectra have been vertically shifted for clarity.

clearly observed in the single segment GaAsP NWs (samples A and C). Moreover, considerable Raman scattering was observed in the single segment NWs (samples A and C) in the interval between the TO and LO GaP-like phonons. Such Raman scattering was not found in the encapsulated NW (sample B), where the surface was passivated. Therefore, it is likely due to the surface modes present in the NWs with open surfaces [180, 181]. The relative frequency positions (ν_{LO}^{GaP}, ν_{LO}^{GaAs}) and integral intensities (I_{LO}^{GaP}, I_{LO}^{GaAs}) of the GaP-like and GaAs-like LO phonons in samples A and C allow a determination of the P-concentration of the $GaAs_{1-x}P_x$ alloy according to Equations (2.12) – (2.14).

The frequencies and the integral intensities of the GaP-like and GaAs-like LO phonons were obtained from fits of the experimental Raman spectra by Gaussian lines. The integral intensities yield $x \approx 0.48$, while the positions of the GaAs-like and GaP-like LO phonon frequencies (interpolated to room temperature) give $x \approx 0.43$ and $x \approx 0.42$, respectively. In comparison, a composition $x \approx 0.44$ was obtained from EDXS analysis for the centre of the NW base and $x \approx 0.32$ elsewhere. Raman scattering cannot distinguish between contributions from different parts of the NW. Instead, the Raman lines will consist of the weighted average contributions of the entire NW. In addition, compositional determination by Raman is complicated by scattering effects within the NWs [182].

The Raman data obtained in the encapsulated NWs (sample B) clearly demonstrate the effect of the core-shell misfit accommodation. The GaP-like LO phonon line is considerably blue-shifted with respect to the corresponding lines in the single segment NWs (samples A and C). Moreover, the LO phonon line of the GaP shell is red-shifted with respect to the frequency of the bulk GaP LO phonon (404 cm^{-1}). This is a manifestation of the stressed GaAsP core and the tensile GaP shell, which is expected from the difference in corresponding lattice constants.

The PL spectra of the NWs are depicted in Figure 3.21. The single segment NWs (samples A and C) emitted narrow PL lines with peak positions near 1.8 eV. The slightly different PL peak positions of samples A and C (a difference of about

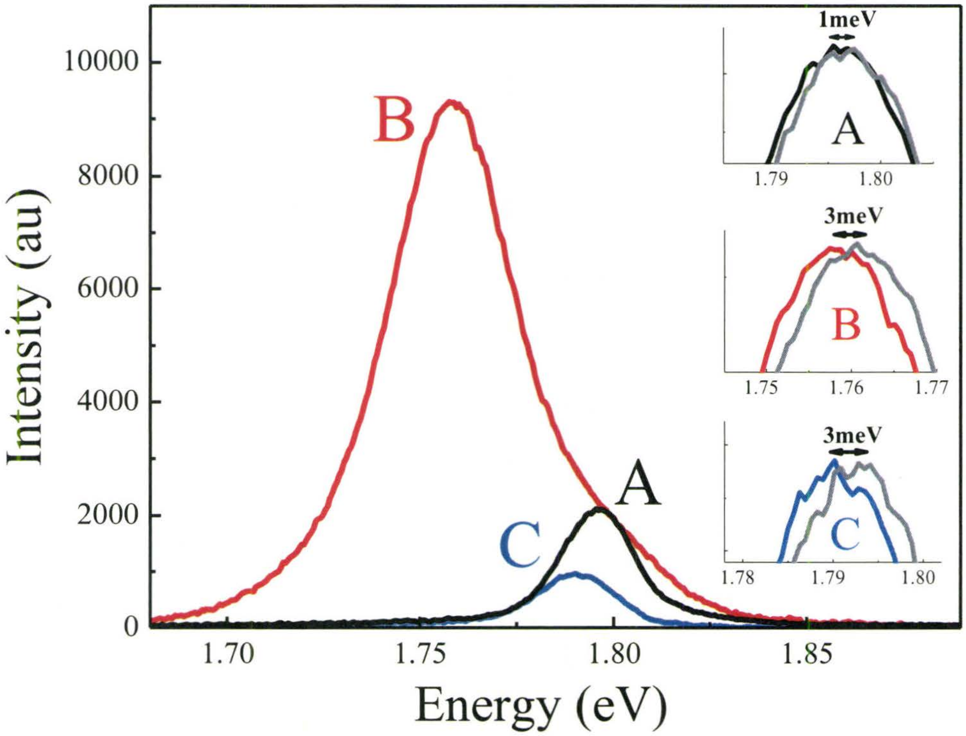

Figure 3.21 – Photoluminescence spectra of the samples A (black), B (red), and C (blue) measured at T = 1.6 K. Insets show the comparisons between the PL measured close to the peak positions without the magnetic field (black, red, and blue lines for groups A, B, and C, respectively) and in the magnetic field $B = 10$ T (gray lines).

6 meV) is likely caused by the effects of spatial confinement. The TEM analysis indicated an average NW diameter (full-width at half-length) of 53 nm for sample A and 101 nm for sample C (see Table 3.2 and Figure 3.17). The large diameter of the sample C NWs does not result in a significant quantization of the electron energy. However, for sample A, a confinement energy of about 1.5 meV was calculated by the envelope function approximation using the parameters from Ref. [152]. The difference between the experiment (6 meV) and the calculation (1.5 meV) may be explained by assuming a smaller effective "electronic" diameter of

sample A caused by spatial confinement due to surface depletion, as discussed further below.

The effects of the spatial confinement were further measured by magneto-PL measurements. The magnetic field does not influence the electron energy when the NW diameter $D_{NW} < L_B$, where $L_B = \sqrt{\hbar/eB}$ is the magnetic length. In the magnetic field of B = 10 T the magnetic length is about 10 nm. In such a magnetic field one expects a blue-shift of the PL measured in the $GaAs_{1-x}P_x$ NW samples of about 7 meV (calculated as the energy shift of the lowest Landau level). The PL peak intensities in the magnetic field B = 10 T are compared with the PL intensities measured without the field in the insets of Figure 3.21. Only a very small (about 1 meV) blue-shift was found in sample A with the nominal diameter of 53 nm. An absence of the anticipated blue-shift in sample A indicates a considerably smaller effective "electronic" diameter which results in determination of the electron energy mainly due to spatial confinement. Larger blue-shifts of the PL lines (about 3 meV) measured in the magnetic field of 10 T were observed in samples B and C indicating less spatial confinement compared to sample A. When the magnetic length is much larger than the effective electronic NW diameter ($L_B > D_{NW}$) the electron energy is completely determined by the NW size quantization. In such a case, no variation of the PL energy with the magnetic field is expected. In the opposite limit ($L_B < D_{NW}$) the magnetic field is responsible for the electron energy quantization. In the bulk GaAsP, in the magnetic field B = 10T ($L_B \approx$ 10 nm), the magnetic field induced PL blue-shift of about 7 meV is expected. In samples B and C, we measured blue-shifts of 3 meV meaning that, in these samples, the magnetic field considerably influences the electron energy. The total electron energy, thus, is determined by the effect of the applied magnetic field and the effect of spatial confinement. Accordingly, D_{NW} is on the order of, but somewhat larger than, $L_B \approx 10$ nm in samples B and C. In sample A, a much smaller shift was observed (about 1 meV) in the magnetic field. Hence, the effective nanowire diameter, $D_{eff} < L_B \approx 10$ nm in sample A, which is consistent with the previously presented zero-field blue-shift of the PL peak position of sample A compared to C.

The most striking effect is the significant red-shift and the substantial increase in intensity of the PL found in the encapsulated core-shell sample B compared to A and C. A similar increase of the PL intensity was found by Skold et al. in the case of core-shell InGaP/GaAs NWs [183]. The increase in PL emission upon encapsulation of the NWs is due to passivation of the surface states which cause non-radiative recombination of the excited electrons. Another striking observation is the red-shift of the PL in the passivated NWs of sample B, while a blue-shift is expected due to the shell strain [183].

The Franz-Keldysh effect [184, 185], caused by the built-in surface electric field and observed recently in InP [186], also cannot explain our observed red-shift of the PL emission. Passivation of surface states responsible for the built-in electric field eliminates the effect of the surface band bending. Therefore, a blue-

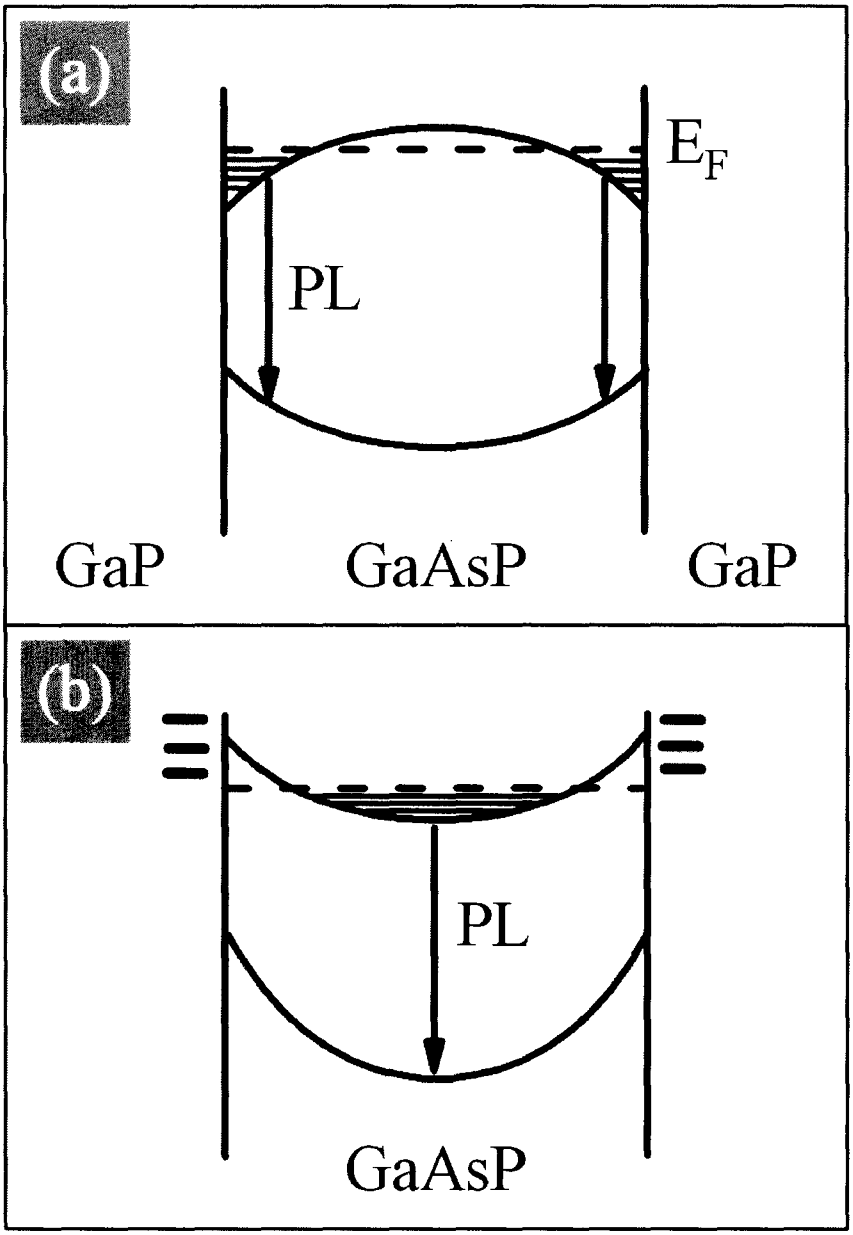

Figure 3.22 – Model for the radial distribution of the electron gap in the (a) core-shell GaAsP/GaP group B NWs and (b) in the single segment GaAsP groups A and C NWs. The electron transitions active in the photoluminescence are shown by the vertical arrows.

shift of the PL emission, opposite to our observed red-shift, is expected in the encapsulated NWs.

Based on the extensive structural analysis of the NWs presented earlier, a model is developed to account for the observed modification of the PL emission. We suppose that the P-enrichment of the central GaAsP segment found through the EDXS analysis plays a crucial role in the detected red-shift of the PL emission. The model radial distribution of the electron potential assumed in the passivated sample B NW is shown in Figure 3.22. The P-enrichment of the central part of the core-shell GaAsP/GaP NWs causes the radial gradient of the electron gap energy shown in Figure 3.22(a). Electrons are confined in the narrow ranges of the NWs close to the GaAsP/GaP interface. This circular range occupied by the electrons is responsible for the PL emission. The band bending due to surface states of the single segment GaAsP (samples A and C) produces the built-in electric field which depletes the electron states and shifts the range where the electrons are confined to the inner part of the NW with the larger gap (higher P content in the centre of the NW base). The corresponding radial gap variation is depicted in Figure 3.22(b). Therefore, the energy of the core-shell NWs decreases as compared to the single segment NWs. This model also accounts for the smaller effective "electronic" diameters of the NWs mentioned above.

3.5 – Chapter Conclusions

The growth of GaAsP/GaP core-shell heterostructured NWs on Si (111) surfaces has been investigated. The epitaxial growth was accomplished via Au-assisted VLS-type growth, as confirmed by the presence of characteristic Au particles at the NW tips. Structural analysis demonstrated the monolithic integration of free-standing, orthogonally-oriented NWs on Si substrates, grown along the [0001] direction of the hexagonal crystal lattice. Through EDXS line-scan studies, a model for the heterostructure geometry was defined. Indeed, a core-multishell arrangement was confirmed, in which adjacent NW layers were arranged coaxially.

The crystal structure of the NWs was characterized as hexagonal wurtzite with periodically positioned stacking faults in the form of lateral zincblende insertions. It was shown that growth interruptions implemented prior to the growth of each compositionally variant segment allowed for the control of crystalline phase-purity. This was attributed to the decrease of growth species supersaturation in the Au seeds during the growth interruptions, and particularly to the purging of Ga. Through the growth of superlattice NWs, with regular growth interruptions introduced at the heterostructure interfaces, defect-free crystal assembly was achieved.

Finally, through extensive cross-sectional analysis of single NWs composed of GaAsP, it was found that preferential incorporation of P occurs in the early stages of growth, leading to a P-rich core and P-deficient shell within a single NW segment. This preferential incorporation was accounted for by the difference in diffusion length of As_2 and P_2 dimers and the evolution of their relative contributions at various stages of growth. The radial variation of the P-composition detected through EDXS mapping measurements was shown to drastically influence the PL emission. The combined effects of the radial P-distribution, leading to distinct bandgap energies, and of surface charge depletion were observable in the M-PL spectra of the corresponding NW samples. A qualitative model was presented for the PL emission from GaP/GaAsP coaxial NWs, considering the role of surface passivation and preferential P-incorporation.

Chapter 4

GaAs Nanowires on Foreign Substrates

4.1 – Introduction

In this Chapter, the growth of GaAs nanowires (NWs) on several foreign substrates is presented. The aim is to define a suitable growth surface on which high crystalline quality III-V semiconductor NW structures can be assembled and utilized for opto-electronic device applications. Foreign substrates are considered as a means of realizing additional functionality and significant cost advantages in comparison to otherwise conventional homo-epitaxial growth alternatives. As potential candidates for suitable substrates, we explore Si (100) and (111) surfaces, stainless-steel films, borosilicate glass substrates with polycrystalline buffer layers, single-walled carbon-nanotube composite films (as previously reported in Ref. [119]), and highly-ordered pyrolytic graphite substrates. The distinct pre-growth sample preparation details, post-growth structural analysis, and the potential merits for device fabrication are presented with regards to each NW-substrate combination. We conclude that the hybrid system comprised of GaAs NWs on carbon-nanotube composite films is the most favourable alternative for opto-electronic device applications.

4.2 – Growth of GaAs Nanowires on Si (100) and (111) Substrates

4.2.1 – Experimental Details

Boron-doped, 2-inch diameter Si (100) and (111) substrates, as purchased from Virginia Semiconductor, Inc., were used as growth surfaces for the assembly of GaAs NWs. As in the case of the GaAsP/GaP NWs discussed in Chapter 3, the Si substrates utilized in the current study were subjected to a 20 min. ultraviolet ozone treatment for the growth of a sacrificial oxide layer followed by a wet-etching procedure for 30 s in a 10:1 buffered HF solution, and subsequent deionized (DI) water rinse. The surface treated substrates were then transferred in ambient air to an electron-beam evaporation system for the metallization of a 40 Å thick Au film, as monitored by a quartz crystal thickness monitor. Upon transfer to the GS-MBE system, discussed in Section 2.1, the Au-deposited Si wafers were heated to a growth temperature of 550 °C and subjected to an inductively coupled H_2 plasma treatment, under an As_2 overpressure, for the spontaneous formation of Au nanoparticles.

The opening of the Ga effusion cell, fixed at a temperature yielding a constant nominal deposition rate of 1 μm/hr, marked the commencement of the growth sequence. A constant V/III flux ratio of 1.5 was employed for NW growths, over a period of 30 min, after which the Ga shutter was closed, signifying the termination of the growth sequence. The samples were then allowed to cool under a constant As_2 flux.

Post-growth analysis of as-grown NW samples was carried out with a JEOL JSM-7000 F scanning electron microscope (SEM), for investigations on NW orientation, density, and morphology. Single NW structural characterization experiments were conducted with a Philips CM12 transmission electron microscope (TEM) and a JEOL JEM 2010F high-resolution transmission electron microscope (HR-TEM).

4.2.2 – Results and Discussion

Densely packed growth of GaAs NWs, with lengths up to 2.5 μm and full-width at half-length dimensions between 20 nm and 100 nm, were achieved on Si (100) and Si (111) substrates. In both cases, the preferred NW growth directions can be surmised from plan-view SEM images, based on the orientation of the NWs with respect to the (110) oriented wafer flats, and from cross-sectional SEM images, based on the NW orientations with respect to the substrate surface. First, we shall consider NWs grown on Si (100). Figure 4.1(a) and (b) show planar and cross-sectional SEM views, respectively, of as-grown GaAs NWs on (100) oriented Si. In Figure 4.1(a), the substrate flat is positioned parallel to the bottom edge of the image. Hence, in the plan-view, NWs grown in the equivalent <111> directions of the crystal lattice will be projected at 45° relative to the wafer flat. Although, a variety of growth directions are seen in Figure 4.1(a), it is clear that

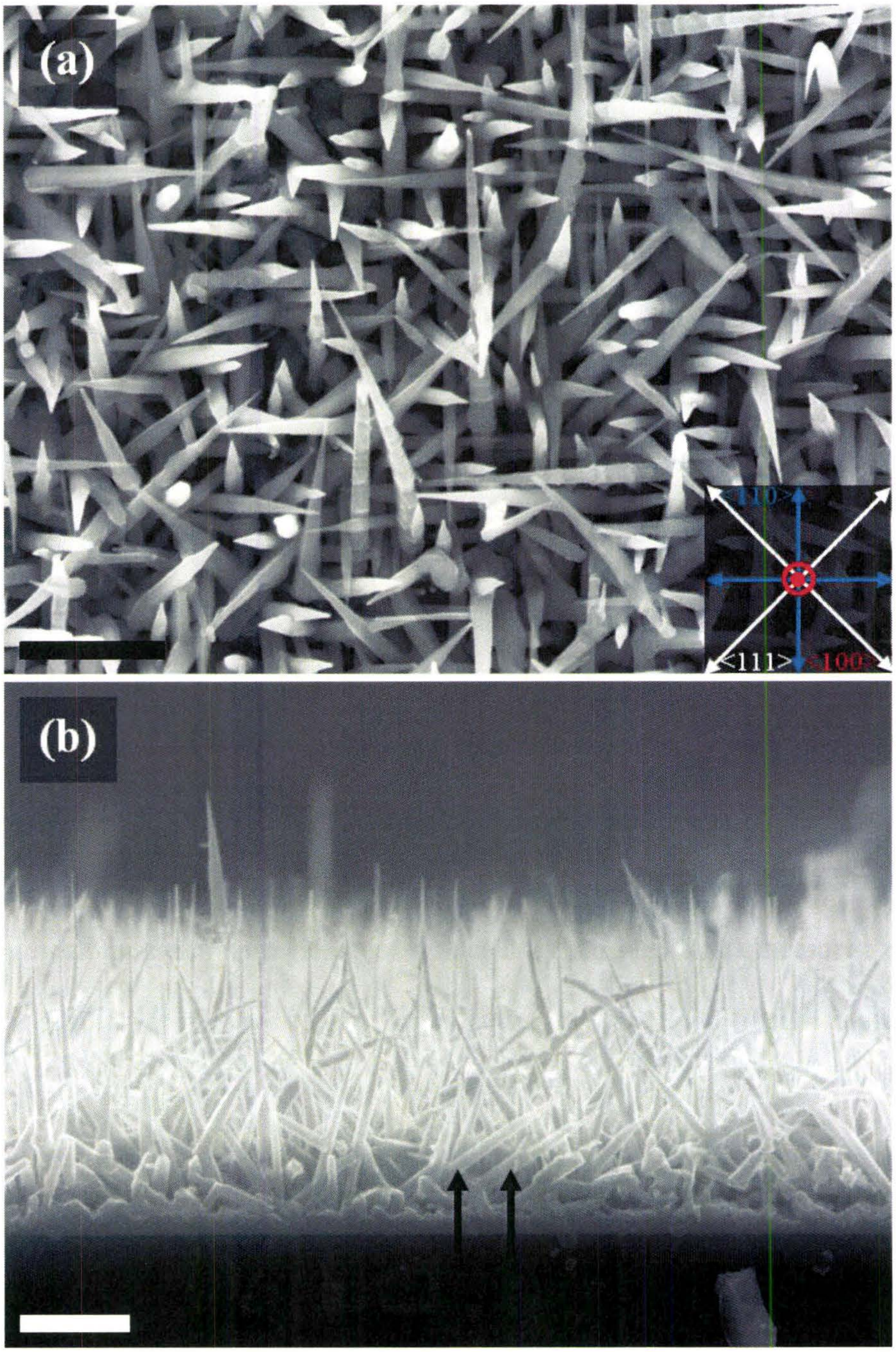

Figure 4.1 – (a) Plan-view and (b) cross-sectional view of GaAs NWs grown on Si (100) substrates. The inset in (a) demonstrates the projections of the lower index growth directions. The black arrows in (b) indicate examples of NWs grown in the <111> directions. Scale bars represent a 1 μm length.

the energetically favourable <111> direction is dominant. As discussed in Section 1.3, this is accounted for by the greatest areal density of bonds formed in the <111> directions [93]. The cross-sectional SEM image shown in Figure 4.1(b) demonstrates the various NW orientations, while examples of NWs grown in the <111> directions (oriented at 35.3° relative to the substrate surface) are indicated by black arrows.

In the case of growth on Si (111) substrates, the NWs are oriented orthogonally with respect to the substrate surface. Orthogonal growth on (111) surfaces demonstrates the epitaxial relationship between the fabricated NWs and the underlying substrate [10, 157, 158]. Figures 4.2(a) and (b) show planar and cross-sectional SEM images of GaAs NWs grown on Si (111) substrates. In the inset of the Figure 4.2(a) the hexagonally facetted structure of the NWs can be clearly seen. The thickness of the planar GaAs film, deposited in tandem with NW growth on substrate regions not activated by Au seeds, was measured to be roughly 200 nm in the case of growths on both (100) and (111) oriented surfaces, as seen in Figures 4.1(b) and 4.2(b), respectively.

The morphology and structure of the GaAs NWs grown on Si substrates was investigated by TEM. Independent of the surface orientation of the Si wafers, three main NW morphologies were observed including rod-shaped NWs, tapered or 'pencil-shaped' NWs, and curved NWs with irregularly faceted sidewalls. TEM images showing examples of each NW morphology are shown in Figure 4.3. Growth of rod-shaped NWs was restricted to the peripheral regions of the

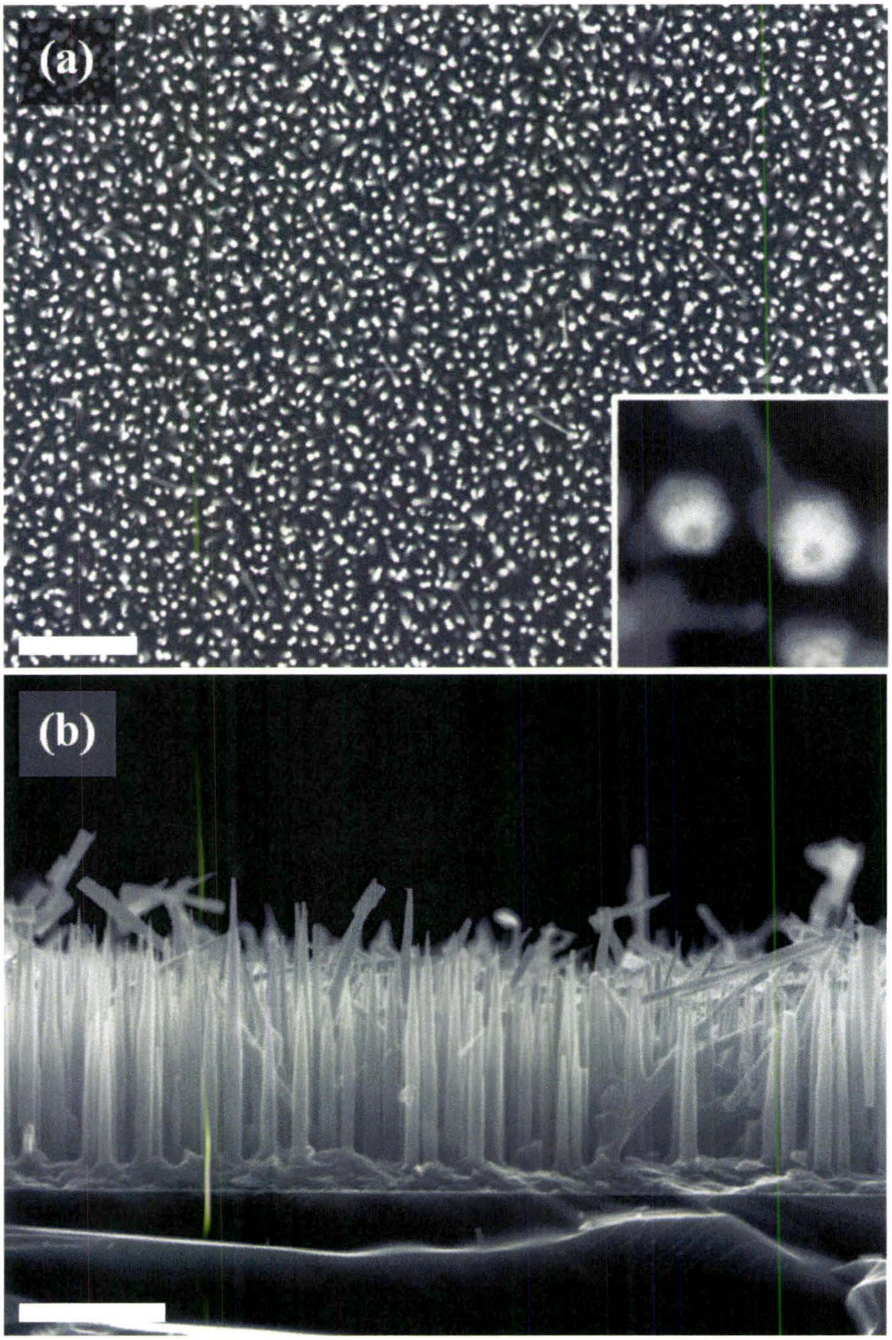

Figure 4.2 – (a) Plan-view and (b) cross-sectional view of GaAs NWs grown on Si (111) substrates. The inset of (a) shows a magnified plan-view of two NWs, showing their hexagonally facetted cross-sections. The broken NWs seen in (b) resulted from the sample cleaving procedure. Scale bars represent a 1 μm length.

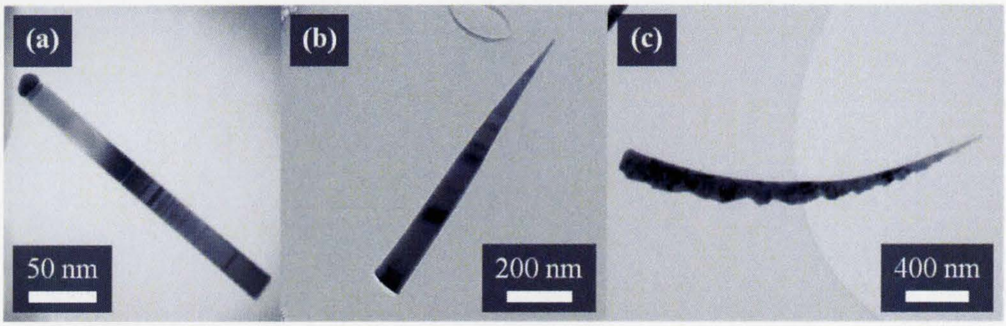

Figure 4.3 – TEM images showing example of three distinct NW morphologies including (a) a rod-shaped NW, (b) a tapered or 'pencil'-shaped NW, and (c) a curved NW

substrate, as confirmed through SEM imaging, examples of which are shown in Figure 4.4. During growth, the peripheral substrate regions are shadowed by edges of the molybdenum substrate holder such that adatom impingement fluxes are reduced in this region, in comparison to all other regions of the substrate surface. Due to the reduction of available growth species, NW growth rates are reduced in the peripheral regions. This inhibits the growth of NWs located at the edges of the substrate, such that they do not exceed the critical length beyond which significant sidewall growth ensues [95, 100] Thus, the NWs grown along the peripheral regions of the substrate exhibit rod-shaped morphologies, as in Figure 4.3(a). In contrast, NWs grown elsewhere experience sufficient growth species fluxes, both through direct impingement and diffusion regimes, such that their heights exceed the aforementioned critical height. Beyond this point, the evolution towards step-flow growth on the sidewalls promotes the assembly of NWs with tapered morphologies, such as the NW shown in Figure 4.3(b). A third NW morphology is also observed in the case of growths on Si (100) and (111)

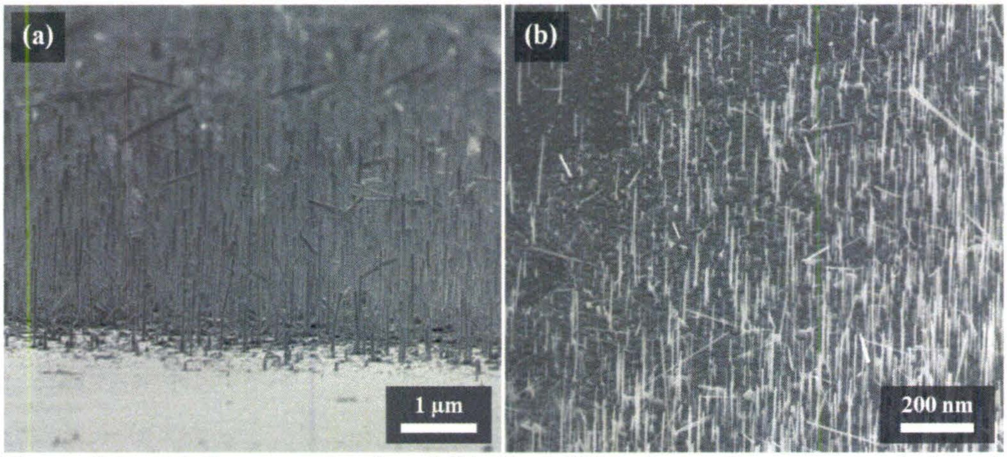

Figure 4.4 – (a) Cross-sectional and (b) tilted SEM views of as-grown rod-shaped NWs at the peripheral regions of a Si (111) substrate.

wafers, as shown in Figure 4.3(c). Here, a curved NW is observed, with its width exhibiting a clear tapering from base to tip. Interestingly, one side of the structure is observed to have a smooth sidewall structure, while the opposite side demonstrates a step-wise faceted morphology with step lengths on the order of tens of nanometres. As seen in the TEM image, the step size decreases from base to tip, in proportion to the NW diameter. Based on tilted-view and cross-sectional SEM imaging, an example of which can be seen in Figure 4.2(b), it was distinguished that for all NWs grown with such curved morphologies, the step-wise facetted side was the side exposed to the incident adatom flux during growth, while the smooth sidewall always faced the substrate. Although the nature of the growth mechanism associated with such morphologies is currently unknown, similar structures have been observed upon chemical vapour deposition (CVD) synthesis of Si/Ge NW systems [187]. In this example, the authors attributed the surface roughening to dislocation-mediated strain relaxation within Si shell layers,

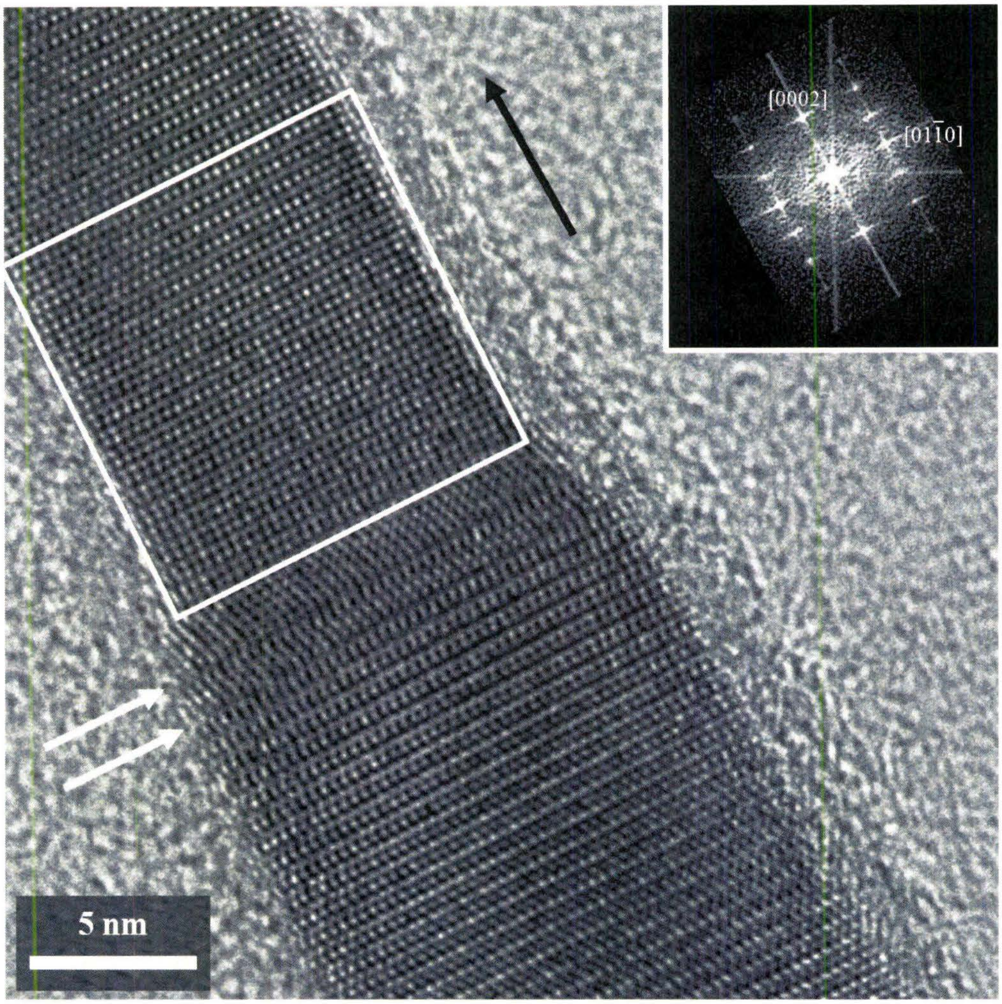

Figure 4.5 – HR-TEM image of single NW showing the distinctive ABABAB atomic layer stacking sequence of the wurtzite crystal with intermittent zincblende stacking fault insertion. The white arrows show the locations of stacking faults, whereas the black arrow points towards the NW tip. The white box outlines a region from which the fast Fourier transform (FFT) shown in the inset was obtained. The FFT in the inset is characteristic of the hexagonal wurtzite structure.

which were lattice-mismatched with respect to Ge core segments. However, in the present study, the surface roughening is strictly isolated to only one side of the NW structure, while the homo-epitaxial relationship between the axial growth and sidewall growth regions rules out the potential for lattice-mismatch associated strain relief.

Finally, the NW crystalline structure was examined through analysis of single NW specimens. Figure 4.5 shows an HR-TEM image of a single 'pencil'-shaped NW, with the black arrow indicating the growth direction. Here, the atomic layer stacking sequence is observed to be of the ABABAB type, indicative of the hexagonal wurtzite crystal structure, as discussed in Section 3.2. Furthermore, as indicated by the white arrows, disruption of the wurtzite stacking arrangement occurs by transformation of the stacking sequence to the ABCABC configuration, indicative of zincblende layers. As before, this polytypic transformation in an otherwise wurtzite crystal is characterized as a stacking fault. Throughout the length of all NWs examined, the presence of stacking faults was regularly observed. The hexagonal wurtzite structure, however, was the dominant structure in all cases. This is evident by the characteristic wurtzite fast Fourier transform (FFT) pattern obtained from the region indicated by the white box in Figure 4.5, and shown in the inset. Therefore, as in the case of NWs discussed in Chapter 3, GaAs NWs grown on Si substrates also exhibit a predominant hexagonal crystal structure, with growth along the [0001] direction, and intermittent zincblende stacking fault insertions.

4.3 – Growth of GaAs Nanowires on Stainless Steel Foils

4.3.1 – Experimental Details

Stainless steel foils, supplied by Goodfellow Manufacturing (Cambridge, England), were used as mechanically flexible substrates for the growth of GaAs NWs. For the optimization of Au nanoparticle formation on the metal foils, a series of deposition and annealing tests were conducted. First, the stainless steel foils, having thickness of 125 μm, were diced to dimensions of approximately 10 × 5 mm^2, matching the dimensions of the molybdenum sample holder employed for MBE growth. Next, through electron-beam evaporation, Au films of thickness 10 Å, 20 Å, 40 Å, and 80 Å were deposited on 4 different metal foil samples, respectively, as monitored by a quartz crystal thickness monitor The Au coated samples were then subjected to a rapid thermal annealing (RTA) process, under N_2 flow, for 10 min at a temperature of 550 °C, for the dissociation of the Au film and formation of Au nanoparticles.

The annealed films were then imaged using a JEOL JSM-7000 F scanning electron microscope (SEM), operating under low accelerating voltage conditions in backscattered electron (BSE) mode, for enhanced contrast between Au seeds and steel substrate. The purpose of this procedure was to directly image the density, average diameter, and average pitch of the Au nanoparticles resulting from Au films of varying thickness. These results are summarized in Table 4.1

Table 4.1 – Summary of results from Au-film annealing studies.

Film Thickness (Å)	**Nanoparticle Density (μm^{-2})**	**Average Nanoparticle Diameter[a] (nm)**	**Average Pitch[b] (nm)**
10	47	33.74	81.54
20	94	19.62	80.48
40	87	47.68	96.41
80	36	61.46	136.73

[a] Representative of 100 nanoparticle sample populations.

[b] Pitch is defined here as the distance from nearest neighbouring nanoparticle.

Clearly, the optimization results indicated that the highest density of smallest particles resulted from an RTA treatment of the 20 Å thick Au film. In all cases, the observed average nanoparticle pitch was suitable for the prevention of significant NW fusion or merger effects, brought about through direct contact of adjacent NWs upon sidewall growth. The critical pitch, beyond which NW merging effects were observed to transpire, was defined as 37 nm, based on previous analysis of GaAs NWs grown on Si (111) substrates. The diameter and pitch results shown in Table 4.1 represent measurements from sample populations of 100 nanoparticles.

For NW growth, the RTA treated stainless steel foils with surface decorated Au nanoparticles were loaded in the GS-MBE systems, discussed in Section 2.1, held by a customized molybdenum holder housing 6 samples. Cleaved Si pieces were positioned on the backside of the thin metal foils to secure them in place inside the sample holder windows. After reaching the growth temperature of 550 ˚C, under an As_2 overpressure, growth was initiated by opening the shutter to the Ga effusion cell. The growth rate, V/III flux ratio, and growth duration were adjusted to 1 μm/hr, 1.5, and 30 minutes, respectively Growth was terminated by closing the Ga cell shutter and the samples were allowed to cool to 350 ˚C under a constant As_2 flux. After growth, the as-grown samples were imaged using the JEOL JSM-7000 F SEM system, operated in secondary electron (SE) imaging mode at moderate accelerating voltages (5 – 10 kV).

4.3.2 – Results and Discussion

Imaging of as-grown samples demonstrated the synthesis of randomly aligned NWs with tapered morphologies on the stainless steel surface of the substrates. The random alignment can be attributed to either the random surface orientation of the substrate grains or to a non-epitaxial growth relationship between the substrate and assembled NWs. Pre-growth analysis demonstrated definitive surface roughness with faceted grain features, as exemplified by the plan-view SEM image shown in Figure 4.6(a). In previous studies we have determined that NWs grow preferentially along the [0001] direction and that their orientation relative to the substrate surface is a function of the orientation and periodicity of the latter Given that the surface of the stainless steel foils demonstrated no long range periodicity but, rather, a random configuration of polycrystalline grains, it is expected that the orientation of NWs grown on this

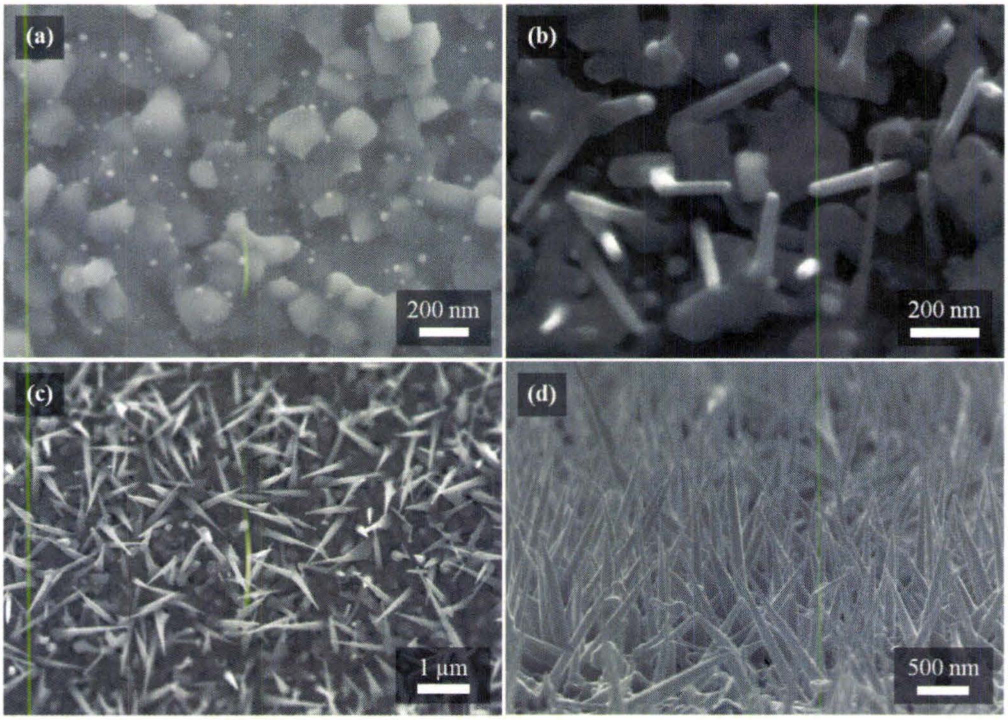

Figure 4.6 – (a) Plan-view SEM image of Au nanoparticles on the surface of a stainless steel foil substrate, prior to growth, demonstrating the granular surface structure. Plan-view SEM image of as-grown NWs (b) at sample edge region and (c) at the central sample region. (d) Cross-sectional view SEM image of as-grown NWs, obtained from central sample region.

surface is also random. It is currently unclear whether or not the substrate provides epitaxial guidance. Further TEM analysis is required in future works to resolve this matter.

Figure 4.6 also shows SEM images of the as-grown NW samples. In Figure 4.6(b), the shadowed sample edge is shown, demonstrating rod-shaped NW geometries. As mentioned in the previous section, this exemplifies the early stages of growth, before the critical NW length is reached. Furthermore, in Figure 4.6(b), the growth direction of the NWs, relative to the orientation of individual surface grains can be seen. Figure 4.6(c) and (d) show plan-view and cross-sectional view images, respectively, representative of the central regions of the as-grown samples. Here, a disparity it observed between the density of NWs grown and the density of nanoparticles observed on the surface prior to growth. Indeed, a lower density of NWs (14 μm^{-2}) was measured after growth. Furthermore, from high-magnification SEM imaging, an average Au-diameter of 41.42 nm was measured at the NW tips, versus 19.62 nm prior to growth. These discrepancies are attributed to the coalescence of Au nanoparticles, due to surface migration, at the stage of the growth sequence prior to the opening of the Ga shutter.

Growth of one-dimensional nanostructures on metal foils for flexible device applications have been previously reported by several groups. Boa et al. have presented the synthesis of bismuth sulphide nanowires through solution-based methods on tungsten sheets [188]. The growth of niobium oxide nanowires on niobium foils through oxygen plasma treatments has been demonstrated by Mozetic and colleagues [189]. The hydrothermal reaction between lead and tellurium powder has been shown to allow for the growth of lead telluride nanowires on lead foils, by Zhang et al [190]. Umar et al. have presented the fabrication of ZnO nanowires on aluminum foils achieved through the thermal evaporation of zinc powder in the presence of oxygen [191]. The wet oxidation of copper films has been shown to lead to the formation of CuO nanowires on Cu foils by Xu and colleagues [192]. Also, the VLS-based growth of Si NWs on stainless steel foils has been shown by Tsakalokos et al. [52]. However, to the author's knowledge, no reports have been made to date on the growth of III-V NWs on metal foils. The proof-of-concept demonstration and preliminary results on the fabrication of the hybrid material combination discussed here shows the potential for a novel class of low cost, flexible opto-electronic devices employing GaAs NWs as the active medium. Routes for the extension of the current work towards that end are presented in Chapter 6.

4.4 – Growth of GaAs Nanowires on Glass Substrates with Polycrystalline Si Buffer Layers

The research presented in this Section represents a collaborative effort between the Department of Engineering Physics, at McMaster University, and the Photonic Silicon Department of the Institute of Photonic Technology (IPHT), in Jena, Germany. Substrate fabrication and buffer layer processing was conducted at IPHT, by Dr. Fritz Falk and colleagues. Surface treatment, pre-growth sample processing, post-growth characterization, device fabrication, and device testing were performed by the author, at McMaster University. The details and discussion related to device fabrication and testing will be presented in Chapter 6.

4.4.1 – Experimental Details

Borosilicate glass (Schott borofloat 33) samples, received from IPHT-Jena, were employed as substrates for growth of GaAs nanowires (NWs). The glass substrates were coated by a SiN layer of approximately 70 nm thickness and encapsulated with laser diode crystallized Si layers. Two distinct sample sets were received with Si buffer layers of 200 nm and 400 nm thicknesses, henceforth referred to as groups A and B, respectively. The laser crystallization process applied to the substrates allowed for the formation of grains in the Si layer with lateral extent on the order of several tens of microns. The buffer layers of both sample groups were highly p-doped with boron to dopant concentrations of approximately 1×10^{19} cm^{-3}.

The glass substrates were first segmented into 10×5 mm^2 sections, corresponding to the area of the sample holder associated with the growth system, using a dicing saw equipped with diamond blades. The segmented glass substrates were next subjected to a two step wet etching process for the removal of the native oxide of the buffer layer. This consisted of a 30 s treatment in 5 % diluted buffered HF, followed by rinsing in de-ionized water, and subsequent dipping in 2 % diluted buffered HF for H-passivation of the surface. The samples were then loaded in an electron beam evaporation system for the deposition of a 40 Å-thick Au layer. The Au coated substrates were transported in ambient and loaded in a gas-source molecular beam epitaxy (GS-MBE) system for NW growth.

Prior to the initiation of the growth sequence, a 15 minute degas procedure was carried out at 300 °C, followed by an inductively coupled hydrogen plasma treatment at 575 °C, for 10 minutes, under a constant As_2 flux. This step allowed for the formation of Au nanoparticles which then acted as collection agents for gas-phase adatoms upon the commencement of growth. Nanowire growth was initiated by opening the shutter of the Ga effusion cell, and terminated after 30 minutes, by closing the shutter. The NWs were doped with Be for the first 7.5 minutes of growth and with Te for the final 17.5 minutes of growth, allowing for the formation a p-n junction within each NW, with a core-shell architecture. The

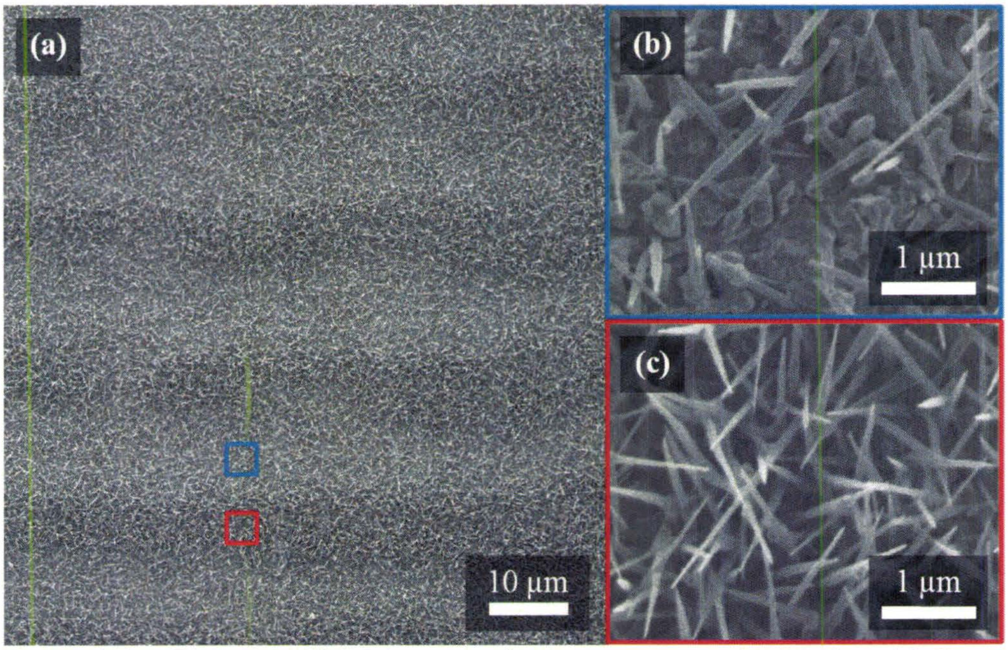

Figure 4.7 – Plan-view SEM images of as-grown group A sample. (a) Low-magnification view showing regions of sparse NW growth (bright contrast) and regions of dense NW growth (dark contrast), confined to horizontally striped zones. (b) Region of sparse NW growth, representative of segment shown in (a) as a blue bordered window. (c) Region of dense NW growth, representative of segment shown in (a) as red bordered window.

dopant concentrations were maintained at 5×10^{18} cm^{-3} and 4×10^{18} cm^{-3}, for Be and Te levels, respectively. The growth conditions were kept constant for both group A and B samples; namely, a growth temperature of 575 °C, a nominal growth rate of 1.5 μm/hr, and V/III flux ratio of 1.5. Upon growth termination, the samples were cooled under an As_2 flux. Preliminary investigations of as-grown samples involved imaging conducted with a JEOL JSM-7000 F SEM system, operated in secondary electron (SE) mode at low accelerating voltages (< 2 kV).

4.4.2 – Results and Discussion

Group A samples, those containing a 200 nm thick Si layer, were observed to accommodate NW growth with non-uniform density across the entire sample surface. As evidenced by the planar SEM image shown in Figure 4.7(a), dense NW growth was confined to "striped-regions" on the sample surface with lateral extent on the order of 10 μm. Sparse NW growth was observed between these regions. Figures 4.7(b) and (c) show the regions of sparsely and densely packed NW growth on group A samples, respectively. Although the details are unknown, the stripes are anticipated to result from the laser crystallization process of the Si layer. It is unclear whether Au nanoparticles preferentially assemble along these striped regions prior to the start of NW growth, or whether the Au is evenly distributed but NWs grow preferentially in certain recrystallized stripes. Additional surface analysis and optimization of the laser crystallization method would be required if this particular substrate were to be employed for future device applications.

In contrast, group B samples, those containing a 400 nm thick buffer layer, allowed for dense NW growth across the entire sample surface. Figure 4.8(a) shows a plan-view SEM image obtained from an as-grown group B sample, while Figure 4.8(b) shows a cross-sectional view of the same sample. Here, the epitaxial relationship between the buffer layer and NWs can be discerned, as NW orientations are noted to vary across different segments, corresponding to the

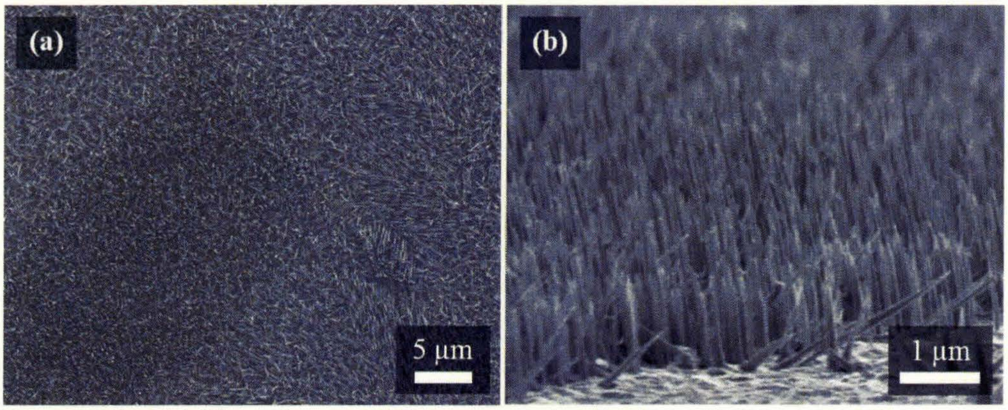

Figure 4.8 – (a) Plan-view and (b) cross-sectional view SEM images of as-grown group B samples of GaAs NWs on glass substrates with polycrystalline Si buffer layers.

distinct surface orientation of individual grains comprising the polycrystalline surface. The NWs were grown with a tapered morphology, having lengths up to 3 µm and approximate full-width at half-length dimensions of 100 nm.

In Chapter 6, the use of the group B samples in the fabrication of NW-based solar cells is presented, along with preliminary performance results and methods for the optimization of the device structure in future research efforts.

4.5 – Growth of GaAs Nanowires on Carbon-Nanotube Composite Films

In this Section, we explore the fabrication of a novel nano-hybrid material system and demonstrate its potential for applications in flexible opto-electronic devices. Metal particle-assisted coaxial p-n junction GaAs NWs were grown on flexible films composed of single-walled carbon-nanotubes (CNTs). The preparation of Au-functionalized CNT films was carried out by Dr. Gregor Lawson, under the supervision of Dr. Alex Adronov (Department of Chemistry, McMaster University). Scanning electron microscopy analysis of CNT composite films and as-grown NW samples was conducted by both Dr. Lawson and the author. Sample preparation, imaging, and analysis of results related to transmission electron microscopy experiments, along with device fabrication and testing were carried out by the author. Optical characterization, through micro-photoluminescence spectroscopy, was conducted by Dr. Christophe Couteau and the author, under the supervision of Dr. Gregor Weihs (Institute for Quantum Computing, University of Waterloo). This work is presented here as previously published in Ref. [119].

4.5.1 – Introduction

Throughout the last decade, carbon-nanotubes (CNTs) and semiconductor nanowires (NWs) have reached the forefront of the nanometre-scale materials sciences by offering novel device architectures and applications that take advantage of their unique material properties [193]. The motivations for the wealth of research conducted in relation to NW growth, characterization, and device applications have previously been considered in Chapter 1. The field of CNT-related research has also garnered tremendous interest, partly on account of the novel electronic device applications in which they can be employed.

In particular, CNTs have been noted for their remarkable conductivity [193] and thermal stability [194-196]. Furthermore, routinely practiced, cost-effective, room-temperature methods can be exercised in the fabrication of thin-films composed of single-walled CNTs, including spin-coating [197], casting [198-200], spraying [201, 202], Langmuir-Blodgett film formation [203], layer-by-layer (LbL) assembly [204, 205], electro-deposition [206], and vacuum filtration [207-211]. Such CNT composite films demonstrate electrical conductivity and optical transparency comparable to conventional transparent conductors such as indium-tin-oxide (ITO) [212], while simultaneously offering enhanced mechanical flexibility [198]. Consequently, the use of CNT films, as alternatives to ITO, has attracted particular interest in relation to specific opto-electronic device applications, such as light-emitting diodes (LEDs) [213-216] and photovoltaic cells [217-219]. Carbon-nanotube sheets have also been reported to behave as p-type Ohmic contacts within GaN-based LEDs, with contact resistances lower than conventional metallic contacts [220]. This unique combination of properties renders CNT thin films excellent candidates for use as flexible conductive substrates for the growth of semiconductor NWs. Although CNTs have been demonstrated as templates for the assembly of various supplementary nanostructures [221-223], little consideration has been made, to date, with regard to their integration with single crystalline semiconductor NWs, over macroscopic scales.

Lawson et al. recently reported a simple method for the preparation of single-walled nanotube (SWNT) thin films decorated with Au nanoparticle clusters [224]. In this work, SWNTs functionalized with highly branched poly(ethylene imine) (PEI) were shown to exhibit impressive aqueous solubility, allowing for the formation of homogeneous thin films by vacuum filtration. Incubation of PEI-functionalized SWNT films in $HAuCl_4$ solution resulted in the formation of Au nanoparticle clusters in high density upon the film surface. In this section, we report the employment of this procedure in the preparation of conductive SWNT films, functionalized with Au nanoparticles, that are demonstrated as suitable substrates for the assembly of III-V semiconductor NWs, according to the vapour-liquid-solid (VLS) mechanism, in a gas source molecular beam epitaxy (GS-MBE) system. Whereas the heteroepitaxial growth of NWs on Si and ITO-coated substrates over large areas has been established [34], the use of CNT composites as the growth surface has hitherto remained unexplored. This work, therefore, represents the first union between the characteristic opto-electronic benefits of GaAs NWs and the inherent flexibility and conductivity offered by CNT films.

4.5.2 – Experimental Details

All Au-functionalized CNT composite films utilized in the current work were prepared according to the vacuum filtration method, described in depth in Ref. [224], the details of which will not be further explored here. For NW growth preparation purposes, traces of remnant $HAuCl_4$ were removed in a dilution bath from the Au-nanoparticle decorated CNT films, which were subsequently dried under nitrogen, removed from the Teflon membrane support on which they had been fabricated, and transferred, Au-nanoparticle side up, to Si wafers, having dimensions of approximately 1 cm^2. The films were then subjected to a rapid thermal annealing (RTA) treatment at 550 °C for 10 minutes, under nitrogen ambient.

For the purposes of this study, two distinct NW architectures were grown, henceforth referred to as NW groups A and B, both of which were grown at a temperature of 550 °C, under a V/III flux ratio of 1.5, and with a nominal planar growth rate of 1.5 μm/hr. Group A NWs were strictly composed of nominally undoped GaAs, while group B NWs were composed of p-n junction core-shell heterostructures. The core-shell structures consisted of an n-doped GaAs core surrounded by a p-doped GaAs shell. For the group A sample, nominally undoped NWs were grown for 30 minutes. In the case of the group B sample, a primary GaAs layer was grown over a 15 minute period, nominally n-doped with Te to a concentration of 10^{18} cm^{-3}. Next, a secondary GaAs layer was deposited for 15 minutes, nominally p-doped with Be to a concentration of 10^{18} cm^{-3}.

Doping concentrations were calibrated using previous depositions of GaAs epilayers on GaAs (100) substrates. For both group A and group B NWs, the growth was terminated, after a total period of 30 minutes, by closing the shutter to the Ga cell and allowing the samples to cool down from the growth temperature under an As_2 overpressure.

The orientation, morphology, and density of the as-grown samples were investigated using a JEOL JSM-7000 F scanning electron microscope (SEM) and a Zeiss SMT NVision40 SII CrossBeam microscope, in secondary-electron mode. The latter, equipped with focused ion beam (FIB) capability, was used in the preparation of lamellae for cross-sectional transmission electron microscopy (TEM) using a Philips CM12 microscope and a JEOL JEM 2010F high-resolution transmission electron microscope (HR-TEM). For analysis of a single NW specimen, the as-grown samples were subjected to a 60 second ultra-sonication process in a small volume of de-ionized water after which suspended NWs were deposited on a holey carbon-coated copper grid. Similarly, single NWs were dispersed on an oxidized-Si substrate for micro-photoluminescence (μ-PL) characterization in a continuous flow helium cryostat at 7 K. Excitation was provided using a laser centered at 532 nm at a power of 80 μW. Excitation and μ-PL collection were achieved through an objective allowing for an excitation spot of roughly 2 μm diameter. PL was resolved by a 75 cm grating spectrometer and detected by a liquid nitrogen-cooled Si charge-coupled device camera.

4.5.3 – Results and Discussion

Planar SEM images of SWNT-Au composite films before and after the RTA treatment are shown in Figure 4.9(a) and (b), respectively. Thermal annealing of PEI-functionalized SWNT films induces decomposition of the functional groups attached to the surface of the CNTs and results in partial restoration of the nanotube electronic structure and conductivity [225]. Furthermore, an annealing treatment ensures removal of volatile organic matter that might otherwise contaminate the MBE chamber used for semiconductor NW growth. Following this treatment, irregularly shaped Au-nanoparticle clusters were found to re-form into smaller, discrete nanoparticles having an average diameter of approximately 38 nm, as shown in Figure 4.9(b).

Analysis of as-grown group A samples through SEM experiments demonstrated dense NW growth over the entire span of the Au-functionalized SWNT films. Example of such SEM images are shown in Figure 4.10. Similar results were obtained from the group B sample. In comparison to the vertically oriented growth of NWs on Si (111) or GaAs (111)B substrates [116, 95], NWs grown on SWNT substrates were observed to be oriented in a variety of angles with respect to the growth surface. This can be understood by considering the well-established premise that NWs preferentially assemble in the thermodynamically favourable <0001> or <111> directions, for wurtzite and zincblende crystal structures, respectively [116, 97]. However, in the case of the

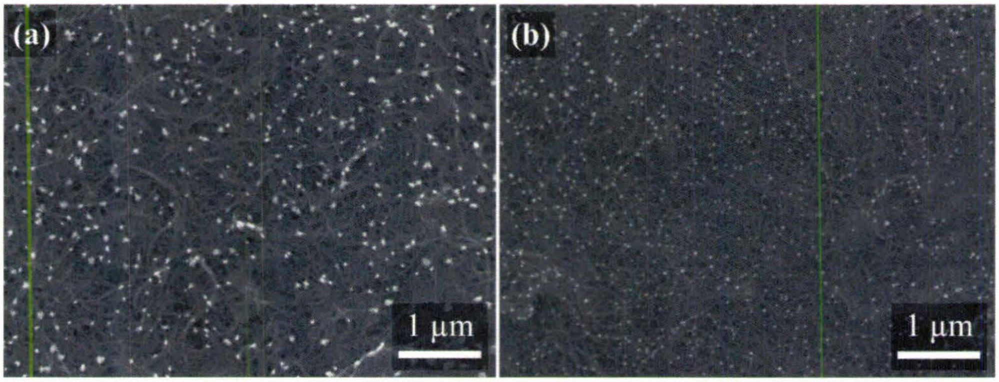

Figure 4.9 – Plan-view SEM images of Au-functionalized CNT composite film surfaces (a) before and (b) after a 10 min. RTA treatment at 550 °C. Regions of bright contrast indicate locations of (a) Au-nanoclusters and (b) Au-nanoparticles.

present study, the growth surface lacks long range spatial periodicity, which is necessary for epitaxial orientation of the NWs, due to the random stacking arrangement of single-walled CNTs in the composite film.

Predominantly, both group A and group B NWs were of characteristic tapered or "pencil-shaped" morphologies, with heights up to 2.5 μm and average full-width at half-length diameters of roughly 100 nm. The tapered NW morphology is attributed to sidewall diffusion-limited radial growth, as previously reported [95]. The simultaneous occurrence of layer-by-layer radial deposition and Au-nanoparticle-based axial growth results in the core-shell architecture of the NWs. A two-dimensional GaAs film, formed concurrently with the NWs, is evident in Figure 4.10(b), above the SWNT substrate. Prior growths on single crystalline Si substrates indicated two-dimensional film thicknesses of 120 nm, as discussed in Section 3.2. In comparison, the present growth resulted in the deposition of a planar film with average thickness of approximately 250 nm,

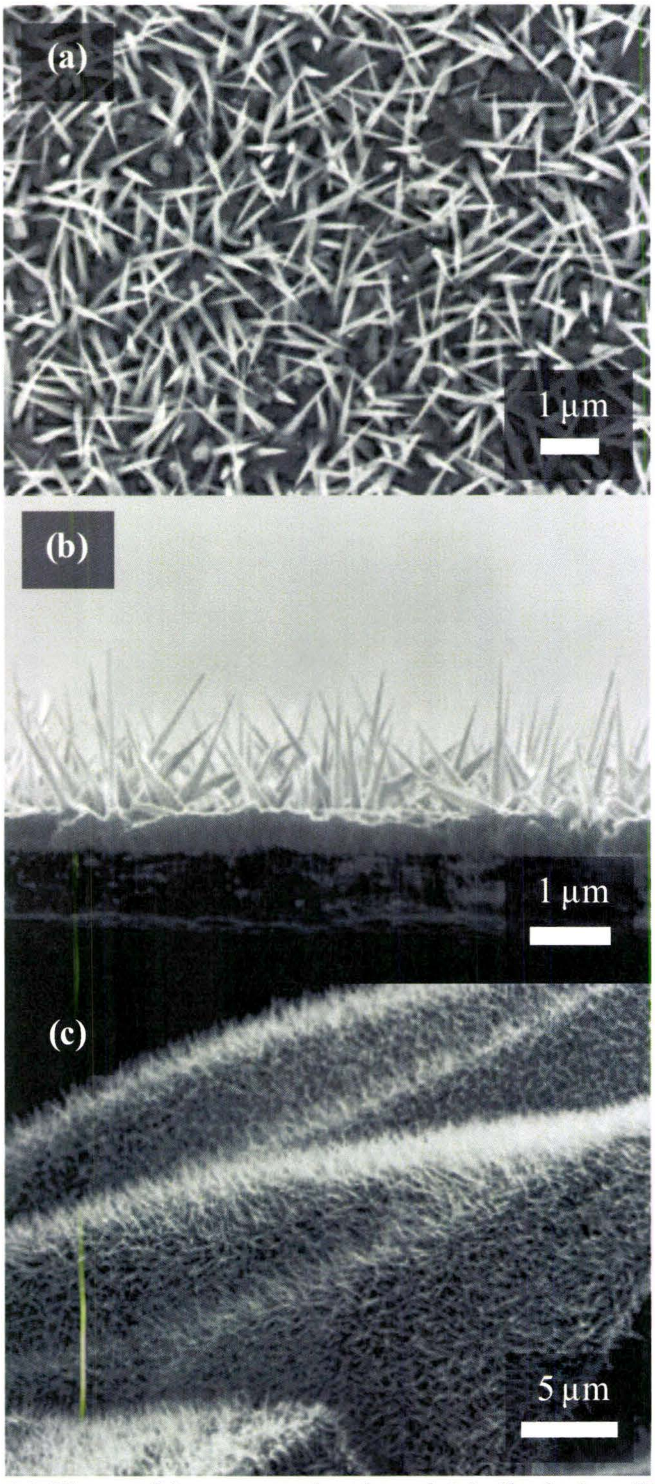

Figure 4.10 – (a) Planar, (b) cross-sectional, and (c) tilted-view SEM images of as-grown samples containing GaAs NWs on CNT composite films.

likely as a consequence of shorter adatom diffusion lengths on the rough surface of the CNT composite films.

Figure 4.10(c) shows a tilted SEM view of an area specifically manipulated to demonstrate the flexibility of a SWNT film containing NWs. It is particularly remarkable that the NWs studied in this project maintained their structural integrity after bending, contorting, rolling, and folding of the underlying flexible substrate, over macroscopic scales.

Structural analysis of numerous nanowires from both the group A and group B samples was carried out by TEM analysis. Figure 4.11(a) shows a TEM image of a NW that is representative of the structure and morphology of practically all group A NWs grown on the CNT films. Figure 4.11(b) reveals a magnified image of the identical NW in Figure 4.11(a). Similar results were obtained for the group B nanowires. Contrast stripes intersecting the NWs indicated the presence of intermittent stacking faults. A selective area diffraction pattern obtained on the <2-1-10> zone axis of a defect-free NW segment, shown in the inset of Figure 4.11(a), confirmed a wurtzite crystal structure with wires growing along the <0001> direction. Consistent with previous experiments involving hetero- and homo-epitaxially grown NWs [116, 164], the stacking faults studied in the present case appeared as atomic layers arranged in a zincblende structure, amongst defect-free wurtzite segments. The Au-nanoparticle at the NW tip provides evidence for growth according to the VLS mechanism.

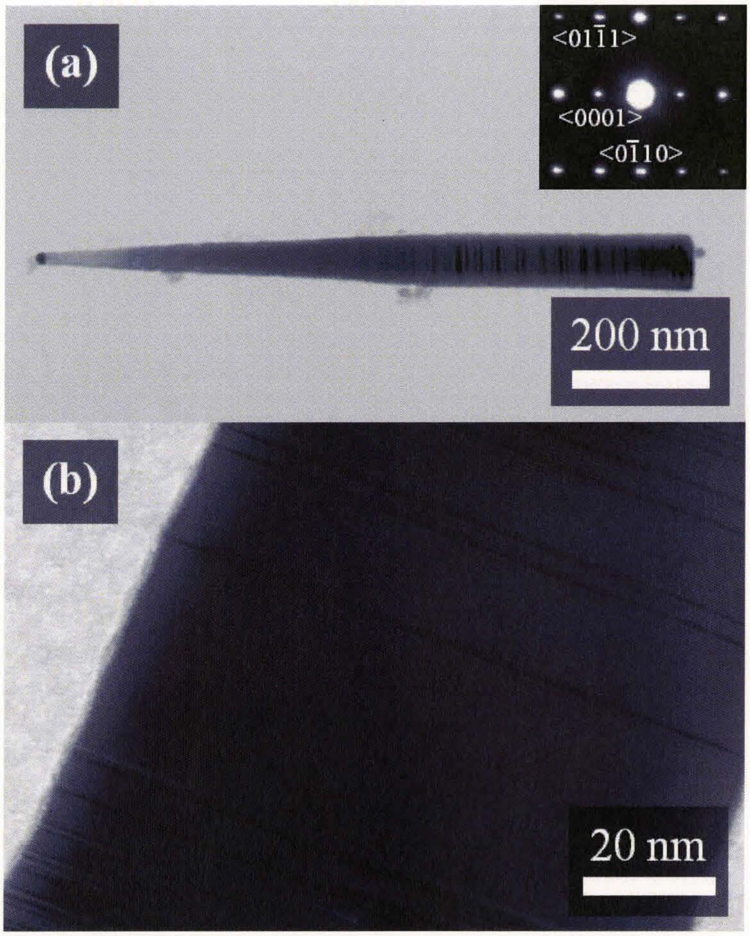

Figure 4.11 (a) TEM image of a single group A NW Inset shows a SAD pattern obtained from the same NW, indicative of the wurtzite structure and <0001> growth direction. (b) Magnified TEM view of stacking faults visible along the NW length.

A point of interest is the nature of the growth surface. Due to the simultaneous deposition of a GaAs film during NW assembly, the NW/CNT interface becomes buried during the growth process. To investigate the NW/CNT interface, thin lamellae were prepared via FIB, allowing for the analysis of small cross-sectional windows where the internal NW structure, GaAs film, and CNT-composite substrate can be examined in a single specimen. In Figure 4.12, a TEM

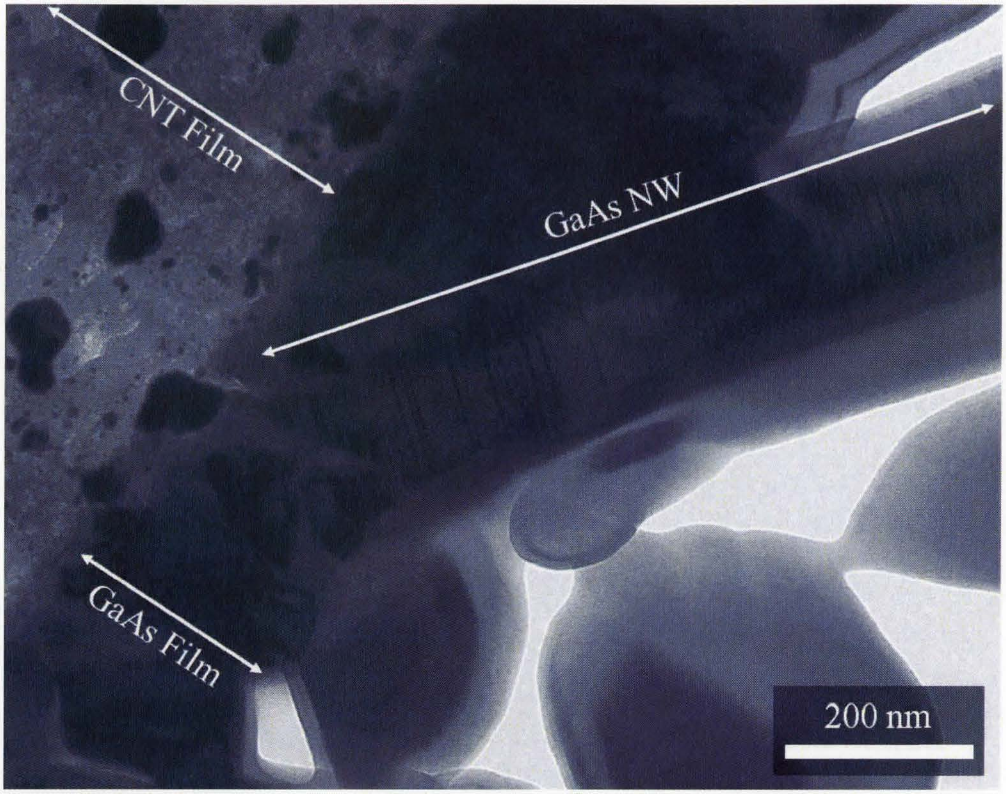

Figure 4.12 Cross-sectional TEM image of interfaces formed between NW, GaAs film, and CNT substrate. The extension of stacking faults within the GaAs film, localized to the lateral extent of the visible NW, indicates NW growth from the CNT surface.

image is shown of a lamella removed from the as-grown sample. The coating surrounding the NW in Figure 4.12 is simply a carbon layer deposited during the sample preparation, as a protective envelope. Stacking faults can be seen throughout the entire length of the NW including the portion buried within the planar GaAs film. This observation leads to the argument that the initial NW nucleation process occurred at the CNT Au interface. As the diameter of the Au nanoparticles is considerably greater than that of a single CNT, each nanoparticle is located upon a unique site which spans several randomly oriented underlying

CNTs. Although the initial GaAs island nucleation can occur over a single CNT, the formation of the initial GaAs layer at the CNT/Au interface, nonetheless, extends over multiple CNTs. Therefore, although Figure 4.12 indicates an intimate contact of the GaAs nanowires to the CNT films, it remains unclear, at present, whether growth is epitaxially initiated. Additionally, a GaAs film grows simultaneously between the NWs, but appears to play a negligible role in the NW growth process. Due to the intimate contact between the NWs, planar film, and CNTs, the role of the planar GaAs layer is of importance to the electrical conduction pathways of this system, as discussed later.

Micro-photoluminescence studies were conducted on single NWs placed on SiO_2 substrates. A typical μ-PL spectrum is shown in Figure 4.13 for a group A NW. Here, a single peak with 12.5 meV line-width is obtained at 7 K, centered at 1.51 eV. The inset of Figure 4.13 shows a plot of the experimental shift in μ-PL peak energy with increasing temperature, as red data points. The expected temperature dependence of the bandgap energy is also plotted in the inset, as a solid black line, according to the Varshni relation for bulk GaAs [151]. The agreement between the measured values and the Varshni curve indicates that the PL emission may be attributed to band-to-band recombination transitions within the undoped, bulk-like, GaAs NW [151]. Agreement between the measured values and the expected trend also illustrates the high crystallinity, purity, and optical quality of the NWs, making these materials promising for use in opto-electronic device applications.

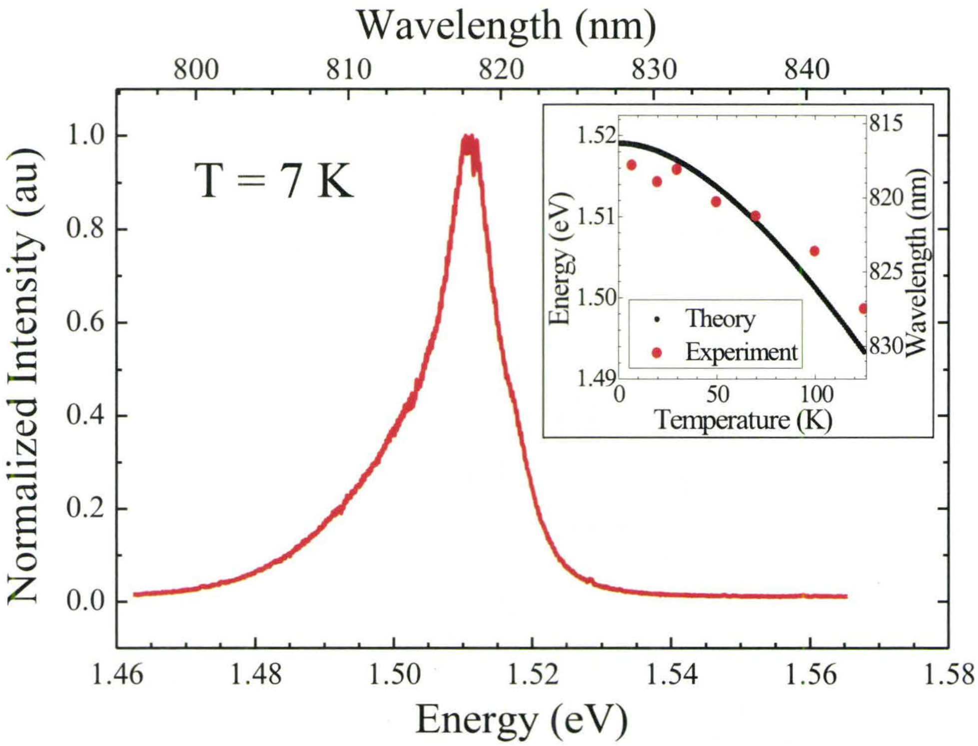

Figure 4.13 – Single NW µ-PL spectrum obtained at 7 K. Inset plots the measured PL peak energy with increasing temperature (red data points) as compared to the theoretical bulk GaAs Varshni curve (black line).

The group A and B samples were further processed for electrical characterization. The main intent in the processing procedure was to ensure intimate electrical contact with the Au-capped NW tips, while avoiding a possible short-circuit pathway through the planar growth region. SEM images of the sample, at the various processing steps employed in device fabrication, are shown in Figure 4.14. First, the entire sample was coated with a SiO_x layer (step a) formed through plasma-enhanced chemical vapour deposition (PE-CVD). This layer provides a conformal insulating shell across all NWs and the surface of the GaAs film, approximately 100 nm in thickness. Next, a polymer layer (S-1808

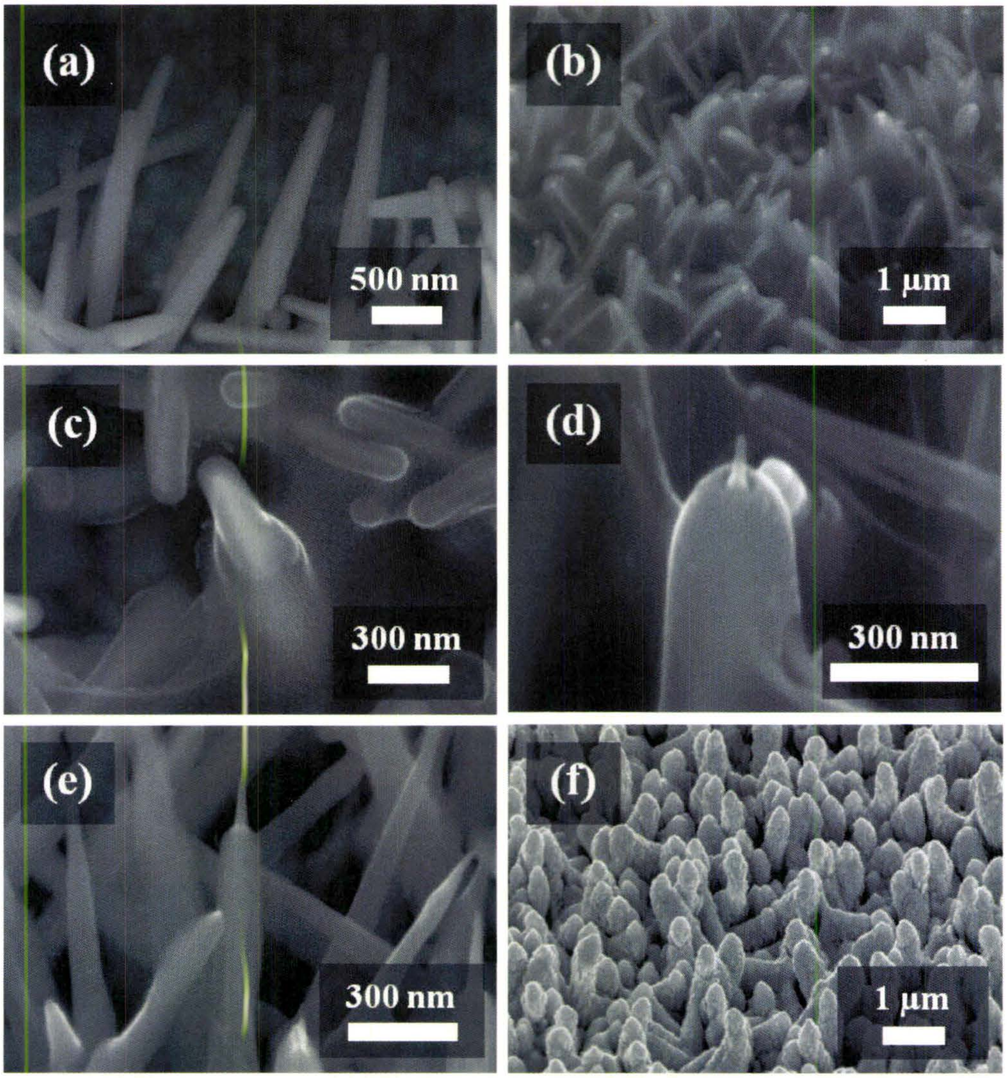

Figure 4.14 – Processing steps in device fabrication: (a) PE-CVD deposition of 100 nm SiO_x layer to coat NWs and planar growth layer. (b) Coating of oxidized NWs with spin-cast polymer (S1808 photoresist) layer. (c) Partial O_2-plasma RIE of polymer layer for exposure of oxidized NW tips. (d) Buffered HF wet etch treatment for the exposure of bare NW tips. (e) Full O_2-plasma RIE for the removal of remaining polymer layer. (f) Deposition of Ti/Pt/Au top contact, followed by RTA treatment.

photoresist) was spin-cast over the oxide-coated NWs (step b). After a 1 min oxygen-plasma reactive ion etching (RIE) treatment, the top-most layers of the spin-on-polymer were removed to expose the oxidized NW tips (step c). At this point, the sample underwent a wet etching process in a 10:1 buffered HF solution for the removal of the thin SiO_x cap at the NW tips (step d). A second, more prolonged, RIE treatment occurred next, etching the remaining photoresist from the surface of the NWs. As seen in Figure 14.4(e), after this processing step, the planar GaAs layer and the body of the NWs remained insulated by the oxide layer, while the NW tips became exposed. Thus, once a Ti/Pt/Au top contact layer was deposited (step f), the intended pathway for electron flow through the NWs to the SWNT film could be realized. Additionally, this process allows for electrical contacting of the nanowires despite the randomness in their tilt angle relative to the CNT substrate.

To study the electrical behaviour of the fabricated devices and to establish the role of Be and Te as dopants, a Ti/Pt/Au layer was deposited by electron-beam evaporation on both group A (undoped GaAs NWs) and group B (p-n junction core-shell NWs) samples. Prior to measurement, the samples were treated at 400 °C for 30 seconds, to produce an Ohmic contact at the contact/NW interface. Figure 4.15 shows the current-voltage (I-V) characteristics of a bare SWNT film (post RTA), a device fabricated using group A NWs, and a device fabricated using group B NWs, under an applied bias of -2 V to 2 V.

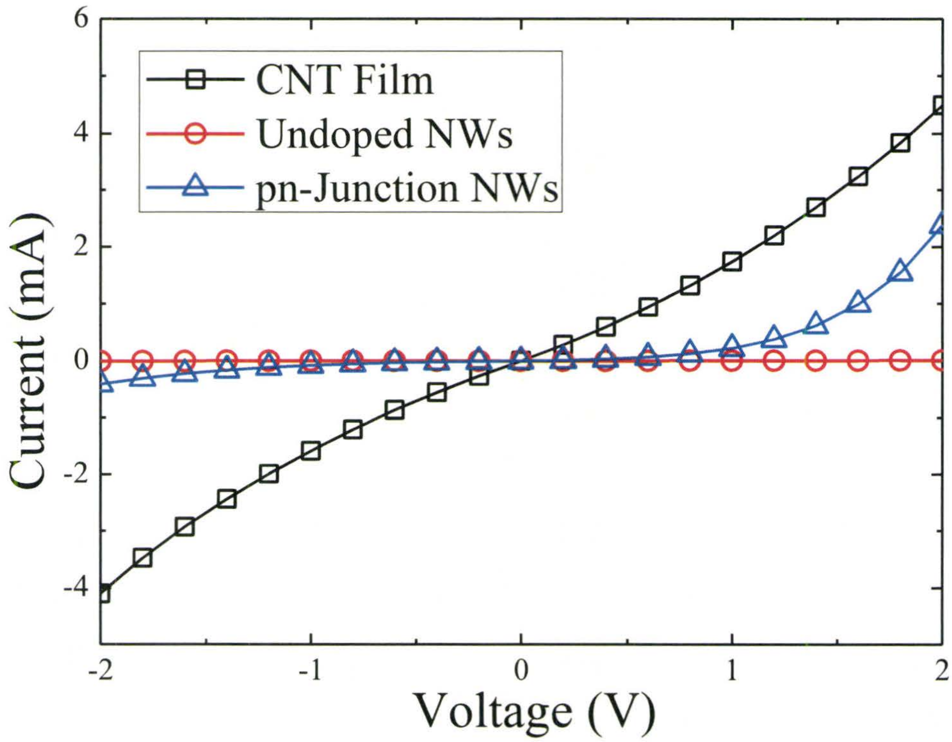

Figure 4.15 – I-V characteristics of purified CNT film, prior to NW deposition (black squares), fabricated devices containing undoped NWs (red circles), and fabricated devices containing p-n junction NWs (blue triangles). Asymmetric rectification in group B devices is indicative of diode-type behaviour from the p-n junction NWs.

It is worthy to note that the SWNT film exhibited a conductive behaviour prior to growth. From the I-V curve (square data points), CNT composite films revealed a sheet resistance of roughly 68 Ω/sq (resistivity of 6.81×10^{-3} Ω·cm) after being subjected to an annealing treatment. This value is in agreement with SWNT composite film resistances previously reported [198, 207, 226] and is comparable to sheet resistances measured in commercial ITO films [198]. The observed slight rectifying behaviour is attributed to Schottky barriers formed between the CNT film and probe tips [227]. The undoped NWs (group A samples, circular data points) demonstrated a high resistivity of roughly 5900 Ω·cm. In contrast, the curve obtained from sample B, containing p-n junction NWs (triangular data points), exhibited asymmetric rectification. Although the specific contribution of the CNT/GaAs interface quality to the electrical behaviour is currently unclear, the observation of diode-type behaviour in group B devices, while not in group A devices, demonstrated the rectifying properties exhibited by the p-n junction NWs. Similar results were reproducibly obtained from at least 15 different contacts on each sample. Furthermore, p-n junction GaAs NWs were epitaxially grown on (100) GaAs or Si substrates (which yielded wires tilted along equivalent <111> directions) or (111)B GaAs substrates (which yielded wires grown vertically from the substrate). These wires were processed and contacted in the same approach as described above, and yielded forward bias currents within the same order of magnitude as those grown on CNT composite films [228]. These results suggest similar behaviour for tilted as compared to vertically oriented NWs and, therefore, show the potential for the utilization of GaAs/CNT hybrid device architectures in a variety of applications, including flexible photovoltaics, light-emitting diodes, and sensors.

4.6 – Growth of GaAs and InAs Nanowires on Highly-Ordered Pyrolytic Graphite Substrates

The research presented in this Section represents a collaborative effort between the Department of Engineering Physics and the Department of Chemistry, at McMaster University. Equal contributions to the experimental planning of this work were made by Dr. Gregor Lawson (under the supervision of Dr. Alex Adronov, Department of Chemistry) and the author. Dr. Lawson was primarily responsible for Au nanoparticle synthesis, preparation of Au-decorated highly-ordered pyrolytic graphite (HOPG) substrates, and the corresponding surface analysis, including scanning electron microscopy. The author was primarily responsible for pre-Au deposition surface modifications and analysis of post-growth samples, including SEM, TEM, EDXS, and SAD characterization experiments.

4.6.1 – Introduction

In the previous section, we demonstrated the growth of randomly oriented GaAs NWs on thin conductive films composed of single-walled CNTs. However, with consideration of device applications, it would be ideally suited to grow NWs on conductive, flexible substrates which could provide long range surface order and epitaxial guidance, while preferentially accommodating the *vertical* assembly of NWs. Through this approach, the undesirable effects of random NW alignment, such as merging of neighbouring NWs and the lack of electrical contact to more acutely-oriented NWs, could be effectively eliminated. Furthermore, enhanced optical absorption, in the case of orthogonally aligned NW arrays, could be exploited for photovoltaics applications [46].

Thin films composed of stacked individual layers of graphene are particularly interesting potential candidates for use as flexible, conductive substrates with long range surface atomic order. Recently, tremendous progress has been achieved in the fabrication of novel opto-electronic devices, based on the integration of graphene monolayers or graphene composite films [229-233]. Graphene thin films offer similar advantages as CNT composite films including impressive mechanical flexibility, optical transparency, high electrical conductivity, and thermal stability [230, 232, 234]. Furthermore, graphene composite thin films can be fabricated through simple and low-cost procedures involving the reduction of graphene oxide [235-238]. However, the randomized stacking of individual graphene monolayers in a graphene thin film can create defect sites at the boundaries of discrete platelets and disturb the long range order of the substrate surface [238].

On account of the regular presence of such surface imperfections, it was decided to first pursue the growth of NWs on highly-ordered pyrolytic graphite (HOPG) substrates. If growth on HOPG could be easily achieved through the VLS method, then routes towards the improvement of graphene film surfaces could be examined and NW growth on the latter could conceivably be achieved. Thus, the growth of GaAs NWs on HOPG substrates was investigated as a possible intermediate step towards realizing growth on graphene composite thin films.

HOPG substrates are widely used in conventional scanning tunnelling microscopy (STM) calibration experiments, on account of their relatively defect free surfaces and conductive nature [239]. Furthermore, HOPG surfaces are chemically inert and exhibit thermal stability at typical MBE growth temperatures. Particularly, in the current study, HOPG substrates are employed due to the long-range, periodically ordered, hexagonal arrangement of their surface carbon atoms.

It has been previously demonstrated that HOPG substrates can be suitably treated as surfaces for the assembly of various nanometre-scale structures. Of particular interest are the formation of surface-parallel metallic NWs, preferentially assembled along step-edges of HOPG substrates [240, 241], and free-standing, single crystalline NWs grown on HOPG surfaces, through both seed-assisted and seed-free methods [242-246]. In this section, we present the Au nanoparticle-assisted growth of randomly aligned GaAs and InAs NWs, and the Au nanoparticle-free growth of orthogonally oriented GaAs NWs, on HOPG substrates. Several surface treatment methods are explored allowing for the foundation of a qualitative model for vertical NW assembly, based on a Ga seed-assisted growth mechanism.

4.6.2 – Experimental Details

Monodisperse Au nanoparticles (NPs) were synthesized in accordance to the well established Turkevich method, based upon the reduction of gold chloride from sodium citrate in aqueous solutions [247, 248]. Through SEM analysis of a sample population of 200 Au NPs, their average diameter was determined to be 21 ± 6 nm, where the uncertainty represents one standard deviation from the mean of a Gaussian fit. HOPG substrates were purchased from SPI Supplies and cut using a scalpel, to dimensions of approximate 10×5 mm^2, corresponding to the area of the MBE sample holder used for annealing and growth studies. As-received HOPG samples were laterally cleaved, through the conventional adhesive tape technique [249], for the preparation of clean substrate surfaces. Suspended Au NPs, in solutions of either deionized (DI) water or ethanol, were drop-cast onto freshly cleaved HOPG surfaces and allowed to dry under ambient condition while subjected to mild agitation for the reduction NP aggregation, during a period of 30 min. Next, the Au-decorated HOPG samples were dried *in vacuo* at a temperature of 50 °C for a duration of approximately 12 h.

The Au-decorated samples were then subjected to annealing tests, consisting of 10 min annealing treatment at 550 °C in a gas-source molecular beam epitaxy (GS-MBE) system. The purpose of this procedure was to determine the degree to which Au NPs coalesce, upon surface migration at standard growth temperatures. The MBE was employed in this process, such that the annealing trials would mimic the exact pre-growth conditions. Upon SEM analysis of

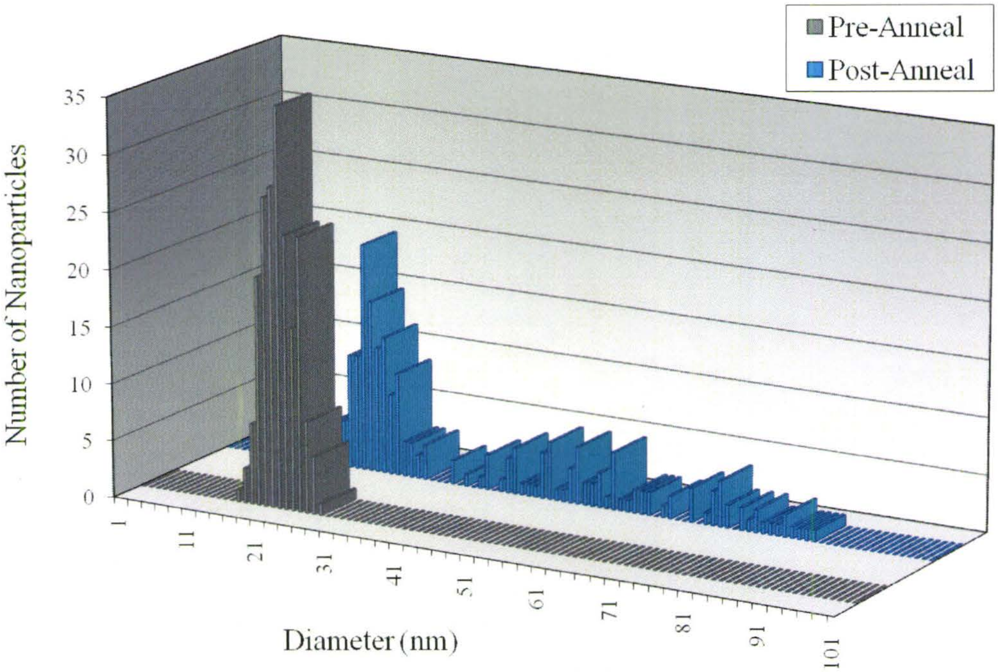

Figure 4.16 – Diameter distributions of Au NPs, deposited on HOPG surfaces, before and after an annealing treatment for 10 min. at 550 °C.

annealed samples (drop-cast from solutions of Au NPs in ethanol), once again, based upon a sample population of 200 individual NPs or clusters of agglomerated NPs, diameters ranging between 16 nm and 84 nm were observed. This observation points toward a significant coalescence of individual nanoparticles, the influence of which will be clarified in the discussion to follow. The results of pre- and post-anneal treatment diameter distributions are summarized in the histogram shown in Figure 4.16.

In the current study, 5 separate NW growths were conducted, henceforth referred to as NW groups A – E, with dissimilar pre-growth surface treatments, growth durations, growth temperatures, and material compositions. The details of the 5 NW groups are summarized in Table 4.2 and described, in turn, below.

Table 4.2 – Description growth details pertaining to NW groups A – E.

NW Group	**Growth Temperature (°C)**	**Growth Duration (min.)**	**Growth Material**	**Surface Treatment Process**
A	550	30	GaAs	Drop-cast Au NPs from DI water
B	550	15	GaAs	B_1. Drop-cast Au NPs from ethanol B_2. Ethanol treated HOPG surface B_3. Untreated HOPG surface B_4. SiO_X deposited HOPG surface B_5. RIE treated HOPG surface
C	550	15	GaAs	1 nm Ga film deposited on HOPG surface prior to growth in MBE
D	600	30	GaAs	Untreated HOPG surface
E	400	30	InAs	E_1. Drop-cast Au NPs from ethanol E_2. Untreated HOPG surface

All NW groups were composed of GaAs, with the exception of group E, which was composed of InAs. All growths were carried out at with a V/III flux ratio of 1.5 and nominal growth rate of 1 μm/hr., as determined through previous thin film deposition calibrations. Likewise, all growths were terminated by closing the shutter of the group III elemental source and allowing the samples to cool under an As_2 overpressure. Group A NWs were grown at a temperature of 550 °C for a period of 30 minutes. Surface treatment for this group involved the deposition of Au NPs, drop-cast from a dilute solution, in deionized water.

Group B NWs were grown at the same temperature as group A NWs, however, for only half the growth period. In this case, 5 different NW samples were simultaneously fabricated (samples B_1 – B_5), each having undergone a distinct surface treatment process prior to growth. Sample B_1 was surface decorated with Au NPs, dispersed on the surface from a solution in ethanol. In the case of sample B_2, an equal volume of ethanol was deposited on the surface. However, no Au NPs were contained in the volume. The purpose of the sample B_2 treatment was simply to explore whether the use of ethanol, on the surface of sample B_1, placed any discernable effect on the HOPG surface, such as surface contamination or surface layer buckling, which in turn could influence NW growth. In contrast to all other group B samples, the HOPG surface of sample B_3 was left untreated after the initial lateral cleavage step. Next, in the case of Sample B_4, an SiO_x layer of 10 nm thickness was deposited on the surface, through plasma-enhanced chemical vapour deposition (PE-CVD). Finally, sample B_5 was subjected to a 60 s O_2-plasma reactive ion etching (RIE) treatment, for the deliberate introduction of surface roughening.

Group C samples were loaded into the GS-MBE chamber with no additional surface treatment subsequent to lateral cleavage. However, prior to the initiation of GaAs growth, a 10 Å film of Ga was deposited at 550 °C. The sample was then subjected to an inductively coupled H_2-plasma treatment, for dissociation of the Ga film and the formation of a randomly distributed collection of Ga NPs. Growth was then initiated by simultaneously opening the shutters to the Ga and As_2 sources. After a growth period of 15 minutes, the group III source was terminated and the samples allowed to cool under a group V overpressure.

Group D NWs were grown under conditions identical to group A NWs. However, two major parameters were altered in this case. First, the HOPG surface was left untreated and, second, an increased growth temperature of 600 °C was employed. As discussed in Section 1.3.3, growth at higher temperatures leads to the promotion of group III adatom diffusion lengths while also inducing the enhancement of group V growth species desorption. In the case of group D NWs, the use of a higher growth temperature was intended to promote preferential Ga island nucleation.

Finally, group E NWs were grown, composed of InAs. Here, two different samples were used (E_1 and E_2), with dissimilar surface treatment processes prior to growth. Sample E_1 was surface decorated with Au NPs, dispersed from a solution in ethanol (as with sample B_1). In contrast, sample E_2 was left untreated after a pristine HOPG surface was exposed upon lateral cleavage. Growth was carried out at a temperature of 400 °C, based on the optimal growth rate of Au-assisted InAs NWs fabricated via MBE [250].

As-grown NW samples were imaged using a JEOL JSM-7000 F scanning electron microscope (SEM). Single NW specimens were investigated using a JEOL JEM 2010 F high-resolution transmission electron microscope (HR-TEM). This system was also employed in analytical TEM-based experiments including energy dispersive X-ray spectrometry (EDXS) and selective area diffraction (SAD). Site-specific sample preparation for TEM was achieved using a Zeiss SMT NVision 40 SII CrossBeam focussed ion-beam (FIB) system, according to the procedure outlined in Section 2.2.2.

4.6.3 – Results and Discussion

First, we focus on the initial series of GaAs growths, conducted on HOPG substrates, namely, those which were previously classified as group A samples. Post-growth SEM analysis of as-grown samples led to 4 main observations of interest: (1) Orthogonally oriented NWs, of rod-shaped morphologies, with maximum lengths of 2 μm were distinguished. These structures were observed to be grown in very low densities on the substrate surface, quantified by an areal density of 29 NWs per 100 μm^2. (2) NWs were observed to be situated amongst a much greater number of individual polycrystalline island formations. (3) The polycrystalline islands were noted to be seeded from facet-free formations, and grown along the substrate surface. (4) No randomly aligned NWs were distinguished.

Figure 4.17 shows 45° tilted-view SEM images, representative of the as-grown group A samples. In Figure 4.17(a), the low density of columnar NWs amongst a large collection of island formations is clearly seen, whereas Figure 4.17(b) demonstrates the direct vertical growth of a single rod-shaped NW on the HOPG surface. The NW diameter, corresponding to the extent of the tip, was measured to be approximately 60 nm.

In contrast to the NW structures, polycrystalline island formations were also observed on the sample surface. An example of such an island is shown in the 45° tilted-view SEM image, shown in Figure 4.18. Here, superimposed EDXS line-scans of Ga (red), As (green), and Au (purple) are plotted, corresponding to

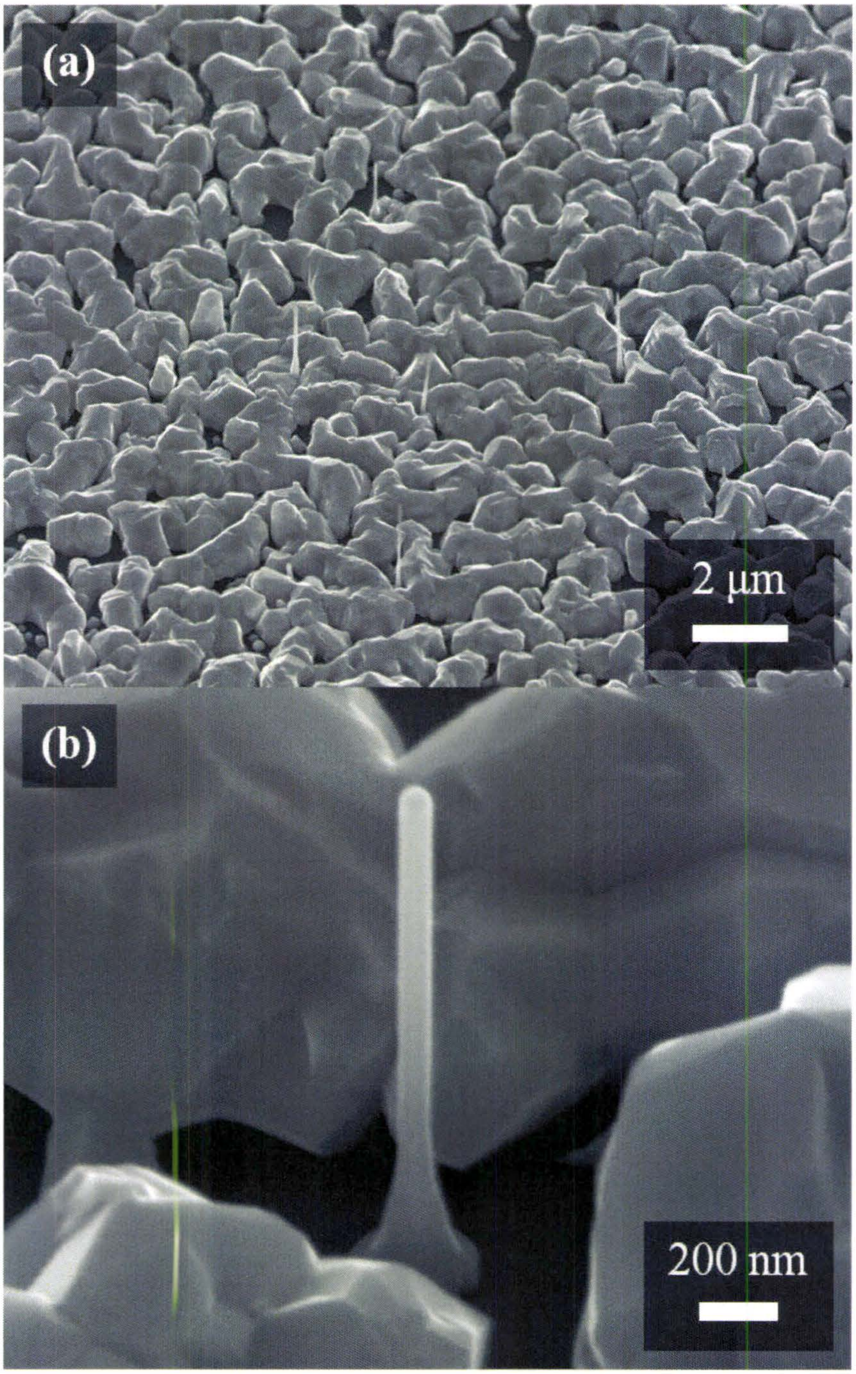

Figure 4.17 – 45° tilted-view SEM images of as-grown group A NW samples. (a) Low-magnification view demonstrating a number of sparsely situated NWs, orthogonally aligned with respect to the substrate surface. (b) Magnified view of a single NW structure, showing rod-shaped morphology and direct growth on the substrate.

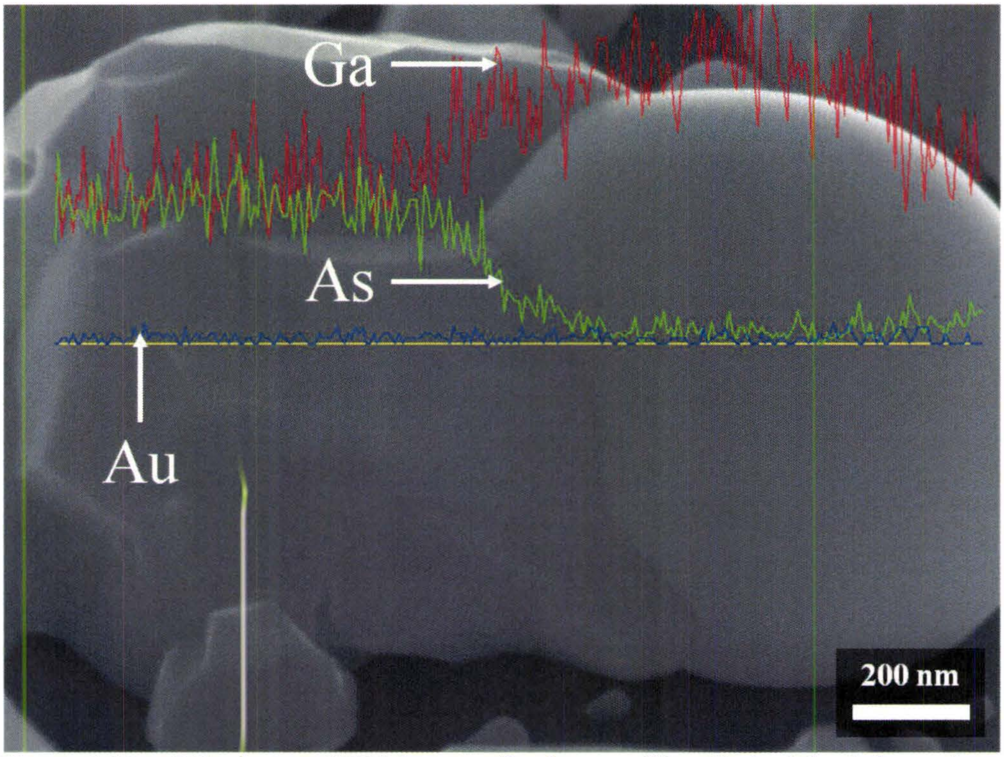

Figure 4.18 – Tilted-view SEM image of polycrystalline GaAs island formation, seeded from a large Ga particle, on an HOPG substrate, with superimposed line-scans of elemental Ga (red), As (green), and Au (purple).

the detection of characteristic X-ray counts, as induced by the primary electron (PE) beam scanned along the structure, in SEM. Here, two points of interest arise. First, scanning of the polycrystalline region of the sample exhibits equal counts of Ga and As, representative of a stoichiometric GaAs crystal. However, scanning of the facet-free or smooth structure, on the right-hand side of Figure 4.18, results in the abrupt decline of As counts and the clear increase of Ga counts. Thus, it can be concluded that the facet-free structure is a large collection of Ga, which appears to have seeded the surface growth of a GaAs crystal. The second remarkable observation is the lack of Au detection throughout the entire structure. This will be further elaborated in relation to the TEM results, in the following discussion.

Further structural analysis of single NW specimens grown on the group A samples was conducted via analytical TEM experiments. In this case, samples were prepared through the removal of lamellae from regions of interest on as-grown samples using FIB. Figure 4.19(a) shows a TEM image of a vertical NW removed from a group A sample. Higher magnification images of the NW tip, midsection, and base are respectively shown in Figures 4.19(b), (c), and (d). Starting from the base, in Figure 4.19(d), we note the atomic-layer abruptness of the interface formed by the NW and the underlying HOPG surface. Next, variations in the crystalline stacking arrangement are observed along the growth direction in Figure 4.19(c), indicative of polytypic growth; this will be considered in greater detail in a later discussion on crystal structures, based on SAD patterns obtained from the same NW. A more immediate point of interest, however, is the lack of a discernable particle at the NW tip, as observed in Figure 4.19(b).

Upon EDXS analysis of the same NW shown in Figure 4.19, it was determined that no detectable concentrations of Au were present along the NW. Rather, axial EDXS line-scans confirmed the GaAs composition of the NW, while simultaneously demonstrating an increased detection of elemental Ga at the tip. These results are illustrated in Figure 4.20, where an HAADF image of the same NW shown in Figure 4.19, with superimposed EDXS line-scans of elemental Ga (green), As (blue), C (red), and Au (purple), is represented. Starting from the NW

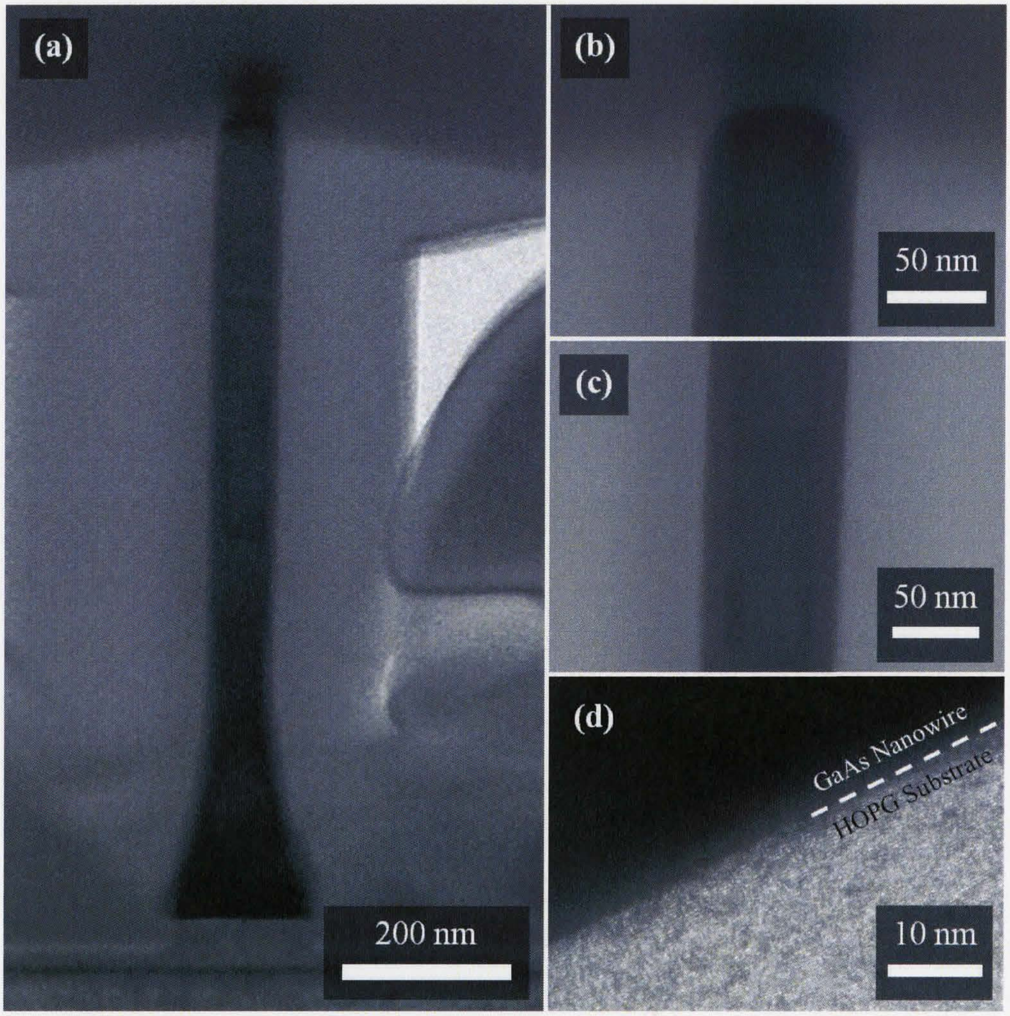

Figure 4.19 – TEM image of (a) single vertical group A NW with magnified views of taken from the same NW showing the (b) tip, (c) midsection, and (d) base. The HR-TEM image shown in (d) demonstrates the atomically abrupt interface formed between the NW and substrate.

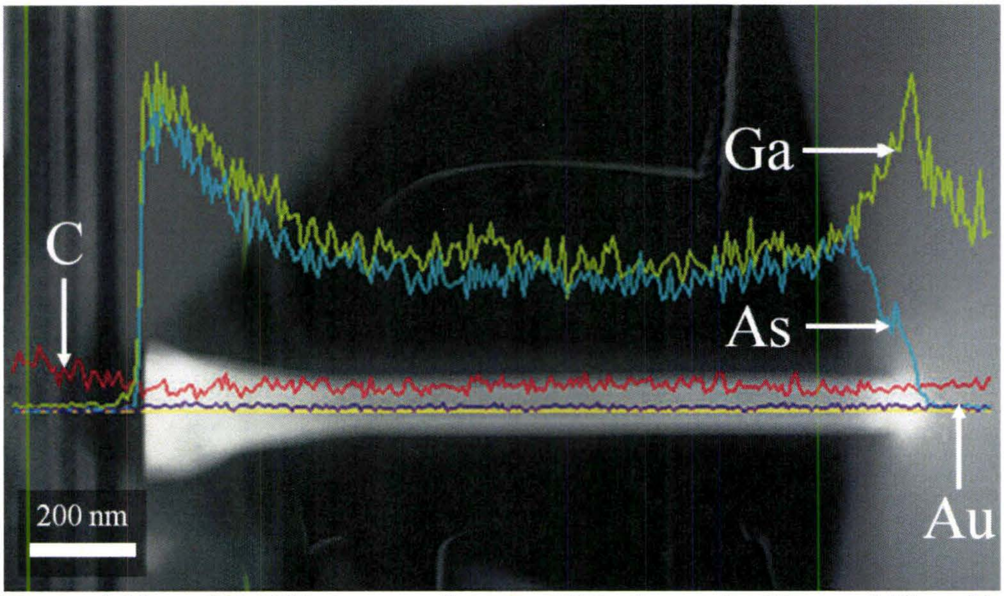

Figure 4.20 – HAADF image of same NW shown in Figure 4.19, with superimposed EDXS line-scans of elemental Ga (green), As (blue), C (red), and Au (purple).

base (left-hand side of Figure 4.20), we note that Ga and As counts suddenly increase as the PE beam is scanned from the substrate onto the NW. Moving towards the NW tip (right-hand side of Figure 4.20), the detected counts of Ga and As decrease slightly, corresponding to a decrease in NW thickness. Excluding this initial drop, the detected signal intensity is stable throughout the remainder of the scan, until the NW tip is reached. Here, we note that the As signal dramatically decreases, while the Ga signal is increased. This observation is consistent with a growth mechanism whereby a Ga seed allows for the assembly of a GaAs crystal, as previously discussed with reference to Figure 4.18. It should be noted that the elemental counts of C are detected with uniform intensity along the NW on account of the presence of a protective C-based envelope deposited during FIB sample preparation.

In addition to the analysis of orthogonal NWs, smaller island formations present on removed lamellae were also investigated. An HAADF image of one such formation is shown in Figure 4.21, distinguished as a region of bright contrast. Elemental EDXS maps of Ga, As, C, and Au were obtained from the corresponding region, as also shown in Figure 4.21. We note, here, that Ga is uniformly detected throughout an area corresponding to the region of bright contrast in the HAADF image. Similarly, C is detected throughout the formation, as would be expected based on the aforementioned sample preparation procedure. However, As counts are not observed within the entire structure. Rather, it is clear that As counts are only detected from the region within the formation situated closest to the substrate (left-hand side of Figure 4.21). This observation, namely, the presence of both Ga and As at the base, while only the presence of Ga detected towards the tip (right-hand side of Figure 4.21), leads to the conclusion that a GaAs crystal has been formed through Ga-assisted, seeded growth, as in the case of the NW and large polycrystalline island, considered above. As before, no Au was detected in the regions mapped. Detection of Ga, in regions beyond the extent of the crystal formation shown in the HAADF image, is attributed to Ga^+ ion implantation during FIB processing.

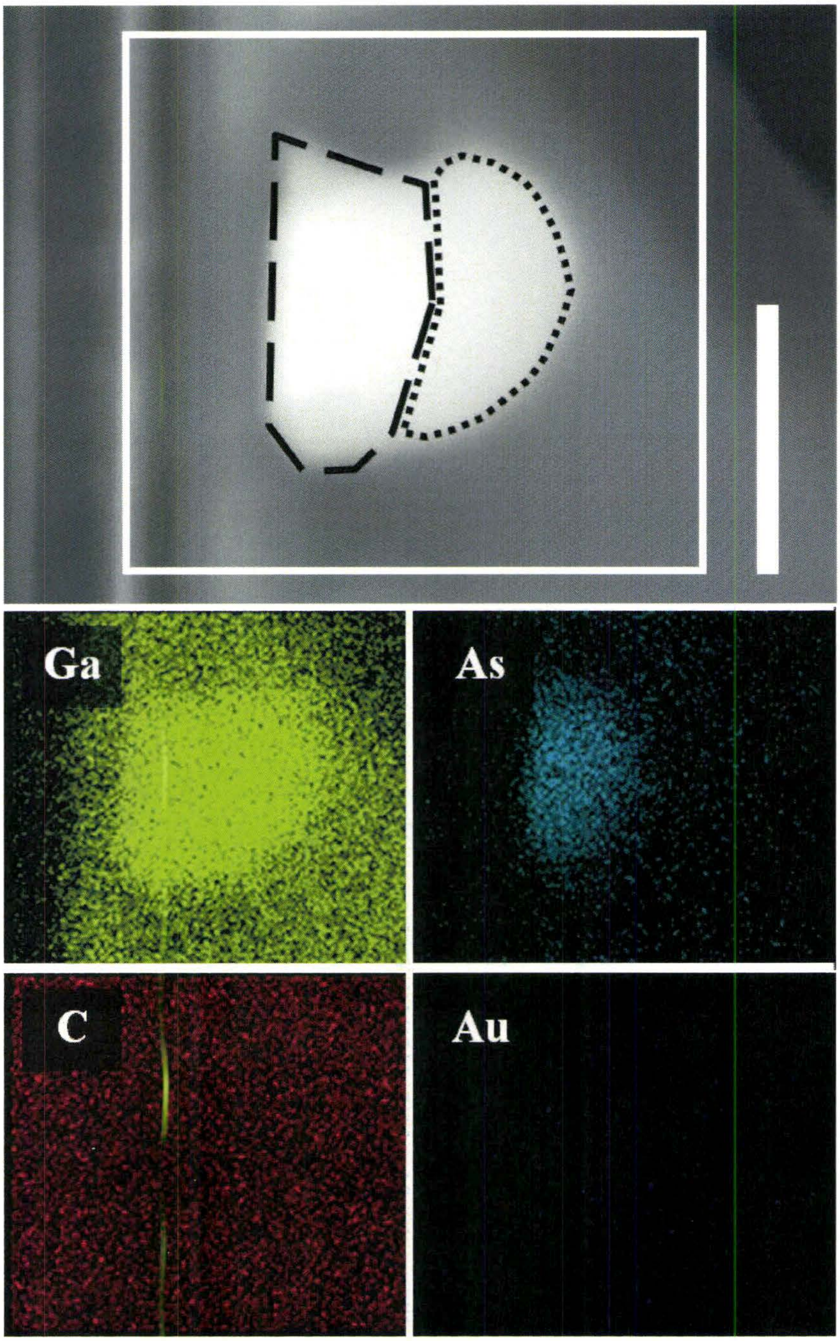

Figure 4.21 – HAADF image of crystalline formation on HOPG substrate (above), appearing as region of bright contrast. The segment outlined with a white border in the HAADF image represents the region from which elemental EDXS maps of Ga, As, C, and Au (below) were obtained. The segments outlined with dashed and dotted borders (above) show the GaAs crystal and Ga seed, respectively. The scale bar associated with the HAADF image represents a 100 nm length.

Upon concluding that the crystalline structures formed in the growth of group A samples were, indeed, the products of Ga-seeded bottom-up assembly, the question arises as to why the Au NPs deposited prior to growth were not detected after growth. In response to this question we consider two possible factors. One possible explanation is related to the use of DI water in the Au NP drop-casting process. As DI water droplets exhibit poor wetting of pristine HOPG surfaces, upon solvent evaporation, the Au NPs situated on the surfaces may have been located in close proximity to one another. If the coalescence of neighbouring NPs in close proximity, during pre-growth stage, allowed for the formation of large Au clusters, the Au-seeded growth would be expected to transpire at low formation rates. Assuming that Au-seeded growth rates were significantly lower than the formation rate of Ga-seeded polycrystalline islands, then the islands would conceivably engulf and bury the Au-seeded structures. Another possible explanation assumes that Au NPs alloyed with the larger clusters of Ga which, in turn, seeded the growth of GaAs structures. If Au-Ga alloys were formed, with Au concentrations less than 0.1 at. %, then EDXS measurements would fail to detect the Au content [138].

Based on the above structural and compositional analysis of group A samples, the formation of GaAs NWs and islands is attributed to a Ga-assisted growth mechanism, otherwise referred to as a self-catalytic growth process. Recently, several reports have been presented on the formation of GaAs NWs according to a Ga-seeded model [251-258]. The majority of these studies [253-

258] have concluded that the presence of a silicon-based oxide layer, over the growth surface, is essential for the growth of Ga-assisted GaAs NWs. Foncubertta i Morral et al. have argued that in the presence of a sufficiently thin SiO_2 layer, Ga adatoms preferentially accumulate in the defects of the oxide films, such that liquid-phase Ga can react with solid-phase SiO_2, forming a liquid-phase Ga-Si eutectic alloy while liberating O_2 [255]. In this scenario, pinholes are broadened within the oxide such that Ga-Si liquid alloys can physically extend to the underlying substrate, accommodating epitaxial growth according to the VLS model. Furthermore, it was concluded that in order for the Ga-based seeds to extend to the substrate, the SiO_2 film thickness must be less than 30 nm. Mandl et al. have, instead, put forth that the function of the oxide layer is to restrict the mobility of the group III adatoms and inhibit the formation of large droplets [257]. Also, the use of an SiO_x layer, as opposed to the use of an SiO_2 layer, was found to place negligible influence on NW growth [257].

In contrast to the above Ga-assisted growth processes utilizing an oxide layer, Jabeen et al. [251] and Plissard et al. [252] have effectively demonstrated that GaAs NWs, seeded from Ga particles, do not necessarily require a reaction between Ga adatoms and an SiO_2 film, prior to the initiation of growth. Particularly, in the case of the former study, the preferential formation of Ga particles was attributed to substrate surface roughness and the reduced sticking coefficient of Ga adatoms on foreign substrates, relative to As-terminated GaAs substrates [251].

Based on the above analysis of group A samples, and informed by the Ga-assisted GaAs NW synthesis models presented in the related literature, several new growth experiments were designed in order to better assess the nature of the growth mechanism involved. In the fabrication of group B samples, the growth period was reduced to 15 minutes, such that the earlier assembly stages of NWs and polycrystalline islands could be more explicitly observed. Additionally, 5 different surface treatment methods were employed in the group B study, as summarized in Table 4.2. First, sample B_1 was surface decorated with Au NPs, drop-cast from an ethanol solution. Here, ethanol was used, rather than DI water, on account of its superior wetting of the HOPG surface. Thus, the aim was to limit Au NP coalescence and to proceed with growth based upon a post-annealing treatment NP distribution more closely represented by the distribution shown in Figure 4.16. Next, sample B_2 was simply surface treated with ethanol, so that any possible role this solvent may play in the surface modification of HOPG could be distinguished. In contrast to all other samples, sample B_3 was left untreated, after the initial lateral cleavage process. In the case of sample B_4, an SiO_x layer of 30 nm thickness was deposited on the HOPG surface, through PE-CVD. The sample was then subjected to a wet etching treatment in 10:1 buffered HF solution for 12 s. Based on ellipsometry measurements, the SiO_x layer thickness was reduced to 10 ± 1 nm, after the etching process. Thus, sample B_4 would allow for testing of the oxide-mediated model for Ga-assisted GaAs NW growth [255]. Finally, the HOPG substrates employed in group B_5 samples were subjected to a 1 minute O_2-

RIE treatment for the intentional introduction of surface roughening. This sample would then allow for confirmation of the oxide-free model based on surface roughness promotion of Ga NP assembly, proposed by Jabeen et al. [251].

In Figure 4.22, a tilted-view SEM image of the as-grown group B_1 sample is shown. Here, we see a more densely packed collection of randomly aligned and vertically grown NWs. Upon closer inspection of the samples, as shown in the magnified view within the inset of Figure 4.22, it is distinguished that two dissimilar groups of NW structures were formed. First, a smaller collection of rod-shaped, vertically oriented NWs are observed, indicated by the white arrows in the inset, with no distinguishable particle of bright contrast at their tip. These NWs are present with an areal density of 32 NWs/100 μm^2. Second, a larger collection of pencil-shaped, predominantly randomly aligned NWs are observed, indicated by the yellow arrows in the inset, with Au particles of bright contrast located at their tips. Based upon EDXS measurements, the presence of Au NPs, at the tips of this second class of NWs, was confirmed. Furthermore, the diameter of the Au NPs measured, corresponded to the range of diameters measured in the post-annealing treatment study, as presented in Figure 4.16. Thus, it is likely that the use of ethanol in the drop-casting process allowed for an enhancement of average NP separation and, thereby, a reduction in coalescence. The Au-assisted NWs were observed with an areal density of 184 NWs/100 μm^2.

The conclusions drawn, based on the detection of two distinct types of NWs, is that those appearing in higher densities resulted from an Au-assisted

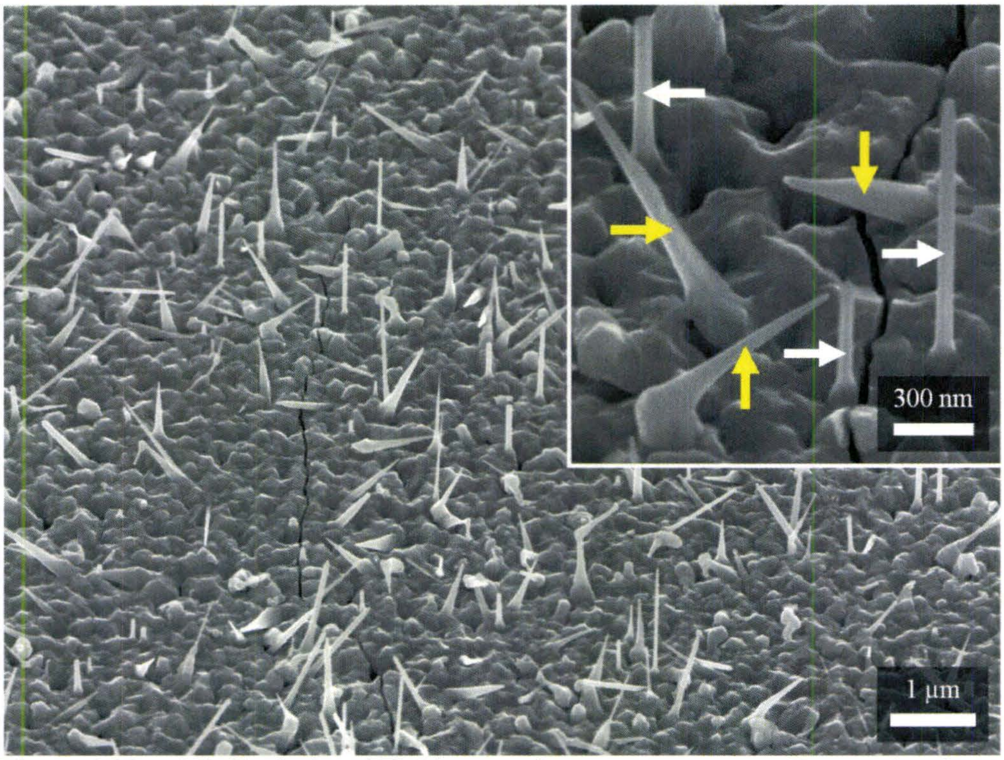

Figure 4.22 – 45° tilted-view SEM image of an as-grown group B_1 sample. Inset shows a higher magnification view of the same sample, indicating vertical, Ga-assisted NWs and randomly aligned, Au-assisted NWs with white and yellow arrows, respectively.

growth regime, while those appearing in lower densities likely resulted from the same Ga-assisted mechanism that led to the growth of group A NWs. Although the nature of the random alignment of Au-seeded NWs as compared to the vertical alignment of Ga-seeded NWs requires further investigation, the discrepancy may potentially be rooted in the dissimilar interactions of Au and Ga particles with HOPG surfaces. It has been shown that while Ga is unreactive with respect to HOPG surfaces, under the aforementioned annealing conditions, Au particles can form pits beneath the surface [259]. Epitaxial growth from the facets revealed as

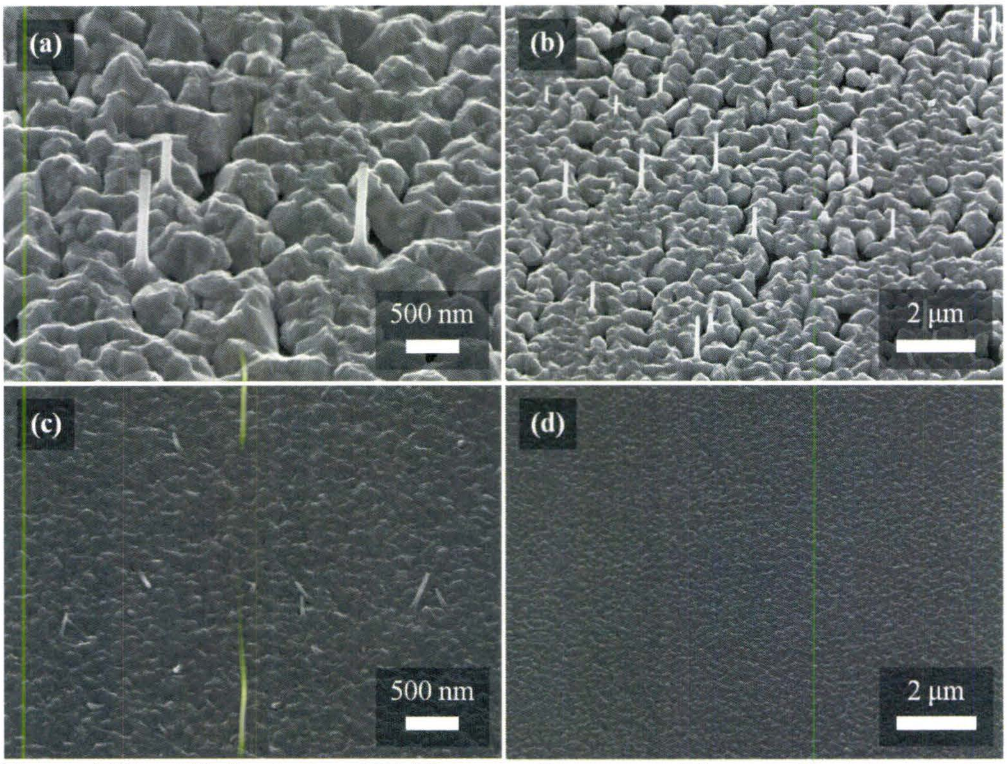

Figure 4.23 – 45° tilted-view SEM images of as-grown (a) group B_2, (b) group B_3, (c) group B_4, and (d) group B_5 samples.

a result of pit formation may then result in the growth of misaligned NWs. In future efforts, the presence of such sub-surface features could be investigated through TEM and EDXS experiments.

Figure 4.23 shows representative tilted-view SEM images, obtained from the other group B samples. The as-grown ethanol surface treated sample (group B_2) is shown in Figure 4.23(a). Here, vertical NWs with no discernable particles at their tips were observed to be grown with a density of 27 NWs/100 μm^2. Structures of effectively identical morphology were grown, in the case of the untreated (group B_3) samples, as shown Figure 4.23(b). The areal density of these

NWs was measured as 31 NWs/100 μm^2. Thus, the use of ethanol in the pre-growth surface treatment process altered the HOPG surface in no significant manner. Next, the group B_4 sample, on which an SiO_x layer was deposited prior to growth, is shown in Figure 4.23(c). It is clear from the SEM image that vertical NW growth is quenched, on account of the SiO_x layer inhibiting epitaxial guidance from the HOPG substrate. Possibly, the suitable formation of pinholes accommodating the extension of the liquid-phase Ga seeds to the underlying substrate was restricted under the growth conditions employed. The density of the randomly aligned NWs observed in the case of the group B_4 samples was measured to be 22 NWs/100 μm^2. Finally, the as-grown surface of the intentionally roughened sample (group B_5) is shown in Figure 4.23(d). Here, no NW growth was established. The formation of surface defects likely prevented the necessary surface diffusion of Ga adatoms needed for the formation of Ga droplets. Instead, as the result of reduced Ga adatom mobility under an As_2 overpressure, a polycrystalline GaAs film was formed.

The results from growths on the 5 distinct group B samples can be summarized as follows: (1) a sparse distribution of Au-NPs leads to the growth of randomly aligned NWs, (2) ethanol surface modification is of negligible influence on NW growth, (3) Au plays no role in Ga-assisted NW formation, (4) pitted Ga-assisted growth, based on the oxide layer mediated model of Fontcubertta i Morral et al. [255], is eliminated as a potential model for growth on HOPG, and (5) orthogonal NW growth is quenched with increasing surface disorder.

Next, we focus on the growth of GaAs on samples initially coated with a 10 Å thick layer of Ga, previously referred to as group C samples. Here, the pre-Ga deposited HOPG surface was left untreated, as in the case of group B_3 samples. The main intention in Ga deposition was the enhancement of Ga droplet formation, similar to the method previously reported in Ref. [251]. Post-growth SEM analysis of group C samples demonstrated the assembly of orthogonally aligned GaAs NWs, with an areal density of 26 NWs/100 μm^2. Therefore, the deposition of a 10 Å thick Ga film failed to promote localized Ga concentrations in the form of Ga droplets, and no improvement in NW density was observed. Figure 4.24(a) shows a tilted-view SEM image representative of the as-grown group C samples.

In the last of the series of GaAs NW growths on HOPG substrates, the growth temperature was increased from 550 °C, in previous growths, to 600 °C. Here, the motivation for the temperature increase was two-fold: (1) the enhancement of Ga surface diffusion, intended to promote Ga cluster formation and, (2) the enhancement of As_2 desorption, intended to inhibit the surface crystallization of GaAs and, thereby, improve the density of Ga droplets. As shown in Figure 4.24(b), a 50 °C increase in growth temperature was insufficient for the promotion of Ga droplet formation. As in previous growths, orthogonally oriented, rod-shaped NWs were formed, characterized by a comparable areal density of 22 NW/100 μm^2.

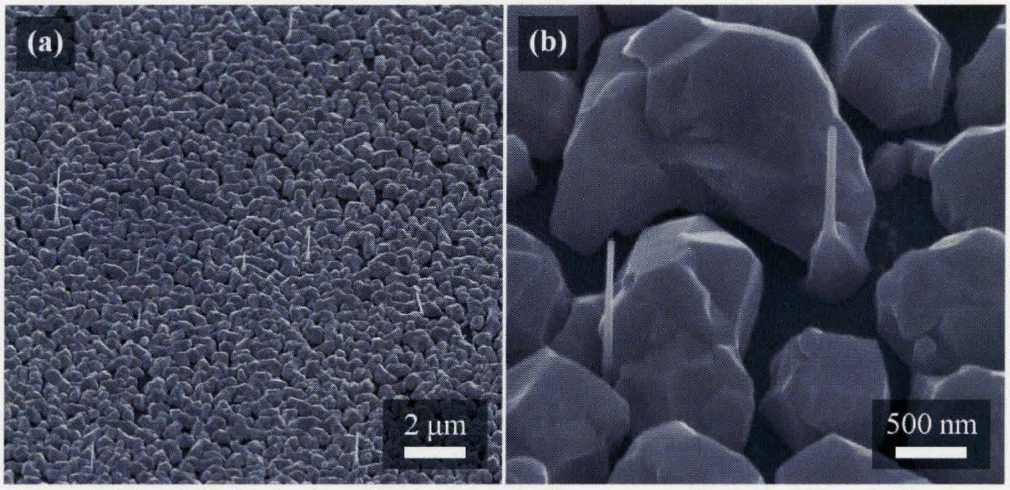

Figure 4.24 – 45° tilted-view SEM images of as-grown (a) group C and (b) group D samples.

Upon completion of the series of GaAs NW growths on HOPG substrates, the NW crystal structures were more closely examined, through SAD and HR-TEM experiments. Figure 4.25(a) and (b) show SAD patterns obtained from the base and midsection of a group A NW, respectively From the diffraction pattern representative of the NW base, a predominantly zincblende structure is revealed, whereas the pattern obtained from the midsection is characteristic of a predominantly wurtzite structure. The additional spots and streaks observed in the SAD patterns are attributed to reflections from rotationally twinned planes [143, 165, 169] and stacking faults [131], respectively In the current study, during the evolution of growth, a clear polytypic shift from zincblende at the base, to wurtzite with lateral zincblende insertions at the midsection, to wurtzite at the NW tip was observed. The same structural shift has previously been observed in the Ga-assisted growth of GaAs NWs [251, 252, 258] While the observed poly-

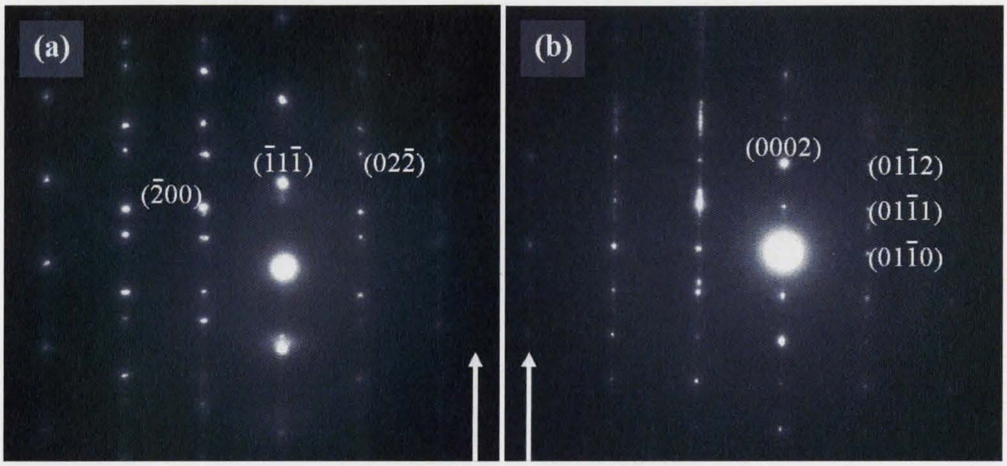

Figure 4.25 – SAD patterns obtained from the (a) base and (b) midsection of a group A NW The white arrows indicate the growth direction.

typic shift has been explained by the preferential atomic layer assembly in the hexagonal wurtzite configuration under reduced group III supersaturation levels in Ref. [252], Krogstrup et al. have attributed the shift from zincblende to wurtzite to temperature variations within the liquid seed during growth [258] Although the nature of this structural shift is currently not unambiguously understood, a likely explanation may be rooted in the change in Ga supersaturation during growth, owing to disproportional Ga replenishment within the seed. This explanation would be in agreement with the results presented in Chapter 3, on the defect-free growth of GaAsP and GaP NW segments under high group V supersaturation levels.

At this point, a question remains: If NW growth is seeded from a Ga nanoparticle, why then is the presence of a Ga seed at the NW tips not clearly observed after the growth of group B, C, and D samples, as expected based on the standard VLS model for Au-assisted growth? The justification for the lack of an observed Ga seed at the NW tips is rooted in the manner in which the NW growth sequence is terminated. All NW growths discussed, thus far, were terminated by closing the shutter of the Ga effusion cell while the samples cooled under a constant overpressure of As_2. In the case of Au-assisted growths, the Ga content present in the seed is purged and incorporated in the NW structure as a result of crystallization with excess group V adatoms. In the case of Ga-assisted growth, upon growth termination, the Ga content, in excess of the concentration required to maintain a supersaturated solution, is similarly incorporated into the crystal. However, at this point, since Ga in the seed is no longer being replenished, the remaining Ga content, which simply constitutes the liquid seed, is consumed and crystallized as GaAs. Thus, no droplet is observed after growth.

Figure 4.26 shows an HR-TEM image of the tip of a NW grown under identical conditions as the group D samples. Here, three distinct regions are differentiated. Towards the bottom left-hand side of Figure 4.26, indicated by the blue arrow, a wurtzite stacking arrangement is noted. Based on the above discussion, the observed hexagonal crystal structure is expected, corresponding to the final stages of growth. Next, in a region defined as the "cooling neck", and indicated by a red arrow, a clear shift to a cubic zincblende arrangement is seen. The presence of a zincblende neck segment has previously been characterized as a region formed after the cessation of growth, sustained by the purging of excess Ga content [108, 110]. Finally, in the region indicated by the black arrow, and labelled as the GaAs tip, we note the presence of a rotational twin-plane, followed

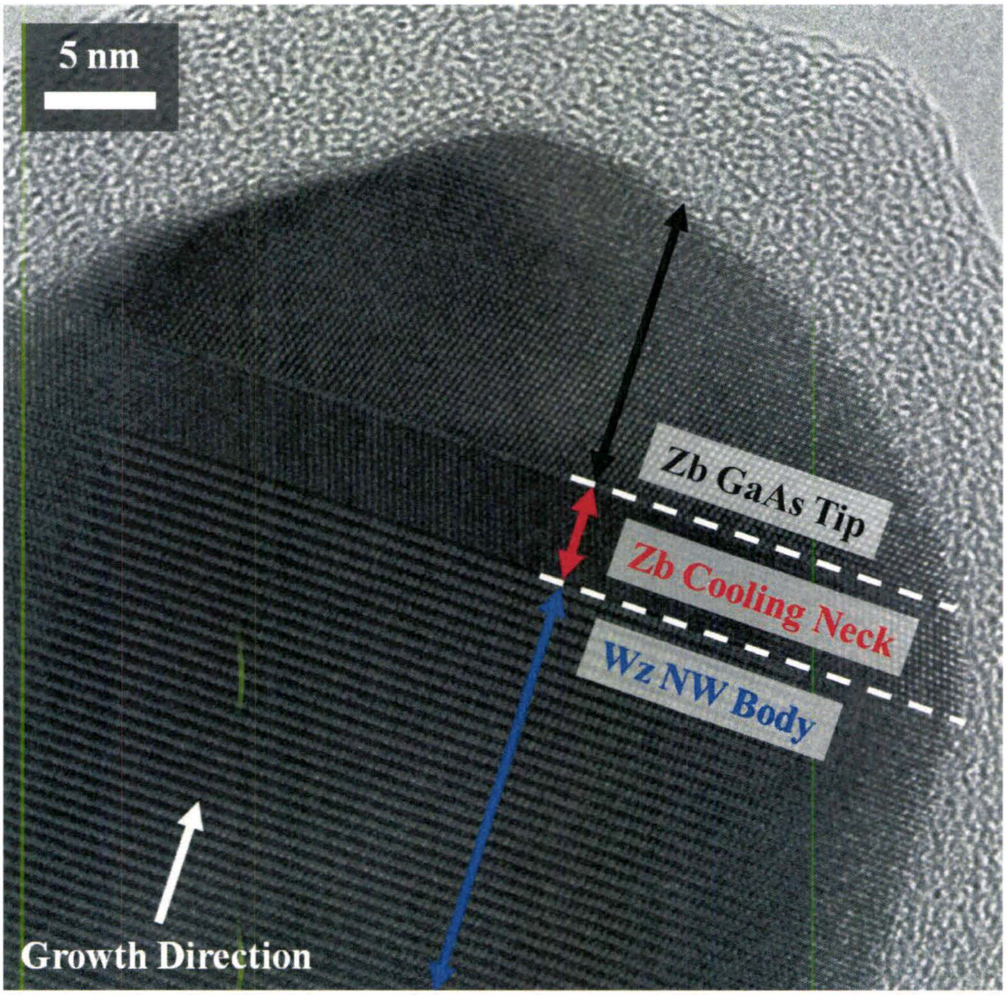

Figure 4.26 – HR-TEM image of the tip of a single NW, grown under identical conditions as the group D sample. A hexagonal wurtzite (WZ) structure is characteristic of the NW region below the tip. A zincblende (Zb) cooling neck is formed next, indicative of excess Ga being purged from the seed. Finally, the Zb GaAs tip is formed as the Ga seed is consumed under an As_2 flux.

by the presence of a cubic zincblende segment, believed to be formed through the consumption of the Ga seed under an As_2 overpressure, during the cooling phase. The growth of Ga-seeded GaAs NWs, terminated under conditions similar to those employed in the current study, has been shown to result in the formation of NWs with identical tip structures [252].

The detection of excess Ga present at the tip of the NW shown in Figure 4.20 (with diameter of 85 nm), while absent at the tip of the NW shown in Figure 4.26 (with diameter of 35 nm), can be explained by the difference in the volume of the seed particles. Assuming similar crystallization rates, a larger Ga particle simply requires a longer period in which it can be crystallized as GaAs, after the termination of growth. In the case of the larger NW, associated with a Ga seed of greater diameter (shown in Figure 4.20), the group V flux was likely terminated prior to full GaAs crystallization of the tip. In contrast, during a cooling period of equivalent duration, the sufficiently small Ga seed at the tip of the thinner NW (shown in Figure 4.26) was fully consumed under the As_2 flux.

Based on the four growths of GaAs NWs on HOPG substrates and the corresponding structural characterizations, a qualitative growth model is put forth, as portrayed pictorially in Figure 4.27. First, we assume near unity sticking coefficients for Ga adatoms on the HOPG substrate, while the sticking coefficient of As_2 is below unity on the non-Ga terminated surface [121]. Since Ga monomer diffusion lengths exceed that of the As_2 dimers, a finite probability exist for the formation of Ga islands, as depicted in Figure 4.27(a). In localized regions where the V/III flux ratio is less than unity, on account of As_2 desorption, Ga nuclei will grow to form liquid droplets, as represented in Figure 4.27(b). The low probability for the formation of such Ga clusters explains the low density of the NWs formed. Upon its formation, a Ga cluster collects additional Ga monomers and As_2 dimers through direct impingement or surface diffusion, mediating the

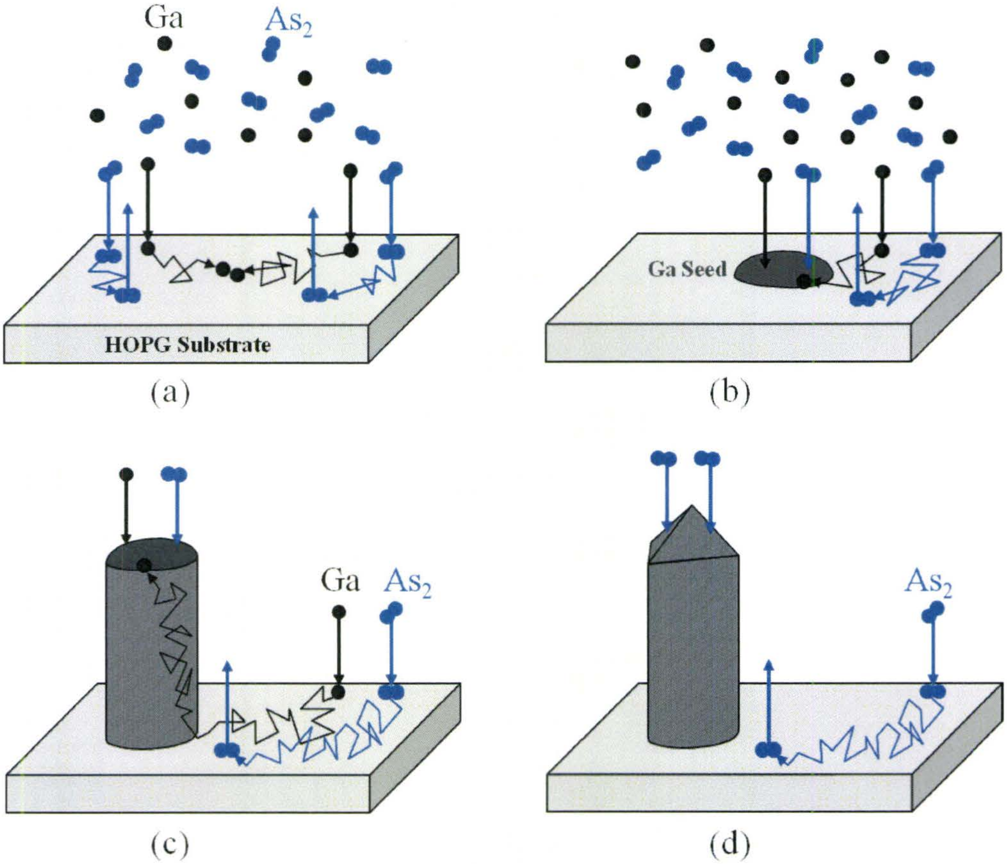

(a) (b)

(c) (d)

Figure 4.27 – Model for the Ga-assisted growth of GaAs NWs on HOPG substrates. (a) Impingement of group III monomers and group V dimers on the HOPG surface, followed by the localized collection of Ga monomers. (b) Growth of Ga seeds in regions where local V/III ratios are less than unity. (c) Supersaturation of Ga seed and nucleation of GaAs. GaAs NW growth is maintained, so long as Ga content is replenished at a rate exceeding the consumption rate of the Ga seed. (d) Termination of growth, consumption of liquid seed, and crystallization of GaAs at NW tip.

precipitation of GaAs nuclei at the interface formed with the substrate. So long as the Ga content is continually replenished through the constant collection of monomers, then the Ga seed is maintained and NW growth transpires. This is depicted in Figure 4.27(c). Upon termination of the group III source, the Ga content comprising the seed is consumed under the constant As_2 overpressure, leading to the crystallization of GaAs at the NW tip, as represented by Figure 4.27(d).

Lastly, one final growth on HOPG surfaces was conducted. In this group E growth, InAs was grown instead of GaAs, in order to examine the potential for In-assisted growth according to a mechanism similar to that defined in the above model. Group E samples were grown at 400 °C, a standard criteria for InAs NW growth via MBE [250]. Two groups of laterally cleaved HOPG samples were subjected to distinct pre-growth surface treatment processes. Group E_1 samples were prepared in an identical manner as the group B_1 samples. As such, 25 nm Au NPs were drop-cast on the surface from a solution in ethanol. The purpose here was to determine the potential for growth of Au-assisted vertically aligned NWs on HOPG. Group E_2 samples, in contrast were left untreated.

A tilted-view SEM image representative of the group E_1 samples is shown in Figure 4.28. Here, two dissimilar structures are distinguished. First, we note the presence of randomly aligned NWs, as indicated by the yellow arrows in the inset. Secondly, the presence of randomly aligned “nano-flakes”, as indicated by the black arrows in the inset, was observed. Au-NPs were indeed distinguished at the tips of both nanostructures, as observed through SEM (BSE imaging mode) and through TEM characterization (discussed below).

The nano-flake structures are noted to be tapered along their growth direction. Their morphology is characterized by a lateral cross-section that is

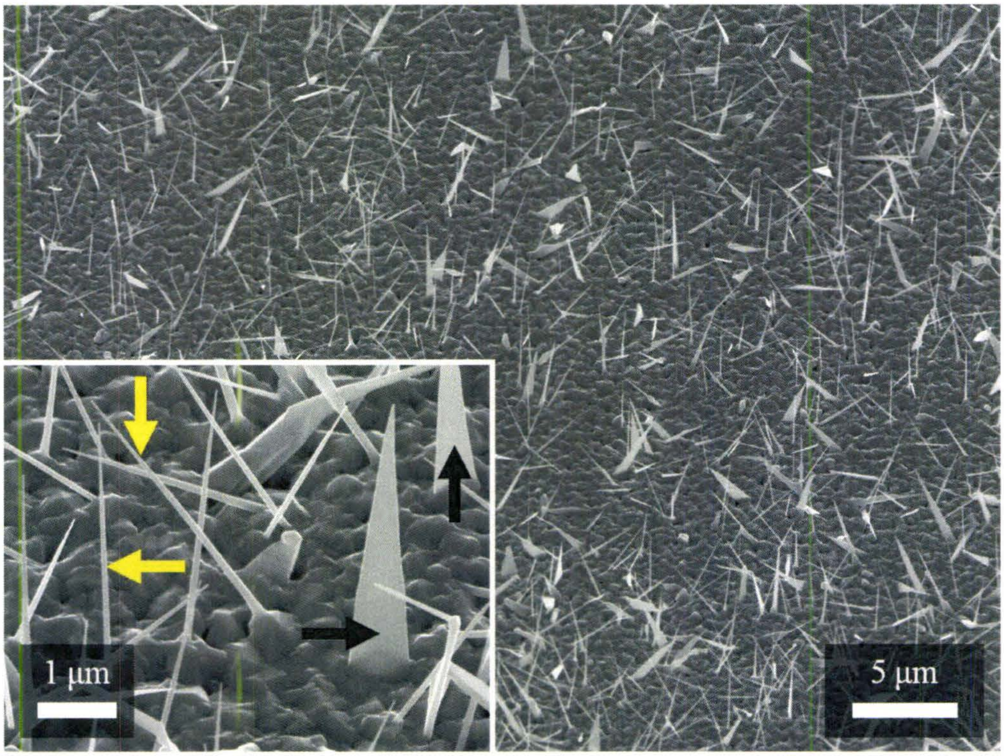

Figure 4.28 – 45° tilted-view SEM image of as-grown group E_1 sample. Inset shows a higher magnification view of the sample wherein NW and "nano-flake" structures are indicated by yellow and black arrows, respectively.

localized to the extent of the Au-NP at their tips, along one axis, while extended along the other axis, creating a planar or triangular plate-like geometry. As measured from the bases, these structure have widths of several hundreds of nanometres, depths of tens of nanometres, and heights up to 3 microns. The tilted and plan-view SEM images shown in Figure 4.29 better exemplify the nano-flake morphology. Particularly, the rectangular cross-section of the nano-flakes is easily distinguished in Figure 4.29(b).

HR-TEM analysis of single NWs and nano-flakes grown on the group E_1 samples demonstrated a cubic zincblende structure with no intermittent stacking

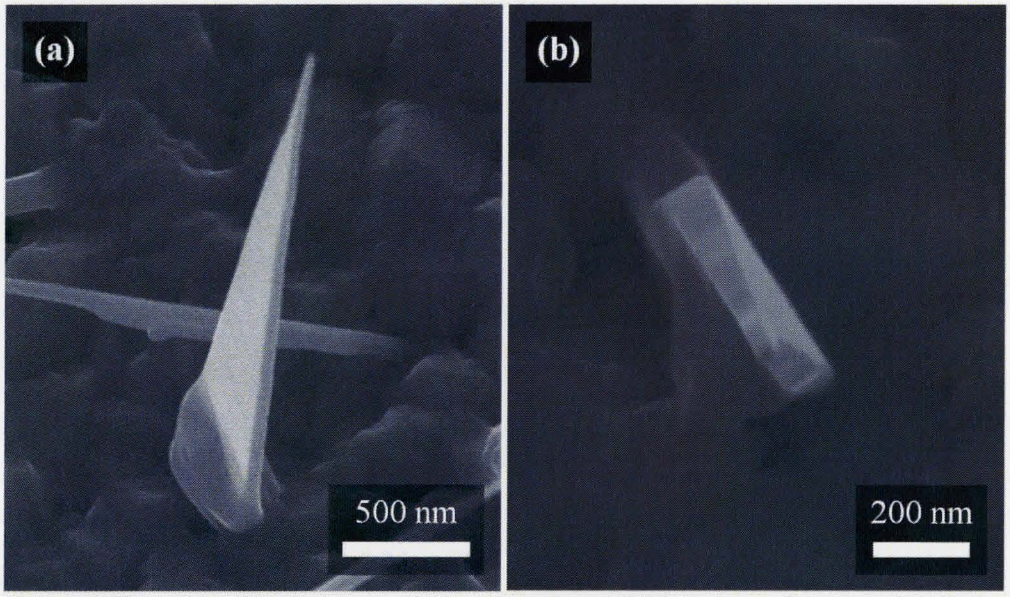

Figure 4.29 – (a) Tilted-view and (b) plan-view SEM image of Au-seeded InAs nano-flake structures grown on HOPG substrates.

faults. A representative HR-TEM image of a nano-flake tip is shown in Figure 4.30. The insets of Figure 4.30 show an SAD pattern from the same nano-flake, characteristic of a stacking fault-free zincblende crystal, and a highly magnified and lattice resolved HR-TEM image of the structure's tip, demonstrating the ABCABC. atomic layer stacking arrangement and abrupt interface formed between the InAs crystal and Au tip. The InAs NWs were observed to be grown along the <111> direction, whereas nano-flakes were observed to grow parallel to the <100> direction of the crystal lattice, as identified in the indexed SAD pattern.

The Au-assisted growth of similar plate-like InAs nanostructures on GaAs substrates via MBE was first demonstrated by Aagesen et al. in 2007 [260] In this study, Au films were deposited on GaAs (100) substrates for the formation of Au-NPs, accommodating growth at a temperature of 420 °C. The model suggested

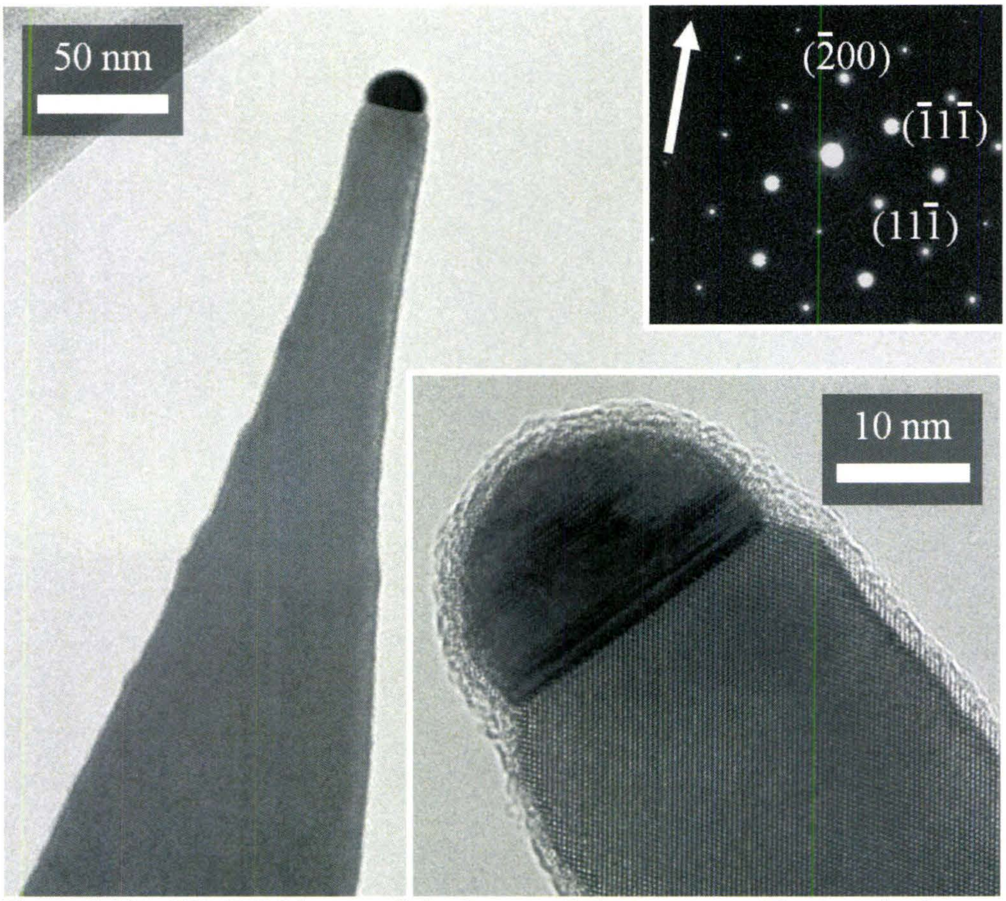

Figure 4.30 – HR-TEM image of single nano-flake structure. The inset in the top right-hand side shows an SAD pattern obtained from the nano-flake, demonstrating the single-phase zincblende structure and growth along the <100> direction, as indicated by the white arrow. The inset in the bottom left shows the characteristic cubic atomic stacking structure and the atomically abrupt interface formed between the InAs NW and the Au NP.

by Aagesen et al., for the growth of InAs nano-flakes, assumes the nucleation and initial formation of an InAs NW, according to either a VLS or VSS mechanism, growing along the <100> direction and having a squared cross-section with {110} sidewall facets. As growth continues, sidewall nucleation commences, progressing at a higher assembly rate on two of the four {110} oriented sidewalls, attributed to a higher growth rate on As-terminated surfaces [261]. Thus, during growth, the nano-flake height increases as a result of Au-assisted axial growth, while preferential sidewall nucleation on two of four lateral facets encourages the formation of a plate-like structure.

In contrast, the group E_2 samples (those with no surface treatment prior to growth) demonstrated no NW formation. SEM and EDXS characterization revealed the presence of a two-dimensional InAs film on the HOPG surface of the as-grown group E_2 samples. Based on analysis of the peripheral regions of the sample, it was concluded that preferential island nucleation was first initiated at the step-edges on the HOPG surface. As adatom deposition progressed, a step-flow growth regime ensued, leading to the formation of polycrystalline InAs film. Thus, no In-assisted NW growth was observed in the studies involving group E_1 or E_2 samples.

In conclusion, the GS-MBE growth of GaAs and InAs NWs on HOPG substrates was investigated. The initial intention was the realization of Au-assisted, densely packed, and vertically oriented crystal growth, and the demonstration of the potential for growth of GaAs NWs on graphene-composite films. This, however, proved to be a challenging endeavour. Instead, it was found that GaAs NWs can be fabricated through a self-catalytic growth mechanism, relying upon the formation of Ga clusters. The resultant NWs were sparsely situated amongst a large density of polycrystalline GaAs islands, indicating that a low probability exists for the formation of Ga droplets, under the growth conditions employed. Various surface treatment processes were carried out prior to growth, allowing for the elimination of Au-Ga alloy assisted growth, oxide-layer mediated Ga-assisted growth, and surface roughness Ga-formation growth models. Instead, a qualitative model was presented based on the finite probability of Ga-cluster formation in regions where the local V/III flux ratio is less than unity. NW growth proceeds, according to this model, so long as the Ga content in the seed is replenished at a rate greater than or equal to the rate at which it is consumed.

Future attempts to optimize NW density, morphology, and crystalline quality based on the above Ga-assisted growth model will benefit from a more expansive study, wherein numerous growths are conducted under various V/III flux ratios, nominal growth rates, and temperatures. Furthermore, it may likely prove favourable to repeat the growth process employed in the case of group C samples, using Ga layer thicknesses in excess of 10 Å.

4.7 – Chapter Conclusions

The assembly of GaAs NWs on a variety of foreign substrates has been investigated, including single crystalline Si wafers, stainless-steel foils, borosilicate glass with polycrystalline Si buffer layers, carbon-nanotube composite films, and highly-ordered pyrolytic graphite substrates. Of the five alternatives presented, all but HOPG substrates accommodated dense NW growth. Stainless-steel foils and CNT sheets, in comparison to the other substrates explored, offer the advantage of additional functionality, with respect to potential device applications, in the form of mechanical flexibility. Furthermore, since the growth of GaAs NWs, according to the standard VLS mechanism, was controllably and reproducibly demonstrated on both flexible substrates, and since both materials are electrically conductive, meaning that additional back-side contacting is eliminated as part of the device fabrication process, metal foils and CNT composite films are chosen as the most suitable alternatives for device applications. However, control over the thickness of CNT films also offers the potential for them to be made optically transparent, allowing for added functionality (for example, through the fabrication of superstrate configuration solar cells). Moreover, the integration of CNT composite films and GaAs NWs represents a novel class of flexible opto-electronic material. Based on the above justifications, the GaAs NW-CNT film hybrid material is used in the fabrication of proof-of-concept flexible solar cells, as presented in the following chapter.

Chapter 5

Fabrication and Performance of GaAs NW-CNT Composite Film Hybrid Photovoltaic Cells

The preliminary studies on the growth and characterization of GaAs nanowires (NWs) on carbon-nanotube (CNT) composite films, presented in Section 4.5, is extended in the current chapter for the fabrication of photovoltaic cells. The purpose of this study is the demonstration of photovoltaic behaviour from the nano-hybrid material, wherein coaxial p-n junction GaAs NWs serve as the active, light-harvesting medium, while CNT films simultaneously function as a flexible substrate and the electrical contact for the emitter layer of the solar cell.

The research presented in the current chapter represents a collaborative effort. Dr. Gregor Lawson, under the supervision of Dr. Alex Adronov (Department of Chemistry), was primarily responsible for the fabrication of Au-decorated CNT films and the corresponding characterization experiments. The author was responsible for NW growth, characterization of the as-grown NW samples, device fabrication, and solar cell testing. This chapter is presented here as recently accepted for publication in Ref. [120].

5.1 – Experimental Details

The Au nanoparticles (NPs) used in the current study were prepared according to the well established Turkevich method [247, 248], resulting in near-monodisperse particle distributions. Deposition of Au NPs was achieved by filtration of a dilute NP solution through a thin film of unmodified single-walled CNTs, prepared by a vacuum filtration process [224]. Thin films comprised of CNTs, such as those prepared in this work, resemble a random finely-interpenetrating network of nanotube bundles.

In the current study, an alternative method for the preparation of Au-decorated CNT films was employed, offering several advantages over the method defined in Section 4.5. In contrast to the previously reported *in-situ* reduction method, which can significantly degrade the electrical conductivity of the CNTs [262], the use of un-functionalized CNTs in the current procedure, is expected not to comprise their structure and electronic properties during film fabrication. As the modified approach requires fewer synthetic steps, the time required for the preparation of each composite film is greatly reduced. Additionally, the current procedure allows for fine control over the size and polydispersity of Au NPs deposited on the surface of the CNT composite films.

Following fabrication, composite films were cut into small sections having dimensions of approximately 5 × 10 mm^2, removed from the filtration membranes and transferred, Au NP side up, to copper substrates. Copper was arbitrarily chosen as a rigid, conductive, and gas-source molecular beam epitaxy (GS-MBE) compatible support material to which the CNT films could easily be transferred for subsequent NW growth or later removed. These samples were then thermally annealed at 550 °C for 10 minutes in nitrogen ambient, ensuring the removal of volatile organic matter which could potentially contaminate the MBE chamber during NW growth.

The GS-MBE system used for NW growths was equipped with a solid elemental effusion cell, for the supply of Ga monomers, and a hydride (AsH_3) gas cracker operating at 950 °C, for the supply of As_2 dimers. Prior to the commencement of the growth sequence, a degas procedure (15 minutes, 300 °C) was performed, followed by an inductively coupled hydrogen plasma treatment (10 minutes, 550 °C), under an As_2 overpressure. At a growth temperature of 550 °C, NW growth was instigated by opening the shutter of the Ga cell. All growths were kept at a constant V/III flux ratio of 1.5 and nominal GaAs growth rate of 1 μm/hr. Upon the completion of growth, prompted by the termination of Ga flux, the samples were cooled under an As_2 overpressure.

For the purposes of investigations presented in this work, two NW groups were grown on CNT composite sheets, henceforth referred to as groups A and B. Group A NWs were designed to contain a p-n junction within a coaxial architecture, based upon diffusion-limited nucleation on the lateral NW facets, wherein an n-GaAs core segment was doped with Te, while a p-GaAs shell was doped with Be. Each segment of the group A NWs was grown for a duration of 15 minutes, resulting in a total growth period of 30 minutes. Group B NWs, in contrast, were entirely n-type doped with Te, also over a growth period of 30 minutes, yielding n-GaAs NWs. Nominal dopant concentrations were maintained at 4×10^{18} cm^{-3} and 5×10^{18} cm^{-3}, for Te and Be levels, respectively, based upon previous calibrations of epitaxial films on GaAs (100) substrates. The group A NWs were primarily used to assess the photovoltaic potential of such NW-CNT hybrid materials, while the group B NWs were employed in investigations into the nature of the photovoltaic response and the conduction pathways between the NWs and their underlying CNT substrates.

Additionally, a third growth was carried out, referred to as group C, wherein a planar p-n junction was incorporated into a thin film deposited upon a CNT composite film containing no Au-nanoparticles. This control sample was grown with the intention of mimicking the structure of the planar GaAs film deposited during the growth, and situated adjacent to the bases, of the group A and B nanowires. The group C samples were prepared consisting of a 150 nm thick Be-doped GaAs layer overlaying a 150 nm thick Te-doped GaAs layer. Identical CNT film processing (surface decoration of Au-nanoparticles, notwithstanding) and GS-MBE growth parameters including temperature, nominal growth rate, III/V flux ratio, and nominal doping concentration were employed during thin film depositions and NW growths. Thus, the GaAs film of sample C was designed to duplicate the properties of the planar film concurrently deposited during NW growth.

To prevent potential short circuit pathways between top contacts and the bottom CNT electrode, a previously reported processing method was employed [54, 119]. Starting with as-grown samples, SiO_x layers, approximately 1300 Å in thickness, were deposited through plasma-enhanced chemical vapour deposition (PE-CVD), to conformally coat the NWs (and the exposed surface of the GaAs films deposited between the NWs) atop the CNT substrate. Subsequent spin-coating of S-1808 photoresist was carried out to encapsulate the oxidized NWs and GaAs film. Next, an O_2-plasma reactive ion etching (RIE) treatment (60 seconds) allowed for the removal of a thin photoresist film, thereby exposing the tips of the oxidized NWs.

The oxidized tips were then chemically etched in a buffered-hydrofluoric acid solution and the remaining photoresist layer was removed in an acetone bath removal procedure. At this stage, the NW bases and adjacently situated GaAs film remained encapsulated by the previously deposited SiO_x layer, while NW tips were exposed as the sole semiconductor surface upon which electrical contacts could be deposited.

Two different conductive materials were employed as top contact layers in the present study. For experiments aimed towards investigations into photovoltaic behaviour, a 10000 Å thick transparent conductive film of indium-tin-oxide (ITO) was deposited via sputter coating, corresponding to a thickness of roughly 200 nm over the NWs. For direct comparison of the conductive behaviour of group A and B NWs, where optimal Ohmic contacts are required, opaque contacts were deposited on the processed samples. In this case, the commonly used Ti/Pt/Au and Ni/Ge/Au layers were deposited on group A and B samples, respectively, via electron-beam evaporation. In all cases, the depositions were made through shadow masks allowing for contact dots roughly 800 μm in diameter. Inspection of plan-view scanning electron microscopy (SEM) images indicated that each contact dot yielded the ensemble contribution of approximately 1.5×10^6 individual NWs. After the deposition of ITO or opaque contacts, the samples were subjected to a rapid thermal annealing (RTA) treatment (30 seconds, 400 °C) for Ohmic contact formation.

SEM imaging was performed during pre-growth inspection of Au-decorated CNT films, during analysis of the orientation and morphology of as-grown NWs, and during each stage of the device fabrication procedure. The SEM imaging was performed using a JEOL JSM-7000F SEM, equipped with a Schottky-type field emission gun filament. In addition, inspection of the CNT films were performed by focused ion beam (FIB) cross-sectioning using a Zeiss SMT NVision40 SII CrossBeam instrument.

The current-voltage characteristics of the various samples were evaluated using a Keithley 2400 source meter. A Newport 96000 solar simulator with an A.M. 1.5 G filter yielding an incident power of roughly 2.6 Suns was used as the illumination source in measuring photovoltaic response. Conversion efficiencies and fill factors were calculated according to standard techniques [263].

5.2 – Results and Discussion

Planar SEM images of CNT-Au composite film samples obtained before and after a thermal annealing treatment are shown in Figure 5.1(a) and (b), respectively. Prior to the thermal anneal, Au NPs with average diameters of 30 ± 5 nm were observed. This value increased to 38 ± 6 nm following the annealing procedure, as a result of the migration and coalescence of a small fraction of Au NPs at elevated temperatures. However, it can be seen, from the SEM images in Figure 5.1 that large scale aggregation of Au nanoparticles does not occur during this process. The density of Au NPs upon the surface of annealed composite films, which was also determined using SEM, ranged between 20 and 86 nanoparticles per 1 μm^2, with an average density of 50 nanoparticles per 1 μm^2.

Cross-sectional images of these films were obtained after focused ion beam (FIB) milling. A trench cut within a CNT-Au composite film, which has not undergone thermal annealing, is shown in Figure 5.1(c). In this secondary electron image, Au nanoparticles are observed to be located predominantly upon the film's surface. Some Au NPs can also be seen in low density within the structure of the CNT film. The presence of Au NPs within the film is not unexpected, given the film's porous microstructure and the dimensions of Au NPs used in this work. In addition to Au nanoparticles, clusters of iron were also detected, embedded within the nanotube film. These clusters, which appear as regions of bright contrast in Figure 5.1(c) and (d) having dimensions on the scale

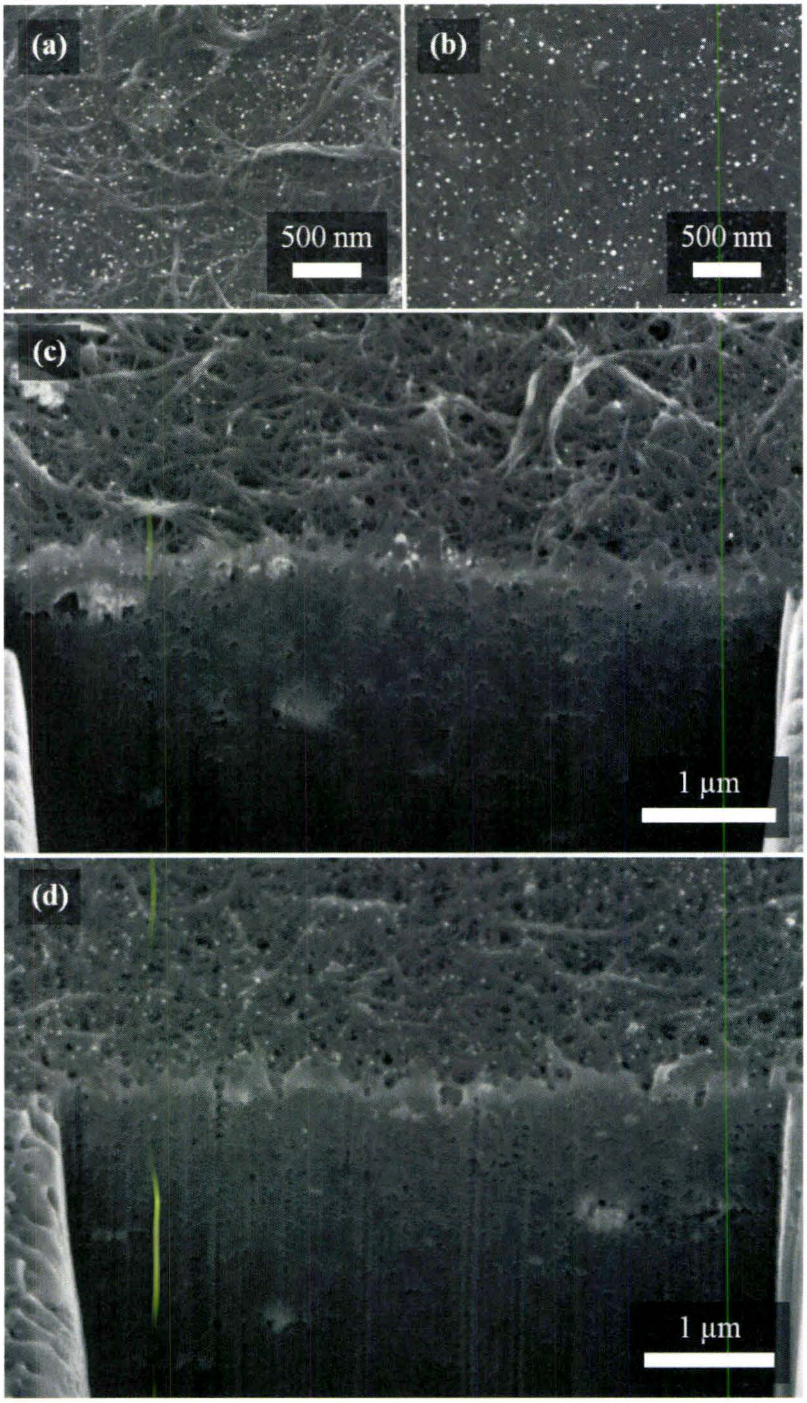

Figure 5.1 – Plan-view SEM images of a Au-decorated CNT film, (a) before and (b) after a thermal annealing treatment, and tilted-view SEM images of trenches milled within Au-decorated CNT films (c) before and (d) after the same annealing procedure.

of 10s to 100s of nanometres, are impurities present in the commercially-purchased nanotube sample used in this work (Fe catalyst from single-walled CNT synthesis). Figure 1(d) illustrates a similar trench produced by FIB milling of a post-annealing treatment sample. From these images it was determined that the distribution of Au NPs throughout our CNT-Au composite films is not significantly altered by the annealing process.

SEM images of group A NWs, shown in Figure 5.2, showed dense NW growth with no preferred NW orientation (similar results were obtained from group B NWs). The random alignment of NWs relative to the substrate surface was previously attributed, in Section 4.5, to the random manner in which CNT bundles comprising the underlying film are situated. As determined from sample sets of over 100 single specimens, the NWs have an average full-width at half-length diameter of roughly 100 nm and heights up to 3.5 μm. The highly tapered morphology is a trademark of diffusion limited sidewall growth and is anticipated for GS-MBE growths under the growth conditions employed [95].

As outlined in the previous section, solar cell fabrication was carried out through a process designed to effectively exploit NWs as the active, energy conversion medium. A schematic representation of the final device structure, showing a single NW for clarity, is depicted in Figure 5.3. In light of recent reports on the inhomogeneity of dopant profiles in semiconductor NWs [264, 265] and the anticipated incongruity in dopant incorporation between the (100) surface of the doping calibration sample and the (111) surfaces of the nanowires, the

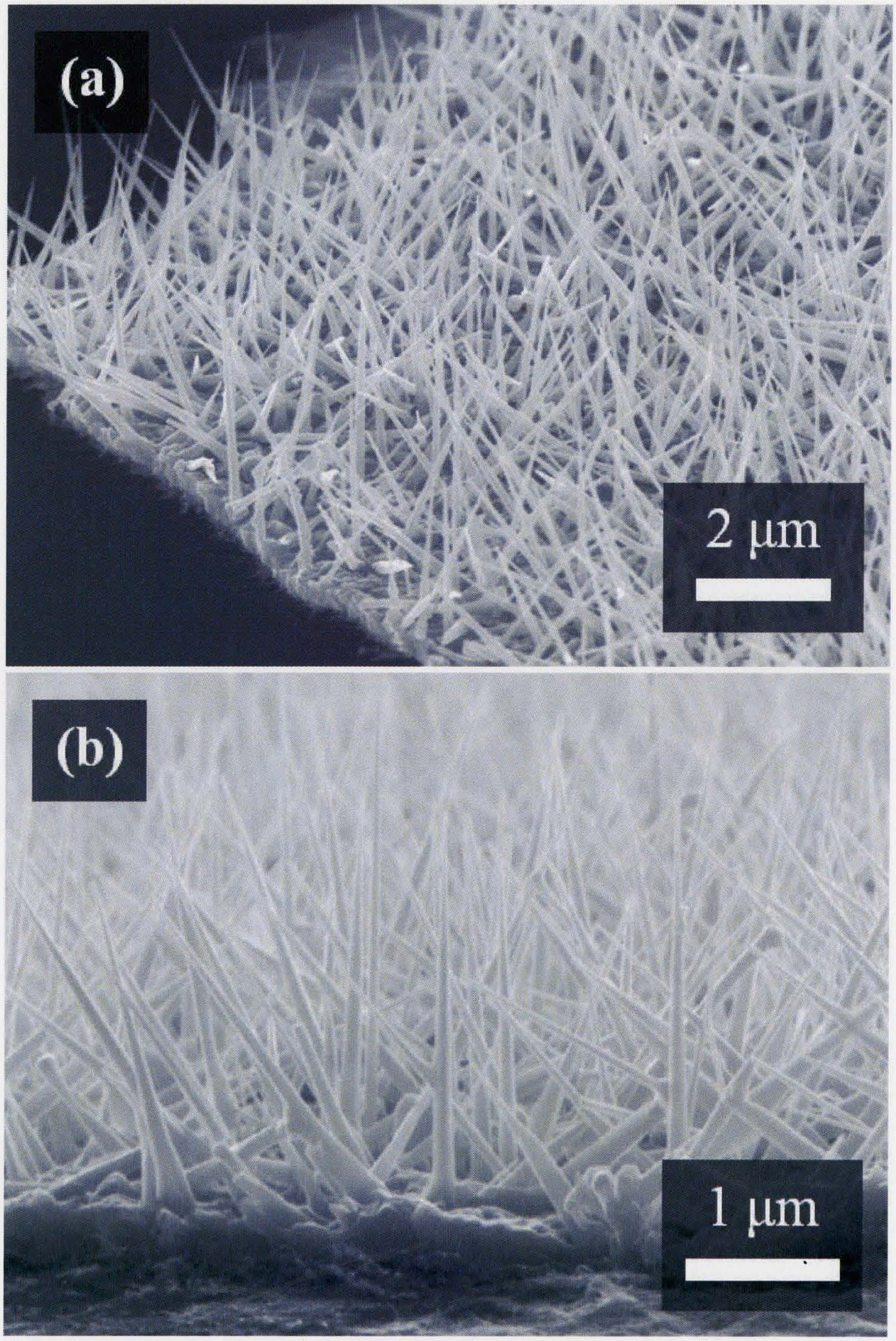

Figure 5.2 – (a) 45° tilted-view and (b) cross-sectional view SEM images of as-grown group A NW samples. Densely packed NWs are grown at various orientations with a highly tapered morphology Similar results were obtained from group B NW samples.

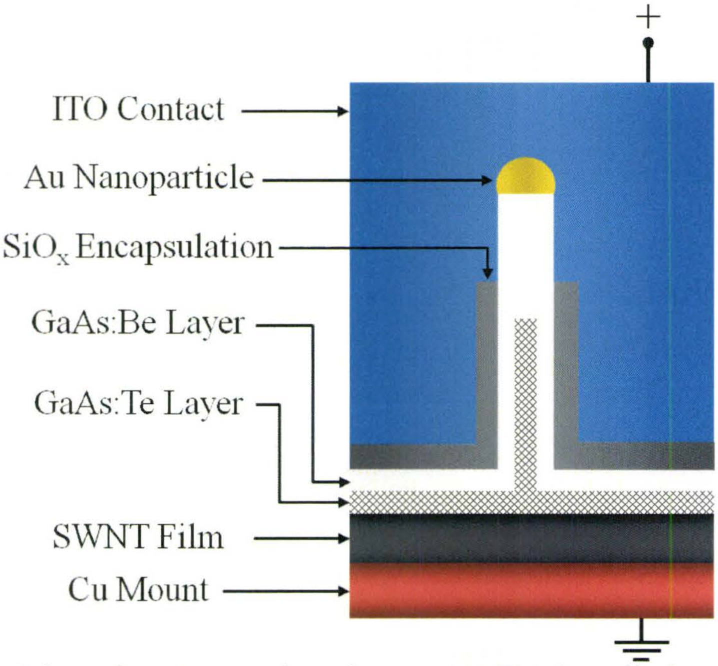

Figure 5.3 – Schematic representation of group A NW solar cell, showing biasing conditions. The NW bases and planar GaAs film are electrically isolated from the ITO top contact. The CNT substrate simultaneously serves as the growth surface and backside contact.

degree of uniformity in the dopant distributions within the samples discussed here remains a matter of further scrutiny. Nonetheless, a clear distinction can be made between group A NWs (those containing a p-n junction in a core-shell homostructure) and group B NWs (those intentionally highly n-doped).

Upon fabrication, the photovoltaic response of the NW solar cells was measured. Figure 5.4 shows the fourth quadrant current-voltage characteristics of an ensemble of ITO contacted group A NWs, under dark (black, circular data points) and 2.6 Sun illumination (red, square data points) conditions. A clear photovoltaic response is evident, attributed to the sum contribution of all contacted NWs in the contact area. Although varying efficiency values were

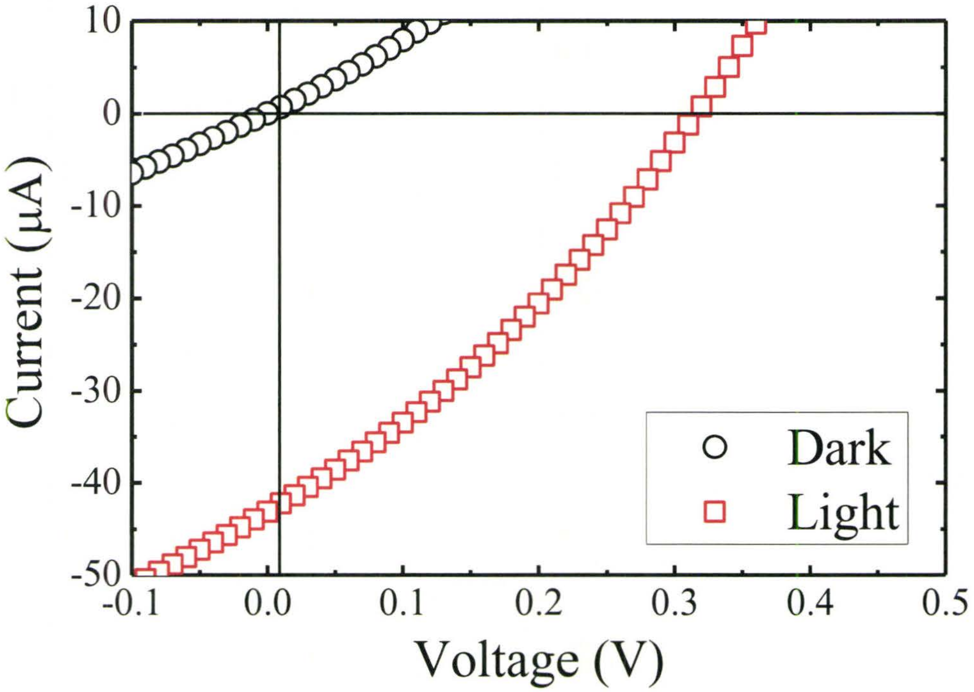

Figure 5.4 – Current-voltage characteristics of group A NWs, with ITO top contacts, under dark (black circles) and 2.6 Sun illumination (red squares) conditions. Group B NWs demonstrated no such photo-response.

measured from different contact dots, likely due to different numbers of NWs contacted by each dot and small growth temperature variances across the sample leading to slightly dissimilar NW structures, each contact dot exhibited reproducible efficiencies. The optimal efficiency curve, shown in Figure 5.4, was characterized by a short circuit current, I_{SC} = 43.1 μA (equivalently, J_{SC} = 8.57 mA/cm^2 for the 800 μm diameter contact dot), an open circuit voltage, V_{OC} = 0.32 V, a maximum power, P_{max} = 42.3 μW, a fill factor of 30.8%, and a maximum conversion efficiency of 0.32%. No such conversion response was evident in group B NWs (n-doped NWs) contacted with the transparent conductive oxide layer, indicating that the PV effect was due to the p-n junctions in group A NWs.

In comparison, previously reported ensemble contacted NW-based solar cells [51-54, 57, 266] have demonstrated maximum measured conversion efficiencies ranging between 0.1% to 4.5%. For example, coaxial p-n Si nanowire cells grown by the vapour-liquid-solid (VLS) process gave an efficiency of 0.1% on stainless steel substrates [52]. Si nanowire cells on glass substrates formed by wet electroless etching yielded efficiencies of 4.4% [266]. Coaxial p-n Si nanowire cells grown by the vapour-liquid-solid (VLS) process gave an efficiency of <1% on Si substrates [53]. An efficiency of 0.1% was reported for VLS-grown Si nanowires on multi-crystalline Si thin films on glass [51]. A single GaAs nanowire cell was recently reported with an efficiency of 4.5% [57]. The design most comparable to that of the current study is detailed in Ref. [54], where a photovoltaic effect was measured from vertically oriented GaAs NWs grown on n-GaAs (111)B substrates with a photo-conversion efficiency of 0.83%.

The lower efficiency values achieved on our CNT films, in comparison to the vertically oriented NWs, may be attributed to two main features. First, growth on CNT films results in NWs grown at a variety of dissimilar angles with respect to the film surface. During the contacting procedure, NWs oriented at more acute angles relative to the CNT film are likely to remain encapsulated by the photoresist layer used during the device processing. Consequently, only the NWs grown at relatively large angles to the substrate will be contacted, meaning that only an undetermined fraction of all NWs will have conductive pathways allowing for their photo-generated holes to be collected. Thus, the total contribution towards the quoted conversion efficiency is not necessarily a reflection of all NWs in the ensemble, but rather only the ones in contact with the ITO film.

Based on the analysis presented in Section 4.5, it is believed that an intimate, atomically abrupt interface exists between the carbon-nanotube film and overlaying GaAs NWs. The distinct Au-nanoparticle decoration technique used in the present study is not expected to dramatically alter the atomic nature of the NW/CNT interface. However, in view of the fact that the CNT film in the present study not only serves as the substrate, but also the electrical contact for the emitter layer of the solar cell, the conduction pathway at this junction requires further consideration. In fact, the second factor contributing to the noted efficiency degradation is the additional series resistance as a result of a barrier at the n-GaAs/CNT interface. Figure 5.5(a) shows a one-dimensional band diagram, with respect to axial distance along a single group A NW, assuming a NW length of 2 μm, and derived using a CNT film work-function of 4.5 eV [267]. The band diagram was calculated using a one-dimensional Poisson-Schrödinger equation solver, based upon a finite-difference method, and is described in Ref. [268]. Here, the p-type GaAs segment is shown on the left side, the n-type GaAs segment in the middle, and the CNT substrate on the right. Conduction band and valence band energies are depicted by black and red lines, respectively, while the

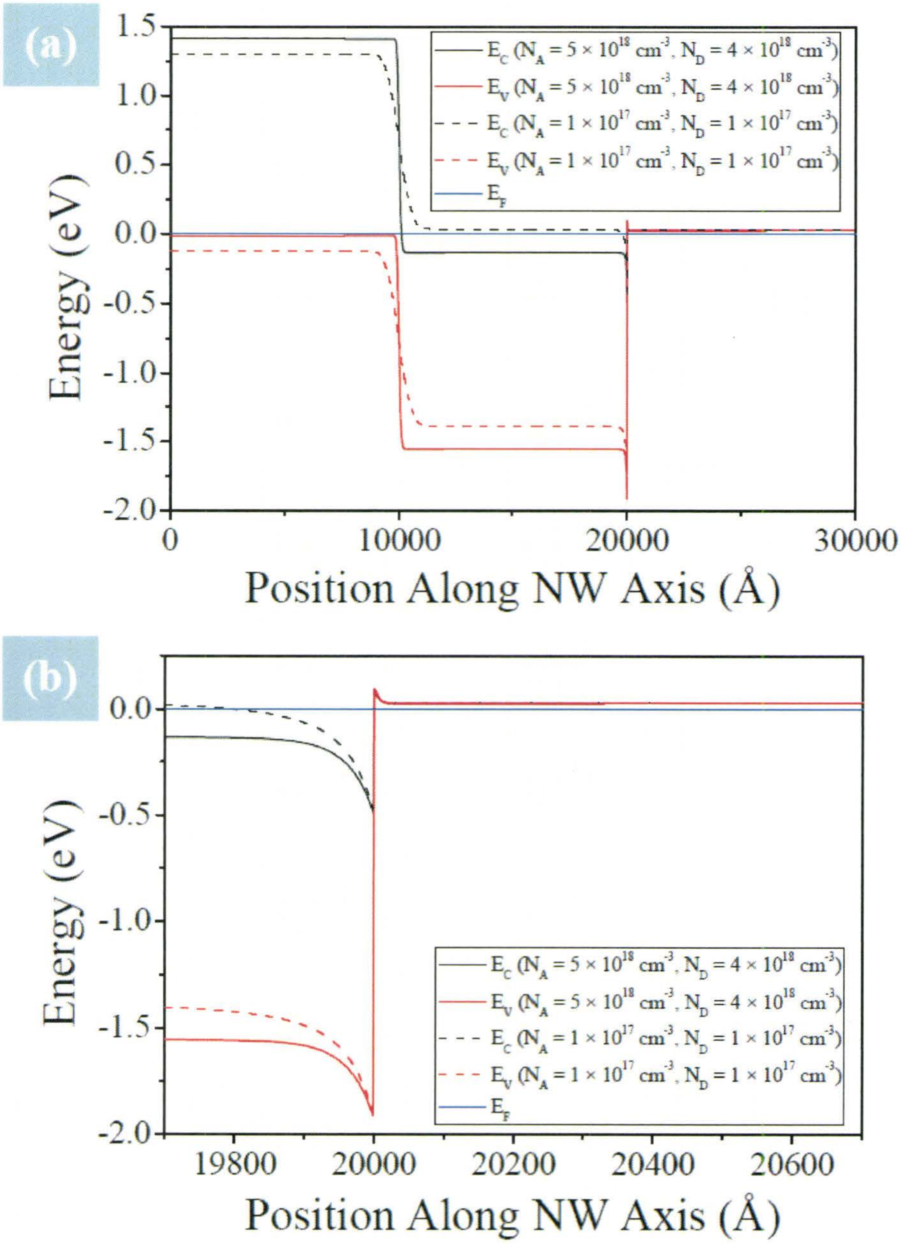

Figure 5.5 – (a) One-dimensional energy band diagram as a function of axial position along a single, 2 μm long, group A NW. The p-type segment, n-type segment, and CNT film are shown from left to right. Black and red lines denote the conduction and valence bands, respectively. The solid lines represent the band energies according to nominal doping levels quoted in the manuscript, while the dashed lines represent energies at a reduced dopant concentration of 1×10^{17} cm^{-3}. The solid blue line represents the Fermi energy, E_F. (b) Magnified view of (a) at the n-GaAs/CNT interface, showing the presence of a small energy barrier.

Fermi level is shown as a solid blue line. The solid lines represent the band structure anticipated from layers with the nominal doping concentrations, discussed previously. The dotted lines, on the other hand represent the energy bands that would result from acceptor and donor concentrations of 1×10^{17} cm^{-3}. This doping concentration is over one order of magnitude less than the quoted nominal level, and is shown as an expected lower limit of dopant incorporation within the nanowire core, according to Perea et al. [264]. Figure 5.5(b) shows a magnified view of the energy barrier present at the n-GaAs/CNT interface. The collection of photo-generated electrons is, therefore, preceded by either carrier tunneling from the n-GaAs NW segment to the underlying CNT film or by thermionic emission, dependent upon the concentration of dopants incorporated within the NW bulk.

It was previously shown, in Section 4.5, that the current-voltage characteristics of a collection of group A-type NWs exhibited asymmetric rectifications, and this diode-type behaviour was attributed directly to the p-n junctions incorporated within the NW structures. Characterization of electrical junctions within composite films has subsequently been conducted to determine the electrical quality of the junctions and whether ideal current flow is inhibited by Schottky effects at the interfaces. In Figure 5.6, the current-voltage characteristics of group A and B NWs, contacted by opaque contacts, are compared. As seen here, the present study shows a similar current rectification from the group A NWs, while group B NWs exhibit a linear behaviour over the

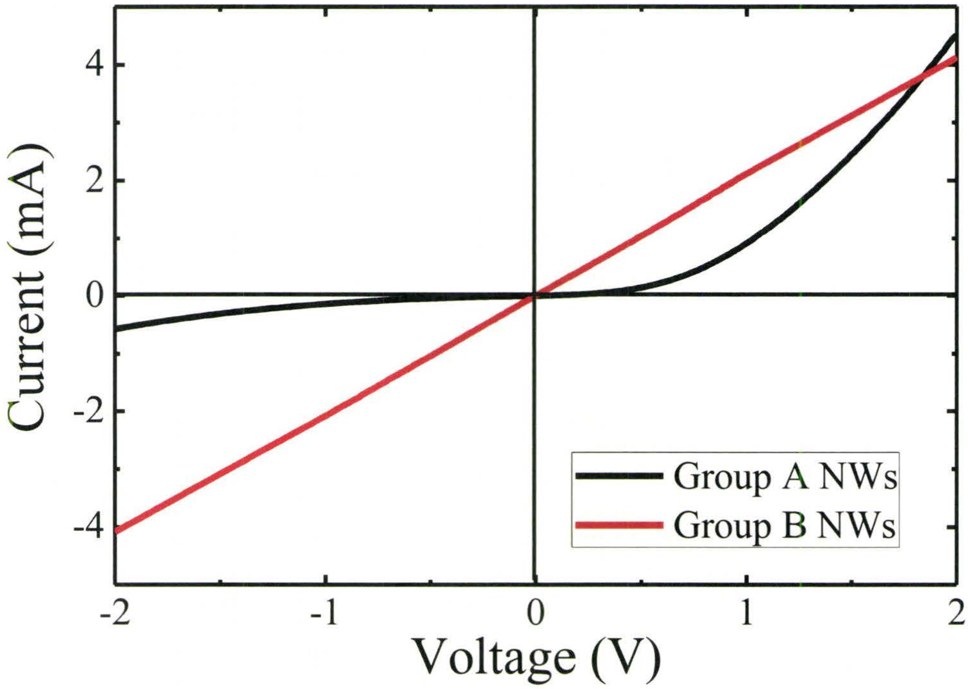

Figure 5.6 – Comparison of current-voltage characteristics of group A (black curve) and group B (red line) NWs, contacted with opaque Ti/Pt/Au and Ni/Ge/Au layers, respectively. Rectification is exhibited by the p-n junction NWs while Ohmic behaviour is exhibited by the heavily n-doped NWs.

same voltage range. Similarly, group B NWs contacted with ITO also exhibited linear current-voltage characteristics. We present this distinguishing feature (rectifying behaviour of p-n junction NWs in sample A versus Ohmic behaviour of n-doped NWs in sample B) as the defining trademark of the desired dopant activation in our NWs, and evidence that the diode-type response previously presented is not merely a manifestation of Schottky barriers at the n-GaAs/CNT interface. The low forward bias currents evident in the group A curve may be attributed to the partial depletion of the NWs. Furthermore, the aforementioned doping levels and NW density under each contact dot should exhibit resistance values on the order of tens of milli-Ohms, while the measured resistance is on the order of one hundred Ohms. This discrepancy may be ascribed to contact resistances suffered during the measurement process, as well as the effect of the GaAs/CNT interface.

The influence of the planar GaAs layer, deposited alongside the NWs, upon the observed photovoltaic effect was also studied. As a lateral p-n junction exists in this layer, it is important to distinguish whether this element contributes to the measured conversion efficiency. To this end, the group C control samples were prepared with total film thickness chosen to mimic the average thickness of the planar GaAs layer in group A NW samples, as determined through cross-sectional transmission electron microscopy analysis. This film was subsequently contacted with ITO dots, equal to the thickness of that situated atop the processed group A NWs (as revealed through SEM inspection), such that optical absorption would be comparable between the control and test samples. Under the illuminated solar cell testing conditions described above, the group C control sample reproducibly exhibited an open circuit voltage of $V_{OC} < 25\ \mu V$ and a short circuit current of $I_{SC} < 20$ nA, from all contact dots tested, representing negligible photovoltaic behaviour. The lack of a photovoltaic response in the control sample is chiefly attributed to a high concentration of grain boundaries in the polycrystalline GaAs film, which act as sites for the recombination of any photo-generated electron-hole pairs. Thus, the planar GaAs layer makes no photovoltaic

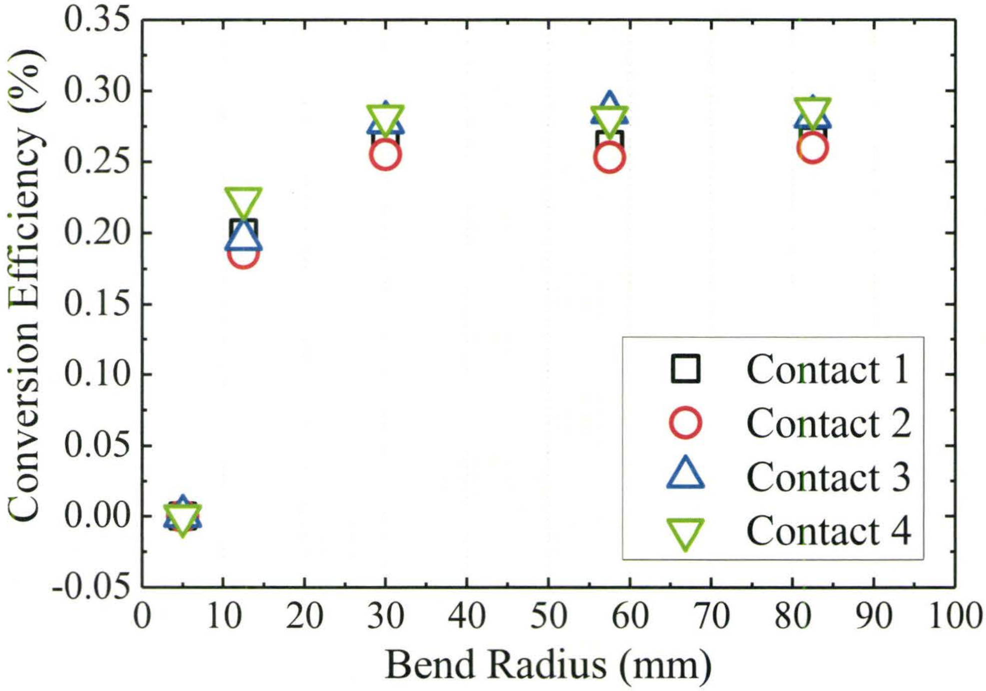

Figure 5.7 – Measured conversion efficiency as a function of device flexure at various bend radii (curvature increasing from right to left). A 25% decrease in efficiency is observed at a radius of 12.5 mm. Additional bending beyond this point results in device failure.

contribution and the energy conversion efficiency observed in group A samples can be attributed to the p-n junction NWs grown atop the CNT composite films.

Similarly, the potential for photocurrent generation resulting from a Schottky contact at the ITO/p-GaAs NW interface is not expected. Havard et al. [269] have shown that, under the annealing conditions employed in this study, Ohmic behaviour is anticipated at the ITO/p-GaAs NW interface. Furthermore, based on the work functions of ITO (4.6 – 5 eV) and p-GaAs (~5.5 eV), the current flow anticipated from a Schottky ITO/p-GaAs interface would occur in a direction opposite to the observed current flow as expected from the NW.

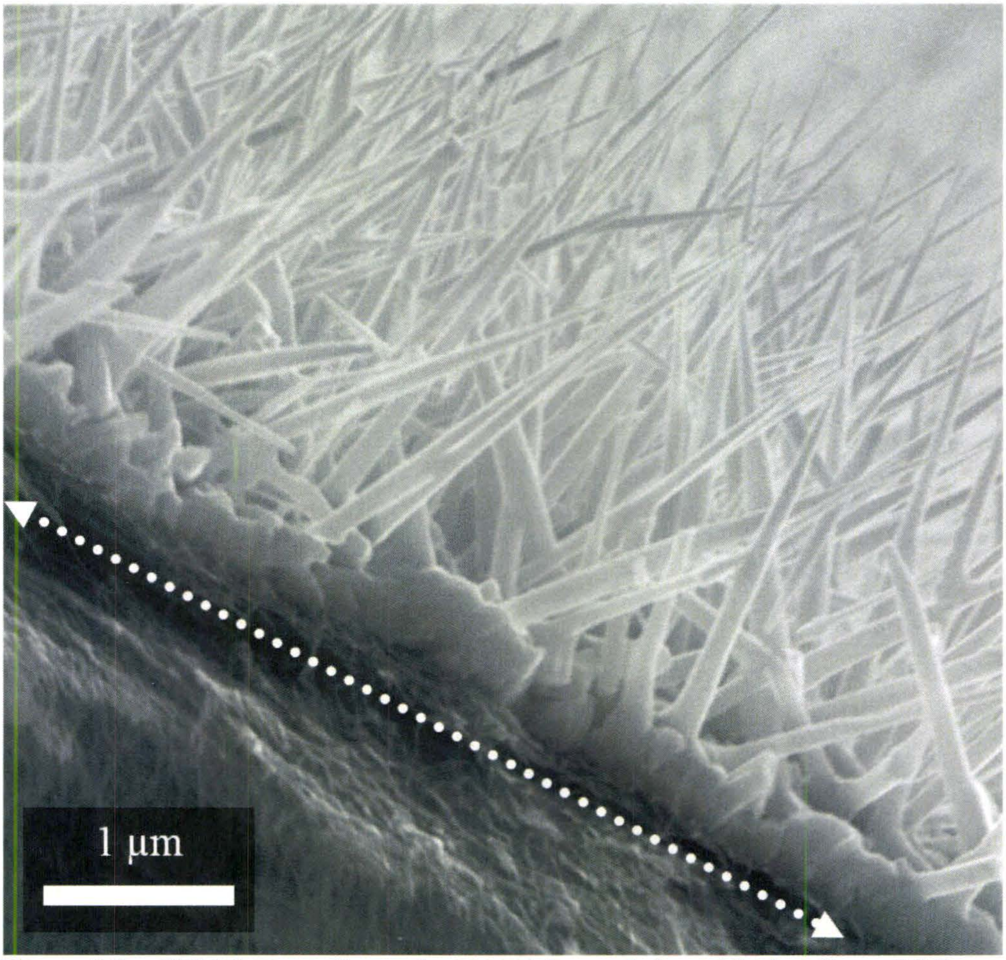

Figure 5.8 - SEM image of sample curved beyond the critical radius of failure. The white, dotted line indicates the fracture plane where the GaAs NWs are separated from the CNT substrate.

A final point of added interest is the degree of flexibility and operable range of the group A NW solar cells. The conversion efficiency of the fabricated devices was measured while being subjected to mechanical bending at various radii of curvature. Figure 5.7 plots measured efficiency as a function of bend radius between 82.5 mm and 5 mm, for 4 particular contact dots. As the curvature of the devices increased (from right to left in Figure 5.7), it was noted that conversion efficiencies were stable to a bend radius of 30 mm. Increasing curvature, to a bend radius of 12.5 mm, resulted in the degradation of efficiency by approximately 25%. Further flexure beyond this point led to the onset of full device failure. Based on SEM analysis of samples intentionally curved past the critical radius of failure, exemplified by the tilted-view SEM image shown in Figure 5.8, we attribute the breakdown mechanism to fracture of the polycrystalline GaAs film and its detachment, along with the NWs, from the conductive substrate. Thus, beyond the critical curvature, the photo-generated carriers are no longer effectively collected.

5.3 – Chapter Conclusions

In this chapter, a modified regime for the fabrication of Au nanoparticle-decorated CNT composite films has been presented, requiring no covalent functionalization of the CNTs. Coaxial p-n junction GaAs NWs were grown upon these flexible, conductive substrates and subsequently employed in the fabrication of photovoltaic cells. Thus, the light-harvesting potential of GaAs NWs on flexible CNT films has been demonstrated. The devices demonstrate photovoltaic behaviour under flexure, up to a bend radius of 12.5 mm. Further curvature leads to failure due to mechanical fracture and detachment of the GaAs film situated between the NWs. This approach may be employed for fabrication of NWs composed of a variety of material groups and of more complex core-shell geometries, suitable for flexible display and sensing applications.

Chapter 6

Conclusions and Future Work

6.1 – Summary and Conclusions

The growth of coaxial nanowires (NWs), composed of binary and ternary III-V compound semiconductor alloys, on foreign substrates has been the focus of the investigations presented in this thesis. The structural, optical, and electrical properties of the resultant NWs were explored and related to the underlying mechanisms that define the vapour-liquid-solid (VLS) growth model. The objective of this research was two-fold: First, to demonstrate control over the morphology and crystal structure of core-shell heterostructured NWs and to characterize the dependence of their properties upon their architecture and, second, to identify a suitable foreign substrate for the fabrication of flexible, NW-based opto-electronic devices.

In Chapter 3, extensive structural characterization of core-multishell GaP/GaAsP/GaP NW heterostructures, based primarily on analytical TEM techniques, was initially presented. Through a cylindrical approximation approach, the composition of the ternary compound segment was defined. The presence of stacking faults in the crystalline matrix of single NWs was directly visualized and described as zincblende lateral insertions in an otherwise wurtzite crystal.

Next, the same material system combination was employed for the extension of this work, in the growth of coaxial GaP/GaAsP superlattice heterostructured NWs. A particularly significant observation was that the formation of stacking faults was effectively quenched upon the introduction of growth interruptions at heterointerfaces. The achievement of phase purity was attributed to the change in group III adatom supply and, consequently, supersaturation of the Au-based seed. Thus, a growth interruption method for the formation of single phase wurtzite NW heterostructures was presented. Prior to the publication of this study, the growth interruption technique for crystal structure control had been otherwise unexplored. However, recently, many groups have adopted the so-called "supply interruption method" (SIM) for the phase perfection of NWs composed of various III-V semiconductor alloys [270-275]. The new method of crystal-phase engineering represents great progress toward the development of twinned superlattice homostructure devices [275].

Lastly, in Chapter 3, we explored the preferential incorporation of P in GaAsP segments, leading to the self-assembly of a P-rich core layer and an As-rich shell layer in each NW. The effect of this compositional variance and of a GaP passivation layer on the optical properties of the active GaAsP layers was examined. Furthermore, through M-PL spectroscopy analysis, an increase of the effective electronic diameter of the NWs was observed with surface passivation.

In Chapter 4, the growth of GaAs NWs on a number of foreign substrates was investigated. The growth surfaces evaluated included Si (100) and (111), stainless steel foils, glass substrates with polycrystalline Si buffer layers, carbon-nanotube (CNT) composite thin films, and highly ordered pyrolytic graphite (HOPG) substrates. Densely packed GaAs NW growth was realized on all growth surfaces, with the exception of HOPG surfaces. Instead, growth on HOPG substrates led to the observation of Ga-particle assisted NW formation. Various surface treatment methods allowed for the determination that growth did not stem from the standard oxide-mediated regime but, rather, from the likely preferential formation of Ga clusters which, in turn, seeded the growth of GaAs NWs.

Of the various substrates employed for growth, CNT thin films were chosen as the most suitable alternative for device applications. The basis for this selection was the high electrical conductivity and mechanical flexibility offered by the CNT composite films and the previously unexplored nature of the GaAs NW/CNT material combination. The GaAs NWs grown on this surface were shown to be optically active and the desired activation of dopants in the NWs was demonstrated.

In Chapter 5, the GaAs NW-CNT composite film system was employed in the fabrication of flexible solar cells. The NWs were demonstrated as the active, light-harvesting medium. Photovoltaic (PV) behaviour was effectively demonstrated, characterized by a conversion efficiency of 0.32 %. The flexible devices were shown to maintain optimal performance, under flexure, up to a bend radius of 12.5 mm.

The research presented here has shown the potential for the integration of high quality, single crystalline III-V semiconductor NWs with functional foreign substrates, allowing for the fabrication of large-area, flexible opto-electronic devices, with significant cost reductions compared to standard film-based technologies and otherwise homo-epitaxial approaches of NW growth. This work provides a foundation which can be extended to the growth of various material combinations and NW heterostructure geometries, and suitable for sensing, display, and energy conversion applications.

6.2 – Outline for Future Work

Several key routes exist through which the current work can be extended in future research efforts. In this final section, we present the preliminary results of three individual experiments, branching from the main focus of this Thesis, whose extension is anticipated to lead to contributions of significance to the field of NW research. These include investigations into the optical properties of core-multishell versus superlattice heterostructured GaP/GaAsP NWs, GaAs NWs grown on glass substrates with Si buffer layers for photovoltaic applications, and the use of CNT thin films as transparent and conductive top contact electrodes in NW-based solar cells and display applications. Additionally, a final consideration is given to the nature of stacking fault formation, worthy of further exploration.

6.2.1 – Optical Properties of Core-Multishell and Superlattice Nanowires

The optical properties of as-grown NW ensembles, as investigated through photoluminescence (PL) spectroscopy, and single NW specimens, as studied through micro-photoluminescence (μ-PL) spectroscopy, are considered in this section. In particular, comparisons are drawn between the optical characteristics of core-multishell and superlattice heterostructured GaP/GaAsP NW systems; namely, a comparison of the properties of the group C and group D systems, discussed in Section 3.3. On account of the indirect energy band structure of GaP, radiative carrier relaxation transitions in this binary alloy are inefficient and sufficient PL signals are not generated. Therefore, we focus, here, on PL emission generated from the GaAsP layers of the coaxial heterostructures.

All μ-PL experiments were conducted in the photonics laboratory of Dr. Gregor Weihs, at the Institute for Quantum Computing, in the University of Waterloo. Single NWs were dispersed on oxidized silicon substrates with surface oxide layers of approximately 350 nm thickness. After deposition of NWs on SiO_2 substrates, the samples were mapped through SEM imaging (conducted prior to μ-PL characterization) such that the locations of single NW specimens could be recorded along with their lengths and diameters. This process allowed for the association of a μ-PL spectra with a particular NW. Illumination was provided by a 532 nm excitation and spectra were recorded from samples maintained at approximately 7 K, unless otherwise stated.

In the case of PL experiments involving as-grown NW samples, all spectra were acquired at the Instituto de Física de São Carlos, at the University of São Paulo, Brazil, by Dr. Yuri Pusep. Here, cleaved as-grown samples were mounted onto Cu stubs and inserted into a liquid He cryostat maintained at 1.6 K. Excitation was provided by a Ar^+ laser centred at 514.5 nm.

We first consider the μ-PL spectra of single group C and D NWs. Recall that group D NWs are those with radial GaAsP layers with thickness on the order of 5 nm, while the group C NWs are of a core-multishell geometry with central GaAsP layers with thickness on the order of several tens of nanometres. Two main features of interest exist, in the comparison of the μ-PL spectra of these two

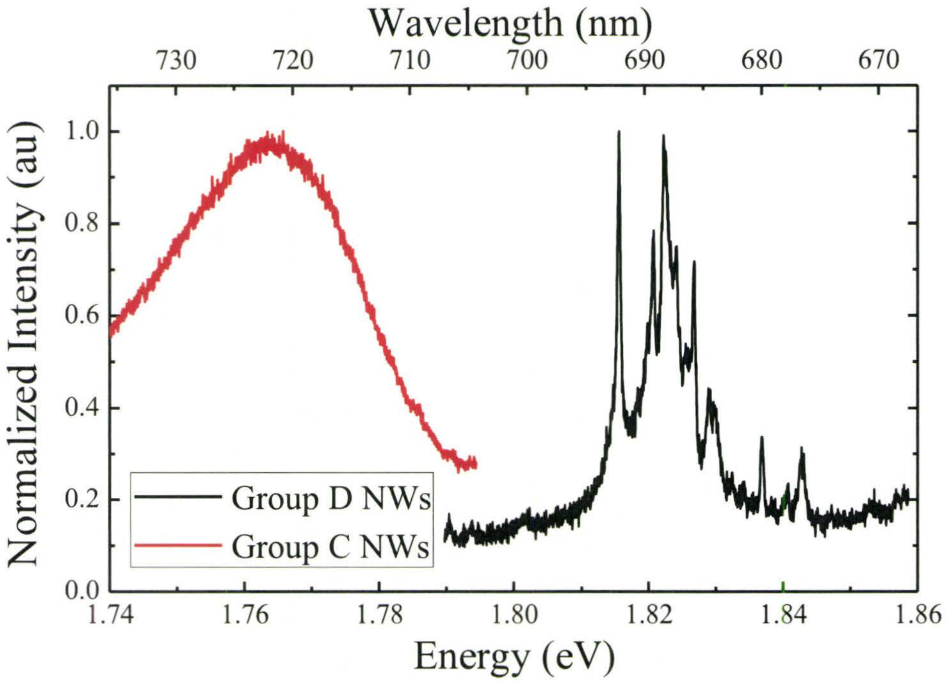

Figure 6.1 – Comparison of μ-PL spectra obtained from a single group C NW, with a core-multishell architecture (red line) and a single group D NW, with a superlattice geometry (black line).

distinct NW systems, as shown in Figure 6.1. The first feature is the clear blue-shift of the group D NW spectra, relative to that of the group C NW. Secondly, while a single broad peak is observed in the case of the core-multishell NW, with thicker GaAsP segment, the spectra of the superlattice NW is composed of multiple narrow features. Both of these spectral characteristics are attributed to the quantum confinement of carriers in the thin GaAsP layers of the superlattice heterostructured NW. Such confinement and discretization of electron states is not achieved in the relatively thick GaAsP layer of the group C NW. Consequently, the observed broad line-width is generated as a result of radiative transitions from a continuum of states present in both the conduction and valence bands. Thus, it can be said that the group C NWs exhibit a bulk-like optical behaviour.

Recently, several studies have been published on the μ-PL characteristics of single semiconductor NWs, with narrow line-width features similar to those present in the spectra of the group D NW shown in Figure 6.1. In these reports [276-281], the various numerous narrow single peaks were attributed to longitudinal Fabry-Pérot-type micro-cavity modes which arise on account of the NW geometry. In contrast, it is contended that the multiple narrow μ-PL signals emitted by the group D NWs cannot be attributed to similar micro-cavity modes, for two reasons: (1) In order to support multiple mode resonances, the NW geometry must consist of uniformly structured facets, with terminating planes at the bases and tips acting as reflecting mirrors [279]. The tapered NWs in the current study possess non-uniform facets with dissimilar base and tip planes. (2) The difference in the peak position or the relative mode spacing, $\Delta\lambda$, is inversely proportional to the length of the cavity (in this case, the length of the NW), L, according to:

$$\Delta\lambda = \frac{\lambda^2 m}{2Ln} \tag{6.1}$$

where λ is the wavelength, while m and n represent the mode number and refractive index of the medium, respectively [276]. In the case of GaAsP with the aforementioned composition, we can assume $n = 3.6$, from the weighted average of n values for GaP and GaAs [151]. As can be seen in Figure 6.1, the spacing of the spectral features is on the order of nanometres. For such small peak position

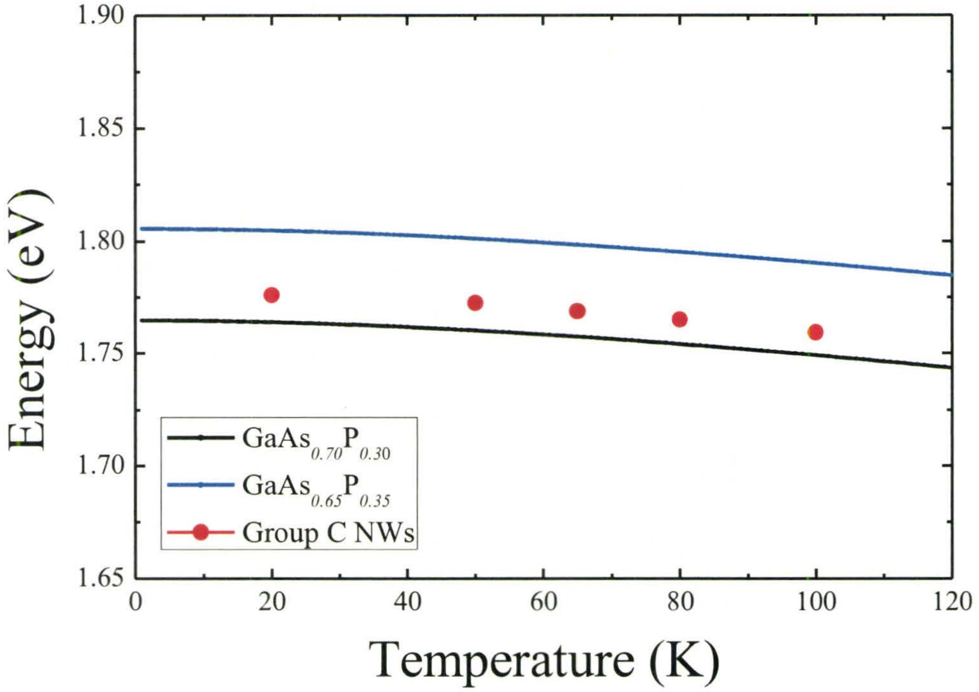

Figure 6.2 – Peak μ-PL measured at various temperatures from a single core-multishell (group C) NW (red data points) plotted alongside the temperature dependent bandgap energy of $GaAs_{0.70}P_{0.30}$ (black) and $GaAs_{0.65}P_{0.35}$ (blue).

differences, the NW length, based on Equation 6.1, should be on the order of tens of microns. Based on the structural analysis discussed in Section 3.3, we know that this condition is not satisfied by the NWs in question. Thus, the argument that the narrow features present in the μ-PL spectra of group D NWs can be attributed to resonant Fabry-Pérot-type micro-cavity modes is effectively disqualified. Rather, the multiple narrow features can likely be attributed to radiative transitions from confined states in GaAsP layers of varying thickness. The number of peaks can be accounted for by radiative transitions from multiple confined states within the same layer and also by transitions within multiple layers of dissimilar thickness, leading to dissimilar confinement energies.

Based on the temperature dependent μ-PL signals acquired from single group C NWs, the composition of the GaAsP layer can be approximated. From the weighted average values for α, β, and E_G $(T = 0)$ obtained for GaAs and GaP, from Ref. [152], the red-shift of the GaAsP bandgap energy with increasing temperature can be plotted according to the Varshni relation, shown in Equation 2.8. In Figure 6.2, this red-shift is plotted with respect to temperature for bulk $GaAs_{0.70}P_{0.30}$ and $GaAs_{0.65}P_{0.35}$. The peak PL position was measured from single core-multishell NWs at several temperatures, and is also plotted alongside the Varshni curve in Figure 6.2. Here, it can be seen that the composition of the GaAsP layer, obtained through μ-PL experiments, is in agreement with the values for composition, as determined through EDXS measurements (Section 3.2), within the aforementioned experimental error range.

The blue-shift observed in Figure 6.1, associated with thin GaAsP layers of the single superlattice NW, is also evident in the PL spectra obtained from a collection of as-grown NWs from the same sample. Figure 6.3 compares the PL signals emitted from an ensemble of group C and D NWs. Once again, a clear shift to higher energy is confirmed in the emission from the group D NWs. As before, the thick GaAsP layers of the group C samples exhibit bulk-type optical behaviour. The lack of narrow line-width peaks in the spectrum of the superlattice NWs can be accounted for by considering that the collective signal of a large number of structurally variant NWs is shown in Figure 6.3, each of which contribute a narrow signal to the total emission energy range.

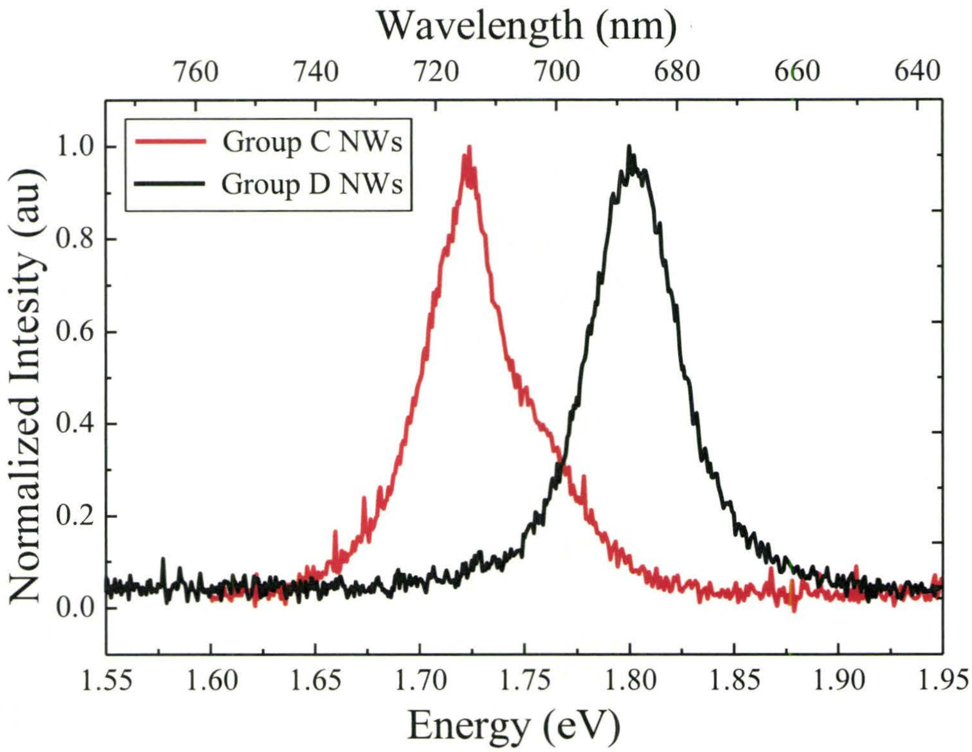

Figure 6.3 – Comparison of PL spectra obtained from a large collection of as-grown group C NWs, with core-multishell geometries (red line), and a large collection of as-grown group D NWs, with superlattice geometries (black line).

In summary, the optical characterization of 3-tiered core-multishell NWs and 11-tiered co-axial superlattice NWs was carried out through μ-PL spectroscopy of single NWs and PL spectroscopy of as-grown samples. The core-multishell NWs having GaAsP layers with thicknesses on the order of several tens of nanometres demonstrated broad line-width luminescence, which red-shifted with increasing temperature in agreement with the Varshni curve of $GaAs_{1-x}P_x$, for $0.30 < x < 0.35$. The superlattice NWs, on the other hand, demonstrated multiple narrow line-width spectral features, blue-shifted with respect to the peak energy of the core-multishell NW PL. This was attributed to confinement effects and discretization of states in the GaAsP layers of the superlattice NWs with thicknesses on the order of a few nanometres, as opposed to the generation of Fabry-Pérot micro-cavity modes in a single NW, as suggested in recent literature.

This work can benefit, in future efforts, from the accurate modelling of the quantization of energy states in GaAsP layers of particular thicknesses, such that each narrow line-width spectral feature, of the type shown in Figure 6.1, could be correlated to a corresponding GaAsP layer within a single SL NW, as determined through TEM experiments. Multiple tuneable wavelength emission could then be realized from stoichiometrically identical GaAsP layers, grown within a single NW, by controlling the radial thickness of each layer.

6.2.2 – GaAs NWs Grown on Glass Substrates for Photovoltaic Applications

The GaAs NWs grown on borosilicate glass substrates with 400 nm thick Si buffer layers (group B NWs, as described in Section 4.4) were employed in the fabrication of photovoltaic cells. The fabrication process utilized was similar to the approach outlined in Chapter 5, with the exception of the procedure for the formation of the back-side electrical contact; namely, the contact to the solar cell base layer. In the current approach, the perimeter of the sample was shadowed during growth, such that no GaAs was deposition on Si surface at the sample edges. After growth, the eight-step fabrication procedure listed below allowed for the formation of top-side contacts with the n-doped NW layers and the formation of back-side contacts with the p-doped substrate surface:

1. Using a mask to shadow the perimeter of the sample surface, a 150 nm thick SiO_x layer was deposited via plasma-enhanced chemical vapour deposition (PE-CVD). This allowed for the encapsulation of the NW surfaces and the surface of the planar GaAs layer.
2. S-1808 photoresist was spin-cast over the oxide-coated NWs.
3. A 60 s O_2-plama reactive-ion-etching (RIE) treatment was carried out for the removal of the photoresist along the oxide-coated NW tips.
4. The samples were subjected to a 5 s wet-etch in 10 % diluted buffered HF solution for the removal of SiO_x along the exposed NW tips.
5. An acetone bath lift-off procedure was carried out for the removal of the remaining photoresist.
6. Indium-tin-oxide (ITO) was deposited via sputtering, through a shadow mask, allowing for contacting of the NWs, covering a circular area with diameter of approximately 800 μm.
7. Using a mask to shadow the ITO contacted NWs in the central region, Al was deposited via thermal evaporation, along the perimeter of the sample surface.
8. A 30 s rapid thermal annealing (RTA) treatment was carried out at 400 °C for the formation of Ohmic contacts.

Figure 6.4 shows a cross-sectional pictorial representation of the fabricated devices. In this case, the Al contact is the contact to the p-doped layer, allowing

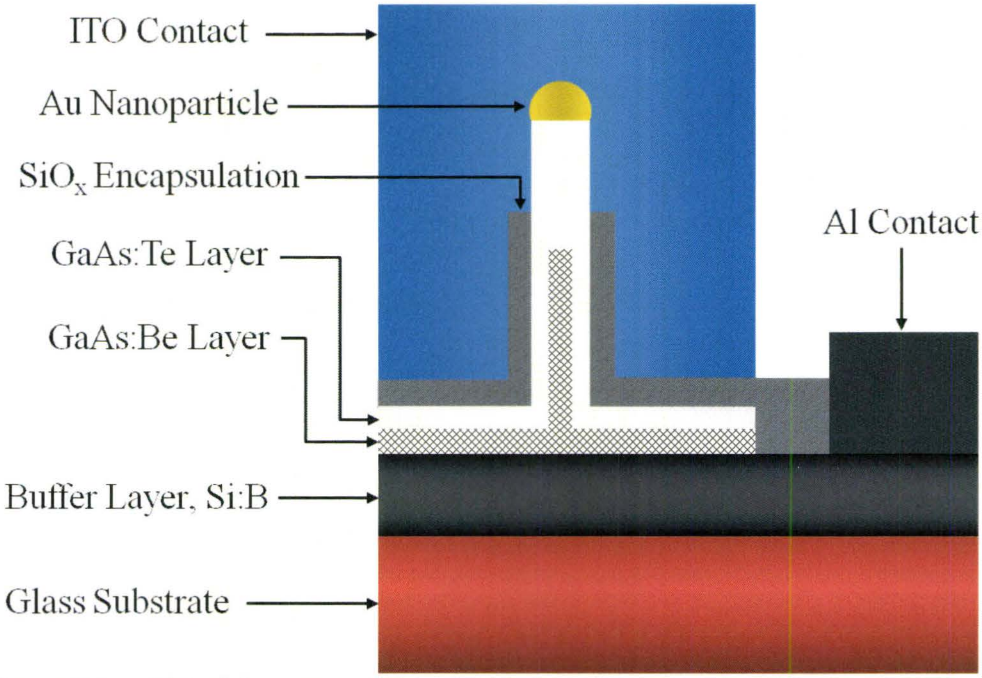

Figure 6.4 – Pictorial representation of fabricated solar cells, demonstrating the contacting scheme.

for a conductive pathway from the Si buffer layer to the ITO contact, through the NWs under a given contact spot.

The photovoltaic response of the fabricated devices was tested using a solar simulator with an A.M. 1.5 G filter, yielding an incident power of 2.6 Sun. The current-voltage characteristics of the devices, under dark and illuminated conditions are shown in Figure 6.5. A small PV response was observed, characterized by a fill factor of 29.2% and a conversion efficiency of approximately 0.01%. The relatively poor performance of these devices may be due to the large number of recombination sites along grain boundaries within the Si buffer layer and the poor quality of the interface formed by the Si and p-type GaAs layers. Furthermore, based on the deposition of a relatively thin GaAs film

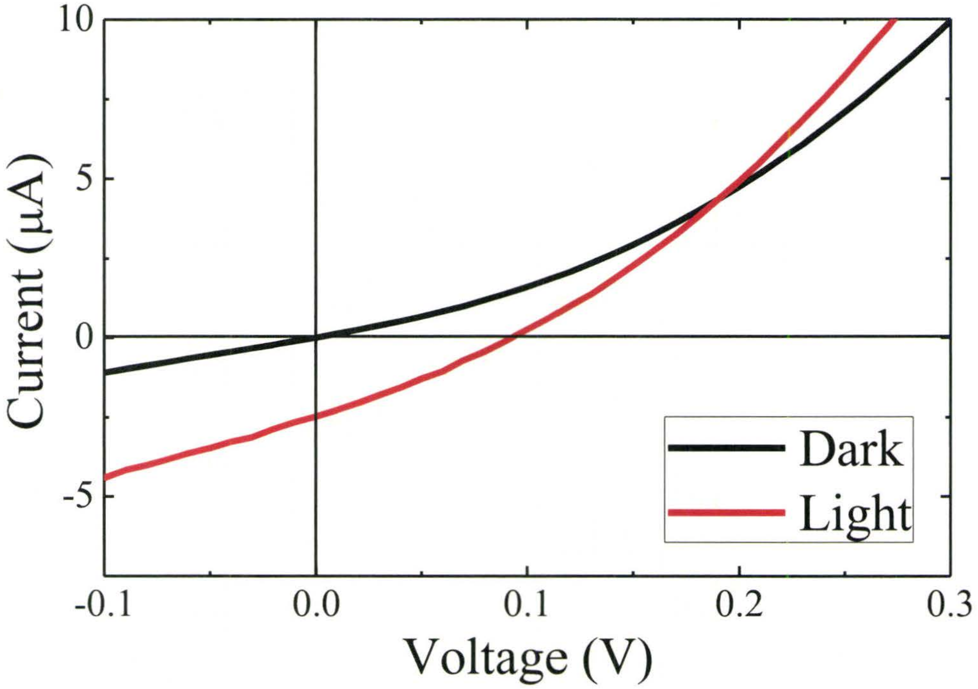

Figure 6.5 – Fourth quadrant current-voltage characteristics of fabricated NW-solar cells under dark (black curve) and illuminated (red curve) conditions.

on Si surfaces during NW growth (as considered in Sections 3.2 and 4.2), potential depletion effects within this layer may also have contributed to the low conversion efficiencies measured. Currently, further investigations into the nature of the GaAs/Si interface and the electrical and optical properties of the planar GaAs film deposited during NW growth are needed. GaAs NWs grown on stainless steel foils, of the type discussed in Section 4.3, could be appropriately doped for the formation of active p-n junction in core-shell morphologies. Similar device fabrication procedures, as described above and in Chapter 5, could then be employed for the production of flexible NW-based PV and LED devices.

6.2.3 – CNT Films as Transparent Electrodes in NW-Based Devices

The use of CNT composite films in NW-based opto-electronic device applications, as an alternative to conventional transparent conductive oxide films, deserves further attention. Although the integration of CNT films as transparent electrodes in standard planar technologies has previously been demonstrated [213-215], their use in NW-based devices has not been explored. Based on the inherent economic incentives and performance improvements offered as compared to indium-tin-oxide (ITO) films [212], the use of CNT films as top-contact layers for NW-based solar cells was investigated. The preliminary results on this contacting approach is presented here.

Three main contacting procedures were considered including spin-coating and drop-casting of single-walled CNTs from solution onto as-grown NW samples, as well as the direct placement of pre-fabricated CNT sheets on NW arrays. Both solution-based contacting procedures proved problematic. Spin-coating methods led to non-uniform coverage over the total area of the as-grown NW samples. Additionally, difficulties in CNT film thickness control arose on samples where NWs were randomly aligned, as evident by the plan-view SEM image shown in Figure 6.6(a). Drop-casting procedures allowed the deposited CNTs to bend and contort the as-grown NWs, compromising the arrangement and alignment of the NWs. This approach also allowed individual bundles of CNTs to contact the planar growth region, forming undesired short-circuit pathways. The plan-view SEM image, shown in Figure 6.6(b), illustrates both of these concerns.

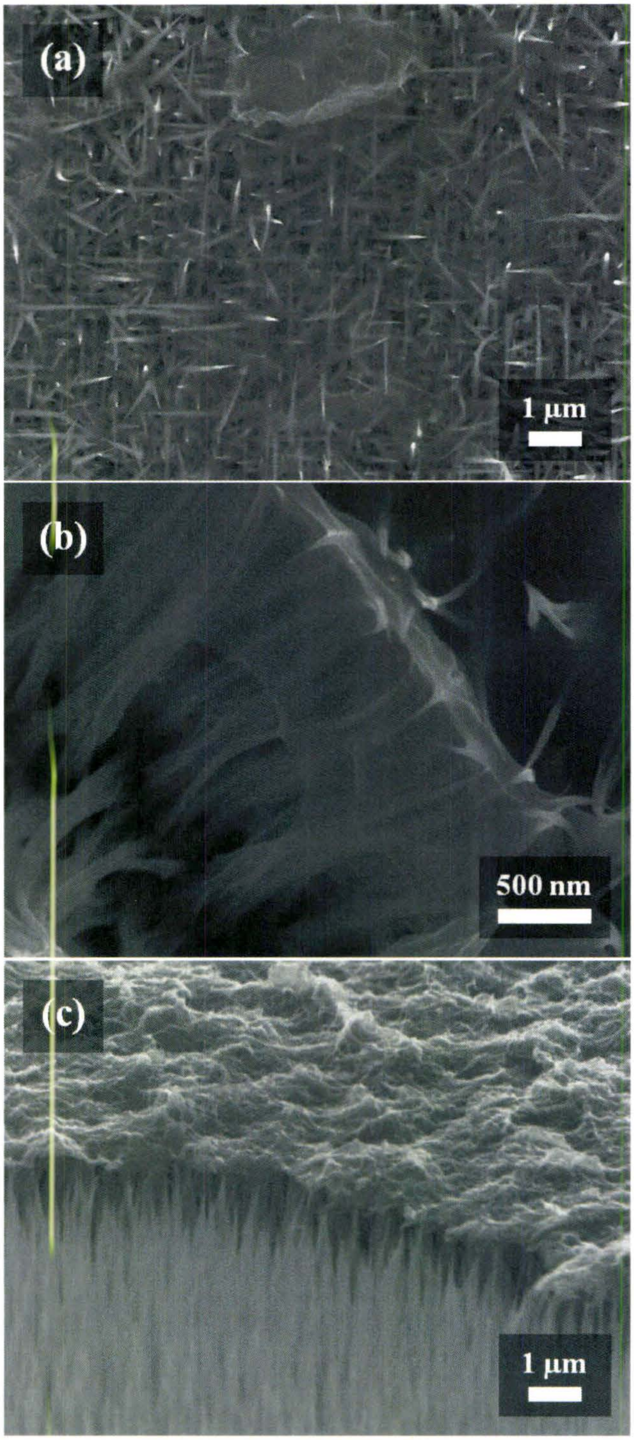

Figure 6.6 – Plan-view SEM images of CNT films contacted to as-grown NWs through (a) spin-coating and (b) drop-casting approaches. (c) Tilted-view SEM image of pre-fabricated CNT film positioned on an as-grown NW sample.

In contrast, the positioning of pre-fabricated CNT films over as-grown NW samples was free of the above contacting challenges. In this approach, CNT sheets of the desired thickness were formed through the previously described vacuum filtration method [224], removed from the Teflon membrane through which CNT solutions were filtered, cut to the desired coverage area, and physically positioned over the as-grown NW arrays. The tilted-view SEM image shown in Figure 6.6(c) demonstrates the positioning of the CNT film over the vertical as-grown NWs. The main benefits of this approach include the following: (1) the planar growth region of the sample is not contacted by the CNT top contact layer, eliminating the need for process intensive device fabrication schemes, (2) control is gained over the thickness, area, and position of the CNT film, and (3) NW structure and arrangement is not compromised in the contacting process.

Preliminary trials comparing the performance of solar cells fabricated from GaAs NWs grown on GaAs (100) substrates, contacted with ITO and CNT films, demonstrated approximately 80 % lower conversion efficiencies from the CNT top contacted devices. The lower efficiency values are attributed to (1) higher series resistance stemming from a contact layer with higher resistivity and (2) lack of contact to shorter NWs and NWs positioned at more acute angles relative to the substrate. The second factor is controllable, simply through the growth of vertical NWs. The first factor, however, requires further attention. Here, a point of interest is that when the CNT top-contacted samples were subjected to a 30 s annealing treatment at 400 °C, a 60 % increase in short-circuit current and an overall 75 % improvement in conversion efficiency was measured. In future efforts, optimization of the electrical conductivity and optical transparency of the CNT film is required. This is dependent not only upon the thickness of the CNT films, but also upon their purity and the formation of Ohmic contacts with the NWs. As such, the optimization of annealing treatments is necessary.

6.2.4 – Dependence of Stacking Fault Formation Upon Local Growth Parameter Fluctuations

The TEM analysis of GaAs NWs grown on Si (111) substrates (discussed in Section 4.2) led to a previously unreported observation of interest. Figure 6.7 clearly shows a nano-structure formed through the merging of three independent NWs. This merging effect is believed to result from the lateral contact of three initially separated, though closely situated, neighbouring NWs after substantial radial growth.

Three key observations can be made from Figure 6.7. First, we note that the sidewall tapering of the two outer NWs is more pronounced on the side that is unobstructed by the adjoined NW. This results from the reduced competition for diffusive adatoms on the sidewall not facing a neighbouring NW. Secondly, the height of the central NW is significantly shorter than that of its conjoined neighbours. In fact, the height of the central NW only slightly exceeds the height

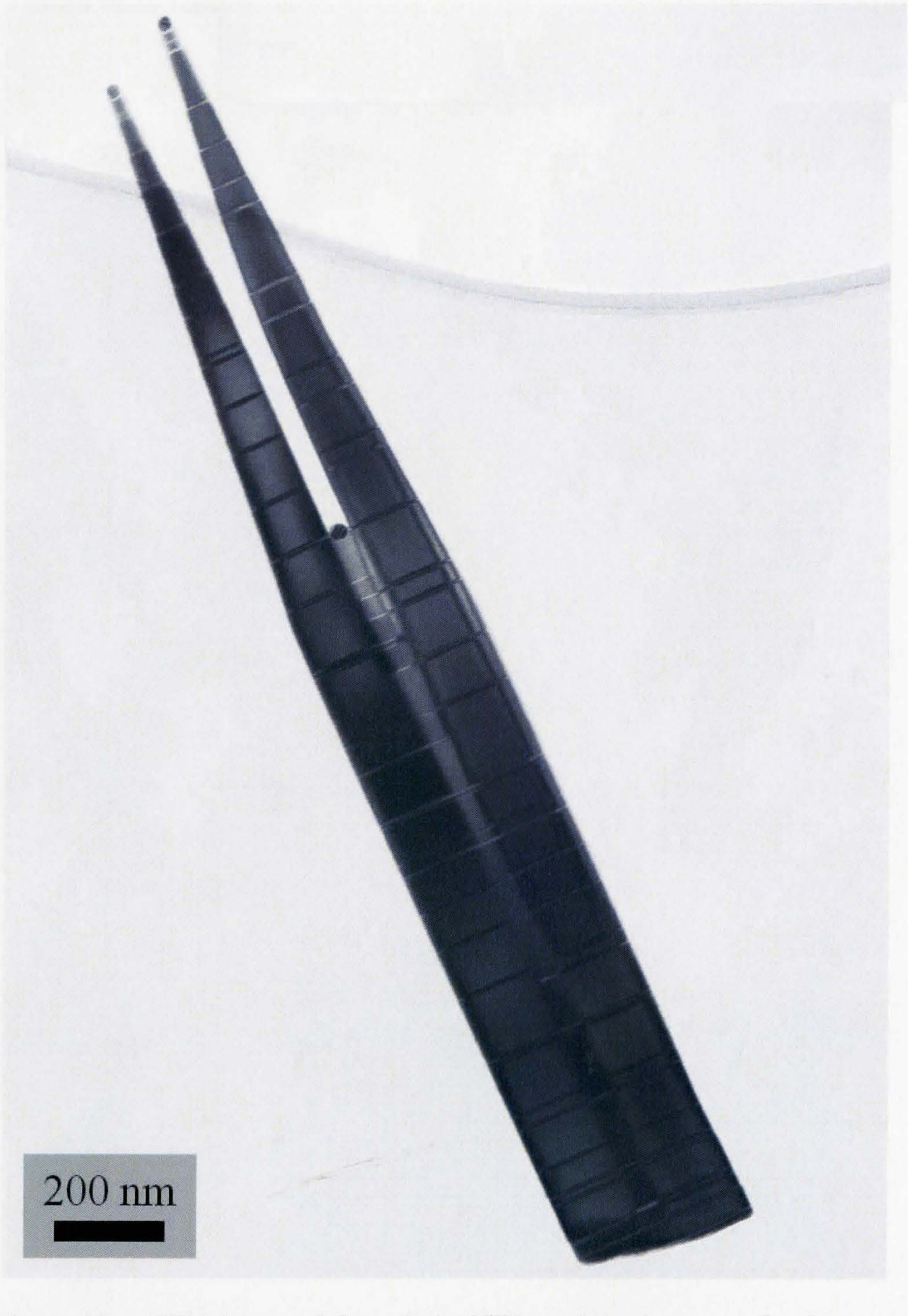

Figure 6.7 – TEM image of three GaAs NWs conjoined as a result of contact through sidewall growth. Coincident stacking fault locations are observed along the base and centre of the three conjoined NWs.

beyond which a tapering effect is observed in its neighbours. This point is, once again, rooted in the competition for diffusive adatoms. As the central NW is obstructed on two sides, in contrast to the outer NWs only being obstructed on one side, its formation is predominantly supported by growth species provided by the direct impingement contribution. Thus, the contribution to growth provided by adatoms impinging on the sidewalls and subsequently diffusing to the Au-seed is effectively reduced, in the case of the central NW.

The final and most noteworthy observation made from Figure 6.7 is the coincidence of stacking fault positions along the length of all three NWs, particularly at the base. The coincidence of stacking faults was consistently observed along all conjoined NW structures investigated. Consequently, it can be argued that the formation of stacking faults, in the initially separated and adjacently located individual NWs, occurred concurrently. This means that the formation of stacking faults is rooted in a phenomenon that is commonly experienced within a given location. Otherwise stated, the formation of stacking faults is dependent upon the local fluctuation of growth conditions. This concept can be further examined in future work through the growth of position- and size-controlled NWs under variable growth conditions.

References

[1] R. S. Wagner and W. C. Ellis, Appl. Phys. Lett. **4**, 89 (1964)

[2] P. Yang, R. Yan, and M. Fardy, Nano Lett. **10**, 1529 (2010)

[3] M. B. Panish and H. Temkin, *Gas Source Molecular Beam Epitaxy*, Springer-Verlag, Berlin (1993)

[4] E. P. A. M. Bakkers, J. A. van Dam, S. De Franceschi, L. P. Kouwenhoven, M. Kaiser, M. Verheijen, H. Wodergem, and P. van der Sluis, Nat. Mater. **3**, 769 (2004)

[5] M. Zervos adn L.-F. Feiner, J. Appl. Phys. **95**, 281 (2004)

[6] L. Pavesi, L. Dal Negro, C. Mazzoleni, G. Franzo, and F. Priolo, Nature **408**, 440 (2000)

[7] Y. Yang, J. Bao, C. Wang, and M. J. Aziz, J. Appl. Phys. **107**, 123109 (2010)

[8] J. Tatebayashi, A. Lin, P. S. Wong, R. F. Hick, and D. L. Huffaker, J. Appl. Phys. **108**, 034315 (2010)

[9] G. Zhang, K. Tateno, H. Gotoh, T. Sogawa, H. Nakano, Jpn. J. Appl. Phys. **49**, 015001 (2010)

[10] T. Martensson, C. P. T. Svensson, B. A. Wacaser, M. W. Larsson, W. Seifert, K. Deppert, A. Gustafsson, L. R. Wallenberg, and L. Samuelson, Nano Lett. **4**, 1987 (2004)

[11] Y. S. Park, S.-H. Lee, J.-E. Oh, C.-M. Park, and T.-W. Kang, J. Cryst. Growth **282**, 313 (2005)

[12] M. S. Gudiksen, L. J. Lauhon, J. Wang, D. C. Smith, and C. M. Lieber, Nature **4**, 617 (2002)

[13] C. P. T. Svensson, T. Martensson, J. Tragardh, C. Larsson, M. Rask, D. Hessman, L. Samuelsson, J. Ohlsson, Nanotechology **19**, 305201 (2008)

[14] K. Tomioka, J. Motohisa, S. Hara, K. Hiruma, and T. Kukui, Nano Lett. **10**, 1639 (2010)

[15] F. Patolsky, G. Zheng, O. Hayden, M. Lakadamyali, X. Zhuang, and C. M. Lieber, Proc. Natl. Acad. Sci. USA **101**, 14017 (2004)

[16] C. E. Linsmeier, C. N. Prinz, L. M. E. Pettersson, P. Caroff, L. Samuelson, J. Schouenborg, L. Montelius, and N. Danielsen, Nano Lett. **9**, 4184 (2009)

[17] C. J. Novotny, E. T. Yu, and P. K. L. Yu, Nano Lett. **8**, 775 (2008)

[18] L. Rigutti, M. Tchernycheva, A. De Luna Bugallo, G. Jacopin, F. H. Julien, L. F. Zagonel, K. March, O. Stephan, M. Kociak, and R. Songmuang, Nano Lett. **10**, 2939 (2010)

[19] A. De Luna Bugallo, M. Tchernycheva, G. Jacopin, L. Rigutti, F. H. Julien, S.-T. Chou, Y.-T. Lin, P.-H. Tseng, and L.-W. Tu, Nanotechnology **21**, 315201 (2010)

[20] C. Soci, A. Zhang, X.-Y. Bao, H. Kim, Y. Lo, D. Wang, J. Nanosci. Nanotechnol. **10**, 1 (2010)

[21] B. Hua, J. Motohisa, Y. Kobayashi, S. Hara, and T. Fukui, Nano Lett. **9**, 112 (2009)

[22] J. C. Johnson, H.-J. Choi, K. P. Knutsen, R. D. Schaller, P. Yang, R. J. Saykally, Nat. Mater. **1**, 106 (2002)

[23] J. Heinrich, A. Huggenberger, T. Heindel, S. Reitzenstein, S. Hofling, L. Woschech, and. A. Forchel, Appl. Phys. Lett. **96**, 211117 (2010)

[24] A. Tribu, G. Sallen, T. Aichele, R. Andre, J.-P. Poizat, C. Bougerol, S. Tatarenko, and K. Kheng, Nano Lett. **8**, 4326 (2008)

[25] H. S. Bennett, J. Res. Natl. Inst. Stand. Technol. **105**, 429 (2000)

[26] A. Nduwimana, R. N. Musin, A. M. Smith, and X.-Q. Wang, Nano Lett. **8**, 3341 (2008)

[27] Z. Zanolli, M.-E. Pistol, L. E. Froberg, and L. Samuelson, J. Phys.: Condens. Matter **19**, 295219 (2007)

[28] A. Lugstein, A. M. Andrews, M. Steinmair, Y.-J. Hyun, E. Bertagnollo, M. Weil, P. Pongratz, M. Schrambock, T. Roch, and G. Strasser, Nanotechnology **18**, 355306 (2007)

[29] K. A. Dick, K. Deppert, M. W. Larsson, W. Seifert, L. R. Wallenberg, and L . Samuelson, Nanotechnology **18**, 035601 (2007)

[30] K. A. Dick, K. Deppert, M. W. Larsson, T. Martensson, W. Seifert, L. R. Wallenberg, and L . Samuelson, Nat. Mater. **3**, 380 (2004)

[31] Y. Huang and C. M. Lieber, Pure Appl. Chem. **76**, 2051 (2004)

[32] F. Qian, S. Gradecak, Y. Li, C.-Y. Wen, and C. M. Lieber, Nano Lett. **5**, 2287 (2005)

[33] N. Skold, M.-E. Pistol, K. A. Dick, C. Pryor, J. B. Wagner, L. S. Karlsson, L. Samuelson, Phys. Rev. B **80**, 041312(R) (2009)

[34] A. Nadarajah, R. C. Word, J. Meiss, and R. Konenkamp, Nano Lett. **8**, 534 (2008)

[35] T. Martensson, M. Borgstrom, W. Seifert, B. J. Ohlsson, and L. Samuelson, Nanotechnology **14**, 1255 (2003)

[36] T. Martensson, P. Carlberg, M. Borgstrom, L. Montelius, W. Seifert, and L. Samuelson, Nano Lett. **4**, 699 (2004)

[37] W. Hallstrom, T. Martensson, C. Prinz, P. Gustavsson, L. Montelius, L. Samuelson, and M. Kanje, Nano Lett. **7**, 2960 (2007)

[38] W. Kim, J. K. Ng, M. E. Kunitake, B. R. Conklin, and P. Yang, J. Am. Chem. Soc. **129**, 7228 (2007)

[39] A. Javey, S. W. Nam, R. S. Friedman, H. Yan, and C. M. Lieber, Nano Lett. **7**, 773 (2007)

[40] T. Ito and S. Okazaki, Nature **406**, 1027 (2000)

[41] A. Kandala, T. Betti, and A. Foncuberta i Morral, Phys. Status. Solidi A **206**, 173 (2009)

[42] B. M. Kayes, H. A. Atwater, and N. S. Lewis, J. Appl. Phys. **97**, 114302 (2005)

[43] B. Tian, T. J. Kempa, and C. M. Lieber, Chem. Soc. Rev. **38**, 16 (2009)

[44] M. D. Kelzenberg, S. W. Boettcher, J. A. Petykiewicz, D. B. Turner-Evans, M. C. Putnam, E. L. Warren, J. M. Spurgeon, R. M. Briggs, N. S. Lewis, and H. A. Atwater, Nat. Mater. **9**, 239 (2010)

[45] L. Tsakalakos, Mater. Sci. Eng. R. **62**, 175 (2008)

[46] O. L. Muskens, J. Gomez Rivas, R. E. Algra, E. P. A. M. Bakkers, and A. Lagendijk, Nano Lett. **8**, 2638 (2008)

[47] N. J. Ekins-Daukes, K. W. J. Barnham, J. P. Connolly, J. S. Roberts, J. C. Clark, G. Hill, and M. Mazzer, Appl. Phys. Lett **75**, 4195 (1999)

[48] W. Shockley and H. J. Queisser, J. Appl. Phys **32**, 510 (1961)

[49] M. D. Kelzenberg, D. B. Turner-Evans, B. M . Kayes, M. A. Filler, M. C. Putnam, N. S. Lewis, and H. A. Atwater, Nano Lett. **8**, 710 (2008)

[50] B. Tian., X. Zheng, T. J. Kempa, Y. Fang, N. Yu, G. Yu, J. Huang, and C. M . Lieber, Nature **449**, 885 (2007)

[51] T. Stelzner, M. Pietsch, G. Andra, F. Falk, E. Ose, and S. Christiansen, Nanotechnology **19**, 295203 (2008)

[52] L. Tsakalakos, J. Balch, J. Fronheiser, B. A. Korevaar, O. Sulima, and J. Rand, Appl. Phys. Lett. **91**, 233117 (2007)

[53] O. Gunawan and S. Guha, Sol. Energy Mater. Sol. Cells **93**, 1388 (2009)

[54] J. Czaban, D. A. Thompson, and R. R. LaPierre, Nano Lett. **9**, 148 (2009)

[55] H. Bi and R. R. LaPierre, Nanotechnology **20**, 465205 (2009)

[56] G. E. Cirlin, A. D. Bouravleuv, I. P. Schnikov, Yu. B. Smasoneko, V. G. Dubrovskii, E. M. Arakcheeva, E. M. Tanklevskaya, and P. Werner, Nanoscale Res. Lett. **5**, 360 (2010)

[57] C. Colombo, M. Heiss, M. Gratzel, and A. Fontcuberta i Morral, Appl. Phys. Lett. **94**, 173108 (2009)

[58] K. A. Dick, Prog. Cryst. Growth Ch. **54**, 138 (2008)

[59] R. Adelung, O. Cenkaktas, J. Franc, A. Biswas, R. Kunz, M. Elbahri, U. Schurmann, and F. Faupel, Nat. Mater. **3**, 375 (2004)

[60] G. Sauer, G. Brehm, S. Schneider, K. Nielsch, R. B. Wehrspohn, J. Choi, H. Hofmaister, and U. Gosele, J. Appl. Phys. **91**, 3243 (2002)

[61] A. Gustafsson, F. Reinhardt, G. Biasiol, and E. Kapon, Appl. Phys. Lett. **67**, 3673 (1995)

[62] E. C. Garnett and P. Yang, J. Am. Chem. Soc. **130**, 9224 (2008)

[63] K.-Q. Peng, Y.-J. Yan, S.-P. Gao, and J. Zhu, Adv. Matter **14**, 1164 (2002)

[64] P. Mohan, J. Motohisa, and T. Fukui, Appl. Phys. Lett. **88**, 013110 (2006)

[65] H. J. Fan, P. Werner, and M. Zacharais, Small **2**, 700 (2006)

[66] F. C. Frank, Discussions Faraday Soc. **5**, 48 (1949)

[67] E. I. Givargizov, J. Cryst. Growth **31**, 20 (1975)

[68] M. Yazawa, M. Koguchi, and K. Hiruma, Appl. Phys. Lett. **58**, 1080 (1991)

[69] M. Yazawa, M. Koguchi, A. Muto, M. Ozawa, K. Hiruma, Appl. Phys. Lett. **61**, 2051 (1992)

[70] M. H. Magnusson, K. Deppert, J.-O. Malm, J.-O. Bovin, and L. Samuelson, J. Nanopart. Res. **1**, 243 (1999)

[71] C. P. T. Svensson, W. Seifert, M. W. Larsson, L. R. Wallenberg, J. Stangl, G. Bauer, and L. Samuelson, Nanotechnology **16**, 936 (2005)

[72] S. A. Dayeh, E. T. Yu, and D. Wang, Nano Lett. **7**, 2486 (2007)

[73] V. L. Colvin, A. N. Goldstein, and A. P. Alivisatos, J. Am. Chem. Soc. **114**, 5221 (1992)

[74] K. C. Grabar, P. C. Smith, M. D. Musick, J. A. Davis, D. G. Walter, M. A. Jackson, A. P. Guthrie, and M. J. Natan, J. Am. Chem. Soc. **118**, 1148 (1996)

[75] A. Doron, E. Katz, and I. Willner, Langmuir **11**, 1313 (1995)

[76] F. Burmeister, C. Schafle, T. Matthes, M. Bohmisch, J. Boneberg, and P. Leiderer, Langmuir **13**, 2983 (1997)

[77] V. G. Dubrovskii, G. E. Cirlin, I. P. Soshnikov, A. A. Tonkikh, N. V. Sibriev, Yu. B. Samsonenko, and V. M. Ustinov, Phys. Rev. B. **71**, 205325 (2005)

[78] J. C. Harmand, G. Patriarche, N. Pere-Laperne, M.-N. Merat-Combes, T. Travers, and F. Glas, Appl. Phys. Lett. **87**, 203101 (2005)

[79] M. C. Plante and R. R. LaPierre, J. Cryst. Growth **286**, 394 (2006)

[80] L. E. Jensen, M. T. Bjork, S. Jeppesen, A. I. Persson, B. J. Ohlsson, and L. Samuelson, Nano Lett. **4**, 1961 (2004)

[81] W. Lee, M. Alexe, K. Nielsch, and U. Gosele, Chem. Mater. **17**, 3325 (2005)

[82] H. J. Fan, W. Lee, R. Scholz, A. Dadgar, A. Krost, K. Nielsch, and M. Zacharias, Nanotechnology **16**, 913 (2005)

[83] Z. H. Wu, X. Y. Mei, D. Kim, and H. E. Ruda, Appl. Phys. Lett. **81**, 5177 (2002)

[84] B. Nikoobakht, C. A. Michaels, S. J. Stranick, and M. D. Vaudin, Appl. Phys. Lett. **85**, 3244 (2004)

[85] R. Glass, M. Moller, and J. P. Spatz, Nanotechnology **14**, 1153 (2003)

[86] R. Glass, M. Arnold, E. A. Cavalcanti-Adam, J. Blummel, C. Haferkemper, C. Dodd, and J. P. Spatz, New J. Phys. **6**, 101 (2004)

[87] I. Regolin, V. Khorenko, W. Prost, F. J. Tegude, D. Sudfeld, J. Kastner, G. Dumpich, K. Hitzbelck, and H. Wiggers, J. Appl. Phys **101**, 054318 (2007)

[88] G. T. Wang, A. A. Talin, D. J. Werder, J. R. Creighton, E. Lai, R. J. Anderson, and I. Arslan, Nanotechnology **17**, 5773 (2006)

[89] F. Martelli, S. Rubini, M. Piccin, G. Bais, F. Jabeen, S. De Franceshi, V. Grillo, E. Carlino, F. D'Acapito, F. Boscherini, S. Cabrini, M. Lazzarino, L. Businaro, F. Romanato, and A. Franciosi, Nano Lett. **6**, 2130 (2006)

[90] M. E. Messing, K. Hillerich, J. Johansson, K. Deppert, and K. A. Dick, Gold Bull. **42**, 172 (2009)

[91] K. Hiruma, M. Yazawa, T. Katasuyama, K. Ogawa, K. Haraguchi, M. Koguchi, and H. Kakibayashi, Appl. Phys. Lett. **77**, 447 (1995)

[92] B. J. Ohlsson, M. T. Bjork, M. H. Magnusson, K. Deppert, L. Samuelson, and L. R. Wallenberg, J. Appl. Phys. **79**, 3335 (2001)

[93] B. Wolfgang, V. M. Kaganer, A. Trampert, H.-S. Schonherr, Q. Gong, R. Notzel, L. Daweritz, and K. H. Ploog, J. Cryst. Growth **51**, 227 (2001)

[94] V. G. Dubrovskii, G. E. Cirlin, and V. M. Ustinov, Semiconductors **43**, 1539 (2009)

[95] C. Chen, M. C. Plante, C. Fradin, and R. R. LaPierre, J. Mater. Res. **21**, 2801 (2006)

[96] J. Johansson, C. P. T. Svensson, T. Martensson, L. Samuelson, and W. Seifert, J. Phys. Chem. B. **109**, 13567 (2005)

[97] J. Johansson, B. A. Wacaser, K. A. Dick, and W. Seifert, Nanotechnology **17**, S355 (2006)

[98] V. G. Dubrovskii and. N. V. Sibriev, Phys. Rev. B. **77**, 035414 (2008)

[99] M. Tchernycheva, L. Tavers, G. Patriarche, F. Glas, J.-C. Harmand, G. E. Cirlin, and V. G. Dubrovskii, J. Appl. Phys. **102**, 094313 (2007)

[100] M. C. Plante and R. R. LaPierre, J. Appl. Phys. **105**, 114304 (2009)

[101] R. L. Schwoebel and E. J. Shipsey, J. Appl. Phys. **37**, 3682 (1966)

[102] G. Ehrlich and F. G. Hudda, J. Chem. Phys. **44**, 1039 (1966)

[103] E. I. Givargizov and A. A. Chernov, Kristallografiya **18**, 147 (1973)

[104] C. Soci, X.-Y. Bao, D. P. R. Aplin, and D. Wang, Nano Lett. **8**, 4275 (2008)

[105] J. B. Hannon, S. Kodambaka, F. M. Ross, and R. M. Tromp, Nature **440**, 69 (2006)

[106] J. C. Harmand, M. Tchernycheva, G. Patriarche, L. Travers, F. Glas, and G. Cirlin, J. Cryst. Growth **301**, 853 (2007)

[107] S. A. Dayeh, E. T. Yu, and D. Wang, Nano Lett. **9**, 1967 (2009)

[108] M. C. Plante and R. R. LaPierre, Nanotechnology **19**, 495603 (2008)

[109] T. I. Kamins, R. Stanley Williams, D. P. Basile, T. Hesjedal, and J. S. Harris, J. Appl. Phys. **89**, 1008 (2001)

[110] A. I. Persson, M. W. Larsson, S. Stenstrom, B. J. Ohlsson, L. Samuelson, and L. R. Wallenberg, Nat. Mater. **3**, 677 (2004)

[111] K. A. Dick, K. Deppert, T. Martensson, B. Mandl, L. Samuelson, and W. Seifert, Nano Lett. **5**, 761 (2005)

[112] K. A. Dick, K. Deppert, L. S. Karlsson, R. Wallenberg, L. Samuelson, and W. Seifert, Adv. Funct. Mater. **15**, 1603 (2005)

[113] H. J. Joyce, Q. Gao, H. H. Tan, C. Jagadish, Y. Kim, X. Zhang, Y. Guo, and J. Zou, Nano Lett. **7**, 921(2007)

[114] K. A. Dick, S. Kodambaka, M. C. Reuter, K. Deppert, L. Samuelson, W. Seifert, L. R. Wallenberg, and F. M. Ross, Nano Lett. **7**, 1817 (2007)

[115] E. J. Schwalbach and P. W. Voorhees, Nano Lett. **8**, 3739 (2008)

[116] P. K. Mohseni, C. Maunders, G. A. Botton, and R. R. Lapierre, Nanotechnology **18**, 445304 (2007)

[117] P. K. Mohseni and R. R. LaPierre, Nanotechnology **20**, 025610 (2009)

[118] P. K. Mohseni, A. D. Rodrigues, J. C. Galzerani, Y. A. Pusep, and R. R. LaPierre, J. Appl. Phys. **106**, 124306 (2009)

[119] P. K. Mohseni, G. Lawson, C. Couteau, G. Weihs, A. Adronov, and R. R. LaPierre, Nano Lett. **8**, 4075 (2008)

[120] P. K. Mohseni, G. Lawson, A. Adronov, and R. R. LaPierre, IEEE J. Sel. Top. Quantum Electron. (In Press: 2010) DOI: 10.1109/JSTQE.2010.2048097

[121] M. Ohring, *Materials Science of Thin Films*, Academic Press, San Diego (2002)

[122] K. G. Günther, Z. Naturforsch. **13**, 1081 (1958)

[123] H. Freller and K. G. Günther, Thin Solid Films **88**, 291 (1982)

[124] J. R. Arthur, Jr., J. Appl. Phys. **39**, 4032 (1968)

[125] A. Y. Cho, J. Appl. Phys. **41**, 2780 (1970)

[126] J. E. Mahan, *Physical Vapour Deposition of Thin Films*, John Wiley & Sons, Inc., New York (2000)

[127] M. C. Plante, *Metal-Assisted Growth of III-V Nanowires by Molecular Beam Epitaxy*, Ph. D. Thesis, McMaster University (2009)

[128] P. R. Berger, K. Chang, P. K. Bhattacharya, and J. Singh, J. Vac. Sci. Technol. B. **5**, 1162 (1987)

[129] J. Y. Tsao, Comp. Mater. Sci. **6**, 140 (1996)

[130] E. Hecht, *Optics*, Addison Wesley, San Francisco (2002)

[131] D. B. Williams and C. B. Carter, *Transmission Electron Microscopy*, Plenum Press, New York (1996)

[132] A. Bogner, P.-H. Jouneau, G. Thollet, D. Basset, and C. Gauthier, Micron **38**, 390 (2007)

[133] L. Reimer, *Scanning Electron Microscopy*, Springer-Verlag, Berlin (1985)

[134] JEOL, Ltd., *JSM-700F Scanning Electron Microscope*, WWW Document (http://www.jeol.com), Accessed: October 1, 2010

[135] P. Gnauck, P. Hoffrogge, and J. Greiser, *A New CrossBeam Inspection Tool Combining an Ultrahigh Resolution Field Emission SEM and a High Resolution FIB*, WWW Document (http://www.zeiss.com), Accessed: October 1, 2010

[136] R. F. Egerton, *Physical Principles of Electron Microscopy*, Springer, New York (2005)

[137] Y. Leng, *Materials Characterization*, John Wiley & Sons, Singapore (2008)

[138] J. Goldstein, D. Newbury, D. Joy, C. Lyman, P. Echlin, E. Lifshin, L. Sawyer, and J. Michael, *Scanning Electron Microscopy and X-Ray Microanalysis*, Springer, New York (2003)

[139] L. A. Giannuzzi and F. A. Stevie, *Introduction to Focussed Ion Beams*, Springer, New York (2005)

[140] N. Yao, *Focussed Ion Beam Systems*, Cambridge University Press, Cambridge (2007)

[141] W. Zhou and Z. L. Wang, *Scanning Microscopy for Nanotechnology*, Springer, New York (2006)

[142] L. Reimer and H. Kohl, *Transmission Electron Microscopy*, Springer, New York (2008)

[143] J. Johansson, L. S. Karlsson, C. P. T. Svensson, T. Martensson, B. A. Wacaser, K. Deppert, L. Samuelson, and W. Seifert, Nature Mater. **5**, 574 (2006)

[144] M. Bugajski and W. Lewandowski, J. Appl. Phys. **57**, 521 (1985)

[145] S. W. Koch, M. Kira, G. Khitrova, and H. M. Gibbs, Nat. Mater. **5**, 523 (2006)

[146] S. Ghosh, Phys. Rev. B **62**, 8053 (2000)

[147] F.-Y. Juang, P. K. Bhattacharya, and J. Singh, Appl. Phys. Lett. **48**, 290 (1986)

[148] J. Singh, K.K. Bajaj, and S. Chaudhuri, Appl. Phys. Lett. **44,** 805 (1984)

[149] W. van Roosbroeck and W. Shockley, Phys. Rev. **94**, 1558 (1954)

[150] J. I. Pankove, *Optical Processes in Semiconductors*, Prentice Hall, New Jersey (1971)

[151] V. Swaminathan and A. T. Macrander, *Materials Aspects of GaAs and InP Based Structures*, Prentice Hall, New Jersey (1991)

[152] I. Vurgaftman, J. R. Meyer, and L. R. Ram-Mohan, J. Appl. Phys. **89**, 5815 (2001)

[153] K. Seeger, *Semiconductor Physics*, Springer-Verlag, Berlin (1991)

[154] C. S. Sergio, G. M. Gusev, J. R. Leite, E. B. Olshanetskii, A. A. Bykov, N. T. Moshegov, A. K. Bakarov, A. I. Toropov, D. K. Maude, O. Estibals, and J. C. Portal, Braz. J. Phys. **32**, 347 (2002)

[155] P. Y. Yu and M. Cardona, *Fundamentals of Semiconductors*, Springer-Verlag, Berlin (1995)

[156] M.-E. Pistol and X. Liu, Phys. Rev. B. **45**, 4312 (1992)

[157] S.-G. Ihn, J.-I. Song, T.-W. Kim, D.-S. Leem, T. Lee, S.-G. Lee, E.-K. Koh, and K. Song, Nano Lett. **7**, 39 (2007)

[158] E. P. A. M. Bakkers, J. A. van Dam, S. De Franceschi, L. P. Kouwenhoven, M. Kaiser, M. Verheijen, H. Wondergem, and P. van der Sluis, Nat. Mater. **3**, 769 (2004)

[159] A. L. Roest, M. A. Verheijen, O. Wunnicke, S. Serafin, H. Wondergem and E. P. A. M. Bakkers, Nanotechnology **17**, S271 (2006)

[160] L. J. Lauhon, M. S. Gudiksen, D. Wang, and C. M. Lieber, Nature **420**, 57 (2002)

[161] M. Koguchi, H. Kakibayashi, M. Yazawa, K. Hiruma, and T. Katsuyama, Jpn. J. Appl. Phys. **31**, 2061 (1992)

[162] T. Akiyama, K. Sano, K. Nakamura, T. Ito, Jpn. J. Appl. Phys. **45**, L275 (2006)

[163] R. Banerjee, A. Bhattacharya, A. Genc, B. M. Arora, Phil. Mag. Lett. **86**, 807 (2006)

[164] D. M. Cornet, V. G. M. Mazzetti, and R. R. LaPierre, Appl. Phys. Lett. **90**, 013116 (2007)

[165] L. S. Karlsson, K. A. Dick, J. B. Wagner, J.-O. Malm, K. Deppert, L. Samuelson, and L. R. Wallenberg, Nanotechnology **18**, 485717 (2007)

[166] C.-Y. Yeh, Z. W. Lu, S. Froyen, and A. Zunger, Phys. Rev. B **46**, 10086 (1992)

[167] T. Ito, Jpn. J. Appl. Phys. **37**, L1217 (1998)

[168] U. Krishnamachari, M. Borgstrom, B. J. Ohlsson, N. Panev, L. Samuelson, W. Seifert, M. W. Larsson and L. R. Wallenberg, Appl. Phys. Lett. **85**, 2077 (2004)

[169] J. Bao, D. C. Bell, F. Capasso, J. B. Wagner, T. Martensson, J. Tragardh, and L. Samuelson, Nano Lett. **8**, 836 (2008)

[170] B. A. Wacaser, K. Deppert, L. S. Karlsson, L. Samuelson, and W. Seifert, J. Cryst. Growth **287**, 504 (2006)

[171] G. Patriarche, F. Glas, M. Tchernycheva, C. Sartel, L. Largeau, and J.-C. Harmand, Nano Lett. **8**, 1638 (2008)

[172] M. P. Kulakov and I. V. Balyakina, J. Cryst. Growth **113**, 653 (1991)

[173] C.-Y. Yeh, Z. W. Lu, S. Froyen, and A. Zunger, Phys. Rev. B **45**, 12130 (1992)

[174] F. Glas, J.-C. Harmand, and G. Patriarche, Phys. Rev. Lett. **99**, 146101 (2007)

[175] V. G. Dubrovskii, N. V. Sibirev, G. E. Cirlin, J.-C. Harmand, and V. M. Ustinov, Phys. Rev. E **73**, 021603 (2006)

[176] B. S. Simpkins, M. A. Mastro, C. R. Eddy, Jr., and P. E. Pehrsson, J. Appl. Phys. **103**, 104313 (2008)

[177] A. R. Spurr, J. Ultrastruct. Res. **26**, 31 (1969)

[178] K. A. Dick, K. Deppert, L. Samuelson, L. R. Wallenberg, F. M. Ross, Nano Lett. **8**, 4087 (2008)

[179] R. R. LaPierre, B. J. Robinson, and D. A. Thompson, J. Appl. Phys. **79**, 3021 (1996)

[180] G. D. Mahan, R. Gupta, Q. Xiong, C. K. Adu, and P. C. Eklund, Phys. Rev. B. **68**, 073402 (2003)

[181] D. Spirkoska, G. Abstreiter, and A. Foncuberta i Morral, Nanotechnology **19**, 435704 (2008)

[182] O. L. Muskens, S. L. Diedenhofen, B. C. Kaas, R. E. Algra, E. P. A. M. Bakkers, J. G. Rivas, and A. Lagendijk, Nano Lett. **9**, 930 (2009)

[183] N. Skold, L. S. Karlsson, M. W. Larsson, M.-E. Pistol, W. Seifert, J. Tragardh, and L. Samuleson, Nano Lett. **5**, 1943 (2005)

[184] W. Franz, Z. Naturforsch. A. **13a**, 484 (1958)

[185] L. V. Keldysh, J. Exp. Theor. Phys. **33**, 994 (1957)

[186] M. H. M. van Weert, O. Wunnicke, A. L. Roest, T. J. Eijkemans, A. Yu. Silov, J. E. M. Haverkort, G. W. 't Hooft, and E. P. A. M. Bakkers, Appl. Phys. Lett. **88**, 043109 (2006)

[187] I. A. Goldthorpe, A. F. Marshall, and P. C. McIntyre, Nano Lett. **8**, 4081 (2008)

[188] H. Bao, C. M. Li, X. Cui, G. Q. Song, and J. Guo, Small **4**, 1125 (2008)

[189] M. Mozetic, U. Cvelbar, M. K. Sunkara, and S. Vaddiraju, Adv. Mater. **17**, 2138 (2005)

[190] L. Zhang, J. C. Yu, M. Mo, L. Wu, K. W. Kwong, and Q. Li, Small **1**, 349 (2005)

[191] A. Umar, B.-K. Kim, J.-J. Kim, and Y. B. Han, Nanotechnology **18**, 175606 (2007)

[192] C. H. Xu, C. H. Woo, and S. Q. Shi, Chem. Phys. Lett. **399**, 62 (2004)

[193] M. Law, J. Goldberger, and P. Yang, Annu. Rev. Mater. Res. **34**, 83 (2004)

[194] K. Metenier, S. Bonnamy, F. Beguin, C. Journet, P. Bernier, M. Lamy de La Chapelle, O. Chauvet, and S. Lefrant, Carbon **40**, 1765 (2002)

[195] M. Yudasaka, T. Ichihashi, D. Kasuya, H. Kataura, and S. Iijima, Carbon **41**, 1273 (2003)

[196] K. M. Liew, C. H. Wong, X. Q. He, and M. J. Tan, Phys. Rev. B. **71**, 075424 (2005)

[197] M. A. Meitl, Y. Zhou, A. Gaur, S. Jeon, M. L. Usrey, M. S. Strano, and J. A. Rogers, Nano Lett. **4**, 1643 (2004)

[198] N. Saran, K. Parikh, D.-S. Suh, E. Munoz, H. Kolla, S. K. Manohar, J. Am. Chem. Soc. **126**, 4462 (2004)

[199] C. Du, J. Yeh, and N. Pan, J. Mater. Chem. **15**, 548 (2005)

[200] V. Bocharova, A. Kiriy, U. Oertel, M. Stamm, F. Stoffelbach, R. Jerome, and C. Detrembleur, J. Phys. Chem. B. **110**, 14640 (2006)

[201] S. Kazaoui, N. Minami, R. Jacquemin, H. Kataura, and Y. Achiba, Phys. Rev. B. **60**, 13339 (1999)

[202] M. Kaempgen, G. S. Duesberg, and S. Roth, Appl. Surf. Sci. **252**, 425 (2005)

[203] Y. Kim, N. Minami, W. Zhu, S. Kazaoui, R. Azumi, and M. Matsumoto, Synth. Met. **135**, 747 (2003)

[204] H. Ko, C. Jiang, H. Shulha, and V. V. Tsukruk, Chem. Mater. **17**, 2490 (2005)

[205] M. Olek, J. Ostrander, S. Jurga, H. Mohwald, N. Kotov, K. Kempa, and M.Giersig, Nano Lett. **4**, 1889 (2004)

[206] Y. Abe, R. Tomuro, and M. Sano, Adv. Mater. **17**, 2192 (2005)

[207] Z. Wu, Z. Chen, X. Du, J. M. Logan, J. Sippel, M. Nikolou, K. Kamaras, J. R. Reynolds, D. B. Tanner, A. F. Hebard, and A. G. Rinzler, Science **305**, 1273 (2004)

[208] F. Hennrich, S. Lebedkin, S. Malik, J. Tracy, M. Barczewski, H. Rosner, and M. Kappes, Phys. Chem. Chem. Phys. **4**, 2273 (2002)

[209] S. Malik, H. Rosner, F. Hennrich, A. Bottcher, M. M. Kappes, T. Beck, and M. Auhorn, Phys. Chem. Chem. Phys. **6**, 3540 (2004)

[210] L. Hu, D. S. Hecht, and G. Gruner, Nano Lett. **4**, 2513 (2004)

[211] H. E. Unalan, G. Fanchini, A. Kanwal, A. Du Pasquier, and M. Chhowalla, Nano Lett. **6**, 677 (2006)

[212] G. Gruner, J. Mater. Chem. **16**, 3533 (2006)

[213] J. Li, L. Hu, L. Wang. Y. Zhou, G. Gruner, and T. J. Marks, Nano Lett. **6**, 2472 (2006)

[214] C. M. Aguirre, S. Auvray, S. Pigeon, R. Izquierdo, P. Desjardins, and R. Martel, Appl. Phys. Lett. **88**, 183104 (2006)

[215] D. Zhang, K. Ryu, X. Liu, E. Polikarpov, J. Ly, M. E. Thompson, and C. Zhou, Nano Lett. **6**, 1880 (2006)

[216] R. A. Hatton, A. J. Miller, and S. R. P. Silva, J. Mater. Chem. **18**, 1183 (2008)

[217] B. J. Landi, R. P. Raffaelle, S. L. Castro, and S. G. Bailey, Prog. Photovoltaics **13**, 165 (2005)

[218] T. M. Barnes, X. Wu, J. Zhou, A. Duda, J. van de Legemaat, T. J. Coutts, C. L. Weeks, D. A. Britz, and P. Glatkowski, Appl. Phys. Lett. **90**, 243503 (2007)

[219] E. Kymakis, E. Stratakis, and E. Koudoumas, Thin Solid Films **515**, 8598 (2007)

[220] K. Lee, Z. Wu, Z. Chen, F. Ren, S. J. Pearton, and A. G. Rinzler, Nano Lett, **4**, 911 (2004)

[221] S. H. Jo, D. Banerjee, and Z. F. Ren, Appl. Phys. Lett. **85**, 1407 (2004)

[222] Y. Zhang and H. Dai, Appl. Phys. Lett. **77**, 3015 (2000)

[223] B. H. Juarez, C. Klinke, A. Kornowski, and H. Weller, Nano Lett. **7**, 3564 (2007)

[224] G. Lawson, F. Gonzaga, J. Huang, G. de Silveira, M. A. Brook, and A. Adronov, J. Mater. Chem. **18**, 1694 (2008)

[225] J. Cabana and R. Martel, J. Am. Chem. Soc. **129**, 2244 (2007)

[226] B.-S. Kong, D.-H. Jung, S.-K. Oh, C.-S. Han, and H.-T. Jung, J. Phys. Chem. C **111**, 8377 (2007)

[227] Y. Liu, Z. Y. Zhang, Y. F. Hu, C. H. Jin, and L.-M. Peng, J. Nanosci. Nanotechnol. **8**, 252 (2008)

[228] Private Communication from Dr. Zhilin Peng: Centre for Emerging Device Technologies, McMaster University (2008)

[229] S. Stankovich, D. A. Dikin, G. H. B. Dommett, K. M. Kohlhass, E. J. Zimney, E. A. Stach, R. D. Piner, S. T. Nguyen, and R. S. Ruoff, Nature **442**, 282 (2006)

[230] P. Blake, P. D. Brimicombe, R. R. Nair, T. J. Booth, D. Jiang, F. Schedin, L. A. Ponomarenko, S. B. Morozov, H. F. Gleeson, E. W. Hill, A. K. Geim, and K. S. Novoselov, Nano Lett. **8**, 1704 (2008)

[231] Y. Xu, H. Bai, G. Lu, C. Li, and G. Shi, J. Am. Chem. Soc. **130**, 5856 (2008)

[232] Q. Liu, Z. Liu, X. Zhang, N. Zhang, L. Yang, S. Yin, and Y. Chen, Appl. Phys. Lett. **92**, 223303 (2008)

[233] M. Frietag, Nat. Nanotechnol. **3**, 455 (2008)

[234] D. Li and R. B. Kaner, Science **320**, 1170 (2008)

[235] J. T. Robinson, M. Zalalutdinov, J. W. Baldwin, E. S. Snow, Z. Wei, P. Sheehan, and B. H. Houston, Nano Lett. **8**, 3441 (2008)

[236] S. Park, J. An, I. Jung, R. D. Piner, S. J. An, X. Li, A, Velamakanni, and R. S. Ruoff, Nano Lett. **9**, 1593 (2009)

[237] G. Eda, G. Fanchini, and M. Chhowalla, Nat. Nanotechnol. **3**, 270 (2008)

[238] H. A. Becerril, J. Mao, Z. Liu, R. M. Stoltenberg, Z. Bao, and Y. Chen, ACS Nano **2**, 463 (2008)

[239] G. Binning, H. Rohrer, Ch. Gerber, and E. Weibel, Phys. Rev. Lett. **49**, 57 (1982)

[240] M. P. Zach, J. T. Newberg, L. Sierra, J. C. Hemminger, and R. M. Penner, J. Phys. Chem. B. **107**, 5393 (2003)

[241] M. B. Zach, K. Inazu, K. H. Ng, J. C. Hemminger, and R. M. Penner, Chem. Mater. **14**, 3206 (2002)

[242] C. Li, D. Zhang, B. Lei, S. Han, X. Liu, and C. Zhou, J. Phys. Chem. B. **107**, 12451 (2003)

[243] C. Tang, Y. Bando, T. Sato, and K. Kurashima, J. Mater Chem. **12**, 1910 (2002)

[244] S. Vaddiraju, A. Mohite, A. Chin, M. Meyyappan, G. Sumansekera, B. W. Alphenaar, and M. K. Sunkara, Nano Lett. **5**, 1625 (2005)

[245] H. T. Ng, J. Li, M. K. Smith, P. Nguyen, A. Cassell, J. Han, and M. Meyyappan, Science **300**, 1249 (2003)

[246] H. Yoon, K. Seo, N. Bagkar, J. In, J. Park, J. Kim, and B. Kim, Adv. Mater. **21**, 1 (2009)

[247] J. Turkevich, P. C. Stevenson, and J. Hillier, Disc. Farad. Soc. **11**, 55 (1951)

[248] G. Frens, Nature Phys. Sci. **241**, 20 (1973)

[249] K. S. Novoselov, A. K. Geim, S. V. Morozov, D. Jiang, Y. Zhang, S. V. Dubonos, I. V. Grigorieva, and A. A. Firsov, Science **306**, 666 (2004)

[250] F. Martelli, S. Rubini, F. Jabeen, L. Felisari, and V. Grillo, J. Cryst. Growth (In Press: 2010) DOI: 10.1016/j.jcrysgro.2010.10.004

[251] F. Jabeen, V. Grillo, S. Rubini, and F. Martelli, Nanotechnology **19**, 275711 (2008)

[252] S. Plissard, K. A. Dick, G. Larrieu, S. Godey, A. Addad, X. Wallart, and P. Caroff, Nanotechnology **21**, 385602 (2010)

[253] S. Plissard, K. A. Dick, X. Wallart, and P. Caroff, Appl. Phys. Lett. **96**, 121901 (2010)

[254] C. Colombo, D. Spirkoska, M. Frimmer, G. Abstreiter, and A. Foncuberta i Morral, Phys. Rev. B. **77**, 155326 (2008)

[255] A. Fontcuberta i Morral, C. Colombo, G. Abstreiter, J. Arbiol, and J. R. Morante, Appl. Phys. Lett. **92**, 063112 (2008)

[256] A. Fontcuberta i Morral, D. Spirkoska, J. Arbiol, M. Heigoldt, J. R. Morante, and G. Abstreiter, Small **4**, 899 (2008)

[257] B. Mandl, J. Stangl, E. Hilner, A. A. Zakharov, K. Hillerich, A. W. Dey, L. Samuelson, G. Bauer, K. Deppert, and A. Mikkelsen, Nano Lett. **10**, 4443 (2010)

[258] P. Krogstrup, R. Popovitz-Biro, E. Johnson, M. H. Madsen, J. Nygard, and H. Shtrikman, Nano Lett. **10**, 4475 (2010)

[259] J. Blackman, *Metallic Nanoparticles*, Elsevier, Amsterdam (2009)

[260] M. Aagesen, E. Johnson, C. B. Sorensen, S. O. Mariager, R. Feidenhans'l, E. Spiecker, J. Nygard, and P. E. Lindelof, Nat. Nanotechnol. **2**, 761 (2007)

[261] E. S. Tok, T. S. Jones, J. H. Neave, J. Zhang, and B. A. Joyce, Appl. Phys. Lett. **71**, 3278 (1997)

[262] E. T. Mickelson, C. B. Huffman, A. G. Rinzler, R. E. Smalley, R. H. Huage, and J. L. Margrave, Chem. Phys. Lett. **296**, 188 (1998)

[263] J. Nelson, *The Physics of Solar Cells*, Imperial College Press, London (2008)

[264] D. E. Perea, E. R. Hemesath, E. J. Schwalbach, J. L. Lensch-Falk, P. W. Voorhees, and L. J. Lauhon, Nat. Nanotechnol. **4**, 315 (2009)

[265] J. E. Allen, D. E. Perea, E. R. Hemesath, and L. J. Lauhon, Adv. Mater. **21**, 3067 (2009)

[266] V. Sivakov, G. Andra, A. Gawlik, A. Berger, J. Plentz, F. Falk, and S. H. Christiansen, Nano. Lett. **9**, 1549 (2009)

[267] A. Behnam, J. L. Johnson, Y. Choi, M. G. Ertosun, A. K. Okyay, P. Kapur, K. C. Saraswat, and A. Ural, Appl. Phys. Lett. **92**, 243116 (2008)

[268] I.-H. Tan, G. L. Snider, L. D. Chang, and E. L. Hu, J. Appl. Phys. **68**, 4071 (1990)

[269] E. Havard, T. Camps, V. Bardinal, L. Salvagnac, C. Armand, C. Fontaine, and S. Pinaud, Semicond. Sci. Technol. **23**, 035001 (2008)

[270] Y. Kitauchi, Y. Kobayashi, K. Tomioka, S. Hara, K. Hiruma, T. Fukui, and J. Motohisa, Nano Lett. **10**, 1699 (2010)

[271] H. J. Joyce, J. Wong-Leung, Q. Gao, H. H. Tan, and C. Jagadish, Nano Lett. **10**, 908 (2010)

[272] J. Johansson, L. S. Karlsson, K. A. Dick, J. Bolinsson, B. A. Wacaser, K. Deppert, and L. Samuelson, Cryst. Growth Des. **9**, 766 (2009)

[273] K. A. Dick, P. Caroff, J. Bolinsson, M. E. Messing, J. Johansson, K. Deppert, L. R. Wallenberg, and L. Samuelson, Semicond. Sci. Technol. **25**, 024009 (2009)

[274] P. Caroff, J. Bolinsson, and J. Johansson, IEEE J. Sel. Top. Quantum Electron. (In Press: 2010) DOI: 10.1109/JSTQE.2010.2070790

[275] J. Bolinsson, *The Crystal Structure of III-V Semiconductor Nanowires: Growth and Characterization*, Ph. D. Thesis, Lund University (2010)

[276] D. J. Gargas, M. E. Toimil-Molares, and P. Yang, J. Am. Chem. Soc. **131**, 2125 (2009)

[277] S. Ruhle, L. K. van Vugt, H.-Y. Li, N. A. Keizer, L. Kuipers, and D. Vanmaekelbergh, Nano Lett. **8**, 119 (2008)

[278] V. G. Bordo, Phys. Rev. B. **81**, 035420 (2010)

[279] B. Hua, J. Motohisa, Y. Ding, S. Hara, and T. Fukui, Appl. Phys. Lett. **91**, 131112 (2007)

[280] B. Hua, J. Motohisa, S. Hara, and T. Fukui, Phys. Stat. Sol. (c) **5**, 2722 (2008)

[281] L. Yang, J. Motohisa, T. Fukui, L. X. Jia, L. Zhang, M. M. Geng, P. Chen, and Y. L. Liu, Opt. Express **17**, 9337 (2009)